SAPIENZA
UNIVERSITÀ DI ROMA

Novel control knobs for multidimensional stimulated Raman spectroscopy

Sapienza, Università di Roma

Dottorato di ricerca in Modelli matematici per l'Ingegneria, Elettromagnetismo e Nanoscienze

XXXI Ciclo

Candidate:

Giuseppe Fumero
ID number 1347711

Thesis advisor:

Prof. Tullio Scopigno

A thesis submitted in partial fulfillment of the requirements for the degree of Doctor of Philosophy in Mathematical models for Engineering, Electromagnetics and Nanosciences

November 2018

Thesis defended on 4 February 2019
in front of a Dissertation Committee composed by:

Prof. Giulio Cerullo
Prof. Antonio Morini
Prof. Massimo Santarsiero

Novel control knobs for multidimensional stimulated Raman Spectroscopy
Ph.D. thesis. Sapienza – Università di Roma

This thesis has been typeset by LaTeX. Frontispiece inspired by the Sapthesis class.

Version: January 27, 2019
Contact: giuseppe.fumero@gmail.com

Alla mia famiglia:
Amedeo, Vittoria, Carlo Alberto & Marco

Contents

Preface

This thesis collects the main results I have obtained during the three years spent working at Sapienza University as a PhD student and University of California, Irvine as a visiting scholar. During this time, I participated in theoretical and experimental research activities mainly devoted to ultrafast spectroscopy and, in particular, to time and frequency domain coherent Raman spectroscopies. As a member of the Femtoscopy group in Rome, I participated in the development of the pump-probe and stimulated Raman research lines. In particular, my experimental activity consisted in the optimization of the impulsive Raman setup and data acquisition software and in gathering the data reported in chapter 4 and 5. Moreover, I had a major role in data analysis and interpretation of the measurements presented in chapter 5 and collaborated in the elaboration of the models and simulations for resonant stimulated Raman and impulsive Raman presented in chapters 1 and 4. I developed the theoretical framework for resonant two dimensional Raman spectroscopy and performed the interpretation and fit of the data collected by the Kukura's group in Oxford, presented in chapter 6. I also participated in writing research articles based on these works, which are enumerated at the end of the thesis.

I would like to thank prof. Tullio Scopigno, prof. Shaul Mukamel, prof. Annamaria Petrozza and prof. Philipp Kukura together with the members of their groups for these ultrafast three years of exciting hikes in science.

G.F.

Introduction

Understanding the behavior of complex systems is greatly simplified when the proper energy and time scales over which their evolution occurs are investigated. Consequently, deciphering the dynamics of atoms and molecules requires to access the domain of femtoseconds, and even shorter timescales are involved in the case of electrons. Probing such extreme phenomena is the challenging task at which ultrafast spectroscopy aims.

In the last forty years, the development of pulsed laser sources and nonlinear optical techniques has allowed the study of phenomena invisible to electronic devices, through the manipulation of matter macroscopic phases on picosecond and sub-picosecond timescales. This technological leap provided sophisticated and customized ultrashort spectroscopic protocols in a wide energy range, from terahertz to x rays, fully realizing the pioneering view of the *ultrafast stroboscope*, dreamed by the father of femtochemistry Ahmed Zewail. Indeed, using the proper technique, short flashes of light are currently able to record stop-motion images of a dynamic processes as fast as a chemical reaction. The study of the nonlinear response due to external impulsive optical perturbations has been applied to a wide range of scientific cases, fueling a parallel boost in electronic and vibrational spectroscopies.

The frontier in ultrafast sciences is now gradually shifting to tackle the interplay between these two degrees of freedom. Vibronic coupling is considered at the grounds of fascinating processes which connect conceptual topics from the foundation of quantum mechanics, as the breakdown of the Born-Oppenheimer approximation, to technological application, as the coherent energy transfer in biomimic photosynthetic devices or the bewildering effects of strong electron-phonon coupling in novel materials as graphene and third generation semiconductors. Probing electronic and vibrational interactions at the same time is complicated by the time and energy scale separation between the two. Thus, one dimensional spectroscopies are weakened by resolution limits which may partially hamper their use in this direction. Multidimensional techniques can cope this limit spreading the information on separate spectroscopic axes, consequently disentangling the relative resolutions. Couplings between different agents in the microscopic description of the sample dynamics are directly revealed through the presence of cross peaks in the multidimensional maps.

In this context, the research presented in this thesis has been devoted to the design, realization and interpretation of novel approaches to multidimensional Impulsive Stimulated Raman Spectroscopy (ISRS). Coherent Raman techniques are indeed able to measure vibrational spectra using visible light, which provides at the same time information about the electronic degrees of freedom when tuned resonant with the absorption edges of the sample. A concerted combination between theory and experiments is the key to successfully probe the quantum properties of the matter on which the vibronic interactions rely. For this reason, the experimental efforts have been flanked by a powerful theoretical toolbox given by the nonlinear response formalism. This framework represents a natural link between theory and experiments and supplies a common language to describe very different techniques, gathering their features to design new experimental protocols. We found that the properties of the probe spectral envelope, the wise tuning of resonant conditions and the choice of the pulses scheme may be used to built multidimensional ISRS maps. The developed schemes have been experimentally tested in three different contexts: the coherent control of ground and excited state vibrations in a liquid solvent, the study of charge photogeneration in a hybrid organic-inorganic perovskite and the vibronic coupling in a

prototypical fluorescent protein.

The research work presented here is structured in seven chapters and one appendix, which summarize the main theoretical and experimental results achieved during the preparation of this doctoral thesis. The core of the thesis is contained in Chapters 4, 5 and 6, which discuss the application of multidimensional ISRS in different scenarios. Since the investigated scientific problems belong to quite different backgrounds, each of these result chapters is introduced by a brief summary of the relevant field. Specifically:

In Chapter 1, we introduce the context in which this thesis is developed. The basics features of ultrafast spectroscopy based on the pump-probe scheme and nonlinear Raman techniques are briefly discussed. We then present the classical mechanism underlying spontaneous and coherent Raman effects, while the detailed, microscopic derivation is postponed to Chapter 2. The remaining part of the chapter is devoted to introduce how multidimensional information can be encoded in the parameters of time and frequency domain stimulated Raman spectroscopies, following the key words in the title of the thesis. As an example, the lineshapes from stimulated Raman spectra measured in hemeproteins are studied as a function of the resonance and the vibrational mode.

In Chapter 2, the nonlinear response theory is presented as the unifying framework in which all the different experiments in the thesis are conceived, designed and interpreted. In the first part, the principles of quantum mechanics in the density matrix framework are briefly revised, defining the properties of the Liouville space. Then, the concept of nonlinear polarization is introduced and calculated perturbatively in this space. The light matter interaction is derived from both the classical and quantum treatment of electromagnetism, showing that Feynman diagrams are a convenient way to isolate the relevant terms in the perturbative expansion. Finally, we report the rules to derive expressions for the nonlinear signal in the time and frequency domains directly from the diagrams.

In Chapter 3, the experimental setups and the data acquisition are described in detail. We analyze the tools and the physical mechanisms at the base of the generation and handling of the ultrashort pulses used in the experiments and also provide an overview of the data analysis routine applied to the impulsive stimulated Raman measurements presented in the thesis.

Chapter 4 is the first of the three chapters presenting the main results of this work. Here, we discuss how the broadband envelope of a supercontinuum probe pulse can be shaped to manipulate vibrational coherences in ISRS. In particular, probe wavelength resolved ISRS maps of a liquid solvent are measured changing the chirp of the probe pulse and interpreted in the light of the diagrammatic framework. As a starting point, the effect of the probe chirp and sample length are investigated to rationalize previously unexplained dependencies of low frequency modes on the dispersed probe wavelength. Then, the probe chirp is demonstrated as a control knob to coherently control ISRS modes and to assign spectral features to specific electronic states.

In Chapter 5, broadband ISRS is applied to study electron-phonon coupling in lead halide hybrid perovskites. After briefly revising the field of organic-inorganic perovskite optoelectronics, we present experimental measurements on methylammonium lead bromide thin films, comparing the ISRS response of the system upon excitation above and below the band gap. The results are interpreted in the light of the recently proposed polaronic nature of photocarriers in these materials.

In Chapter 6, we present a novel multidimensional ISRS scheme, which combines the capabilities of two dimensional Fourier transform techniques with the structural sensitivity of resonant stimulated Raman. We show how this technique can be used to probe mode couplings between different active sites in molecular compounds and determine the shape of vibrationally structured excited state potential energy surfaces. We apply the diagrammatic approach to design 2D ISRS and assign the origin of the different spectral features in a model system. Then, the proposed scheme is benchmarked by addressing vibronic coupling in Green Fluorescent Protein during the first steps of its photoinduced dynamics.

Finally, in Chapter 7, the main results obtained in this work are summarized and analyzed

under a common perspective. The appendix reports the calculation of transition integrals for the linearly displaced harmonic model. A list of the publications and contributions to international conferences of the author is included at the end of the thesis.

1 Stimulated Raman spectroscopy in the time and frequency domains

Vibrational spectroscopy is diffusely used in science for its elevated sensibility in probing the structural properties of molecules. It concerns the study of electromagnetic coupling between radiation and the vibrational degrees of freedom of matter, whose frequencies range from a few to thousands wavenumbers. The vibrational energies of the molecule can be studied exploiting infrared absorption and the Raman effect. In this work, we focus in particular on techniques based on the latter. In the last decades, the development of femtosecond laser sources led to the implementation of nonlinear vibrational spectroscopies that allowed to gain new insights in a broad class of topics, crossing the borders between Physics, Chemistry and life sciences [1]. Among them, stimulated Raman spectroscopies represent a valuable tool for scientific investigation, because of their high temporal and spectral resolution [2].

Recently, the interest of the ultrafast community focused in studying the role of vibronic effects in molecules and electron-phonon coupling in solids, looking closely at the concerted evolution of vibrational and electronic degrees of freedom, with the aim to better understand the structural properties of the matter during excited state dynamics. This need fueled the conception and development of novel spectroscopic schemes that make use of multiple parameters to probe vibronic interactions, resulting in a multidimensional approach to stimulated Raman scattering.

In this chapter, the fundamentals of ultrafast spectroscopy and Raman effect are presented. We then introduce two different approaches to stimulated Raman scattering in the time and frequency domains, with particular emphasis on the features that make these techniques multidimensional in nature.

1.1 Spectroscopic tools

The principal experimental tool exploited in the investigation of ultrafast processes is the *pump-probe* scheme. In a typical pump-probe experiment, sketched in Fig. 1.1, two femtosecond pulses are used to investigate the ultrafast response of the sample. The dynamics of interest is started by means of a first ultrashort laser *pump* pulse which photoexcites the system. The arrival time of the pump pulse establishes a temporal reference, in respect of which the evolution of the sample is probed. For this purpose, a second laser pulse, called *probe* pulse, is sent after a tunable time delay and used to detect the pump induced modifications to the optical response of the material. As we will discuss in detail in Chapter 2, in pump-probe, the spectroscopic signal is generated in the same direction of the probe pulse and the measured quantity is ultimately the interference between the signal and the probe. Collecting the transmitted probe pulse at different time delays allows to follow the temporal dynamics.

A critical issue in a pump-probe experiment is the synchronization of the laser pulses, because only a strict control of the time delay enables the achievement of high temporal resolution. Since in ultrafast spectroscopy timescales far below the nanosecond are reached, electronic synchro-

nization is not possible. Thus, the relative timing between the pulses is generally accomplished by generating the pump and probe beams from a common source and sending either one or the other along an adjustable delay line, changing its optical path. The resolution limit on the time delay accesible by moving the delay line through a common translator with micrometric precision is $\sim 2\frac{\mu m}{c} = 6$ fs. Therefore, the main limitations are due to the pulses duration. Since the advent of mode-locked laser source in the early '60s [3], technological advancements have enabled to decrease more and more the minimal reachable duration. Nowadays, mode-locked sources coupled to nonlinear optics techniques to manipulate the generated pulses allow to synthesize pulses in the frequency range that spans from mid IR to UV as short as a few optical cycles [4, 5]. Moreover, the recent innovations in intense femtosecond x-ray free electron lasers and high harmonic generation in tabletop ultrafast setups promise the extension of nonlinear optical techniques in the pump-probe scheme to the extreme-ultraviolet (EUV), soft and hard x-ray regime, with the possibility to access the attosecond domain [6–10].

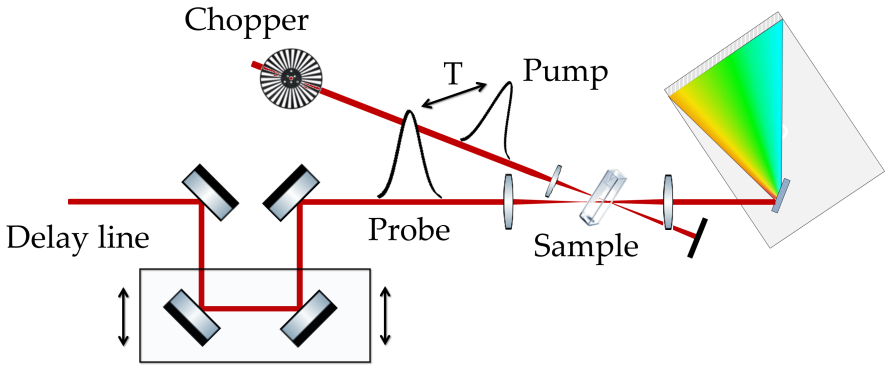

Figure 1.1: Schematic representation of a typical pump-probe setup. The output of the laser source is split in two: a fraction is used as pump, while the other, optically delayed, serves as probe pulse. The probe, after the interaction with the sample, is spectrally resolved by the detector.

The feature that guarantees the success and the wide applicability of the pump-probe approach is its versatility. Indeed, this scheme can be generalized using multiple pulses, shaped in their temporal and spectral envelopes, in each of the two stages which compose the experiment, the preparation and the detection. In this way, different optical effects can be exploited to generate the spectroscopic signal. Thus, the pump-probe scheme defines a toolbox in which many different techniques are stored, discriminated by the pulse geometry and characteristics and by the exploited physical effect. Among the wide class of ultrafast phenomena recently studied through these techniques there are isomerization, bond breaking and recombination in molecules, charge transfer and energy redistribution upon excitation of short living intermediates, ultrafast magnetisms and the photophysics of novel materials such as graphene and organic semiconductors [11–18].

The simplest geometry feasible with a pump-probe setup is the Transient Absorption (TA) [19, 20], in which the absorption of the detected pulse is measured in the probe part of the experiment. TA can be used to follow many types of time-dependent relaxation processes, as population relaxation from electronic excited states, chemical kinetics and quantum beats. Even if the principle under this technique is the same of linear absorption, TA is a nonlinear effect and gives information about the dynamics of the sample. In a typical experiment, one pump and one probe pulse, centered at the same or at two different wavelengths (one and two color TA), are separated by a time delay T and spatially overlapped on the sample. The pump causes the transition to a non-equilibrium state whose time-dependent property are detected by monitoring the pump induced intensity change of the transmitted probe. The depletion of the incident probe, which usually is broadband, is collected for different time delays and spectral components of probe beam. Thus, the transient absorption data are obtained by the acquisition

of the probe intensity in presence or absence of the pump induced excitation in the sample, by means of mechanical or optical chopping of the pump pulse. The collection of the pump-off spectra allows to monitor the sample degradation and have a continuous absorption reference to compare with the transient data. The quantity of interest in TA experiments is:

$$\Delta A(\lambda, T) = \frac{A_{\text{on}}(\lambda, T) - A_{\text{off}}(\lambda)}{A_{\text{off}}(\lambda)} \tag{1.1}$$

where the subscripts on and off refer to the absorption spectrum A of the transmitted probe with or without the pump pulse focusing on the sample, T is the pump-probe delay and λ the dispersed probe wavelength. In general, the contributions in a TA spectrum arise from

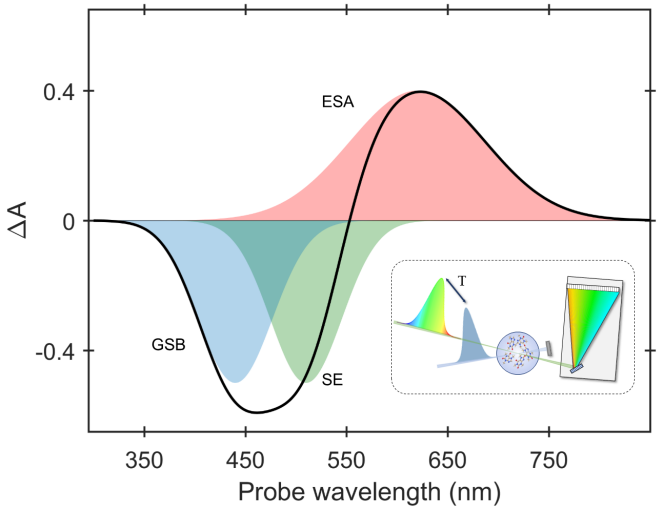

Figure 1.2: Contributions to the TA signal for a fixed delay T: ground state bleach (blue shaded area), stimulated emission (green shaded area), excited-state absorption (red shaded area) and the sum of these contributions (black solid line). The inset sketches the pulses scheme.

ground state bleach (GSB), stimulated emission (SE) and excited state absorption (ESA). GSB is originated from the decrease of ground state population, due to the promotion of a fraction of the molecules in the sample to the excited state. Hence, the ground-state absorption in the excited sample becomes less than that in the non-excited sample, resulting in a negative signal in the TA spectrum, in the same wavelength region of the linear absorption. At the same time, SE and ESA occur for optically allowed transitions. In SE, a photon from the probe pulse induces the relaxation of excited molecules in the sample through the emission of a stimulated photon. Both the photon emitted and the probe photon are measured, resulting in an increase of the light intensity on the detector and, thus, to a negative TA signal. For the opposite mechanism, a positive signal for ESA is observed in the TA spectrum, due to the absorption of light by the excited state population. These contributions are depicted in Fig. 1.2.

Transient absorption techniques are characterized by high temporal resolution, controlled by the time duration of the pulses involved, but are not able to probe the fine vibrational structure of the sample, both on the ground and excited state. To overcome this limit, the pump-probe scheme has been extended in order to exploit nonlinear optical effects as probes, driven by multiple pulses interacting in a controlled geometry. In particular, in this chapter we will focus on time-resolved vibrational spectroscopies based on the Raman effect. Notably, since Raman spectroscopies exploit visible and UV light to excited the sample, it is possible to probe at the same time the vibrational structure, to which the Raman effect is sensitive, and the electronic resonances, tuning the pulses in resonance with one of the absorption edge of the material. This peculiarity opens to the possibility of studying the interaction between the two degrees of freedom, provided that wisely planned schemes are adopted to select the wanted piece of information and understand its physical origin.

1.2 Spontaneous vs stimulated Raman Scattering

The Raman effect consists in the inelastic scattering of incident light photons by a system of atoms or molecules with the generation of new frequencies during the light-matter interaction. It was first discovered by C. V. Raman [21] and by Grigory Landsberg and Leonid Mandelstam [22], independently.

When a monochromatic light beam of frequency ω interacts with the matter, the majority of the incident photons are scattered elastically and do not change their frequency. This phenomenon is known as *Rayleigh scattering*. However, if the scattered light is spectrally analyzed, it is found that a small fraction is scattered at new frequencies $\omega' = \omega \pm \omega_{v_i}$, where ω_{v_i} is one of the characteristic roto-vibrational modes of the sample. This process is known as *spontaneous Raman scattering*. Incident photons inelastically scattered to lower and higher frequencies are called Stokes and anti-Stokes photons, respectively.

These optical effects can be understood, on first approximation, by classical argumentations, as resulting from the interaction of the electric field component of the electromagnetic incident radiation with the charged particles of the material. Generally, positive and negative charges are slightly displaced from their equilibrium position by the applied field. If we consider a wave in the visible or near-IR region of the electromagnetic spectrum, the electric field associated with the radiation oscillates with a frequency which is too high for the nuclei to follow. Then, optical resonances in this frequency range are predominantly related to the electronic degrees of freedom of the sample. The rearrangement of the local charge density due to the incident light induces an electric dipole moment:

$$\mu(t) = -e \cdot r(t) \tag{1.2}$$

being e the charge of the electron and $r(t)$ its displacement from the equilibrium. Although only electrons are directly involved in the interaction with the radiation field, the information about the nuclear dynamics is contained in their motion, since the adiabatic electronic potential depends on the nuclear coordinates. As a consequence, it is useful to connect the electric dipole moment to the polarizability tensor $\alpha(t)$, which depends on nuclear coordinates Q. Under the assumption of light pulses far from electronic resonances, we can write:

$$\mu(t) = \alpha(t)E(t) \tag{1.3}$$

From the classical theory of electrodynamics, it is well known that a dipole, oscillating with frequency ω, emits electromagnetic radiation whose electric field component is

$$E_S(\omega) = \frac{\omega^2}{4\pi\epsilon_0 c^2}|\mu(t)|\frac{e^{ikr}}{r}sin\theta \tag{1.4}$$

where r and θ are the distance from the dipole location and the observation point and the angle relative to the dipole axis. The outgoing energy flux is given by the time averaged Poynting vector S:

$$S = \frac{\epsilon_0 c}{2}|E_S|^2 \tag{1.5}$$

whose integral over the unit sphere gives the total energy radiated by the single dipole.

In a non physical picture in which nuclear dynamics is absent, the polarizability α can be approximate by a constant α_0. However, since roto-vibrational modes are present in the sample, these modes will be involved in the light-matter interaction, producing small modifications to α. We can express the polarizability in terms of the nuclear normal coordinates Q_i and expand it in a Taylor series:

$$\alpha = \alpha_0 + \sum_k \left(\frac{\partial\alpha}{\partial Q_k}\right)_0 Q_k + \frac{1}{2}\sum_{k,l}\left(\frac{\partial^2\alpha}{\partial Q_k \partial Q_l}\right)_0 Q_k Q_l + \dots \tag{1.6}$$

where the subscript 0 means the equilibrium condition. In harmonic approximation, the nuclear motion along Q reads

$$Q_k = Q_{k_0}\cos(\omega_k t + \phi_k) \tag{1.7}$$

Breaking the expansion at the first order in eq. 1.6, we obtain

$$\alpha_k = \alpha_0 + \alpha'_k Q_{k_0} \cos(\omega_k t + \phi_k) \tag{1.8}$$

where $\alpha'_k = \left(\frac{\partial \alpha}{\partial Q_k}\right)_0$. If we write the incoming field as $E(t) = E_0 \cos(\omega t)$ and recall eq. 1.3, after some mathematical handling, we finally obtain the expression of the induced dipole moment that accounts for nuclear modes:

$$\mu(\omega) = \alpha_0(\omega) E_0 \cos(\omega t) + \frac{1}{2} \sum_k \alpha'_k Q_{k_0} \left[\cos(\omega t + \omega_k t + \phi_k) + \cos(\omega t - \omega_k t - \phi_k)\right] \tag{1.9}$$

The first term on the right-hand side of eq. 1.9 describes the elastic Rayleigh scattering. However, it is evident from the second term that the dipole oscillates also with frequencies $\omega \pm \omega_k$, due to Stokes and anti-Stokes Raman contributions. We note that while every molecule exhibits Rayleigh scattering, because non vanishing components of α_0 always exists, Raman features are present in the scattered spectra only if at least one component of the polarizability tensor is not constant in Q, as the Raman term in eq. 1.9 is proportional to $\frac{\partial \alpha}{\partial Q}$. The polarizability depends strongly on the symmetry of the nuclear mode, which gives rise to the selection rules in Raman transitions. Using the expression for the dipole radiation in eq. 1.4, we obtain the averaged intensity of the Raman scattered light:

$$I(\omega) = \frac{\omega^4}{12\pi\epsilon_0 c^3} Q_0^2 |E_0|^2 |\frac{\partial \alpha}{\partial Q}|^2 \tag{1.10}$$

We stress that the scattered intensity depends linearly on the intensity of the pump beam $I_0 = |E_0|^2$. The classical model allows to predict the existence of the Raman effect as well as the main characteristics, even tough the fine description requires a quantum mechanical treatment. For example the relative intensity between the Stokes and anti-Stokes features comes from the Boltzmann distribution. Indeed, from the material point of view, the Raman scattering concerns a transition from a population state a to a population state b, through a non steady state, the vibrational coherence. Whether the energy of the state a is lower or higher than that of the state b, the Raman process is further defined as Stokes or anti-Stokes scattering. In Stokes scattering, the population of the ground state is involved in a transition to the excited states, whereas in anti-Stokes scattering, a portion of the vibrationally excited state population is transferred to the ground state. Thus, in a Raman spectrum taken at room temperature, Stokes features are more intense than the anti-Stokes ones because the latter, originating from an excited state population, are proportional to a lower occupation factor, due to the Boltzmann distribution.

So far, we have considered only one oscillating dipole as the source of the scattered field. In general, considering N electric dipoles per unit volume, the macroscopic polarization reads:

$$P(t) = N\mu(t) \tag{1.11}$$

An important issue when dealing with a set of emitting sources is considering the interference effect when we sum the fields of the different dipoles. The phase ϕ_k of the Raman scattered light in eq. 1.9 is dependent on the nuclear mode. At equilibrium, the vibrations of different molecules are uncorrelated and each dipole field is emitted with random phase. Therefore different fields interfere destructively. The total signal is incoherent and its intensity is proportional to the number of Raman scatterers in the sample. Thus we refer to this effect as spontaneous.

Coherent signals are characterized by well-defined phase relationships between their sources. Among them Coherent Raman Scattering (CRS) provides an important tool in ultrafast spectroscopy. CRS effects are nonlinear and arise in light-matter interaction when the action of multiples incident fields or very intense radiation is involved so that the linear response theory becomes inadequate. In this case, the dependence between the driving electric fields and the induced polarization is not linear anymore, but corrections are needed. If these corrections are small enough, the macroscopic polarization P can be expanded in power series of the fields.

$$P = \epsilon_0 \left[\chi^{(1)} E + \chi^{(2)} E^2 + \chi^{(3)} E^3 + \dots\right] = P^{(1)} + P^{(2)} + P^{(3)} + \dots \tag{1.12}$$

where $\chi^{(n)}$ is the nth order susceptibility and E is the total field applied[1]. Here, we present a classical description of coherent Raman scattering [23]. For the sake of simplicity, we consider the action of only two monochromatic light fields that interact with a single harmonic nuclear mode per molecule. The general case comes straightforward.
As for spontaneous Raman, we classically assume that the vibrational coordinates obey a damped harmonic oscillator equation of motion with a resonance frequency ω_v. The total field incident on the sample is the sum of two monochromatic intense fields:

$$E_i(t) = A_i e^{-i\omega_i t} + c.c. \quad i = 1,\, 2 \tag{1.13}$$

with $\omega_1 > \omega_2$ and $\omega_i \gg \omega_v$. Since the frequencies of the incoming fields are far from the resonance of the oscillator, only the electron cloud surrounding the nuclei is driven efficiently. In addition, due to the high intensity of the fields, nonlinear effects arise and the polarization results oscillating at combination frequencies. Let us consider the difference frequency $\Omega = \omega_2 - \omega_1$. The driven oscillation of the electrons forms an effective force acting on the vibrational coordinates:

$$F(t) = \left(\frac{\partial \alpha}{\partial Q}_0\right)\left[A_1 A_2^* e^{-i\Omega t} + c.c.\right] \tag{1.14}$$

The nuclear motion thus obeys a forced oscillator equation:

$$\frac{d^2Q}{dt^2} + 2\gamma\frac{dQ}{dt} + \omega_v^2 Q = \frac{F}{m} \tag{1.15}$$

whose solution oscillates with frequency Ω and amplitude:

$$Q(\Omega) = \frac{1}{m}\left(\frac{\partial \alpha}{\partial Q}_0\right)\frac{A_1 A_2^*}{\omega_v^2 - \Omega^2 - 2i\Omega\gamma} \tag{1.16}$$

The nuclear mode is driven indirectly by the joint action of the incident fields. The amplitude of the oscillation depends on the applied field and on the electronic polarizability. Furthermore when the difference frequency Ω matches the oscillator's one, a resonance enhancement is experienced by the nuclear motion.

As a consequence of this mechanism, the optical properties of the medium are influenced by the nuclear motion. Thus the electric fields E_1 and E_2 experience an altered electronic polarizability, while propagating through the sample. The macroscopic polarization results from the sum of dipole moments in a linear and a nonlinear part. Considering eq. 1.13, the latter can be written as

$$P_{NL} = P(\omega_{cs})e^{-i\omega_{cs}t} + P(\omega_1)e^{-i\omega_1 t} + P(\omega_2)e^{-i\omega_2 t} + P(\omega_{as})e^{-i\omega_{as}t} + c.c. \tag{1.17}$$

The nonlinear polarization contains contribution not only at the fundamental frequencies ω_1 and ω_2, but also at the combination frequencies $\omega_{cs} = 2\omega_2 - \omega_1$ and $\omega_{as} = 2\omega_1 - \omega_2$. Thus the coherent Raman spectrum consists in four components. The contributions to P_{NL} at ω_1 and ω_2 account for stimulated Raman loss (SRL) and gain (SRG), while those at ω_{cs} and ω_{as} are known as coherent Stokes Raman scattering (CSRS) and coherent anti-Stokes Raman scattering (CARS). For example, the nonlinear polarization that gives rise to the CARS signal reads

$$P(\omega_{as}) = \frac{N}{m}\left(\frac{\partial \alpha}{\partial Q}_0\right)^2 \frac{A_1^2 A_2^*}{\omega_v^2 - \Omega^2 - 2i\Omega\gamma} = 6\epsilon_0 \chi^{(3)}_{CARS}(\Omega) A_1^2 A_2^* \tag{1.18}$$

where $\chi^{(3)}_{CARS}$ is the component of the third order susceptibility responsible for CARS. The nonlinear dependence on the incident fields amplitudes is evident. Similar results are obtainable for the other components of the coherent Raman signal. The physical process just depicted is

[1] The expression 1.12 is given in the SI system of units. In nonlinear optics, it is also common to work in gaussian units, in which the electric field and the polarization are expressed in the same units. In gaussian units, eq. 1.12 reads $P = \chi^{(1)}E + \chi^{(2)}E^2 + \chi^{(3)}E^3 + \dots$.

an example of *four wave mixing*.

Because of the dependence on the nuclear degrees of freedom carried by the Spontaneous Raman and CRS signals, Raman spectra contains informations about the energy level structures of the sample. In particular, spontaneous Raman provides important advantages when used to investigate matter [24]:

- both polar and non-polar molecules can exhibit Raman active modes, thus it is possible to study systems for which IR absorption spectroscopy is non suitable, since they do not present a permanent electric dipole.
- The frequency of the incident radiation can be chosen arbitrarily and conveniently, because Raman spectroscopy measures signals at frequencies different from that of the incident fields frequency.
- Using visible or ultraviolet radiation rather than infrared, higher spatial resolution is achieved.

On the other side, Spontaneous Raman spectroscopy has to face some intrinsic limitations, first of all a very small cross section. As a consequence, Raman signals are easily overwhelmed by other effects, as fluorescence emission. Furthermore, Raman effect produces incoherent radiation, spreading over the whole solid angle.

Moreover, important limitations of spectroscopic techniques based on the spontaneous Raman effect arise in time-resolved studies. Indeed, in order to investigate ultrafast processes, the exploited pulses should be short enough, with a duration lower or comparable to the time scale involved. As a consequence of the Fourier transform limit, spectral broadening has to be faced. For example, for Gaussian envelopes, subpicosecond pulses are needed to obtain atomic spatial resolution:

$$\Delta E \cdot \Delta t \geq 15\, cm^{-1} ps, \tag{1.19}$$

Therefore, using a single probe pulse, it is not possible to study vibrational dynamics below the picosecond time scale without facing spectral resolution issues. For this reasons, nonlinear spectroscopic techniques are preferable. Indeed, coherent Raman scattering is exploited in many techniques used in ultrafast spectroscopy and Microscopy [2, 25].

Among the different coherent Raman processes, in this work we particularly focus on Stimulated Raman effect [26, 27]. In this process, two different light pulses, usually called Raman ($\mathcal{E}_R$) and probe ($\mathcal{E}_S$) pulses, are used to stimulate a Raman process in the sample. The output signal is coherently generated with a cross section higher than the spontaneous case by several orders of magnitude and proportional to the Raman pulse intensity. As discussed at the beginning of this section, the excitation of vibrational coherences by visible light requires two colors, whose frequencies difference matches that of the Raman active mode. Thus, a Raman transition is fundamentally composed by two light matter interactions. In stimulated Raman spectroscopies, two of these transitions are used to generate and detect the vibrational coherence. Indeed, stimulated Raman is a third order optical process and requires three interaction with the external fields, two of them with the Raman pulse. Consequently, because of energy and momentum conservation, the signal emission is collinear with the probe pulse $\mathbf{k}_{\text{sig}} = \mathbf{k}_R - \mathbf{k}_R + \mathbf{k}_S$. Therefore, the detection occurs in a small solid angle and Raman signals can be distinguished from the isotropically generated fluorescence.

The stimulated nature of this process is justified at two levels. Firstly, it regards the way the Raman resonance is created: indeed, the Raman active mode is driven into oscillation in a stimulated fashion, with an initial phase controlled by the relative phase difference between the pulses. Moreover, in the language of second quantization, the signal photons are detected in a field mode that is initially occupied by one of the input field (the probe). Thus, the signal photons emission is stimulated in the detection mode. In this respect, stimulated Raman spectroscopies are *heterodyne* detected, as opposed to other techniques in which the generated

signal is found in a previously vacant mode, called *homodyne* detected. We will deepen this distinction in the next chapter.

1.3 Different protocols to measure stimulated Raman signals

Stimulated Raman techniques can be broadly classified as time domain or frequency domain, depending on the strategy adopted for the detection. For example, narrowband Stimulated Raman spectroscopy (SRS) is a frequency domain technique which exploits two narrowband pulses temporally and spatially overlapped on the sample. One pulse, the Raman, is fixed at the frequency ω_R, while the other pulse, the probe, is scanned across the spectral region of interest and detected after the interaction with the sample, leading to the signal $S(\omega_S)$. Sampling the detected frequencies ω_S, Raman peaks are observed in frequency domain as the difference $\omega_R - \omega_S$ matches one of the vibrational frequencies of the sample.

Another possibility is to measure the vibrational coherence directly in the time domain using two femtosecond pulses. In this case, the evolution of the vibrational coherence induced by the Raman pulse is followed in time with femtosecond precision by a delayed probe pulse, which is then detected, for example with a photodiode, for different values of the delay. This is the scheme used in Impulsive Stimulated Raman Spectroscopy (ISRS).

The main difference among the two protocols is the way the vibrational frequencies are encoded in the experimental parameters. In SRS, the Raman signatures are observed looking at the signal variations with the detected frequencies. Conversely, in ISRS the vibrational information is carried by the dependence of the signal intensity on the delay between the two pulses and the Raman spectrum is obtained by Fourier transformation. In this section, we present the main features of SRS and ISRS in view of their frequency and time domain nature.

1.3.1 Stimulated Raman in the frequency domain

Narrowband SRS provides a powerful tool especially when few key vibrational markers are needed. However, when the vibrational bands of interest are not known a priori or are extended across a wide spectral region, the need to scan multiple frequencies may become an issue. In this respect, an alternative and particularly useful approach is the broadband SRS. It is obtained by using a narrowband Raman pulse and a femtosecond probe pulse with a broad spectral envelope, for example a white light continuum (WLC). In this scheme, the broad bandwidth of the WLC probe pulse allows the simultaneous detection of vibrational features, over a large spectral window ($\sim 1500\,cm^{-1}$). The Raman pulse has usually a time duration of few picoseconds and a very narrow spectral width ($0.1 \div 1\,cm^{-1}$). Using a tunable Raman pulse, its central frequency can be set in correspondence of one of the electronic edges of the sample to exploit the resonant enhancement. The probe pulse has usually a time duration of tens of femtoseconds. When it is spectrally resolved after the interaction with the sample and the narrowband Raman pulse, sharp Raman features appear on the top of the its envelope, as shown in figure 1.3. Consequently, SRS features can be positive peaks or negative losses, depending on whether a higher or lower number of photons are detected at a given frequency in presence of the Raman pulse, with respect to the reference provided by the probe spectral envelope.

In particular, for electronically off resonant pulses, positive peaks are obtained on the lower frequency side of the broadband probe envelope (red side) with respect to the Raman pulse central frequency, while losses are obtained on the higher frequency side (blue side). This aspect is peculiar of SRS and discriminates stimulated from spontaneous spectra, where only positive features are observed. The generation of SRS features can be rationalized as a redistribution of photons between the spectral components of the broadband probe [28]. In resonant condition this can also lead to an energy flow between fields and matter.

A possible complication in the interpretation of SRS spectra is due to the overlap condition required to generate the signal. Overlapping intense pulses in time usually leads to additional

contributions which have to be considered and modeled in the data analysis routine, as cross phase modulation and higher order effects [29]. This is not the case for time domain techniques.

It is common to present SRS signal by calculating the *Raman Gain* (RG)

$$RG = \frac{\Delta I_S}{I_{S_0}} \tag{1.20}$$

being $\Delta I_S = I_S - I_{S_0}$, with I_{S_0} and I_S the detected intensity of the probe pulse in absence and in presence of the Raman pulse. Alternatively, the RG is also defined in literature as the ratio between the probe spectrum with and without the Raman pulse[2]: $RG = I_S/I_{S_0}$. In any case, the RG is usually reported as a function of Raman shift $\omega_S - \omega_R$. We note that since

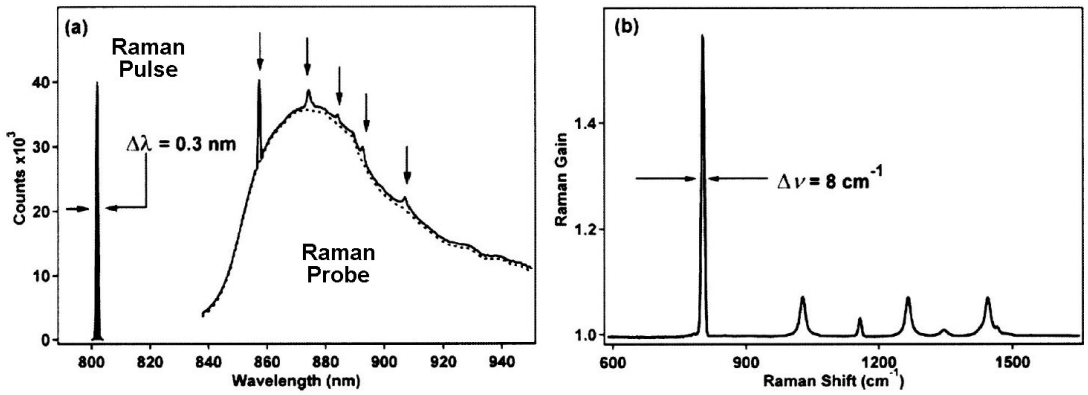

Figure 1.3: (a) The spectra of Raman pulse and probe pulses for a typical off resonant broadband SRS experiment on the liquid solvent cyclohexane. The probe spectrum in absence of the Raman pulse is shown as the dotted line. As the Raman pulse is switched on, the Raman peaks from the cyclohexane are clearly visible in the output probe spectrum. (b) The ratio of the probe spectrum with and without the Raman pulse gives the Raman gain spectrum. Since the Raman pulse is centered at a frequency lower than those of the probe envelope, only positive features are observed. Image adapted from [30]

the femtosecond probe pulse arrival time can be chosen within the longer temporal envelope of the Raman pulse, broadband SRS provides a two dimensional signal $S(\omega, T)$ which depends also on the delay between the two pulses T. However, as further discussed in the last section of this chapter, while the dependence on ω is used to retrieve the Raman spectrum, T serves as a control parameter.

Remarkably, in a recently developed pump-probe implementation, called Femtosecond Stimulated Raman Spectroscopy (FSRS) [16, 18, 31–34], SRS is used to probe the photoinduced effects due to an additional femtosecond actinic pump, preceding the Raman and probe pair on the sample. The femtosecond duration of the actinic and WLC probe provides precise references to sample the time delay between the photoexcitation and the SRS process, leading to high temporal resolution. At the same time, spectral resolution is guaranteed by the narrowband Raman pulse.

1.3.2 Stimulated Raman in the time domain

Impulsive Stimulated Raman Scattering (ISRS)[3] exploits a time-domain probe protocol consisting in two ultrashort temporally separated laser fields to stimulate and read out vibrational

[2]The difference between the two RGs is simply an offset, so the used definition becomes clear from the baseline value, either zero or one.

[3]In literature, many different names can be found for the same technique, as impulsive vibrational spectroscopy or femtosecond time-domain Raman spectroscopy

coherences on a given electronic state [35–39]. We will call the two pulses, in analogy with SRS, impulsive Raman $\mathcal{E}_R$ and probe $\mathcal{E}_S$ pulses. Differently from SRS, in this case the Raman pulse is also a femtosecond pulse. Thus, ISRS shares the same geometry of TA, and the same experimental setup can be used to acquire both the signals. As we will discuss in details in Chapter 4, ISRS is a third order process, since it grounds on stimulated Raman effect. Firstly, the sample interacts twice with the Raman pulse, which induces a vibrational coherence by means of its large bandwidth. Then, the coherent oscillation is detected after a delay T by the probe pulse, whose optical transmission through the sample results consequently modulated at the period of the associated Raman active mode $T_{vib} = 2\pi/\omega_{vib}$. Scanning the relative arrival time of the Raman and probe pulses, the oscillation can be temporally sampled, provided that both the excitation pulses are sufficiently short, with a duration below the period of the vibrational mode $\tau_{S/R} < T_{vib}$. On one side, short pulses are required to achieve the necessary subpicosecond precision in the sampling time step to probe the oscillating coherence. Moreover, femtosecond durations are needed to coherently drive the oscillations. Considering transform-limited pulses, this condition implies that in the frequency domain pulses have bandwidths larger than the Raman frequency, as shown in Fig. 1.4a.

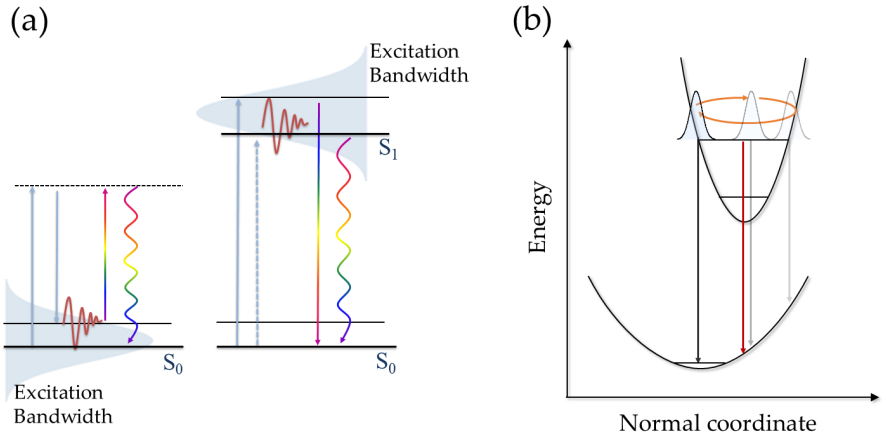

Figure 1.4: Concepts of impulsive stimulated Raman spectroscopy. (a) Ladder diagrams of ISRS processes generating vibrational coherences on the electronically ground (left) and excited (right) states. Ladders in the diagrams represent the energy levels of the system, while the arrows indicate light matter interactions within the third order perturbation theory as detailed in Chapter 2. Importantly, in order to generate and read out the coherence, the excitation bandwidth must exceed the vibrational energy. (b) Classical interpretation of excited state ISRS: upon generation of vibrational coherences, the energy of the SE transition from the excited state depends on the position of the oscillating wavepacket. Consequently the transient absorption spectrum is modulated in time, oscillating at higher and lower wavelengths with respect to the static one (red line).

The classical picture represented in Fig. 1.4b can be used to sketch the mechanism of signal generation in ISRS. We consider, as an example, an ISRS process from the excited state driven by resonant pulses. In this case, a vibrational wavepacket is promoted by a resonant Raman pulse on a displaced excited state potential, whose minimum is shifted with respect to the ground state potential. Upon photoexcitation, the out-of equilibrium wavepacket starts moving along the potential surface to reach the new minimum and then oscillates around it. When a probe pulse resonant with the SE region of the transient absorption interacts with the sample, its transient spectrum will be affected by the motion of the wavepacket in time. As a consequence, considering a fixed wavelength, the intensity of the associated transient feature oscillates in time with the frequency of the coherent motion. Therefore, Raman-active vibrations are recorded directly in the time domain, and the Raman spectra are simply retrieved through

Fourier transformation along the delay T.

Coherent wavepackets can be generated also on the ground state, whether the pulses are resonant or not. Even if in this case the mechanism underlying the coherence generation is less intuitive, it can be sketched classically as an impulsive kick transferred to the sample by the short excitation pulse [36, 40]. A more precise description of both excited and ground state ISRS processes requires a microscopic framework that will be derived in Chapter 4 using the perturbation theory presented in the next chapter.

In general, ISRS and SRS are somehow similar and complementary at the same time: they both allow to obtain the Raman spectrum on the ground and excited state but the way the spectroscopic information is registered gives rise to a series of differences between the techniques:

- At odds with frequency domain stimulated Raman, the ISRS signal is not collected necessary around the wavelength of the Raman pulse. Consequently, the low frequency region of the Raman spectrum is more easily accessed because it is not masked by the tails of the Rayleigh peak and the elastic scattering from the Raman pulse.
- Since in time domain techniques the pulses are not required to be temporally overlapped in order to generate the signal, ISRS is not hampered by the background signals induced by the temporal overlap of multiple pulses, affecting frequency domain experiments [37, 41].
- On the other hand, this implies that, in ISRS, the acquisition times are generally longer, since a full scan of T along the vibrational period is needed to achieve the Raman spectrum, with a sampling rate higher than double the Raman frequency, as requested by the Nyquist theorem.
- A consequence of the impulsive excitation is that the higher is the Raman frequency the shorter are the required pulses to probe it. For example, to probe peaks at frequency higher than 3000 cm^{-1} , the excitation pulses must be shorter than 10 fs.
- The spectral instrumental resolutions in the ISRS and SRS are ruled by different parameters: the length of the time acquisition window for the former and the duration of the Raman pulse for the latter. Both of them needs to be long compared to the lifetime of the detected mode.

A more specific advantage of time over frequency domain Stimulated Raman arises in time resolved studies. Indeed, ISRS measures the full vibrationally coherent evolution of the system. The information relative to time scales shorter than the vibrational dephasing times is hidden in a frequency domain measurement. Extracting it requires to apply Kramers-Kronig relation and reconstruct the time-dependent complex signal from the experimental data. This procedure, however, is often jeopardized by the background, which inevitably introduces artifacts in the reconstructed data. If a time domain measurement is performed these artifacts are eliminated [37].

Similarly to SRS, ISRS signal is obtained by a heterodyne detection of the probe. A powerful approach consists in using a white light probe and spectrally resolving it by a grating. The obtained signal in this case depends not only on the delay T but also on the dispersed probe wavelength. Therefore, it is possible to design advanced ISRS schemes which exploit this additional dimension to store spectroscopic information.

1.4 The multidimensional approach

The ability to simultaneously control multiple frequencies and time delays recently fueled the development of multidimensional spectroscopy. In the glossary of nonlinear spectroscopy, this term is more typically reserved to Fourier transformed time domain spectroscopies. In these techniques, multiple delayed pulses interact with the sample at tunable times, following the pump-probe concept. The detected time domain signal is subsequently transformed to the

frequency domain, giving a correlation map along multiple dimensions [42–44]. Multidimensional Fourier-transform methods were firstly developed and applied in nuclear magnetic resonance (NMR) in the 1970s [45], and they are now principal actors on the stage of ultrafast laser spectroscopy. Today, two dimensional (2D) Fourier transformed spectroscopies are routinely performed in the UV-visibile (2D electronic spectroscopy, 2D ES) and infrared (2D IR) ranges to probe electronic and vibrational correlations, respectively [46–48]. The extension to Raman-based probes has been demonstrated to be more challenging [44], as we discuss in details in chapter 6 addressing 2D ISRS. A sketch illustrating the difference in the pulse schemes and signals for one dimensional and two dimensional ISRS is reported in Fig. 1.5. In 2D ISRS, three femtosecond delayed pulses, instead of two, are used to generate two different vibrational coherences and follow their evolution between the interactions with the electromagnetic fields. Accordingly, the signal depends on two tunable delays, T_1 and T_2, and oscillates as a function of them with the frequencies of the Raman modes, photoactivated by the first two pulses. The coherent oscillations modulate the transmission of the third pulse, similarly to 1D ISRS. As a result, Raman features, obtained by a 2D Fourier transform along T_1 and T_2, are associated with the correlations between different modes, which give rise to cross and combination peaks in the 2D map. In chapter 6, we will show that by means of a wise choice of the pulse scheme, 2D ISRS can be applied to map the vibrational structure which shapes electronically excited state potential energy surfaces in molecules.

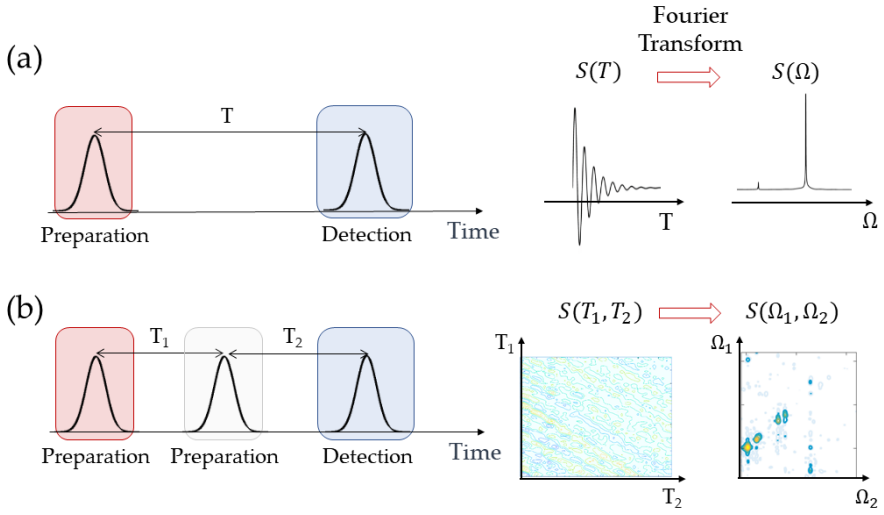

Figure 1.5: The concept of multidimensional Fourier transform spectroscopy. The sketch illustrates the extension from 1D ISRS to 2D ISRS. In 1D ISRS, two pulses are used and the signal is measured as a function of their delay and then Fourier transformed to obtain the 1D Raman spectrum. In the two dimensional extension, one pulse and one delay are added and a frequency-frequency correlation map is obtained by means of 2D Fourier transformation along T_1 and T_2. Similarly, signals of higher dimensionality can be measured increasing the number of pulses and delays.

Generally speaking, we remark that the 2D Fourier transformed time domain protocol is in principle extensible to higher dimensions increasing the number of pulses, but the price to pay is a considerably higher complexity, experimentally as well as in the interpretation of the measurements. Technological challenges include a strict control on the pulse stability and, in some cases as in multidimensional ES, also on the phases. In any case, point-by-point sampling of the delay between pulses starts becoming unfeasible already after three dimensions due to the long acquisition times. Nevertheless, the way to higher order multidimensional measurements has been paved thanks to more advanced methods, which enable fast acquisition. These methods include the use of chirped pulses, spatial encoding via birefringent wedges and pulse shaping

[49–53]. For example, the measurement of six dimensional signals has been recently reported in literature [54, 55].

In this thesis, we aim to discuss multidimensional spectroscopy under a more general point of view. In a broader sense, any nonlinear signal that is a function of more than one variable is able to produce a multidimensional spectrum. Consequently, every set of parameters on which a nonlinear signal depends, can be exploited to built the multidimensional extension of that signal, provided that the correlation between them carries some meaningful physical information that we are able to extract.

In particular, we are interested in exploiting those experimental parameters that come almost naturally from the measurement strategy, as the probe wavelength upon spectrally resolved detection, the phase of the probe pulse and the resonance tuning, following a multidimensional approach to time domain stimulated Raman spectroscopy. Our aim is to exploit this multidimensionality, using them as control knobs to address in particular the interaction between electronic and vibrational degrees of freedom in a wide class of materials. Since the topics presented in the thesis deal mainly with ISRS, for the sake of comparison we present here an example using SRS.

1.4.1 Excursus in the frequency domain: using resonances in broadband Stimulated Raman Scattering

As already anticipated, spectrally resolved Stimulated Raman signals are bidimensional since they depend on both the delay T between the Raman and probe pulses and on the probe dispersed frequency ω. In the case of ISRS, T is the variable used to obtain the Raman spectrum, while the dispersed frequency can be used to encode additional information on the electronic state underlying the vibrational transition, as we will show in details in the next chapters.

In SRS, the Raman variable is ω, while T determines the trade-off between the spectral resolution and the signal intensity[4] and is usually fixed at an optimal value [56]. Thus, we discuss here the dependence of the SRS signal on another parameter, namely the resonant condition of the narrowband Raman pulse.

In Fig. 1.6, we present the experimental signatures of resonance effects in SRS, measured in a paradigmatic heme protein, the ferrous Myoglobin (Mb), by tuning the Raman pulse in the spectral region of the Soret absorption band [57]. Specifically, the maps report the Raman gain as a function of the Raman shift and the Raman pulse central wavelength λ_R, for the red (left panel) and blue (right panel) sides of the SRS spectrum. Additionally, we show the Mb absorption spectrum in the side panel of each map.

Remarkably, SRS features show a complex lineshape dependence on the electronic resonance condition induced by the Raman pulse wavelength λ_R, with a substantial difference between the two sides of the spectrum. In the red side of the spectrum, i.e. at negative Raman shifts, upon scanning λ_R, Raman bands intensity undergoes a resonance enhancement which approximately follows the profile of the absorption, while the spectral lineshape does not significantly change. On the contrary, the lineshapes in the blue side of the spectrum (at positive Raman shifts) depend drastically on the resonance condition, evolving from gains to losses through dispersive profiles. Taking as an example the ν_4 band at 1355 cm^{-1}, a positive Lorentzian lineshape is observed upon tuning the λ_R at 465 nm and a weak loss, peculiar of the SRS off resonant spectrum, occurs by red-shifting or blue-shifting the Raman pulse by ∼20 nm from this value. Between these two limiting cases, the lineshape is dispersive and changes symmetry as it crosses the maximum at λ_R =465 nm.

Critically, the maximum resonant enhancement in the blue side is obtained at a different λ_R with respect to the red side and it is mode-specific, since it is shifted approximately by one

[4] In SRS, the spectral resolution is maximized when the probe precedes the Raman pulse, remaining within its temporal envelope. On the other hand, the intensity of the signal is affected by two concurring terms: the amplitude of the Raman pulse at the probe arrival time and the length of the interaction window, given by the portion of the Raman pulse temporal envelope following the probe. Due to these two competing factors, the maximum signal intensity appears at slightly negative time delays, i. e. when the probe slightly precedes the Raman pulse. Consequently, an optimal delay T exists, which maximizes signal intensity and resolution.

vibrational quantum from the maximum of the Soret band at 435 nm. In particular, the higher is the frequency of the vibrational mode, the lower is the energy of the Raman pulse photon needed to match the resonance, as can be seen by comparing the ν_7 (670 cm^{-1}) and ν_4 Raman bands in Fig. 1.6. We remark that, at odds with its spontaneous analogue, in SRS the red and

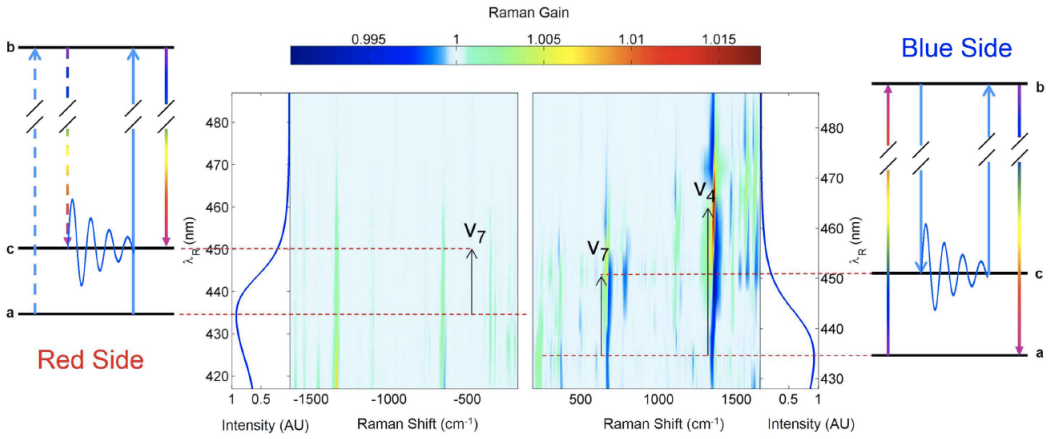

Figure 1.6: Stimulated Raman spectra of Myoglobin. Central panel: colormaps of broadband Stimulated Raman spectra in the red (left panel) and blue (right panel) sides of the spectrum showing the dependence on the Raman pulse wavelength. Side plots report the Soret absorption spectrum. The SRS signal is always a gain in the red side of the spectrum, while in the blue side it shows different profiles depending on the resonance condition. In particular, the maximum of the signal in the blue side is shifted by one vibrational quantum from the peak of the absorption, as highlighted by the horizontal dotted lines. On the contrary, the resonant enhancement of the red side follows the profile of the absorption band, with small deviations due to the resonant excitation profile. Arrows highlights the energies of two prominent vibrational modes (ν_7 and ν_4). Left and right panels: four-wave mixing energy level diagrams representing the processes which originate the SRS spectrum in the red (left) and blue (right) sides for the ν_7 band. In these diagrams, the light matter interactions are represented by arrows connecting the energy levels of the sample, through the density matrix formalism described in chapter 2. The blue and rainbow arrows represent interactions with the Raman and probe pulses, respectively. In particular, the dotted arrows indicates a change of the state of the bra side of the density matrix, while solid arrows represent changes of the ket state.

blue components are not related to Stokes and anti-Stokes processes as in conventional Raman spectroscopy [58]. Conversely, they arise from different four wave mixing processes in which the time ordering of the interactions between the pulses and the matter is changed. Using the density matrix formalism, these processes can be calculated perturbatively by means of diagrammatic techniques [28, 59–61] and the main terms responsible for the SRS signals in the red and blue sides are depicted in the right and left panels of Fig. 1.6. The horizontal lines indicate the ground (a) and electronically excited (b) states and the vibrationally excited level (c), while interactions with the Raman and probe pulses are represented by blue and rainbow-colored arrows, respectively. In the next chapter, we will derive the perturbation theory for the density matrix and present the rules to interpret diagrams and calculate the associated spectroscopic signals. Here, we note that the energy levels involved in the interactions with the Raman pulse are different in the red and blue side diagrams. Indeed, in the red side diagram, the Raman pulse connects the levels a and b while the diagram for the blue side, it connects b and c. This correspond to a different resonance condition for the two processes, which becomes clear as the signal expression is calculated from the diagram.

The experimental signal can be calculated from the expression of the Raman gain in resonant

conditions:

$$I(\omega, \lambda_R) = A(\lambda_R) \cdot \Im \left(\frac{P^{(3)}(\omega, \lambda_R)}{E_P^0(\omega)} \right) \tag{1.21}$$

where $E_P^0(\omega)$ indicates the probe pulse in absence of raman pulse and $A(\lambda_R)$ is a positive adjustable parameter which accounts for the effect of the Raman Excitation Profile (REP), the spectral implication of the Franck-Condon principle [62, 63]. The third order polarizations $P^{(3)}(\omega, \lambda_R)$ for each side of the spectrum are directly obtained from the diagrams. The full calculation is reported in [57]. In particular, for the limit case of a monochromatic Raman pulse and a instantaneous (temporal delta function) probe, the following expressions can be obtained

$$P_{Red}^{(3)}(\omega, \omega_R) = \frac{|\mu_{ab}|^2 |\mu_{bc}|^2}{(\omega_{bc} - \omega - i\gamma_{bc})(\omega_R - \omega_{ba} - i\gamma_{ab})(\omega - \omega_R + \omega_{ca} + i\gamma_{ac})} \tag{1.22}$$

for the red side and

$$P_{Blue}^{(3)}(\omega, \omega_R) = \frac{|\mu_{ab}|^2 |\mu_{bc}|^2}{(\omega - \omega_{ba} + i\gamma_{ba})^2 (\omega - \omega_R - \omega_{ca} + i\gamma_{ca})} \tag{1.23}$$

for the blue side. In eq. 1.22 and 1.23, μ_{ij} is the dipole transition moment between the i and j states, $\omega_{ij} = \omega_i - \omega_j$ is the frequency difference between levels i and j, and γ_{ij} is the vibrational dephasing rate of the $|i\rangle \langle j|$ induced coherence. By inspection of two equations, it is clear that in the red side, eq. 1.22, the resonance condition arises for $\omega_R = \omega_{ba}$, in analogy with spontaneous Raman. In the blue side, eq. 1.23, the resonance condition depends on the energy of the vibrational mode ω_{ca} involved in the process, being $\omega_R = \omega_{ba} - \omega_{ca}$. This dependence rationalizes the observed correlation between the vibrational frequency and the lineshapes of the resonant SRS signal in the blue side observed in Myoglobin.

This result has a general validity and provides a procedure to extract the REP factor $A(\lambda_R)$ from the additional dependence of the blue side SRS on the resonance condition. Moreover, the possibility to selectively enhance different Raman bands, combined with the larger cross section under resonance conditions, identifies the blue side of SRS spectra as a powerful tool to investigate Frank-Condon effects and to extract quantitative information about vibrational mode displacement and vibronic coupling, provided that the dependence of the SRS spectra on the Raman wavelength is taken into account.

2 Perturbative description and diagrammatic tools

In the response function formalism, coherent optical signals are calculated by a two-step procedure in which the material treated quantum-mechanically interacts with either classical or quantum fields [59]. The two approaches are known as the semiclassical and full quantum derivation. In both the cases, as a first step, the nonlinear polarization $P^{(n)}$ induced in the system by the external fields has to be calculated microscopically, using the quantum Liouville equation for the density matrix. Secondly, $P^{(n)}$ acts as a source in the macroscopic Maxwell equation to generate the signal field.
The semiclassical approach provides a powerful description of coherent signals, equivalent to the full quantum treatment for most of the cases. It takes into account the accessible states of the matter and the transitions between these states, expressed in material parameters such as transition dipole moments. On the other hand, a quantum electrodynamical (QED) formulation is needed to describe situations in which strong quantum effects arise, coupling matter and fields degrees of freedom. In this chapter, we briefly review the response function formalism that will be applied in the rest of this thesis as a tool to simulate and decipher stimulated Raman processes in a broad range of scientific cases.

2.1 Dynamics in the Liouville space

The nonlinear response functions are calculated summing over all the possible states that the density matrix of a system may acquire during the nonlinear process. Since the Liouville space is the configurational space in which the density matrix lives, understanding its properties is essential for calculating coherent optical signals. Here we introduce the Liouville space and derive a perturbative expansion to describe the dynamics of the density matrix.

2.1.1 Density matrix formalism

In the Schrödinger picture, a quantum system can be fully described by a time dependent state $|\psi(t)\rangle$ in an Hilbert space. The expectation value of any observable A is given by

$$\langle A\rangle = \langle\psi(t)|\, A\,|\psi(t)\rangle \tag{2.1}$$

The temporal dependence is carried by the state $|\psi(t)\rangle$ and can be evaluated solving the time dependent Schrödinger equation:

$$\frac{\partial}{\partial t}\,|\psi(t)\rangle = -\frac{i}{\hbar}H\,|\psi(t)\rangle \tag{2.2}$$

H being the total Hamiltonian of the system. We assume that the set $\{n\}$ is an arbitrary orthonormal basis for the Hilbert space in which $|\psi(t)\rangle$ is defined. Expanding $|\psi(t)\rangle$ in this

basis and taking the complex conjugate, the expectation value 2.1 can be expressed as

$$\langle A \rangle = \sum_{n,m} c_n(t) c_m^*(t) \langle m | A | n \rangle = \sum_{n,m} c_n(t) c_m^*(t) A_{mn} \tag{2.3}$$

A more general description of a quantum system is obtained defining the density operator ρ

$$\rho(t) = |\psi(t)\rangle \langle \psi(t)| \tag{2.4}$$

Expanding in the $\{n\}$ basis, ρ becomes

$$\rho(t) = \sum_{n,m} c_n(t) c_m^*(t) |n\rangle \langle m| = \sum_{n,m} \rho_{nm}(t) |n\rangle \langle m| \tag{2.5}$$

where we have defined the density matrix $\rho_{nm}(t) = \langle n | \rho | m \rangle = c_n(t) c_m^*(t)$. Using the density matrix formalism we recast the expectation value expression 2.1 as

$$\langle A \rangle = \sum_{n,m} A_{nm} \rho_{nm}(t) = Tr[A\rho(t)] \tag{2.6}$$

The introduction of the density matrix allows to extend the definition of quantum state. In the wave function approach to quantum mechanics the state of a system is represented by a vector, while in the density operator formalism the same role is played by a matrix. A quantum system that can be represented by a wave function is said to be in a *pure state*. A pure state is completely defined by the first postulate of quantum mechanics and the density matrix gives only an equivalent description. However, a general state of a quantum system may or may not be pure. Considering an ensemble of system being in the state $|\psi_k(t)\rangle$ with non negative and normalized probability $P_k \geq 0$, we can still define the density operator of the system as

$$\rho(t) = \sum_k P_k |\psi_k(t)\rangle \langle \psi_k(t)| \tag{2.7}$$

If $P_k = 0 \; \forall k \neq i$, $P_i = 1$, the state is pure. Otherwise the state of the system is not completely defined; it is impossible to represent it with a single wave function and the system is said to be in a statistical mixture or mixed state. This is the case for example of a collection of atoms coming directly out of a hot oven [64]. The distinction between pure and mixed state is fundamental and does not depend on the representation.
The density matrix satisfies the following properties that come straightforward by its definition and by the properties of the trace

1. The density operator is Hermitian: $\rho = \rho^\dagger$
2. The diagonal elements of the density matrix are real and non negative

$$\rho_{nn} = \sum_k P_k \left| \langle n | \psi_k \rangle \right|^2 \geq 0$$

   The off diagonal elements ρ_{nm} with $n \neq m$ are in general complex.
3. $Tr(\rho) = 1$, from the normalization condition of P_k.
4. $Tr(\rho^2) \leq 1$, where the equality holds only for pure states.

The diagonal elements of the density matrix is usually referred to as *populations* and off diagonal elements as *coherences*.
Another important advantage of using the density matrix formalism is the possibility to perform a description of a subsystem living in a complex composite quantum system. For example, we consider the evolution of a system A described by a few degrees of freedom α but coupled to a complicated bath B. Typically, the total number of degrees of freedom in the joint system and

bath state is too high to solve the problem explicitly. In this case, it is convenient to define the *reduced density matrix* ρ^A, depending only on the degrees of freedom of interest, with elements

$$\rho^A_{\alpha\alpha'} = Tr_B \langle\alpha| \rho^{AB} |\alpha'\rangle = \sum_\beta \langle\alpha\beta| \rho^{AB} |\alpha'\beta\rangle \tag{2.8}$$

where we used the complete basis set of the total system given by the tensorial product between the system and bath eigenvectors $|\alpha\beta\rangle$ and defined Tr_B as the partial trace, summed over the degrees of freedom β of the bath only. Then, the evaluation of the expectation value of an observable that depends only on the system degree of freedom can be considerably simplified by means of the reduced density matrix. The price to pay is neglecting the interaction between the system and the bath, but in many context this is a good approximation for the problem under consideration.

2.1.2 Liouville equation

Applying the time derivative to the density matrix of a pure state $|\psi(t)\rangle$ we get

$$\frac{\partial\rho}{\partial t} = \frac{\partial}{\partial t}\left(|\psi\rangle\langle\psi|\right) = \left(\frac{\partial}{\partial t}|\psi\rangle\right)\cdot\langle\psi| + |\psi\rangle\cdot\left(\frac{\partial}{\partial t}\langle\psi|\right) \tag{2.9}$$

where the evolution of the ket and bra is ruled by the Schrödinger equation. Using eq. 2.2, we obtain the *Liouville-Von Neumann* equation

$$\frac{\partial\rho}{\partial t} = -\frac{i}{\hbar}[H,\rho] \tag{2.10}$$

Since the density operator for a mixed state is a superposition of pure state density operators, eq. 2.10, which is linear in ρ, is still valid for mixed states. An important feature of the Liouville-Von Neumann equation is the presence of the commutator which allows interactions with the Hamiltonian to be from both the ket and the bra sides of the density operator. Thus, starting from a population state, $\rho(t)$ is able to evolve in a generic coherence state through eq. 2.10.
It is convenient, at this point, to introduce the notion of *Liouville representation* [59, 65]. For a N level system, the density matrix is constituent by N^2 elements ρ_{ij}. Clearly, each matrix element obeys the relative (Liouville-Von Neumann) equation

$$\frac{\partial\rho_{ij}}{\partial t} = -\frac{i}{\hbar}\sum_m \left(H_{im}\rho_{mj} - \rho_{im}H_{mj}\right) \tag{2.11}$$

Introducing the *Liouville operator* $\mathbf{L}$, we can write eq. 2.11 as

$$\frac{\partial\rho_{ij}}{\partial t} = -\frac{i}{\hbar}\sum_{m,n}\mathbf{L}_{ij,mn}\rho_{mn} \tag{2.12}$$

By comparison of eqs. 2.11 and 2.12, we obtain

$$\mathbf{L}_{ij,mn} = (H_{im}\delta_{jn} - \delta_{jn}H_{im}) \tag{2.13}$$

Using the operator formalism, we recast eq. 2.12 as

$$\frac{\partial\rho}{\partial t} = -\frac{i}{\hbar}\mathbf{L}\rho \tag{2.14}$$

Eq. 2.14 defines the Liouville representation. In Liouville space, the density operator ρ becomes a vector and the operator $[H,\dots]$ is written as a four labelled tensor, namely a *superoperator* $\mathbf{L}$. As an example, the well known optical Bloch equations describing light matter interactions in a two level system are based on this formalism [66]. We note that the Liouville equation 2.14 is formally identical to the Schrödinger equation. The importance of the Liouville representation

lies in this equivalence that allows to extend all the results obtained for the wave function in Hilbert space to the density matrix in Liouville space. In other words, we can say that there is a homomorphism between the Hilbert and Liouville spaces. Additionally, the Liouville representation proves to be the most natural when dephasing effects are considered. Dephasing broadly indicates the process in which a coherent or an excited population state induced by a perturbation decays in time, while the system collapse into the ground state. This effect can be directly included in the Liouville equation through an additional term $\mathbf{\Gamma}$

$$\frac{\partial \rho}{\partial t} = -\frac{i}{\hbar}\mathbf{L}\rho - \mathbf{\Gamma}\rho \tag{2.15}$$

where $\mathbf{\Gamma}$, as well as $\mathbf{L}$, is a superoperator in Liouville space. As a consequence, density matrix elements evolve as

$$\rho_{ij}(t) = e^{-i\omega_{ij}(t-t_0)-\Gamma_{ij}(t-t_0)}\rho_{ij}(t_0) \tag{2.16}$$

in which ω_{ij} is the difference of the Hamiltonian eigenvalues for the state i and j: $\omega_{ij} = \omega_i - \omega_j$ and Γ_{ij} is the dephasing matrix element. In particular, Γ_{ij} for a coherence state can be decomposed in two contributions:

$$\Gamma_{ij} = \frac{\Gamma_i + \Gamma_j}{2} + \gamma_{ij} \tag{2.17}$$

where the first term is the averaged lifetimes of the pure states participating in the coherence and γ_{ij} is a *pure dephasing* term. The microscopic origin of the dephasing terms arises from the coupling of the system with a surrounding bath. For example, coupling to a continuum of states induce population decay in the Wigner-Weisskopf problem [67]. Pure dephasing originates from coupling to a thermal bath, well described by the stochastic theory of Kubo for lineshape and relaxation in a molecule [68]. In this model, the vibrational frequencies show time dependent fluctuations $\omega_{ij}(t) = \omega_{ij} + \delta\omega_{ij}(t)$, due to collision with other molecules of the sample or the solvent, and eq. 2.16 needs to be calculated by an ensamble average

$$\rho_{ij}(t) = e^{-i\omega_{ij}(t-t_o)}\langle e^{-i\int_{t_0}^{t} dt'\delta\omega_{ij}(t')}\rangle\rho_{ij}(t_0) \tag{2.18}$$

The solution of 2.18 is generally calculated by cumulant expansion [59].
Going back to time evolution in Hilbert space, in Schrödinger picture the only time dependence is contained in the wave function; hence, when all the degree of freedom of the system is included in the Hamiltonian, the Hamiltonian itself is time independent. However, in many cases, it is more convenient to narrow the phase space and treat some degree of freedom as external forces with a known time evolution even if the price to pay is handling with a time dependent Hamiltonian.

Considering a time dependent Hamiltonian $H(t)$, the state of the system at time t can be expressed by means of the evolution operator or propagator $U(t, t_0)$ defined by

$$|\psi(t)\rangle = U(t, t_0)\,|\psi(t_0)\rangle \tag{2.19}$$

$U(t, t_0)$ satisfies the following properties:

1. $U(t_0, t_0) = 1$
2. $U(t_2, t_0) = U(t_2, t_1)U(t_1, t_0)$
3. $U^{-1} = U^{\dagger} \Rightarrow U^{\dagger}(t, t_0) = U(t_0, t)$
4. $U(t, t_0)$ depends only on the interval $t - t_0$

Substituting the definition of the propagator in the Schrödinger equation and integrating from t_0 to t, we find

$$U(t, t_0) = 1 - \frac{i}{\hbar}\int_{t_0}^{t} dt' H(t')U(t', t_0) \tag{2.20}$$

Eq. 2.20 can be solved iteratively [69]

$$U(t,t_0) = 1 + \sum_{n=1}^{\infty} \left(-\frac{i}{\hbar}\right)^n \int_{t_0}^{t} dt_n \int_{t_0}^{t_n} dt_{n-1} \cdots \int_{t_0}^{t_2} dt_1 H(t_n) H(t_{n-1}) \dots H(t_1) \tag{2.21}$$

It is important to note that in eq. 2.21 the integrated time variables are fully ordered: $t_0 \leq t_1 \leq t_2 \leq \cdots \leq t_{n-1} \leq t_n \leq t$. Because in general the Hamiltonians computed at different times do not commute, we can not recast expansion 2.21 as a simple exponential. Nevertheless, we can introduce the *time ordering operator* T

$$T\left[H(t_i)H(t_j)\right] = \begin{cases} H(t_i)H(t_j) & \text{if } t_i \geq t_j \\ H(t_j)H(t_i) & \text{if } t_i < t_j \end{cases} \tag{2.22}$$

and write eq. 2.21 in a more compact form as a positive time ordered exponential:

$$U(t,t_0) = T\, exp\left[-\frac{i}{\hbar}\int_{t_0}^{t} H(t')dt'\right] \tag{2.23}$$

where we have extended all the interval of integration to t and compensated the additional integration range, dividing for $(n!)^{-1}$. When the propagator acts on the state $|\psi(t)\rangle$, we get

$$|\psi(t)\rangle = |\psi(t_0)\rangle + \sum_{n=1}^{\infty} \frac{1}{n!}\left(-\frac{i}{\hbar}\right)^n T\left[\int_{t_0}^{t} dt_n \int_{t_0}^{t} dt_{n-1} \cdots \int_{t_0}^{t} dt_1 H(t_n) \dots H(t_1) |\psi(t_0)\rangle\right] \tag{2.24}$$

2.1.3 Interaction picture

The form obtained for eq. 2.24 is not very useful. Clearly, it would be practical to truncate the summation at a fixed order but, even though such an expansion may be valid for short times, it blows up at larger times because we are trying to treat the entire Hamiltonian perturbatively. One possible solution to this problem is working in the *interaction (or Dirac) picture*. We suppose that it is possible to separate the Hamiltonian in two parts

$$H(t) = H_0 + H'(t) \tag{2.25}$$

H_0 is a non-interacting Hamiltonian which is time independent or carries a time evolution that can be solved exactly, while H' is a small term with respect to the parameters of the problem and can be treated perturbatively. The propagator U_0 of the time independent Hamiltonian H_0 reads

$$U_0(t,t_0) = e^{-\frac{i}{\hbar}H_0 \cdot (t-t_0)} \tag{2.26}$$

The interaction picture is obtained trough a unitary transformation from the Schrödinger picture; this obviously does not change the physics of the problem. The interaction wave function is defined as

$$|\psi(t)\rangle = U_0(t,t_0)\,|\psi_I(t)\rangle \tag{2.27}$$

where $|\psi(t)\rangle$ is the wave function in the Schrödinger picture while the subscript I stands for interaction. We define also the operator evolution in the interaction picture as

$$H'_I(t) = U_0^{\dagger}(t,t_0)H'(t)U_0(t,t_0) \tag{2.28}$$

Using this definition together with the unitarity of the propagator in the Schrödinger equation, we get

$$\frac{\partial}{\partial t}|\psi_I(t)\rangle = -\frac{i}{\hbar}H'_I(t)\,|\psi_I(t)\rangle \tag{2.29}$$

Eq. 2.29 shows that, in the interaction picture, states evolves in a Schrödinger like manner but under the action of the perturbation H' alone. On the other hand, the operators evolve under

the action of the unperturbed Hamiltonian H_0, as H'_I in eq. 2.28. The expansion 2.21 in the interaction picture becomes

$$|\psi_I(t)\rangle = |\psi_I(t_0)\rangle + \sum_{n=1}^{\infty} \left(-\frac{i}{\hbar}\right)^n \int_{t_0}^{t} dt_n \int_{t_0}^{t_n} dt_{n-1} \cdots \int_{t_0}^{t_2} dt_1 H'_I(t_n) H'_I(t_{n-1}) \dots H'_I(t_1) |\psi_I(t_0)\rangle \tag{2.30}$$

Going back to Schrödinger picture, we get

$$\begin{aligned} |\psi(t)\rangle = |\psi^{(0)}(t)\rangle + \sum_{n=1}^{\infty} \left(-\frac{i}{\hbar}\right)^n \int_{t_0}^{t} dt_n \int_{t_0}^{t_n} dt_{n-1} \cdots \int_{t_0}^{t_2} dt_1 \\ U_0(t,t_n) H'(t_n) U_0(t_n,t_{n-1}) H'(t_{n-1}) \dots U_0(t_2,t_1) H'(t_1) U_0(t_1,t_0) |\psi(t_0)\rangle \end{aligned} \tag{2.31}$$

where the first order $|\psi^{(0)}(t)\rangle$ evolves under the free Hamiltonian alone. The main difference from the previous result of eq. 2.21 is that now the expansion is written in powers of the perturbative term H' and is valid for long times, even when truncated at a low order. Furthermore, eq. 2.31 provides a clear physical interpretation: the system described by $|\psi(t)\rangle$ evolves freely under the action of the unperturbed H_0 up to time t_1, as indicated by $U_0(t_1,t_0)$, then it interacts with the perturbation $H'(t_1)$ and propagates freely again up to t_2. This happens for all the times t_i.

Now we can extend this results to the Liouville space in order to obtain the density matrix perturbative expansion. We separate the superoperator $\mathbf{L}$ as for H in eq. 2.25

$$\mathbf{L} = \mathbf{L}_0(t) + \mathbf{L}'(t) \tag{2.32}$$

where

$$\mathbf{L}_0 A = [H_0(t), A]$$
$$\mathbf{L}'(t) A = [H'(t), A]$$

The definition of density matrix for a pure state in the interaction picture is

$$\rho(t) = |\psi(t)\rangle \langle\psi(t)| = U_0(t,t_0) \cdot |\psi_I(t)\rangle \langle\psi_I(t)| \cdot U_0^\dagger(t,t_0) = U_0(t,t_0) \cdot \rho_I(t) \cdot U_0^\dagger(t,t_0) \tag{2.33}$$

and, from its linearity in ρ, it follows that the definition can be extended to mixed states. Taking advantage of the result 2.30 we get immediately

$$\rho_I(t) = \rho_I(t_0) + \sum_{n=1}^{\infty} \left(-\frac{i}{\hbar}\right)^n \int_{t_0}^{t} dt_n \int_{t_0}^{t_n} dt_{n-1} \cdots \int_{t_0}^{t_2} dt_1 \mathbf{L}'_I(t_n) \mathbf{L}'_I(t_{n-1}) \dots \mathbf{L}'_I(t_1) \rho_I(t_0) \tag{2.34}$$

where

$$\mathbf{L}'_I(t) = \mathcal{U}_0^\dagger(t,t_0) \mathbf{L}'(t) \mathcal{U}_0(t,t_0)$$

being $\mathcal{U}$ the propagator related to $\mathbf{L}_0$. Recovering the Schrödinger picture, we finally obtain

$$\begin{aligned} \rho(t) = \rho^0(t) + \sum_{n=1}^{\infty} \left(-\frac{i}{\hbar}\right)^n \int_{t_0}^{t} dt_n \int_{t_0}^{t_n} dt_{n-1} \cdots \int_{t_0}^{t_2} dt_1 \\ \mathcal{U}_0(t,t_0) \cdot \Big[H'_I(t_n), \big[H'_I(t_{n-1}, \dots \big[H'_I(t_1) \rho(t_0) \big] \dots \big] \Big] \cdot \mathcal{U}_0^\dagger(t,t_0) \end{aligned} \tag{2.35}$$

This expression can be interpreted similarly to eq. 2.31. The difference is that here the interactions can be with both the ket and the bra sides of the density matrix. This will justify the adoption of double sided Feynman diagrams presented later in the chapter.

Assuming that $\rho(t_0)$ represents a steady state, we can send $t_0 \to -\infty$ and write

$$\rho(t) = \rho^{(0)}(-\infty) + \sum_{n=1}^{\infty} \rho^{(n)}(t) \tag{2.36}$$

As we further detail in the next section, radiation matter interaction is often well described by the dipole Hamiltonian $H'(t) = E(t) \cdot \mu$, being μ the dipole moment of the system. Treating μ as an operator, in the interaction picture it depends on t as

$$\mu_I(t) = U_0^\dagger(t, t_0)\mu U_0(t, t_0) \tag{2.37}$$

while in Schrödinger picture it is constant. Because of that there is no ambiguity and we can suppress the subscript I and write directly $\mu(t)$ or μ, referring to one or the other representation. Explicitly the n-th order of the density matrix with respect to radiation matter interaction is

$$\begin{aligned}\rho^{(n)}(t) = \left(-\frac{i}{\hbar}\right)^n \int_{-\infty}^{t} dt_n \int_{-\infty}^{t_n} dt_{n-1} \cdots \int_{-\infty}^{t_2} dt_1 E(t_n)E(t_{n-1}) \dots E(t_1) \\ U_0(t, t_0) \cdot \Big[\mu(t_n), \Big[\mu(t_{n-1}), \dots \big[\mu(t_1)\rho(-\infty)\big] \dots \Big]\Big] \cdot U_0^\dagger(t, t_0)\end{aligned} \tag{2.38}$$

2.2 Semiclassical and full quantum treatment of nonlinear optics

All the results presented in this thesis has been derived under the classical assumption for the fields, or equivalently substituting to the QED field operator its expectation value. Because of that, the first part of this section is devoted to the second steps of the semiclassical approach, calculating the signal associated to a nonlinear polarization induced by classical electromagnetic fields. The full quantum approach will be presented in the second part of the section.

2.2.1 Maxwell equations and wave mixing

It is common to classify optical phenomena expanding the induced polarization in powers of the electric field. At low intensities, the polarization $P(\boldsymbol{r}, t)$ is a linear function of the field. Defining the linear response function $S^{(1)}(t)$, it reads

$$P(\boldsymbol{r}, t) = \epsilon_0 \left(S^{(1)} \circledast E\right)[\boldsymbol{r}, t] = \epsilon_0 \int S^{(1)}(\boldsymbol{r} - \boldsymbol{r}_1, t - t_1)E(\boldsymbol{r}, t_1)dt_1 \tag{2.39}$$

where $\circledast$ indicates the convolution operator. As the intensity increases, for example when an intense laser source is involved, this is no longer true and we need to expand the polarization in higher powers of E:

$$P(\boldsymbol{r}, t) = \epsilon_0 \left(S^{(1)} \circledast E\right)[\boldsymbol{r}, t] + \epsilon_0 \sum_n \left(S^{(n)} \circledast E^n\right)[\boldsymbol{r}, t] \tag{2.40}$$

We can easily recast the expressions 2.39 and 2.40 in the frequency domain as proportional to the product of fields, exploiting the convolution theorem. Adopting a convention for the Fourier transform

$$P(\omega) = \int_{-\infty}^{+\infty} \frac{dt}{\sqrt{2\pi}} P(t)\, e^{+i\omega t}$$

and defining the susceptibility tensor χ, the ith component of the frequency domain polarization can be written as [70]

$$P_i(\omega) = \epsilon_0 \sum_j \chi_{ij}^{(1)}(\omega; \omega_j)E_j(\omega_j) + \epsilon_0 \sum_{jk} \chi_{ijk}^{(2)}(\omega; \omega_j, \omega_k)E_j(\omega_j)E_k(\omega_k) + \dots \tag{2.41}$$

where the indexes i, j and k refer to the Cartesian components while $\chi^{(1)}$ and $\chi^{(n)}$, with $n \geq 2$ are the linear and nonlinear contribution to the susceptibility tensor, respectively. The various orders account for different nonlinear processes: for example linear absorption is explained as

a $\chi^{(1)}$ process, while sum and difference frequency generation and second harmonic generation are all related to $\chi^{(2)}$. Because of the tensor nature of the susceptibility, each order in eq. 2.41 contains a huge number of terms. However, the components of $\chi^{(n)}$ are related by formal symmetry properties that can be used to reduce the number of the terms needed to solve a specific nonlinear problem [70]. In centrosymmetric media [1], even order nonlinear contributions to the susceptibility vanish because the sign of the polarization must change when the optical fields are reversed. Therefore the lowest nonlinearity is due to the third order $\chi^{(3)}$ and involves three interactions with the fields.

Our aim is to find expressions for the nonlinear response functions and susceptibilities using the Liouville formalism, and consequently determine the optical signal generated by the induced polarization, using eq. 2.41 as a source in the macroscopic Maxwell equations. For nonmagnetic media and in absence of free charges, that is $M = 0$ and $\rho = 0$, the Maxwell equations read

$$\nabla \times E = -\mu_0 \frac{\partial H}{\partial t} \tag{2.42a}$$

$$\nabla \times H = \epsilon_0 \frac{\partial E}{\partial t} + \frac{\partial P}{\partial t} + J \tag{2.42b}$$

$$\nabla \cdot E = -\frac{1}{\epsilon_0} \nabla \cdot P \tag{2.42c}$$

$$\nabla \cdot H = 0 \tag{2.42d}$$

Taking the curl of eq. 2.42a and putting it equal to the time derivative of eq. 2.42b, we obtain the general wave equation

$$\nabla \times \nabla \times E = -\frac{1}{c_0^2} \frac{\partial^2 E}{\partial t^2} - \mu_0 \frac{\partial^2 P}{\partial t^2} - \mu_0 \frac{\partial J}{\partial t} \tag{2.43}$$

where we made use of the relation between the vacuum permittivity ϵ_0 and permeability μ_0 and the speed of light in the free space c_0: $c_0 = \sqrt{\frac{1}{\mu_0 \epsilon_0}}$. We can exploit a well known vector property and write $\nabla \times \nabla \times E = \nabla(\nabla \cdot E) - \nabla^2 E$. For transverse field $\nabla \cdot E = 0$; consequently, considering non conductor media, eq. 2.43 assumes the simpler form

$$\nabla^2 E(\mathbf{r}, t) - \frac{1}{c_0^2} \frac{\partial^2 E(\mathbf{r}, t)}{\partial t^2} = \mu_0 \frac{\partial^2 P(\mathbf{r}, t)}{\partial t^2} \tag{2.44}$$

To simplify the derivation, we derive the response function in the scalar approximation, considering a plane wave which propagates along the $\hat{z}$ direction. The scalar approximation works well when dealing with isotropic media and pulses sharing the same polarization, and the results can be generalized by solving sets of one dimensional equations for each tensorial components of the response functions. The macroscopic polarization P is given by the expected value of the dipole operator

$$P = Tr(\mu \rho(t)) \tag{2.45}$$

where, as already derived, the time evolution of the density matrix is ruled by the Liouville equation. Collecting the terms of the same orders from eqs. 2.36 and 2.40, it follows

$$P^{(n)} = Tr(\mu \rho^{(n)}(t)) \tag{2.46}$$

and, exploiting eq. 2.38, we obtain the nonlinear polarization

$$\begin{aligned} P^{(n)}(t) = \left(-\frac{i}{\hbar}\right)^n \int_{-\infty}^{t} dt_n \int_{-\infty}^{t_n} dt_{n-1} \cdots \int_{-\infty}^{t_2} dt_1 E(t_n) E(t_{n-1}) \dots E(t_1) \\ Tr\left(\mu(t) \cdot \Big[\mu(t_n), \Big[\mu(t_{n-1}), \dots \big[\mu(t_1)\rho(-\infty)\big] \dots \Big]\Big]\right) \end{aligned} \tag{2.47}$$

[1] A point group is said to be centrosymmetric if for every point $x = \{x_1, x_2, \dots x_n\}$ in the unit cell there is an indistinguishable point $-x = \{-x_1, -x_2, \cdots - x_n\}$. This symmetry is also named inversion symmetry.

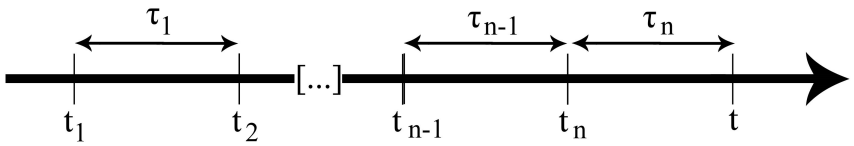

Figure 2.1: Time intervals and instants.

Eq. 2.47 is usually written as a function of time intervals τ_i, during which the density matrix evolves freely, instead of instant variables t_i, at which the interactions happen. Through a variable substitution, represented schematically in Fig. 2.1, we obtain

$$\begin{aligned} P^{(n)}(t) = &\int_0^\infty d\tau_n \int_0^\infty d\tau_{n-1} \cdots \int_0^\infty d\tau_1 \\ &E(t-\tau_n)E(t-\tau_n-\tau_{n-1})\dots E(t-\tau_n-\cdots-\tau_1)\cdot S^{(n)}(\tau_n\dots\tau_1) \end{aligned} \tag{2.48}$$

in which we have introduced the nonlinear response $S^{(n)}$

$$\begin{aligned} S^{(n)}(\tau_n,\dots\tau_1) = &\left(-\frac{i}{\hbar}\right)^n \theta(\tau_n)\dots\theta(\tau_1) \\ &Tr\left\{\mu(\tau_n+\cdots+\tau_1)\left[\mu(\tau_{n-1}+\cdots+\tau_1),\dots\left[\mu(0),\rho(-\infty)\right]\dots\right]\right\} \end{aligned} \tag{2.49}$$

From eq. 2.49 it is clear the mechanism of the physical process that leads to the generation of nonlinear signals. The first $n-1$ interactions prepare a coherence state which oscillates with one of the characteristic frequencies of the matter. Then, the last interaction $\mu(\tau_n+\cdots+\tau_1)$, which does not take part in the commutator, stimulates the emission.
Our aim is finding a solution for eq. 2.44 in presence of a nonlinear polarization. To this purpose, we split P in its linear and nonlinear components

$$P(z,t) = P_L(z,t) + P_{NL}(z,t) \tag{2.50}$$

and focus on the nonlinear contribution to the generated field

$$\frac{\partial^2 E}{\partial z^2} - \frac{1}{c^2}\frac{\partial^2 E}{\partial t^2} = \mu_0 \frac{\partial^2 P_{NL}}{\partial t^2} \tag{2.51}$$

where $c = c_0/n$ is the speed of light in the medium. In coherent nonlinear spectroscopy, the total field E interacting with the sample is usually the sum of two or more incoming fields. In this respect, the derivation just presented can be extended to multiwave mixing. An $n+1$-wave mixing process starts with n incoming fields that interact with the matter

$$E(z,t) = \sum_{j=1}^{n}\left[\mathcal{E}_j(z,t)e^{ik_j z - i\omega_j t} + \mathcal{E}_j^*(z,t)e^{-ik_j z + i\omega_j t}\right] \tag{2.52}$$

and induce the nonlinear polarization

$$P_{NL}(z,t) = \sum_{n>2} P^{(n)}(t)e^{-i(\omega_p t - k_p z)} \tag{2.53}$$

whose frequency and wave vector are given by any combination of the incoming wavevector and frequencies and wave vectors of the incident fields

$$\begin{aligned} k_p &= \pm k_1 \pm k_2 \pm \cdots \pm k_n \\ \omega_p &= \pm\omega_1 \pm \omega_2 \pm \cdots \pm \omega_n \end{aligned}$$

The + and − signs refer to interactions with the fields components $\mathcal{E}_i$ and $\mathcal{E}_i^*$. Imposing some conditions on ω_i and k_i, we select a specific contribution to the nonlinear signal. We look for a solution of the form

$$E(z,t) = \mathcal{E}_s(z,t)e^{-i\omega_s t + ik_s z} + c.c \tag{2.54}$$

and assume the *Slowly Varying Envelope Approximation* (SVEA)

$$\frac{\partial^2 \mathcal{E}_s}{\partial z^2} \ll k_0 \frac{\partial \mathcal{E}_s}{\partial z} \tag{2.55}$$

We obtain the nonlinear propagation for the envelope A_s

$$\frac{\partial \mathcal{E}_s}{\partial z} = \frac{2\pi i \omega_s}{n_s c} P^{(n)}(t) e^{i\Delta k z} \tag{2.56}$$

where $n_s = \frac{ck_s}{\omega_s}$ and we have defined the phase mismatch $\Delta k = k_p - k_s$, determined by the frequency dispersion within the sample as well as the geometry of the experiment. It is important to stress the role of the term $e^{i\Delta k z}$, which expresses the momentum conservation. Integrating both sides of eq. 2.56 over z in a sample of length L, we obtain a solution to the nonlinear wave equation as

$$\mathcal{E}_s(L,t) = \frac{2\pi i \omega_s}{n_s c} P^{(n)}(t)\,\mathrm{sinc}(\Delta k L/2) e^{i\Delta k L/2} \tag{2.57}$$

Because of the sinc function, which is large for $\Delta k L \ll \pi$, the signal is maximum for $\Delta k = 0$. This is known as the *self matching condition*. Another property that follows immediately from eq. 2.57 is that the generated field is proportional to the polarization but phase shifted by $\pi/2$.

The relation between the nonlinear field calculated in eq. 2.57 and the spectroscopic signal is ruled by the detection strategy, which strongly determines the capabilities and range of application of a given technique. Generally two possible schemes are available: heterodyne and homodyne detection. When the nonlinear signal is generated at a new optical frequency different from the incoming ones, the homodyne detected signal intensity is proportional to the squared modulus of the signal field E_s, i.e. $S \propto |E_s|^2$. If the emitted field occurs at a frequency contained in the spectrum of the incident radiation E_{probe}, it is not possible to isolate the signal directly and the detected intensity is proportional to the squared modulus of the sum, $|E_s + E_{probe}|^2$. Therefore it contains a mixing term. In this case, the isolation of the signal may be achieved by detecting the interference pattern with a known reference, namely the incident field. This strategy is called heterodyne detection. In general, even if the signal frequencies do not overlap with the spectrum of E_{probe}, heterodyne detection can be achieved using as the reference an additional incoming field E_{LO} at the same wave vector of the signal, called *local oscillator*. The origin of the name comes from the oscillator in radio waves receiver stations. The detected intensity thus reads

$$S = |E_s(t) + E_{LO}(t)|^2 \propto I_{LO} + I_s + 2\Re(E_{LO}^*(t)E_s(t)) \tag{2.58}$$

Subtracting the reference I_{LO}, since the term I_s is generally negligible, we obtain:

$$\Re(E_{LO}^*(t)E_s(t)) \propto \Re(E_{LO}^*(t) i P^{(n)}(t)) = -\Im(E_{LO}^*(t)P^{(n)}(t)) \tag{2.59}$$

We note that heterodyne detection is linear rather than quadratic in the weak nonlinear polarization $P^{(n)}$. Thus, heterodyne is also effective to enhance a weak background free signal for which the homodyne detection is not sufficiently sensitive. Moreover, by controlling the relative phase between E_{LO} and $P^{(n)}$ it may be possible to detect both the imaginary or the real part of the signal separately.

2.2.2 Quantum electrodynamics

In the previous section, the semiclassical theory for nonlinear optical phenomena has been presented. Here we introduce an alternative approach in which both matter and fields are

treated on the same footing, by means of quantum electrodynamics (QED) [71]. This formalism allows for a fully microscopic description of the interaction between radiation and matter. The advantages of the QED approach particularly arise when the phenomenon under investigation is intrinsically related to the quantum nature of the field. This is the case for example of incoherent effects and spontaneous light emission processes, such as fluorescence and spontaneous Raman [66, 72]. Indeed, even if classic and semiclassical approximations can be used to describe these effects with increasing precision, their detailed comprehension requires to introduce the vacuum field mode [59]. Other situations in which field quantum effect are dominating involve nonclassical or entangled light, whose application in nonlinear spectroscopy is currently object of studies [73, 74]. The first step in the full microscopic description of Raman processes is the quantization of the electromagnetic field. To this purpose, the electromagnetic degrees of freedom are described by a wavefunction, which we denote as $|\psi_F\rangle$. In second quantization, the field operator is given by [66]

$$E(\mathbf{r},t) = \sum_j \mathcal{E}_j(t) e^{i\mathbf{k_j}\cdot\mathbf{r}} + \sum_j \mathcal{E}_j^\dagger(t) e^{-i\mathbf{k_j}\cdot\mathbf{r}} \tag{2.60}$$

where $\mathcal{E}_j$ and $\mathcal{E}_j^\dagger$ are the positive and the negative frequency components for the mode j

$$\mathcal{E}_j = \left(\frac{\hbar\omega_j}{2\epsilon_0\mathcal{V}}\right)^{\frac{1}{2}} \hat{a}_j e^{-i\omega_j t} \tag{2.61}$$

$$\mathcal{E}_j^\dagger = \left(\frac{\hbar\omega_j}{2\epsilon_0\mathcal{V}}\right)^{\frac{1}{2}} \hat{a}_j^\dagger e^{+i\omega_j t} \tag{2.62}$$

In eq. 2.61 and 2.62 $\mathcal{V}$ is the quantization volume of the photon mode j, while $\hat{a}_j$ and $\hat{a}_j^\dagger$ are the boson annihilation and creation operators, respectively. Formally, they are defined by their action on the field state $|\psi\rangle_f$

$$\hat{a}_j^\dagger \; |\psi^j(n)\rangle_f = n_j^{\frac{1}{2}} \; |\psi^j(n+1)\rangle_f \tag{2.63}$$

$$\hat{a}_j \; |\psi^j(n)\rangle_f = (n_j - 1)^{\frac{1}{2}} \; |\psi^j(n-1)\rangle_f \tag{2.64}$$

where the integer n is the occupation number of the mode j.
The total Hamiltonian which describes the system includes the contributions from both the fields and the matter degrees of freedom as well as an interaction term H':

$$H = H_0 + H_F + H' \tag{2.65}$$

The field Hamiltonian H_F is given by

$$H_F = \sum_j \hbar\omega_j \hat{a}_j^\dagger \hat{a}_j \tag{2.66}$$

The Hamiltonian H_0 is determined by the Physics of the problem under consideration and rules the free evolution between the interactions in eq. 2.47. In the dipole approximation [66], H' takes the form of the Power-Zienau [75] radiation-matter Hamiltonian

$$H' = (V + V^\dagger) \sum_j (\mathcal{E}_j + \mathcal{E}^\dagger) \tag{2.67}$$

The coupling between the material and the fields is mediated by the dipole operator

$$V(\mathbf{r}) = \sum_{a,b>a} \mu_{ab} \, |a\rangle \, \langle b| \tag{2.68}$$

with

$$\mu_{ab} = \langle a| e \sum_{\alpha=1}^{N} \boldsymbol{r_\alpha} |b\rangle$$

and the index α runs over all molecules in the sample.

In the quantum field formalism, the nonlinear signal can be calculated through two approaches that are characterized by a different point of view. In the first, the signal is considered from the material perspective [76]. In particular, the transitions between states are explicitly accounted for, by means of the Fermi 's golden rule. Because the field and the material are coupled, transitions between material states affect also the fields degrees of freedom and energy exchanges between the fields and the matter modes are possible. Here, we will follow another method, describing the optical signal from the field perspective. In this approach the signal is defined as the change in the mean photon occupation number of the detected mode ω_S:

$$S = \left\langle N_s(t) \right\rangle - \left\langle N_s(0) \right\rangle = \int_{-\infty}^{\infty} dt' \frac{d}{dt'} \left\langle \hat{a}_S^\dagger \hat{a}_S \right\rangle \tag{2.69}$$

being $\langle \cdot \rangle$ the trace operator. The expectation value can be calculated by solving the density matrix for the total system $\rho(t)$ which now includes both the radiation and matter degrees of freedom. The time derivative in eq. 2.69 can be calculated using the Heisenberg equations of motion and the Hamiltonian 2.65

$$\frac{d}{dt} \left\langle \hat{N}_S \right\rangle = \left\langle \frac{d}{dt} \hat{N}_S \right\rangle = \left\langle \sum_j \frac{i}{\hbar} \left[H'(t), \hat{a}_S^\dagger \hat{a}_S \right] \right\rangle \tag{2.70}$$

Expanding the commutator we obtain

$$\begin{aligned} \left[H', N_S\right] =& (V + V^\dagger) \sum_j \left(\left[\mathcal{E}_j, a_S^\dagger a_S\right] + \left[\mathcal{E}_j^\dagger, a_S^\dagger a_S\right] \right) = \\ =& (V + V^\dagger) \sum_j \left(\left[\mathcal{E}_j, a_S^\dagger\right] a_S + a_S^\dagger \left[\mathcal{E}_j^\dagger, a_S\right] \right) = \\ =& (V + V^\dagger)(\mathcal{E}_S - \mathcal{E}_S^\dagger) \end{aligned} \tag{2.71}$$

where we have used the commutation relation for the ladder operators: $\left[a_i, a_j^\dagger\right] = \delta_{ij}$. Using eq. 2.71 in eq. 2.70, the stimulated signal can be expressed in the time and frequency domain as

$$S = \frac{i}{\hbar} \int_{-\infty}^{\infty} dt' \left\langle (V + V^\dagger)(\mathcal{E}_S - \mathcal{E}_S^\dagger) \right\rangle = \frac{2}{\hbar} \Im \int_{-\infty}^{\infty} dt' \left\langle \mathcal{E} V - \mathcal{E}^\dagger V \right\rangle = \frac{2}{\hbar} \Im \int_{-\infty}^{\infty} d\omega' \left\langle \mathcal{E} V - \mathcal{E}^\dagger V \right\rangle \tag{2.72}$$

When the resonance condition holds the radiation-matter interaction Hamiltonian in the rotating wave approximation (RWA) reduces to $H'(t) = -V(t)\mathcal{E}^\dagger + h.c.$ and eq. 2.72 reduces to

$$S = -\frac{2}{\hbar} \int_{-\infty}^{\infty} dt' \Im \left\langle \mathcal{E}^\dagger(t') V(t') \right\rangle = -\frac{2}{\hbar} \int_{-\infty}^{\infty} d\omega' \Im \left\langle \mathcal{E}^\dagger(\omega') V(\omega') \right\rangle \tag{2.73}$$

In real experiments, the range of the integrations in eq. 2.73 is restricted by the response function of the detector [61]. For example, considering a narrow time gate with nearly instantaneous response $\delta(t - t')$

$$S_t(t) = -\frac{2}{\hbar} \Im \left\langle \mathcal{E}^*(t) V(t) \right\rangle \tag{2.74}$$

We note that, considering classical radiation, the field can be substituted by its expectation value and taken outside the bracket $\langle \mathcal{E} \rangle = \mathcal{E}$, leading to a result equivalent to the classical expression 2.59. Similarly, for the frequency resolved detection by a spectrometer with a narrow spectral response $\delta(\omega - \omega')$ we obtain

$$S_f(\omega) = -\frac{2}{\hbar} \Im \left\langle \mathcal{E}^*(\omega) V(\omega) \right\rangle \tag{2.75}$$

When the frequencies of the interacting pulses are such that no electronic excited levels can be involved, an excitation to a virtual state is coupled to an instantaneous de-excitation to a real state, since by the Heisenberg uncertainty principle the system can only spend a very short time on the intermediate state. In this case, equation 2.70 can be computed using the effective Hamiltonian

$$H'(t) = \alpha(t) \sum_{i,j} \mathcal{E}_j^\dagger(t)\mathcal{E}_i(t) + h.c. \tag{2.76}$$

where α is the excited state polarizability. Although the physics under these two situations is different, we will show that the diagrammatic description in either case is similar.

We can now use the Liouville formalism developed in the first section to calculate the expectation value in 2.73. To this aim, we introduce a more compact notation in terms of Liouville space left and right superoperators. We define the superoperator A_L, acting on any operator X in Hilbert space, as a left superoperator if

$$A_L X = AX \tag{2.77}$$

Equivalently the right superoperator A_R is defined by

$$A_R X = XA \tag{2.78}$$

Furthermore, we define the combinations $A_\pm$ of left and right superoperators:

$$A_\pm = \frac{1}{\sqrt{2}}(A_L \pm A_R) \tag{2.79}$$

In terms of superoperators, the stimulated optical signal can be expressed by

$$S = \frac{d}{dt}\left\langle \hat{N}_S \right\rangle = -\frac{2}{\hbar}\Im\left[\left\langle T\mathcal{E}_L(\mathbf{r},t)V_L^\dagger(t)exp\{-\frac{i}{\hbar}\int_{-\infty}^{t} d\tau\sqrt{2}H'_-(\tau)\}\right\rangle_\rho\right] \tag{2.80}$$

where we wrote explicitly the subscript to indicate that the mean value is calculated with respect to the density matrix ρ in the joint field and matter Liouville space: $\langle\cdot\rangle = Tr[A\rho(t)]$. Finally, we stress that the exponential in eq. 2.80 can be expanded in power series equivalently to eq. 2.47. The different orders can be accounted for through a graphic representation as shown in the next section.

2.3 Double sided Feynman Diagrams

In the previous section, we derived the signal generated in a wave mixing process. It has been found that it is proportional to the imaginary part of the nonlinear polarization. It is necessary at this point to write explicitly the commutator in eq. 2.47, or equivalently in 2.80. To this purpose, double sided Feynman diagrams are a valuable tool, which allows to easily account for all the contributions in every pulse configuration. We introduce Feynman diagrams directly from the first and third order polarization. Then we present a set of rules for their usage in the general situation. The linear polarization in the time domain reads

$$P^{(1)}(t) = \int_0^\infty d\tau_1 E(t-\tau_1)S^{(1)}(\tau_1) \tag{2.81}$$

where the first order response function $S^{(1)}$ is

$$S^{(1)}(\tau_1) = -\left(\frac{i}{\hbar}\right)^3 Tr\left(\mu(\tau_1)\left[\mu(0),\rho(-\infty)\right]\right) \tag{2.82}$$

Expanding the commutator and using the invariance of the trace operator under cyclic permutation we obtain two terms

$$Tr\left(\mu(\tau_1)\mu(0)\rho(-\infty)\right) - Tr\left(\mu(\tau_1)\rho(-\infty)\mu(0)\right) = Tr\left(\mu(\tau_1)\mu(0)\rho(-\infty)\right) - Tr\left(\rho(-\infty)\mu(0)\mu(\tau_1)\right) \tag{2.83}$$

The two terms in eq. 2.83 are complex conjugates. We can rewrite the first using the explicit form of $\mu(\tau_1)$ in terms of the evolution operator:

$$Tr\left(\mu(\tau_1)\mu(0)\rho(-\infty)\right) = Tr\left(U^\dagger(\tau_1)\mu U(\tau_1)\mu\rho(-\infty)\right) = Tr\left(\mu U(\tau_1)\mu\rho(-\infty)U^\dagger(\tau_1)\right) \tag{2.84}$$

This expression offers a clear physical interpretation: the density matrix interacts twice with the fields from the ket side through μ and evolves in between under the free Hamiltonian H_0 for a time τ_1. Importantly, the role of the last μ which is outside the commutator is different: it does not (necessarily) represent an interaction with an external field, but instead the emission of the signal due to the relaxation of the non equilibrium polarization prepared by the external pulses. The last arrow is usually called *free induction decay*, with a term derived from NMR spectroscopy [77]. In heterodyne detected signals, the free induction decay is stimulated by a incident field in the same mode.

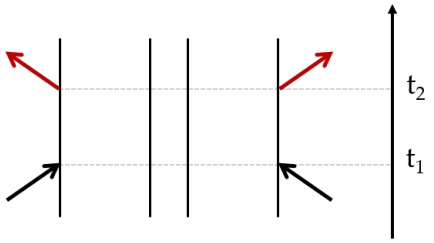

Figure 2.2: The double sided Feynman diagrams associated to the first order of the perturbation theory from an equilibrium density matrix in the ground state. The dressing with the fields can be performed immediately in the RWA, since de-excitation is not possible from the ground state and consequently the direction of the first arrow is constrained.

We can operate on the same lines for higher order perturbations. The third order polarization reads

$$P^{(3)}(t) = \int_0^\infty d\tau_3 \int_0^\infty d\tau_2 \int_0^\infty d\tau_1 E(t-\tau_3)E(t-\tau_3-\tau_2)E(t-\tau_3-\tau_2-\tau_1)S^{(3)}(\tau_1,\tau_2,\tau_3) \tag{2.85}$$

where the response function $S^{(3)}$ is

$$S^{(3)}(\tau_1,\tau_2,\tau_3) = -\left(\frac{i}{\hbar}\right)^3 Tr\left(\mu(\tau_3+\tau_2+\tau_1)\left[\mu(\tau_1+\tau_2),\left[\mu(\tau_1),\left[\mu(0),\rho(-\infty)\right]\right]\right]\right) \tag{2.86}$$

Expanding the commutator we get eight terms

$$S^{(3)}(\tau_1,\tau_2,\tau_3) = \left(\frac{i}{\hbar}\right)^3 \sum_i (R_i - R_i')$$

where $i = 1,\ldots,4$. It is easy to prove that the terms R_i' are the opposite of the complex conjugate of R_i. This is a general result: only half of the 2^n terms arising from the nth order polarization are independent and need to be calculated. Therefore the independent terms are

$$R_1 = Tr\left[\mu(\tau_1+\tau_2+\tau_3)\mu(0)\rho(-\infty)\mu(\tau_1)\mu(\tau_1+\tau_2)\right] \tag{2.87a}$$
$$R_2 = Tr\left[\mu(\tau_1+\tau_2+\tau_3)\mu(\tau_1)\rho(-\infty)\mu(0)\mu(\tau_1+\tau_2)\right] \tag{2.87b}$$
$$R_3 = Tr\left[\mu(\tau_1+\tau_2+\tau_3)\mu(\tau_1+\tau_2)\rho(-\infty)\mu(0)\mu(\tau_1)\right] \tag{2.87c}$$
$$R_4 = Tr\left[\mu(\tau_1+\tau_2+\tau_3)\mu(\tau_1+\tau_2)\mu(\tau_1)\mu(0)\rho(-\infty)\right] \tag{2.87d}$$

In order to better understand the physical meaning of the terms R_i, we can rearrange them, exploiting the properties of the propagator and the trace invariance under cyclic permutations, as done for the first order term. Choosing R_1 as a working example

$$\begin{aligned} &Tr\left(\mu(\tau_3+\tau_2+\tau_1)\mu(0)\rho(-\infty)\mu(\tau_1)\mu(\tau_1+\tau_2)\right) = \\ &= Tr\left(U^\dagger(\tau_3)U^\dagger(\tau_2)U^\dagger(\tau_1)\mu U(\tau_3)U(\tau_2)U(\tau_1)\mu\rho(-\infty)U^\dagger(\tau_1)U^\dagger(\tau_2)\mu U(\tau_1)U(\tau_2)\right) = \\ &= Tr\left(\mu U(\tau_3)U(\tau_2)U(\tau_1)\mu\rho(-\infty)U^\dagger(\tau_1)\mu U^\dagger(\tau_2)\mu U(\tau_1)U(\tau_2)U^\dagger(\tau_2)U^\dagger(\tau_1)U^\dagger(\tau_3)\right) = \\ &= Tr\left(\mu U(\tau_3)U(\tau_2)U(\tau_1)\mu\rho(-\infty)U^\dagger(\tau_1)\mu U^\dagger(\tau_2)\mu U^\dagger(\tau_3)\right) \end{aligned} \tag{2.88}$$

Eq. 2.88 allows to follow the evolution of the density matrix through the interactions:

$$Tr\left(\underbrace{\mu}_{(7)}\underbrace{U(\tau_3)}_{(6)}\underbrace{U(\tau_2)}_{(4)}\underbrace{U(\tau_1)}_{(2)}\underbrace{\mu}_{(1)}\rho(-\infty)\underbrace{U^\dagger(\tau_1)}_{(2)}\underbrace{\mu}_{(3)}\underbrace{U^\dagger(\tau_2)}_{(4)}\underbrace{\mu}_{(5)}\underbrace{U^\dagger(\tau_3)}_{(6)}\right) \tag{2.89}$$

1. The dipole acts on the ket side of the density matrix;
2. after the interaction, ρ evolves freely during τ_1;
3. the dipole acts on the bra;
4. the density matrix evolves freely during τ_2;
5. the dipole acts on the bra;
6. again, there is a free evolution period during τ_3;
7. finally the dipole operator interacts with the ket and the trace is calculated.

Thus, the term R_1 describes two interaction with the bra side of the density matrix and one with the ket. These three interactions prepare the system in a coherent state. Finally, the free induction decay occurs and the nonlinear signal is generated.
This sequence of bra and ket interactions justifies the introduction of double sided Feynman diagrams shown in Fig. 2.2 for the two contributions to the first order of eq. 2.83 and in Fig. 2.3, which represent the various terms in the expansion 2.86.

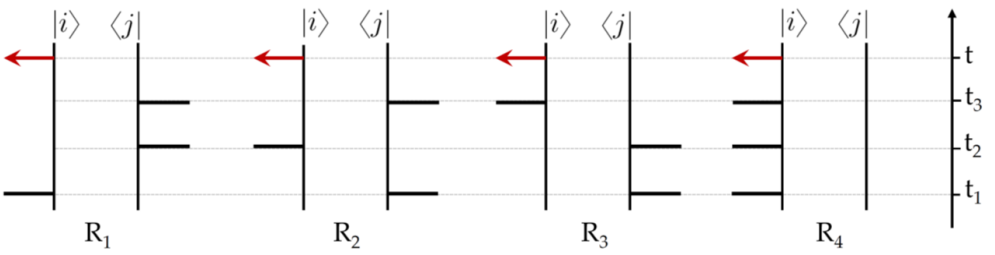

Figure 2.3: The double sided Feynman diagrams associated to the terms R_1-R_4 in eq. 2.87.

Feynman diagrams consist in two vertical lines showing the evolution of the two sides of the density matrix and a series of arrows standing for light-matter interactions at precise times. Conventionally, the left represents the ket while the right accounts for the bra. Using diagrammatic techniques greatly simplifies the calculation of nonlinear signals. Indeed, the n^{th} order polarization is given by the sum of all the pathways in the Liouville space. The number of contributions, however, raises as 2^{n-1} with the order of perturbation and increases dramatically when considering the boundary conditions, as multiple incoming fields and the specific properties of the system. Notably, diagrams can be selected before computing the result, restricting the calculation only to the pathways that effectively contribute to the specific signal of interest. The selection starts from the bare diagrams, as those in Fig. 2.3, which then need to be dressed considering all the possible permutations of the fields. The relevant diagrams are selected by enforcing the conservation of the energy and the experimental conditions as phase matching, beam geometry, resonance scheme and time ordering between the pulses. This further testifies the proximity between the response function formalism and experiments. The material properties are considered choosing a level scheme and a model molecular Hamiltonian H_0 to calculate the dipoles. If multiple states are available, i.e. are connected by non-vanishing dipole coupling terms, the response of each diagram must be summed over all the possible combinations of matter states which can be reached. To obtain the experimental signal, the diagrams are interpreted to retrieve the associated perturbative term by means of the rules presented in the next section. Finally, we remark that an equivalent diagrammatic description is provided by energy level diagrams. An example has been reported for SRS in chapter 1, in which dotted and solid arrows connecting the levels in the energy scheme of the sample represents interactions with the bra and the ket, respectively.

2.3.1 Rules in time and frequency domain

We define the Green's function in time domain as

$$G(t_1 - t_2) = -\frac{i}{\hbar}\theta(t_1 - t_2)e^{-iH_0(t_1-t_2)} \tag{2.90}$$

where H_0 is the free matter Hamiltonian. The Feynman diagram can be interpreted using the following rules

1. Interactions are ordered in time between the two branches of the diagram. Time runs from bottom to top.
2. At time zero, the density matrix starts in a population state $|i\rangle\langle i|$ which leads to a Boltzmann factor $\mathtt{P}(i)$ in the nonlinear response.
3. The last arrow represents the signal, generated by $Tr(\mu\rho^{(n)}(t))$.
4. Each diagrams gives an overall sign $(-1)^n$, where n is the number of interactions on the bra side.
5. A field mode is represented by an arrow. An arrow pointing to the right represents the interaction of $\mathcal{E}_j(t)$ and brings a term $e^{-i\omega t+ikr}$, while an arrow pointing to the left represents $\mathcal{E}_j^\dagger(t)$, carrying the associated $e^{+i\omega t-ikr}$ factor. The frequency and the wavevector of the light emitted is simply given by the sum of the input frequencies and the wavevectors. This comes from energy and momentum conservation.
6. In RWA, an arrow pointing towards the diagram represents an induced excitation of the ket or the bra, depending on the side on which the interaction occurs. An arrow pointing out represents a de-excitation. Thus, each term $\mathcal{E}_j(t)$ is accompanied by a dipole operator $V^\dagger$, each interaction with $\mathcal{E}_j^\dagger(t)$ by a dipole operator V.
7. Between two consecutive interactions, the system evolves under the unperturbed Hamiltonian H_0. The free evolution periods are accounted for by a Green's function $G(t_1 - t_2)$, which represents forward evolution in time.

8. The last interaction at the observation time t must leave the system in a population state.

Since conjugate diagrams give conjugates responses, it is sufficient to calculate only diagrams with the last interaction on the same side. Following a widely used convention, we select diagrams in which free induction decay arise from the ket[2].
As a consequence of our definition of eq. 2.90 in time domain, the frequency domain Green's function is

$$G(\omega) = \frac{1}{\hbar(\omega - H_0 + i\eta)} \tag{2.91}$$

Rules in frequency domain become

1. Interactions are ordered in time between the two branches of the diagram. Time runs from bottom to top.
2. At time zero, the density matrix starts in a population state $|i\rangle\langle i|$ which leads to a Boltzmann factor $\mathtt{P}(i)$ in the nonlinear response.
3. The last arrow represents the signal, generated by $Tr(\mu\rho^{(n)}(\omega))$.
4. Each diagrams gives an overall sign $(-1)^n$, where n is the number of interactions on the bra side.
5. A field mode is represented by an arrow. Arrows pointing to the right represent interaction with the field annihilation operator $\mathcal{E}_j(\omega)$, while arrows pointing to the left represent interaction with the field creation operator $\mathcal{E}_j^\dagger(\omega)$.
6. In RWA, each interaction with $\mathcal{E}_j(\omega)$ is accompanied by a dipole operator $V^\dagger$, each interaction with $\mathcal{E}_j^\dagger(\omega)$ by a dipole operator V.
7. For each period of free evolution on the left branch we write a Green's function $G(\sum_j \omega_j)$, where the sum goes over all earlier interactions along the diagram, i.e. the frequency arguments of the various propagators are cumulative; additionally, the ground state frequency ω_g is added to all arguments of the propagators.
8. The last interaction at the observation time t must leave the system in a population state.
9. Signal expression contains a delta function $2\pi\,\delta(\sum_{j=1}^{n+1}\omega_j)$, accounting for energy conservation.

Even though the Hamiltonian 2.67 and 2.76 describe different physical processes, these can be depicted by similar diagrams. To write down the signal from the diagrams in off-resonance condition, we can follow the same rules reported above with the exception of rule 6 that has to be modified accordingly to the substitution $\alpha \to V$:

6' Arrows pointing to the right represent interaction with the field annihilation operator $\mathcal{E}_j(t)$, while arrows pointing to the left represent interaction with the field creation operator $\mathcal{E}_j^\dagger(t)$. The interactions are with pairs of arrows $\mathcal{E}_i\mathcal{E}_j^\dagger$ and are accompanied by the polarizability α.

In the most general case a single process can involve both resonant and off resonant pulses. As a consequence, the optical response, obtained from the diagrams, will contain one V for each resonant interaction and one α for each off resonant interaction. We stress that, in off resonant condition, interactions are with a couple of arrows, without any free propagation on the virtual state prepared by the excitation, while a resonant interaction involves one arrow.

[2]The last interaction can be chosen to occur from the left or the right sides and this choice does not affect the result because of the cyclic invariance of the trace. But as a consequence of our definition of Green's functions, choosing the last interaction to be from the right results in an extra minus sign.

3 Experimental Realization

In nonlinear optics experiments, as those reported in this thesis, there is the need to generate and manipulate laser pulses of femtosecond duration. The solutions to this technological challenge have been recently achieved and are continuously improving with the development of novel ultrafast sources and setups. In this chapter, we present the experimental tools required to perform ultrafast pump-probe and stimulated Raman experiments in the time and frequency domain.

3.1 Overview of the optical setup

The sketch in Fig. 3.1 gathers the different lines used for transient absorption (TA), two and three beams impulsive stimulated Raman experiments (2bISRS and 3bISRS) and frequency domain Stimulated Raman Spectroscopy (SRS) presented in this work. The TA, 2bISRS and SRS data have been collected by the author and the Femtoscopy group at Sapienza University of Rome. All the lines are seeded by a common femtosecond laser source. A chirped white light continuum (WLC) and the compressed output of a noncollinear optical parametric amplifiers (NOPA 1) serve as the probe (orange line) and Raman (green line) pulses for TA and 2bISRS. The chirp of the probe can be linearly varied by introducing optical glass (N-BK7) plates of variable widths on the WLC path. SRS is realized using the same WLC path and the output of a collinear Optical Parametric Amplifier (OPA), frequency doubled in a Barium β Borate (BBO) crystal, as narrowband Raman pulse. The 3bISRS data presented in Chapter 6 have been collected by the Kukura's group at University of Oxford, using a similar setup in which the OPA branch is substituted by another noncollinear amplifier (NOPA 2) to generate an additional femtosecond Actinic pulse.

In each experiment, the relative pulses are focused on the sample in a noncollinear geometry. This expedient allows to limit the unwanted Raman and Actinic scattered light on the detector. Finally, the WLC is spectrally resolved in the detector apparatus, consisting in a spectrometer coupled to a camera. Additional details of the laser source, pulses generation and detection scheme are given in the next sections. Two different delay lines (DL 1 and 2) are used to tune the relative arrival time of the pulses on the sample in the pump-probe geometry. Together with the control of time overlap, an important role while performing the experiment is played by the spatial overlap of the pulses when they are focused on the sample. The goodness of the overlap controls the intensity of the Raman and transient absorption signals, since the nonlinear effects are maximized in the focus. This is controlled through separate focusing optics on each pulse path. Fig. 3.1 summarizes the different experimental tools used as control knobs in this thesis: the tunability of the narrowband pulse realized in the OPA branch allowed to retrieve the vibrational selectivity in resonant SRS presented in Chapter 1; controlling the spectral properties of the WLC, and in particular its chirp, led to the results presented in Chapter 4; finally, the tunable wavelength of the impulsive excitations realized with the NOPAs allowed the application

of 1D and 2D ISRS to the study of the electronically excited state Raman spectra presented in Chapters 5 and 6. We stress that, since we were interested in the variety of information encoded in the broadband probe pulse, the common ingredient in all the presented approaches has been the spectrally resolved detection.

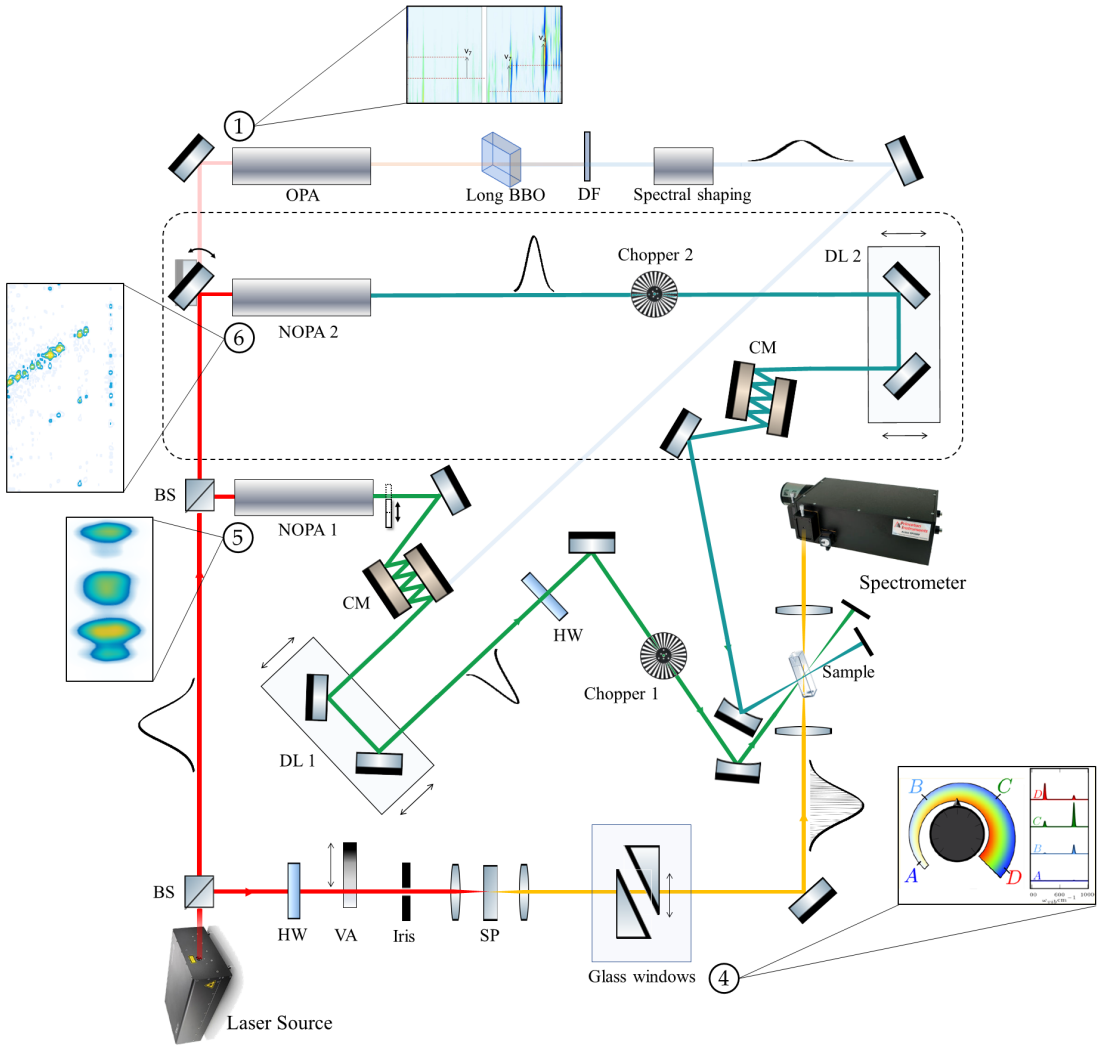

Figure 3.1: Experimental apparatus for multidimensional Stimulated Raman spectroscopy. In the three beams ISRS scheme, the output of a mode-locked laser source is split by two beam splitters (BS). In two symmetric branches, the femtosecond Actinic pump and the Raman pulse are generated through two noncollinear optical parametric amplifiers (NOPA 1 and 2) that produce tunable visible pulses and compressed using chirped mirrors (CM). Two computer-controlled delay lines (DL 1 and 2) allow for scanning time intervals between the pulses. The probe is synthesized focusing part of the source on a Sapphire plate (SP). The chirp of the probe pulse can be modulated by glass windows. Two synchronized choppers block alternating Actinic and Raman pulses to record the modification induced to the transmitted WLC probe, which is frequency-dispersed by a spectrometer onto a CCD device. In the two beam ISRS geometry, the Actinic pulse branch (highlighted by the dotted rectangle) is absent. Alternatively, frequency domain SRS is performed using the same WLC path the OPA path which produces a narrowband pulse by means of frequency doubling in a long BBO crystal. DF: dichroic filter VA: variable attenuator. HW: half waveplate. The insets highlight the experimental tools used as control knobs in the thesis within the specified chapter.

A choppering scheme is employed to detect differential signals. Two choppers, synchronized at half (500 Hz) and a quarter (250 Hz) of the source repetition rate, alternatively block the Actinic and Raman pulses or allow them to reach the sample, while the WLC is always detected. The choppers are also synchronized with the detection software and require a detector device able to measure the probe in shot-to-shot mode.

3.2 Pulses generation and detection

In this section, we specify the details of the general setup just discussed, in particular referring to that developed in Sapienza (Fig. 3.2). Since the majority of the results presented in this thesis is focused on two and three beams ISRS, we discuss in details the WLC and NOPAs branches which are used to synthesize the femtosecond Actinic, Raman and probe pulses. We also briefly describe the generation of narrowband pulses exploited in the SRS experiment presented in Chapter 1.

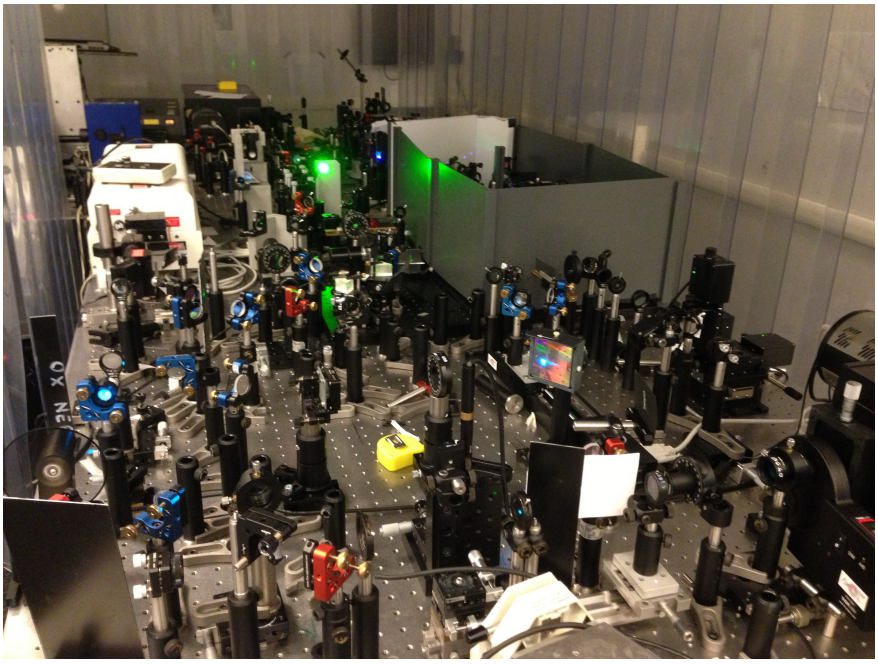

Figure 3.2: Panoramic photo of the Femtoscopy experimental setup.

3.2.1 Laser Source

The different optical branches of the setup are seeded by a 800 nm laser beam with a time duration of approximately 40 fs. The laser source is composed by two main components: an 80 MHz oscillator and a regenerative amplifier with 1 KHz repetition rate. The oscillator provides ultrashort pulses, operating in a mode-locking regime. These pulses are then amplified through the Chirped Pulse Amplification (CPA) technique [78]. In our setup, the oscillator (Coherent Micra) is a Ti:sapphire based mode-locked system pumped by a solid state laser (Coherent Verdi), which provides a 5 W beam centered at 532 nm. Using a Ti:sapphire crystal as active medium provides a large gain bandwidth centered around 800 nm, allowing the generation of ultrashort pulses via passive mode-locking.

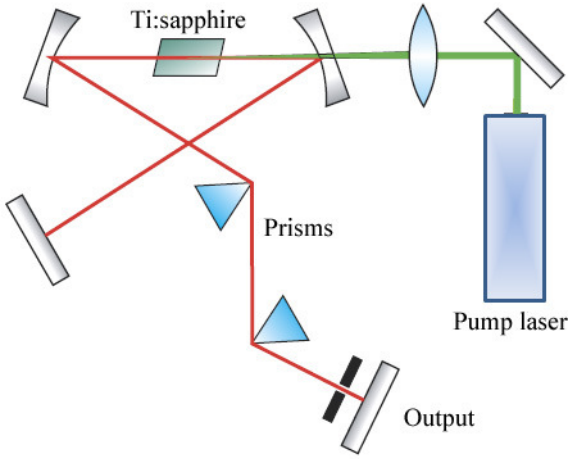

Figure 3.3: Scheme of the mode-locked Ti:sapphire oscillator.

To achieve femtosecond pulse generation, the passive system must have a fast, virtually instantaneous response. To this aim, the Coherent Micra oscillator exploits the lens effect induced in the gain medium by a Kerr nonlinearity [1] [79]. This mechanism allows to trigger the mode-locking, operating on the pulse profile. Together with the Kerr-lens mode-locking, prism compression provides the requested duration for the output beam, compensating the spectral dispersion produced in the cavity. The output beam of the Coherent Micra oscillator has a power of ≈ 400 mW, a wavelength of 800 nm and a bandwidth that ranges from 30 to over 100 nm.

The regenerative amplifier (coherent Legend Elite) is also based on a Ti:sapphire crystal. The optical excitation of the crystal is achieved by pumping with a Q-switched pump laser (Coherent Evolution-15), whereas the amplification is obtained by forcing multiple round trips of a single laser pulse through the gain medium in a resonator. The pulse is trapped in the resonator by means of an optical switch, constituted by two Pockels cells, and experiences an intensity gain over 10^6. After a tunable number of round trips, usually from ten to fifteen, a voltage is applied to the output Pockels cell and the pulse can leave the resonator.

The direct amplification of an ultrashort pulse is not feasible, because the damage threshold of the active medium can be easily reached due to high peak powers involved. This issue is overcome by CPA. In this technique, the output beam from the oscillator is firstly stretched in time, lowering the peak power, by means of a pair of gratings which introduce a known amount of chirp, and then safely amplified through the regenerative amplifier. Thereafter, the resulting pulse can be compressed again by a second pair of gratings which removes the chirp introduced by the stretcher, nearly achieving the initial duration. The output of the Legend amplifier is characterized by the parameters listed in Table 3.1

Center Wavelength	Time duration	Energy	Repetition rate
~ 800 nm	~ 40 fs	~ 3.5 mJ	1 kHz

Table 3.1: Parameters of the laser source output

[1] The optical Kerr effect is a third order nonlinear phenomenon occurring when intense light propagates in a medium leading to a dependence of the refractive index of the medium on the intensity of light itself. It is related to the electronic degrees of freedom of the medium (deformation of the electronic orbitals) that cause a very fast response (a few femtoseconds) [70].

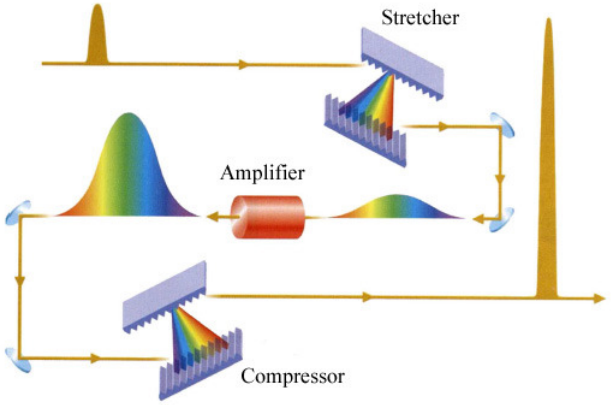

Figure 3.4: Scheme of the Chirped Pulse Amplification technique exploited by the regenerative amplifier. Adapted from [80]

3.2.2 White light probe generation and detection

The broadband probe pulse is synthesised through a supercontinuum generation process obtained focusing a portion of the ultrashort pulse from the source on a transparent plate, such as silica, calcium fluoride (CaF_2) or sapphire. The competition between two nonlinear effects, self-focusing and self-phase modulation, leads to a significant spectral broadening [81, 82]. The shape of the spectral envelope can be varied by changing the material used for the WLC generation, the pump power and the focus properties, controlled by an iris and a variable attenuator. The resulting pulse is a WLC whose bandwidth spans hundreds of nanometers. Our setup exploits a sapphire plate by means of which it is possible to cover a spectral range from 440 nm to the NIR. Alternatively, we can generate the WLC using a CaF_2 plate to reach lower wavelengths. In this case, the plate needs to be continuously moved by mechanical translators when exposed to light, in order to reduce photodamaging. Depending on the experiment, the spectral region of interest can be further selected by filters, which remove the residual of the fundamental at 800 nm and avoid the saturation of the detector. In particular, for the experiments presented in this thesis we probed the visible region. The WLC spectra obtained using the two materials and the action of the filter are shown in Fig. 3.5. In all the experimental realizations presented here, the WLC serves as the probe pulse and is detected. The detection strategy is heterodyne: the spectroscopic information, generated by the interaction of all the pulses with sample, is encoded in the spectral envelope of the probe pulse itself as it pass through the sample and retrieved measuring the differential transmission in presence and in absence of the additional preparation pulses. To collect the wavelength dependent data, the probe needs to be spectrally resolved by focusing it on a monochromator slit after the interaction with the sample, synchronizing the spectra recording with the choppers operating on the other pulse lines. The device used in our setup is composed by a optical multichannel analyser (OMA), which provides the simultaneous acquisition of a large wavelength range, combined with a charge-coupled device (CCD) array. The detection is shot-to-shot to reduce the noise of measurement. The monochromator (Acton sp 2500i), using one among the three available gratings with respectively 150, 1200, 2400 grooves/mm, disperses the beams onto a CCD array (Princeton Pixis 400) with 1340 horizontal and 400 vertical pixels. The horizontal number of pixels determines the lower bound of the instrumental spectral sensitivity.
Finally, an home-built Graphical User Interface (GUI) and an acquisition software, based on MATLAB platform, is used to control the hardware and the setup parameters. This software is also responsible for the synchronization between the laser source, which triggers the choppers, and the data acquisition.

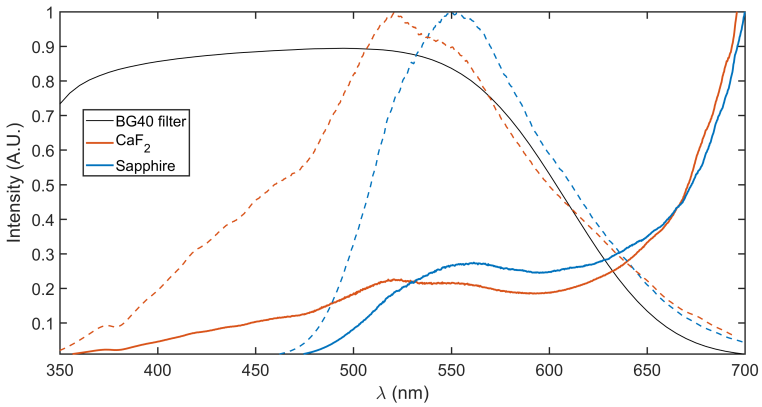

Figure 3.5: Normalized WLC spectra generated using a sapphire plate and a calcium fluoride (CaF_2) crystal. Dashed and continuous lines report the spectra with and without the action of a BG40 filter, respectively. The transmission function of the filter is also reported as a black line. CaF_2 provides a bluer spectrum and a stable continuum even below 450 nm, but requires to be moved during the experiment since it can be damaged by exposition to the femtosecond radiation.

3.2.3 Impulsive Actinic and Raman pulse

Collinear and non collinear OPAs [83, 84] exploit a second order nonlinear optical effect to obtain broad frequency tunability of short pulses. The OPA working principle grounds on the coherent energy transfer from an intense pump beam at frequency ω_p to a weak seed at a lower frequency $\omega_s < \omega_p$. Additionally, to satisfy energy conservation a third color idler beam is produced at $\omega_i = \omega_p - \omega_s$. When the pump frequency is fixed, the amplified color ω_s is selected by the phase matching condition, which needs to be satisfied to achieve efficient amplification, typically using a birifrangent material. For collinear OPA, phase matching is ruled by a scalar equation: $\Delta k = k_p - k_i - k_s = 0$. Once the polarizations of the beams are fixed, phase matching can be fulfilled adjusting the angle θ between the wave vector of the propagating beams and the optical axis of the crystal. For amplification in the visible domain, Type I phase matching is usually exploited, in which the pump and signal have perpendicular polarizations. In case of NOPAs [85–87], the phase matching condition becomes a vector equation and an additional degree of freedom is given by the angle between the pump and seed pulses. This allows to satisfy the phase matching and maximize the spatial and temporal overlap of the traveling wave inside the birifrangent crystal at the same time. The last condition is obtained because the different distances that the signal and idler must travel through the crystal, due to their relative angle, minimize their group velocity mismatch. As a consequence, if wisely designed, NOPAs can fulfill the phase matching condition for a very broad range of signal frequencies at the same time (Fig. 3.6), and, consequently, they can be used to generate pulses significantly shorter than the pump pulse.

The NOPA used to generate the femtosecond Actinic and Raman beams is sketched in Fig. 3.7. A fraction of the laser source output, $\sim 1.2\,mJ$, is split into two beams by an asymmetric beam splitter. The minor portion, which serves as a seed, is attenuated and then focused on a 3 mm Sapphire plate to generate a chirped white light continuum extending from 480 to 1000 nm. The larger portion of the input is exploited as pump beams for the amplifier and frequency doubled by a 1 mm BBO crystal to generate a pulse centered at 400 nm via Second Harmonic Generation (SHG). The seed and pump beams are spatially overlapped on a 2 mm BBO crystal crossed at the phase matching angle, in order to amplify a portion of the continuum. The relative delay between pump and seed, controlled by a delay line on the pump branch, determines the amplified color within the seed envelope due to the different arrival times of the WLC spectral components. The NOPA output can then be tuned in the range $\sim$ 480-700 nm with an average

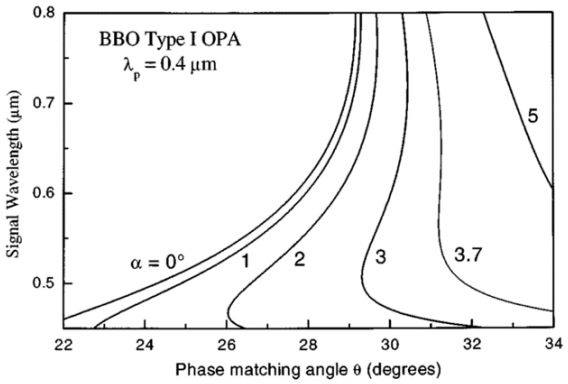

Figure 3.6: Phase matching angle θ as a function of the wavelength for different values of the seed to pump angle α for a tyoe I NOPA operating at a ω_p=400 nm. For a collinear geometry ($\alpha = 0^{\circ}$), the phase matching angle is different for each wavelength, preventing broadband amplification; as α increases, the dependence of θ on the wavelength becomes weaker. For example, at $\alpha = 3.7°$, a large portion of the visible is amplified for the same value of $\theta \sim 31°$. Image from [83].

power of the order of the micro Joule.
The broadband amplification achieved by NOPAs allows for significantly reducing the time duration of the pulses by means of compression. For example, multiple reflections on a pair of chirped mirrors introduce a negative dispersion proportional to the number of bounces. Adjusting this number, the chirp of the NOPA output is compensated and pulses below 10 fs can be obtained. The time duration of the pulses is measured by second harmonic noncollinear autocorrelation.

3.2.4 Narrowband Raman pulse

An efficient nonlinear protocol to obtain picosecond pulse from a femtosecond source is based on spectral compression via second harmonic generation (SHG-SC) [88–90]. In this protocol, the second harmonic generation process is performed in the presence of large group-delay-mismatch (GDM) between the fundamental frequency (FF) and the second harmonic (SH) pulse. The resulting narrow bandwidth is given essentially by the inverse of GDM. This process leads to a highly efficient conversion from the broadband FF to the narrowband SH, explained by the fact that SH photons are generated not only by direct SHG, but also by an intra-pulse SFG between FF spectral components that are symmetric with respect to the SHG phase-matching frequency. In our setup, the SHG-SC is performed aligning the output of a commercial two stage OPA (TOPAS-C) on a long BBO crystal ($\sim$ 2 cm). Through a mechanism similar to that reported in the previous section, TOPAS-C produces a $60\,\mu J$ output at 880 nm from a $1.7\,mJ$ input beam, coming from the source. After the spectral compression narrowband picosecond pulses in the $320 - 750$ nm range are synthesized. In view of SRS application, an inherent limitation of this technique is represented by the unfavorable temporal profile of the obtained narrowband pulse, which is characterized by a steep trailing and a gradual leading edge. This shape causes artefacts appearing as a strong frequency ringing in the Raman spectra. This issue has been circumvented by spectrally filtering the picosecond pulses produced by SHG-SC [91]. For this purpose a double-pass (2f) spectral filter with a single grating (1800 lines/inch, 410 nm blaze) and an adjustable slit in the collimated region of the spectrally dispersed beam are used. Thanks to this, the spectral wings of the incoming pulse can be suppressed narrowing the slit, while the temporal envelope evolves from the asymmetric nose-shaped one characteristic of the unfiltered spectral compressor to a broader, more symmetric profile.

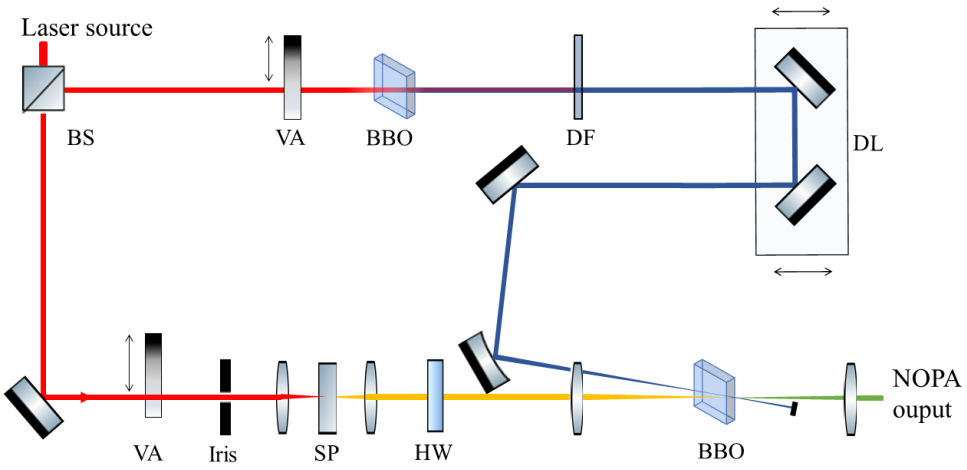

Figure 3.7: Scheme of Noncollinear Optical Parametric Amplifier (NOPA): a portion of the laser beam is divided in two branches. One is used to generate a WLC which is used as seed. The other is frequency doubled in a β-Barium Borate (BBO) crystal and then serves as the pump. Pump and seed are tunably delayed by a delay line (DL) on the pump path and spatially overlapped on a second BBO crystal. DF: dichroic filter. BS: beam splitter. VA: variable attenuator. HW: half waveplate. SP: sapphire plate.

3.3 Collecting the experimental data

In the next two sections, we present the main points of data acquisition and handling. The experiments presented in this thesis involved several samples, from liquid solvents to large proteins and solid state perovskite semiconductors. Consequently, each study required to optimize the measurement technique in the light of the photophysics relevant to the specific sample. Thus, the details on the experimental scheme for each result will be given in the related chapter. In the following, we summarize the general approach for the three techniques: TA, ISRS and SRS.

3.3.1 Delay line calibration

One of the critical issue in every pump-probe experiment is the calibration of the arrival time of the pulses, which, in our setup, is controlled by the two delay lines. The detection of the temporal overlap of two ultrashort pulses that last tens of femtoseconds, as the WLC and the femtosecond pulses used in ISRS, is beyond the capabilities of any electronic device and requires the use of optical expedients. One possibility is to exploit the nonlinear index of refraction through a Kerr gate. The optical Kerr effect consists in the modification of the optical properties experienced by a weak beam due to the presence of a strong beam when they are propagating together in a nonlinear medium. In our case, the strong Actinic (or the femtosecond Raman) pulse rotates the polarization of the WLC by an amount that is maximum when the pulses are overlapped.
Effectively, we focus the Actinic and the WLC on a nonlinear medium with orthogonal polarization (obtained through an half-wave plate on the NOPA output) and detect the transmission of the WLC trough a crossed polariser. The transmitted light grows proportionally to the overlap of the two pulses, as the rotated fraction of the WLC pulse. The zero delay time $T = 0$ between the pulses corresponds to the delay line position in which the maximum of the transmitted signal occurs. Optical Kerr effect can also be used as a direct tool for the verification of the temporal width of the laser beams, if the response time of the material is fast enough. Figure 3.8 provides an example of a Kerr gate measurement; from the Kerr signal, it can be noted that WLC pulse is chirped, as its spectral components are shifted to the red in the leading edge of the pulse and

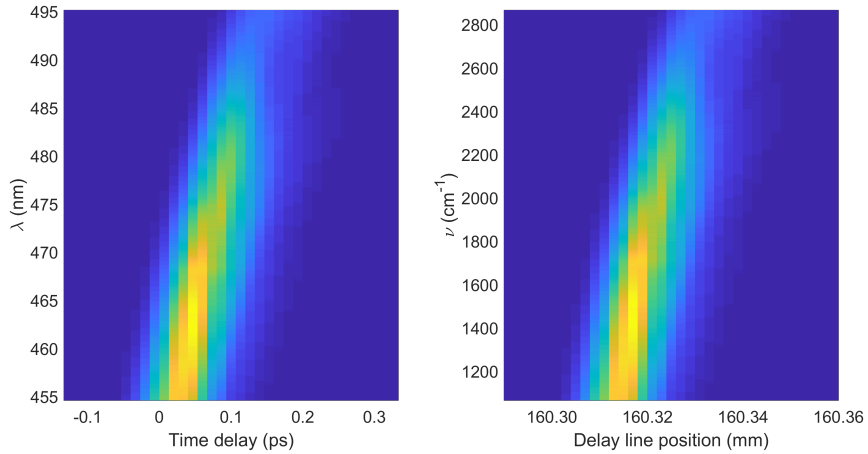

Figure 3.8: Kerr gate measurement of the time delay T between WLC and the NOPA generated pulse: the transmitted amount of the WLC probe by a crossed polarizer is due to modification of the index of refraction induced by the other pulse.

to the blue in the trailing edge. As specified in the next chapter, the chirp is generated by the propagation of the optical pulse through dispersive media [92].

3.3.2 TA

Transient absorption spectroscopy has been performed monitoring the photoinduced changes in the absorption of the WLC pulse induced by the interaction of Raman pulse with the sample, following the pump-probe scheme. The quantity of interest, in this case, is the frequency resolved differential absorption as a function of the time delay T, defined in eq. 1.1

$$\Delta A(T, \lambda_s) = \frac{I_{on}(T, \lambda_s) - I_{off}(T, \lambda_s)}{I_{off}(T, \lambda_s)}$$

where I_{on} and I_{off} are proportional to the CCD counts obtained with and without the Raman pulse on the sample. In particular, it is useful to record also I_{off} at each time step to monitor the degradation of the sample.

3.3.3 ISRS

When sufficiently short Raman and probe pulses are used, i.e. shorter than the vibrational period of the Raman active mode, the same apparatus can be used for both TA and ISRS experiments. ISRS oscillations are measured sampling at different time delays the transient transmission of the probe modulated by the coherence created in the sample by the Raman pulse. To avoid cross phase modulation artifacts, only time delays beyond the pulses temporal overlap region are usually considered in the data analysis. When the Raman pulse is resonant with one of the absorption edges of the sample, this oscillating ISRS response is superimposed to the TA signal. The underlying electronic kinetics responsible for such TA background needs to be subtracted from the detected signal to extract the oscillating temporal dynamics, before Fourier transforming to retrieve the Raman spectra, as sketched in Fig. 3.9. An example is given in Fig. 3.10, showing the probe wavelength resolved TA map of the hybrid organic-inorganic perovskite $MAPbBr_3$ and the associated ISRS oscillation obtained after the subtraction of transient dynamics (see Chapter 5 for further details).

Since ISRS is a time domain technique, the information is not encoded in a single time delay, but at least a period of the vibrational oscillation needs to be sampled in order to extract the

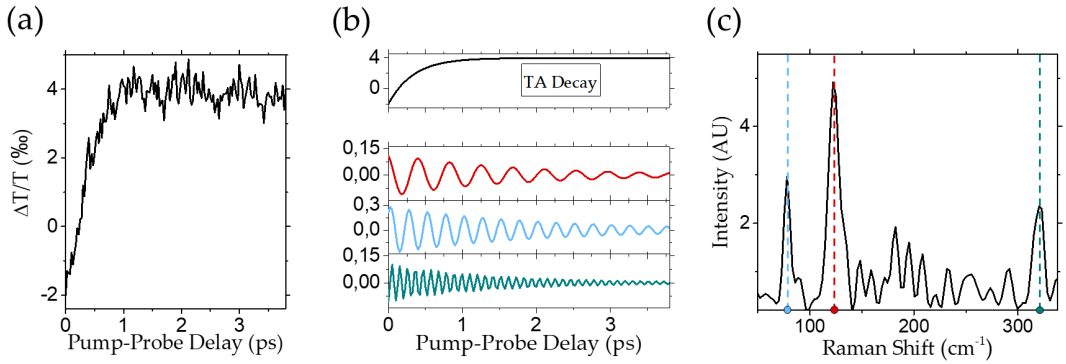

Figure 3.9: The experimentally detected differential signal (Left Panel) from the TA pulse scheme shows the photo-induced modifications of the transmission profile as a function of the time delay between the two pulses. The signal consists in oscillating components, which carry the vibrational frequencies, superimposed to the transient absorption exponential dynamics (Central Panel). The vibrational information is directly obtained by Fourier transforming the experimental data after the subtraction of the TA decay (Right Panel).

Raman spectrum. This issue, together with the often low amplitudes of the oscillations with respect to the background, motivates additional attention to minimize the noise while performing the experiment. Therefore, we optimized the number of consecutively repeated acquisitions for each time step, in order to achieve a trade-off between a sufficient signal to noise ratio and a short acquisition time for the single trace. The last requirement, indeed, is critical to reduce the noise occurring over a single time trace.

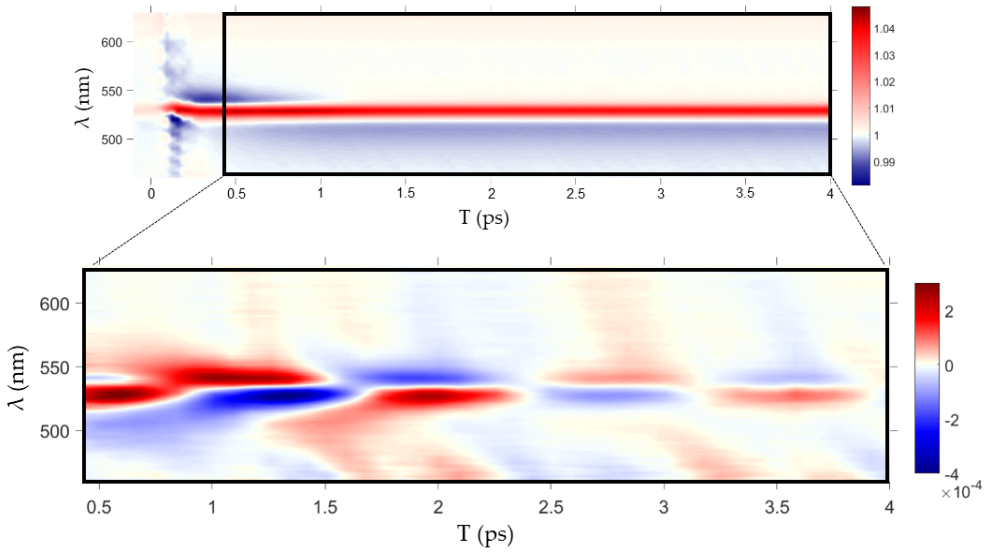

Figure 3.10: Transient absorption map (top) and extracted ISRS oscillation (bottom) in $MAPbBr_3$ perovskite thin films.

Intensity fluctuations within the period of the probed oscillation may hide the vibrational signal. Therefore, a strict control on the pulse and instrumental stability and reducing the acquisition time of a single trace were critical factors to obtain high quality data. To this aim, we monitored the Raman fluence on the sample during the acquisition to correct for fluctuations. Moreover, we repeated the same measurement using different time steps, obtaining the final frequency domain spectra averaging over the data collected with different steps. In this way,

noisy instrumental artifacts are eliminated by destructive interference, further improving the signal to noise ratio. Finally, to improve statistics, the whole experimental routine is repeated and the resulting maps averaged in frequency domain, after Fourier transforming the data. The three beams version grounds on a similar experimental routine and is further detailed in Chapter 6.

3.3.4 SRS

In the SRS scheme, the acquisition of different combinations of a narrowband Raman and WLC pulses is needed to calculate the Raman gain, defined as

$$RG = I_{Ron}/I_{Roff}$$

where I_{Ron} and I_{Roff} are the number of counts on the CCD recorded with and without the presence of the Raman pulse, obtained through the choppering scheme. Thanks to the long duration of the picosecond Raman pulse, the overlap between the WLC probe and the Raman pulse is more easily achieved and adjusted simply maximizing the signal. Because of the mechanism of generation and the optical path, the spectral components of the WLC have different focus depths; as consequence a simultaneous acquisition of the red and the blue side of the FSRS spectrum with respect to the frequency of the narrowband pulse gives artificial differences between the intensity on the two sides. This is due to the necessarily finite precision in controlling the spatial overlap between the narrowband Raman and the blue or red components of the WLC at the same time. To avoid this issue, the spectra for each Raman wavelength reported in the two panels of Fig. 1.6 have been measured separately.

Finally, we remark that the delay line in SRS is used differently. Indeed, since the delay between the narrowband Raman and WLC affects the efficiency of Stimulated Raman Scattering process, the delay line position was fixed at the delay which optimized the trade-off between the spectral resolution and the SRS peak intensity [56].

3.4 Data Analysis

In this section, we report some additional details on the analysis of the ISRS data.

3.4.1 Pump-probe dynamics and baseline subtraction

A global fitting routine, based on a combination of polynomial and exponential functions, is employed to subtract the TA dynamics from the probe wavelength resolved ISRS maps in time domain and isolate the fast oscillating components. The Raman spectrum is hence obtained from the oscillatory temporal signal using the Fast Fourier Transform (FFT) algorithm. An example of the fitting routine output is shown in Fig. 3.11, in which the time domain TA traces obtained in $MAPbBr_3$ are shown for selected probe wavelengths.

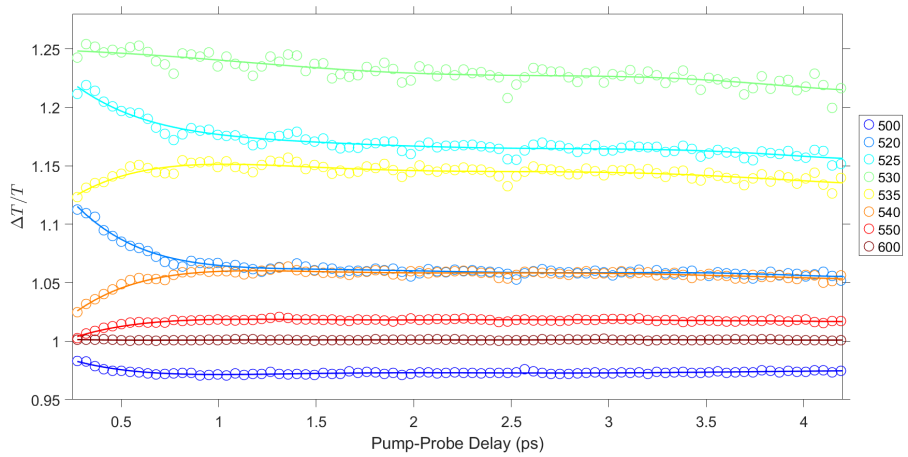

Figure 3.11: Baseline subtraction in $MAPbBr_3$: raw TA traces (dots) in which ISRS oscillations are superimposed to the TA dynamics for selected wavelengths. Six-order polynomial function, reported as continuous lines, were employed in this case to eliminate the TA dynamics and isolate the weak vibrational oscillating components.

3.4.2 Zero padding and windowing

Before Fourier transformation, we post-processed the time domain experimental data to improve the spectral quality of the ISRS plots and maps, using the zero-padding algorithm and the multiplication by a window function [40]. Specifically, pixelation effects are smoothed by adding zeros to end of the time-domain signal to artificially increase the length of the probed time window. However, the effect of zero padding is conceptually similar to measure a longer time window and multiple it by a square window function. This is reflected in the frequency domain as a spectral ringing. To suppress the ringing, zero padded time traces are windowed by Kaiser-Bessel function $\mathcal{W}(N,\beta)$ [93]:

$$\mathcal{W}(N,\beta) = \mathcal{J}(0,\beta)^{-1}\,\mathcal{J}\left(0,\beta\sqrt{1-\left(\frac{n-\frac{N}{2}}{\frac{N}{2}}\right)}\right) \tag{3.1}$$

where β is the width parameter, N is the number of sampled delays, $n = [0, 1, \ldots, N]$ and $\mathcal{J}$ is the modified Bessel function of the first kind. We stress that zero padding does not improve the spectral resolution of the measurements, which is controlled by the actual length of the probed time window.

3.4.3 Measurement of time zero and chirp

The value of the linear chirp C for a given WLC spectrum can be obtained from the probe wavelength dependent time zero $t_0(\lambda_s)$ measured in the Kerr spectrogram, which reports the arrival times of the different color within the pulse envelope. Defining the probe field as

$$E_s(\omega) = |E_s(\omega)|e^{i\varphi(\omega)} \text{ with } \varphi(\omega) = C(\omega-\omega_0)^2 \tag{3.2}$$

we can obtain C from

$$\tilde{t}_0(\omega) = -\frac{d\varphi}{d\omega} = -2\omega C \tag{3.3}$$

where $\tilde{t}_0(\omega) = t_0(\frac{2\pi c}{\lambda_s})$.

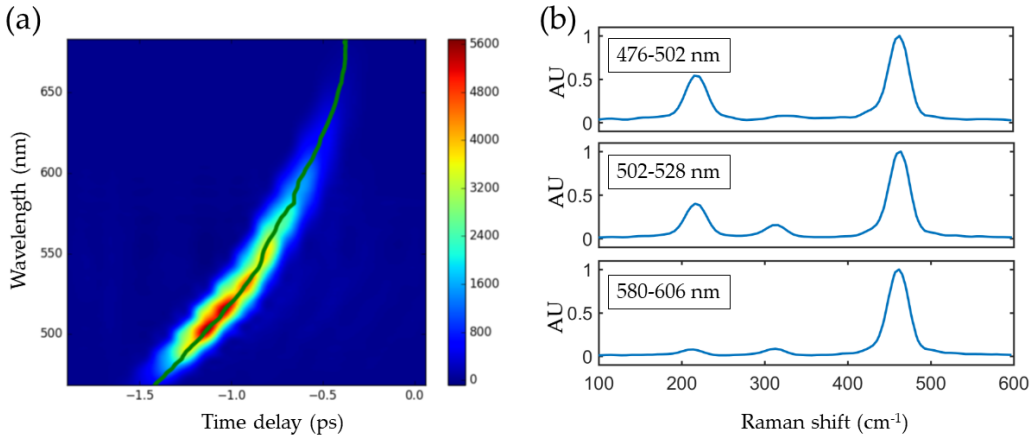

Figure 3.12: Spectrogram of the chirped WLC pulse obtained by a Kerr gate measurement. The extracted value of the chirp for this pulse was ~ 178 fs^2. (b) ISRS spectrum of CCl_4, obtained averaging different spectral regions of the dispersed probe shown in (a).

Alternatively, the probe chirp can be estimated from the relative delay of the onset of oscillations at different probe wavelengths. In off resonant conditions, a more accurately measurement can be performed using the cross phase modulation (XPM) between the Raman and probe pulses. This offers an advantage with respect to the Kerr gate measurement, since the XPM can be detected simultaneously with the ISRS experiment, without any change in the setup. XPM, also known as coherent artifact, is due to the photoinduced nonlinear modification of the material index of refraction felt by the probe as it crosses the sample, due to the simultaneous presence of the intense ultrashort Raman pulse. Since the effect manifests itself in TA spectrum only when both the pulses are present on the sample, it can be exploited to measure the time overlap.

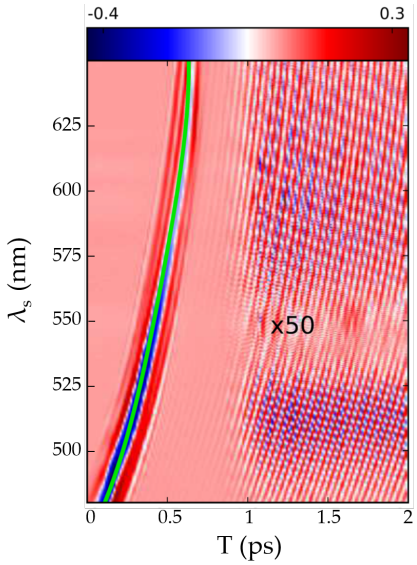

Figure 3.13: XPM artifact and magnified ISRS oscillations in liquid Cyclohexane. Fitting the first momentum of the XPM distribution along the probe wavelength allows for the determination of the WLC chirp simultaneously with the ISRS measurement. In this case, using eq. 3.4, it has been obtained a retrieved chirp of $C = 137$ fs^2.

In particular, a raw estimation of $t_0(\lambda_s)$ can be obtained by calculating the maximum of the XPM at each λ_s. However, we found that an higher accuracy is achieved by choosing $t_0(\lambda_s)$ as its first momentum:

$$\bar{t}_0(\lambda_s) = \frac{\int_{-\tau}^{\tau} t \left| f_{XPM}(t, \lambda_s) \right|^2 dt}{\int_{-\tau}^{\tau} \left| f_{XPM}(t, \lambda_s) \right|^2 dt} = \langle t \rangle_{|f_{XPM}|^2} \tag{3.4}$$

The boundaries integration τ in eq. 3.4 indicate the region in which XPM is observable, while $f_{XPM}(t, \lambda_s)$ is its time-wavelength profile, shown in Fig. 3.13.

4 Broadband Impulsive stimulated Raman Spectroscopy with shaped pulses

Impulsive stimulated Raman Spectroscopy (ISRS) represents a powerful tool to probe vibrational spectra of chemically and biologically relevant molecular systems and solid state samples [36, 94]. The potentialities of ISRS has been recently demonstrated investigating prototypical cases of photoinduced dynamics, including the photochemistry of rhodopsins [95, 96], polymers [97], intermolecular vibrational motions in liquids [98] and the excited-state proton transfer in fluorescent proteins [99]. As we anticipated in Chapter 1, ISRS exploits the large bandwidth of two temporally separated femtosecond laser fields, the Raman and probe pulses, to induce and subsequently probe vibrational coherences on the ground and electronically excited state, in a time-domain scheme. A particularly useful approach is the broadband ISRS which uses a white light continuum as probe pulse [37, 40, 41]. In broadband ISRS, the signal records the changes in the transmitted probe pulse as a function of its temporal delay with respect to the Raman pulse, T, and its wavelength λ_s, thereby resulting in a two dimensional signal. Fourier transforming over the T dimension recovers the Raman spectrum, while heterodyne detection, using the highly directional probe field as local oscillator, suppresses fluorescence and other incoherent processes. Taking advantage of a WLC provides the access to a larger spectral window with respect to conventional approaches, allowing for resonance enhancements over different absorption edges and, at the same time, it does not compromise the temporal resolution [100]. Notably, using broadband pulses offers an additional control knob in performing the experiment: shaping the different components within the spectral envelopes of the pulses.

This strategy falls within a broader research field, directed to many different nonlinear spectroscopies, known as coherent control [101, 102]. Femtosecond light sources have been widely used in control schemes that exploit quantum interference between different dynamics pathways to regulate the outcome of photochemical processes in complex systems [103, 104]. In transient absorption, an approach to coherent control is the pump-dump scheme in which one or multiple pulses are shaped to tune the relative population on the ground and excited state upon photoexcitation [105–107]. Among the possible phase modulations, varying the chirp of the pulses has been demonstrated as experimentally convenient and powerful. The use of chirped pulses has been investigated in different nonlinear techniques from two photon absorption [102, 108] to coherent antistokes Raman Scattering [109]. In particular, using strong chirped pump in a transient absorption geometry allowed chirp-dependent control of the population created onto the excited state [110]. Since ISRS exploits the same setup of TA, similar strategies are extensible from population transfer to control of vibrational coherences. In this chapter, after describing two different geometries to detect vibrational features using stimulated Raman and a broadband probe, we will show how a chirped probe pulse affects the ISRS multidimensional maps, comparing the simulated signal with the experimental measurements on a liquid solvent. Finally, we demonstrate that this dependence may be used to control the relative intensities of ISRS bands and discern between ground and excited state vibrations.

4.1 Different approaches to broadband ISRS

In this section, we present the derivation of the signal for two techniques: the linear detection of a shaped broadband pulse and the two beam ISRS configuration. The derivation of these signals, achieved by means of the perturbative theory presented in Chapter 2 allows to appreciate the role played by the spectral envelope of the probe pulse in a time domain Raman spectroscopy.

4.1.1 Linear detection of a non equilibrium state by a phase shaped probe

The simplest realization of a stimulated Raman experiment may be achieved by using a single pulse. Indeed, shaping the phase within the broadband envelope of a femtosecond pulse enables the measurement of multidimensional vibrational spectra using a single probe beam. This strategy has been experimentally applied using a phase-jump modulation to measure CARS and SRS spectra in Chloroform and Pyridine [111, 112], while a sinusoidal pulse shaping allowed the detection of two dimensional Raman signal in CCl_4 [53]. Notably, this approach reduces the acquisition times and the overall experimental complexity with respect to time domain approach, in which several time-delayed unshaped pulses interrogate the system, even if it may introduce a background due to the spectral modulations.

For this reason, it is important to derive the signal expressions relative to the single shaped pulse geometry and use them as a reference to interpret the experimental results. This can be done using the diagrammatic framework that we have introduced in chapter 2. As an example, here we discuss the phase-jump shaping protocol applied to the detection of a non equilibrium state by a linear probe. We suppose that at time $t = 0$, the system is described by a density matrix ρ_0 prepared by an undetermined pump process. After a delay T, a shaped probe pulse interacts linearly with the system and is heterodyned detected to track the evolution of the prepared state.

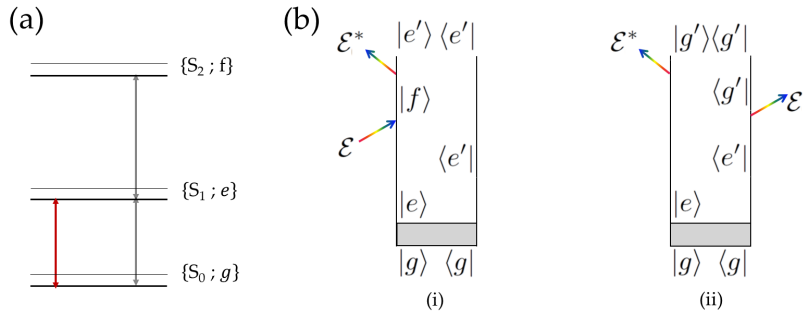

Figure 4.1: Level scheme (a) and Feynman diagrams (b) relevant for linear Raman detection of a prepared state with a shaped ultrashort pulse. The indexes g, e and f (primed and not) refer to the vibrational manifolds of the three electronic states S_0, S_1 and S_2, respectively.

The signal can be calculated by the sum of the diagrams that contribute to the process. We look for all the possible diagrams with two arrows: the linear interaction and the free induction decay. Both the interactions should involve the probe in order to impose self heterodyne detection. Since the free induction decay is represented conventionally by an arrow pointing to the left and acting on the ket side of the diagram, which brings a term $\mathcal{E}^*$, the first interaction has to involve $\mathcal{E}$ in order to preserve energy conservation, as prescribed by the rules in chapter 2. Consequently, the relative arrow points to the right and can act on the ket or the bra side of the density matrix. The two possible diagrams are shown in Fig. 4.1 and lead to the signal expression:

$$S^{(1)}(\omega,\gamma) = \Im \frac{i}{\hbar} \sum_j \int d\Delta \int d\Delta_a \mathcal{E}^*(\omega,\gamma)\mathcal{E}(\omega+\Delta,\gamma)e^{-i\Delta T}\delta(\Delta+\Delta_a)F_j(\Delta,\Delta_a) \qquad (4.1)$$

where we have explicitly expressed the temporal shift of the envelope with respect to the preparation process and $\gamma = \gamma(\omega)$ represents the set of control parameters of the pulse shaping:

$$\mathcal{E}(\omega, \gamma) = \tilde{\mathcal{E}}(\omega) e^{i\phi(\omega,\gamma)}$$

$\tilde{\mathcal{E}}(\omega)$ is the unshaped spectral envelope of the pulse. The correlation functions, given by the two Feynman paths in Fig. 4.1, are given by:

$$F_i(\Delta, \Delta_a) = + \langle V_L G(\Delta + \Delta_a) V_L^\dagger G(\Delta_a) \rangle_{\rho_0} \tag{4.2}$$

$$F_{ii}(\Delta, \Delta_a) = - \langle V_L G(\Delta + \Delta_a) V_R^\dagger G(\Delta_a) \rangle_{\rho_0} \tag{4.3}$$

V is the dipole operator (with dipole matrix elements μ_{ij}), V_L (V_R) is its superoperator representation acting from the left (right) and G is the retarded Green function in frequency domain:

$$G(\omega) = \frac{1}{\omega \mathrm{I} - H_0 + i\epsilon}$$

The brackets in the correlation functions can be evaluated expanding the signal in terms of the eigenstates of the unperturbed system. We consider three electronic states with the associate vibrational manifolds, as shown by the level scheme in Fig. 4.1a. We indicated vibrational states pertaining to different electronic levels with different letters, while primed and not primed versions of the same index represent different modes in the same manifold. In order to obtain the material response, we have to consider all the possible combinations of vibrational indices relative to the states that the density matrix may occupy during the process, so the indices g', e, e', and f are mute and have to be summed over the relative vibrational manifolds. The resulting sum-over-states expressions for diagrams *i-ii* are:

$$S_i^{(1)}(\omega, \gamma) \propto \Im \sum_{f,e,e'} \frac{\tilde{\mathcal{E}}^*(\omega, \gamma) \tilde{\mathcal{E}}(\omega - \tilde{\omega}_{ee'}, \gamma)}{\omega - \tilde{\omega}_{fe'}} e^{-i\tilde{\omega}_{ee'}T} \tag{4.4}$$

$$S_{ii}^{(1)}(\omega, \gamma) \propto \Im \sum_{g',e,e'} \frac{\tilde{\mathcal{E}}^*(\omega, \gamma) \tilde{\mathcal{E}}(\omega - \tilde{\omega}_{ee'}, \gamma)}{\omega - \tilde{\omega}_{eg'}} e^{-i\tilde{\omega}_{ee'}T} \tag{4.5}$$

with $\tilde{\omega}_{ij} = \omega_i - \omega_j - i\Gamma_{ij}$. The signals in eq. 4.4 and 4.5 differ only in the electronic resonance probed, being $S_i^{(1)}$ resonant with the stimulated emission and $S_{ii}^{(1)}$ with excited state absorption. Since here we are interested in the dependence on the pulse shape, which is the same, we can write both using the same expression and denoting with ω_{el} the electronic transition. Making the phase dependence explicit, we obtain:

$$S^{(1)}(\omega, \gamma) \propto \Im \sum_{e,e',el} \frac{\tilde{\mathcal{E}}^*(\omega) \tilde{\mathcal{E}}(\omega - \tilde{\omega}_{ee'})}{\omega - \tilde{\omega}_{el}} e^{-i\tilde{\omega}_{ee'}T} e^{i\psi(\omega, \tilde{\omega}_{ee'}, \gamma)} \tag{4.6}$$

where $\psi(\omega, \omega', \gamma) = \phi(\omega - \omega', \gamma) - \phi(\omega, \gamma)$. For T=0, eq. 4.6 becomes:

$$S^{(1)}(\omega, \gamma) \propto \frac{e^{-b(\omega, \tilde{\omega}_{ee'}, \gamma)} [(\omega - \omega_{el}) \sin(a(\omega, \tilde{\omega}_{ee'}, \gamma)) - \Gamma_{el} \cos(a(\omega, \tilde{\omega}_{ee'}, \gamma))]}{(\omega - \omega_{el})^2 + \Gamma_{el}^2} \tag{4.7}$$

with $a = \Re(\psi)$ and $b = \Im(\psi)$ which are functions of ω and, critically, are evaluated at the vibrational frequency $\omega_{ee'}$. Thus, tuning the $\mathcal{E}$ pulse to resonance switch the signal from a sinusoidal to a cosinusoidal functional behavior.

We note that if the system is initially prepared in a population state, for example leaving it unperturbed in the ground state, $\rho_0 = \mathcal{I}$ and the signal does not depend on the pulse phase and temporal delay and we recover the linear absorption.

In Fig. 4.2, we compare $S^{(1)}(\omega, \gamma)$ at T=0 for a non-shaped pulse with $\phi(\omega) = 0$ with that obtained for a Gaussian phase jump of width σ and centered at the probe central frequency ω_0, which is given by

$$\phi(\omega, \sigma) = \pi e^{-\pi^2 \sigma^2 (\omega - \omega_0)^2}$$

The simulation is performed for a model with a vibrational mode at 123 cm^{-1} . Using unshaped light, the linear detection results in a broad signal which does not carry any vibrational information (panel a in Fig. 4.2). Considering a phase jump with σ comparable to the vibrational dephasing of the mode, we obtained dispersive like features at the vibrational frequency (panel b in Fig. 4.2), superimposed to a broadband background.

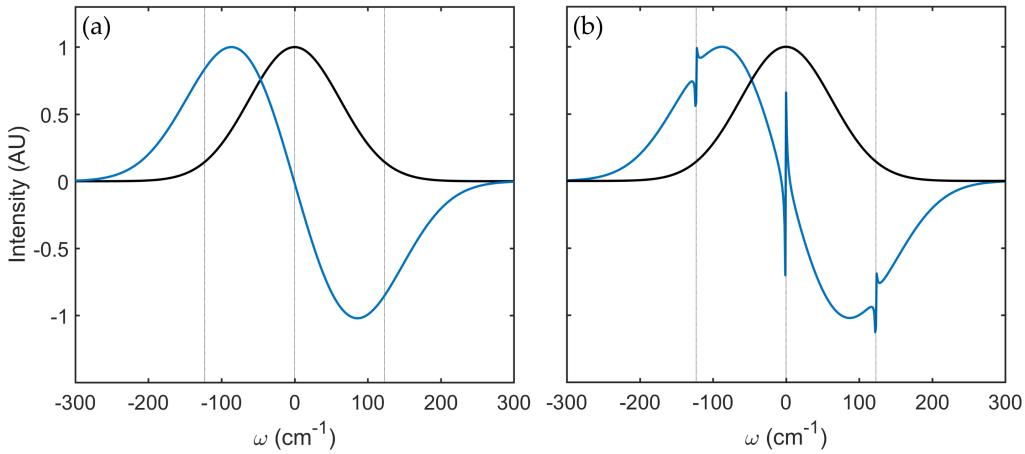

Figure 4.2: Linear detection of a non-equilibrium initial density matrix with a broadband (a) non-shaped and (b) Gaussian jump phase shaped pulse. The vertical lines indicate the value of the vibrational frequency.

As the probe pulse is delayed, the features start oscillating with T, changing from positive to negative dispersive lineshapes. The period of the oscillation corresponds to the vibrational period. Thus, sampling enough delays allows to extract the vibrational information also in the form of a Fourier transformation over T, as in time domain ISRS. However, a two beam geometry is more effective for this purpose, because the resulting signal, at least in off resonant condition, is background free.

4.1.2 Two beam geometry

As we anticipated in the first chapter, the typical ISRS configuration exploits two delayed beams: the Raman pulse $\mathcal{E}_r$ induces the vibrational coherence which is read out after a delay T by the probe $\mathcal{E}_s$, by means of a third order stimulated Raman process. The result is the bidimensional ISRS signal $S(T, \omega_s)$. When both the pulses are centered far from any absorption edge of the sample, ISRS is given by the sum of two Feynman pathways, shown in Fig. 4.3.

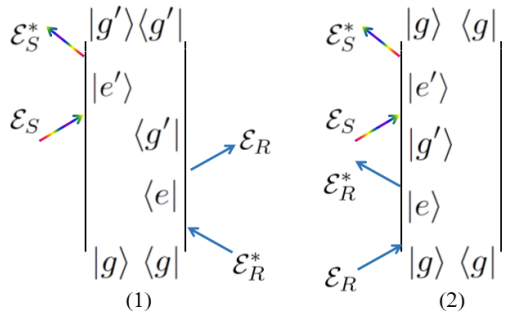

Figure 4.3: Feynman diagrams relative to the two beam ISRS geometry.

Reading from the diagrams, we obtain the expression for the ISRS signal:

$$S(T,\omega_s) = \Im \sum_j \left(\frac{i}{\hbar}\right)^3 \int_{-\infty}^{\infty}\int_{-\infty}^{\infty}\int_{-\infty}^{\infty} d\omega_1 d\omega_2 d\omega_3 \mathcal{E}_r^*(\omega_1,T)\mathcal{E}_r(\omega_2,T)\mathcal{E}_s(\omega_3)\mathcal{E}_s^*(\omega_s) \\ \delta(\omega_s-\omega_3+\omega_2-\omega_1)F_j(\omega_1,\omega_2,\omega_3) \tag{4.8}$$

The correlation functions for the two terms are

$$F_1(\omega_1,\omega_2,\omega_3) = \langle VG(\omega_3-\omega_2+\omega_1)V^\dagger G(\omega_1-\omega_2)VG(\omega_1)V^\dagger\rangle_{\rho_{gg}} \tag{4.9}$$

$$F_2(\omega_1,\omega_2,\omega_3) = \langle VG(\omega_3-\omega_2+\omega_1)V^\dagger G(\omega_1-\omega_2)VG(\omega_1)V^\dagger\rangle_{\rho_{gg}} \tag{4.10}$$

where ρ_{gg} is the equilibrium density matrix and ω_s is the detected frequency. In general, taking into consideration a sample of finite size, dispersion affects the phase matching condition of the two diagrams calculated above. Thus, eq. 4.8 is strictly valid only when the width crossed by the beams inside the sample is negligible. In section 4.2.2, we will show how to account for the sample size and phase matching. Using the delta function to solve one of the integrals and expanding the two correlation functions in their sum-over-states expressions, we obtain

$$S(T,\omega_s) = \Im \sum_{g'} \left(\frac{i}{\hbar}\right)^3 \int_{-\infty}^{\infty}\int_{-\infty}^{\infty} d\omega_1 d\omega_2 \mathcal{E}_r^*(\omega_1,T)\mathcal{E}_r(\omega_2,T)\mathcal{E}_s(\omega_s+\omega_2-\omega_1)\mathcal{E}_s^*(\omega_s) \\ \mu_{e'g}\mu_{eg'}\mu_{e'g'}\mu_{eg}\left[F_1(\omega_s,\omega_1,\omega_2)+F_2(\omega_s,\omega_1,\omega_2)\right] \tag{4.11}$$

with

$$F_1(\omega_s,\omega_1,\omega_2) = \frac{1}{(\omega_s-\tilde{\omega}_{eg'})(\omega_1+\tilde{\omega}_{ge})(\omega_1-\omega_2+\tilde{\omega}_{gg'})} \\ F_2(\omega_s,\omega_1,\omega_2) = \frac{1}{(\omega_s-\tilde{\omega}_{eg})(\omega_2-\tilde{\omega}_{eg})(\omega_2-\omega_1-\tilde{\omega}_{g'g})} \tag{4.12}$$

The summation in g' runs over the vibrational modes of the system. We are interested in calculating the Fourier transform of 4.11, the two dimensional signal $S(\Omega,\omega_s)$

$$S(\Omega,\omega_s) = \int_{-\infty}^{+\infty} dT e^{i\Omega T}\, S(T,\omega_s) \tag{4.13}$$

In the following, we will report the ISRS as a function of λ_s instead of ω_s, $S(\Omega,\lambda_s)$, since this form is more commonly found in literature. In Fig. 4.4, we report both the two dimensional maps $S(T,\omega_s)$ and $S(\Omega,\lambda_s)$, calculated for a system with an active Raman mode at 800 cm^{-1} and a probe pulse centered at 540 nm.

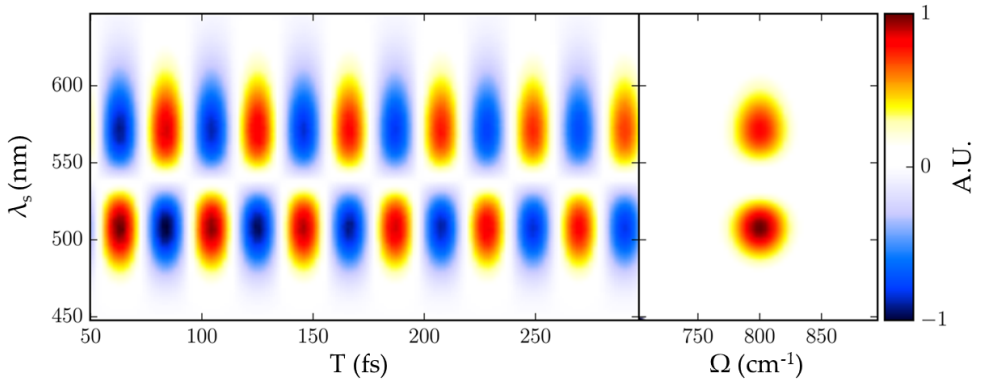

Figure 4.4: Simulation of the non resonant third order ISRS response for a system with a Raman active mode at 800 cm^{-1} in the ground state. The two dimensional map of $S(T,\lambda_s)$ (left panel) and its Fourier transform $S(\Omega,\lambda_s)$ (right panel) are shown.

As can be seen from the simulation, $S(T, \lambda_s)$ consists in an oscillatory signal in T which is maximized around two values of λ_s, which are red and blue shifted with respect to the central wavelength of the probe pulse. This behavior results from the interference of the two Feynman pathways in Fig. 4.3 that generate time oscillations with opposite phases, peaked in different regions of the dispersed map. This can be seen directly from the correlation functions. Indeed, from the denominators in eq. 4.12, it is clear that the two integrations in ω_1 and ω_2 of eq. 4.11 give the maximum contribution when $\omega_2 - \omega_1 = -\omega_{vib}$ for F_1 and $\omega_2 - \omega_1 = \omega_{vib}$ for F_2, where we defined $\omega_{vib} = \omega_{g'} - \omega_g$. Substituting these values in the probe envelope $\mathcal{E}_s(\omega_s + \omega_2 - \omega_1)$ in eq. 4.11, the two diagrams result shifted from the probe central frequency by the vibrational frequency, since the signal results proportional to $\mathcal{E}_s(\omega_s \pm \omega_{vib})$, where the minus sign holds for diagram 1 and the plus for diagram 2. As a results, the two diagrams interfere destructively and cancel out in the central region of the spectrum, where they have comparable intensities, resulting in a bilobed profile along λ_s in the frequency transformed map $S(\Omega, \lambda_s)$.

Interestingly, the resonance condition affects this spectral dependence. When the probe pulse is resonant, the two contributions oscillate with the same phase and the positions of the maxima along λ_s in the resulting ISRS map are ruled by the two denominators $(\omega_s - \tilde{\omega}_{eg'})^{-1}$ and $(\omega_s - \tilde{\omega}_{eg})^{-1}$ appearing in eq. 4.12, for diagram 1 and 2, respectively. Consequently, the response associated with diagram 2 is maximum at the central wavelength of the linear absorption spectrum, while diagram 1 at a value red-shifted from that by the vibrational frequency. Under this regime, we can distinguish between two different cases: for a vibrational frequency larger than the width of the absorption two lobes can be resolved in the ISRS map, while, in the opposite case, only one lobe can be distinguished [40]. Finally, we remark that when the Raman pulse is tuned resonant, this picture is further complicated by the possibility to generate vibrational coherences also on the excited state, and consequently the additional contributions resulting from excited state aborption and stimulated emission transitions must be considered [113].

4.2 Using the probe chirp as a control knob

In the first section of this chapter, we have shown that the phase can be exploited to encode spectroscopic information in a broadband ISRS probe. Here we select one particular way to shape the phase of the probe pulse, namely the chirp. From a certain perspective, chirp can be seen as an issue in pulsed optics and several techniques to remove it has been developed to decrease the temporal broadening of ultrashort pulses. Conversely, we identified in the probe chirp an experimental control knob for coherent control of vibrational feature and for assigning a given vibrational dynamics to the relevant potential energy surface. As a starting point for the discussion, we show how the ISRS signal depends on the probe dispersed wavelength in real experimental conditions. Building on the experimental measurements and on the diagrammatic approach, we demonstrate that the chirp affects the ISRS signal in a mode selective way. Then, we apply the results to establish a method for discerning excited from ground-state vibrational features in a three beam ISRS configuration by means of a chirped probe. Before addressing these topics, we briefly recall the origin of the chirp in pulsed optics.

4.2.1 Chirp in a Gaussian pulse

Chirp is a characteristic effect that arises when a short pulse propagates in dispersive media and manifests itself as a frequency sweep in time. For instance, when a quadratic time dependence is added to the original phase term of a Gaussian envelope

$$\mathcal{E}(t) = A_0 e^{-\Gamma t^2 - i(\omega_0 t + C t^2)} \tag{4.14}$$

the instantaneous frequency varies linearly with time

$$\omega(t) = \frac{d\phi}{dt} = \omega_0 + Ct$$

being more red in the leading edge of the pulse and more blue in the trailing edge, if the pulse is positively chirped $C > 0$, or vice versa if $C < 0$. This effect can be simply derived considering the propagation of a transform-limited Gaussian pulse through a distance x [92]

$$E(\omega, x) = \mathcal{E}_0(\omega) e^{ik(\omega)x} \tag{4.15}$$

where $\mathcal{E}_0$ is the non-propagated pulse envelope at the initial point $\mathcal{E}_0(\omega) = A_0 e^{-\frac{(\omega-\omega_0)^2}{4\Gamma}}$, Γ its spectral width and $k(\omega) = n\omega/c$ the frequency dependent propagator. Expanding $k(\omega)$ as a Taylor's series around the carrier frequency ω_0

$$k(\omega) = k(\omega_0) + k'(\omega_0)(\omega - \omega_0) + \frac{1}{2}k''(\omega - \omega_0)^2 + \dots \tag{4.16}$$

and Fourier transforming back to the time domain, we get

$$E(t, x) = \sqrt{\frac{\Gamma(x)}{\pi}} A_0 \exp\left[-i\omega_0\left(t - \frac{x}{v_\phi(\omega_0)}\right)\right] \exp\left[-\Gamma(x)\left(t - \frac{x}{v_g(\omega)}\right)^2\right] \tag{4.17}$$

$\Gamma(x)$, v_ϕ and v_g are the modified form factor, the phase and group velocity, respectively

$$\begin{aligned} v_\phi &= \left(\frac{\omega}{k}\right)_{\omega_0} = \frac{c}{n(\omega)} \\ v_g &= \frac{d\omega}{dk} \sim v_\phi\left(1 - \frac{\omega}{n(\omega)}\frac{dn(\omega)}{d\omega}\right) \\ \Gamma(x) &= \left(\frac{1}{\Gamma} + 2ik''x\right)^{-1} \end{aligned} \tag{4.18}$$

In particular, $\Gamma(x)$ depends on the frequency through the second order term in eq. 4.16 , which corresponds to the group velocity dispersion (GVD)

$$k'' = \left(\frac{d^2k}{d\omega^2}\right)_{\omega_0} = \frac{d}{d\omega}\left(\frac{1}{v_g(\omega)}\right)_{\omega_0} \tag{4.19}$$

Due to the GVD, each color within the bandwidth of the pulse travels with a different velocity and, consequently, the temporal duration of the pulse increases. Additionally, the pulse phase acquires a chirp term, as can be seen substituting the expressions 4.18 in the second term of eq. 4.17

$$\exp\left[-\frac{\Gamma}{1 + (2\Gamma k''x)^2}\left(t - \frac{x}{v_g}\right)^2 + i\frac{2\Gamma^2 k''x}{1 + (2\Gamma k''x)^2}\left(t - \frac{x}{v_g}\right)^2\right]$$

which shows a phase term quadratic in time.

4.2.2 Vibrational mode tuning in the off resonant two beam geometry

As we derived using the diagrammatic expansion, the broadband ISRS signal depends on the dispersed probe wavelength λ_s in a mode specific manner. This is reflected in Fig. 4.5, were we report experimental measurements on the liquid solvent Cyclohexane C_6H_{12}. From the two dimensional map reported in panel 4.5a, it is clear that the dependence on the probe wavelength of the low frequency modes at 384 and 423 cm^{-1} and that of the higher frequency mode at 801 cm^{-1} are different, being the former monolobed and the latter bilobed as a function of λ_s. In particular, the intensity of the 801 cm^{-1} Raman mode shows a minimum at λ_s =555 nm corresponding to the center of the probe pulse spectral envelope. Two maxima arise at longer and shorter wavelength, shifted by the vibrational frequency, giving rise to the bilobed behaviour. This is in line with the interference between the two Feynman diagrams which generate the off

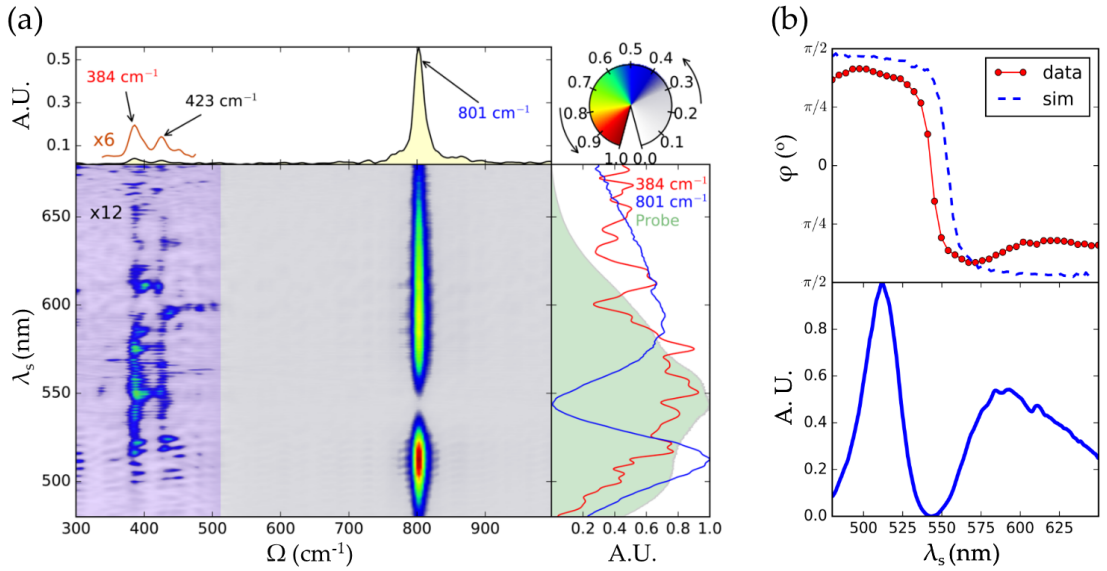

Figure 4.5: (a) ISRS spectrum of liquid cyclohexane as a function of the probe wavelength λ_s and the Raman frequency. The top panel shows the marginal spectrum obtained by integrating over all probe wavelengths. (b) Top panel: Probe wavelength dependent phase $\phi(\lambda_s)$ of the 800 cm^{-1} mode ISRS oscillation, extracted from both experimental data (red circles) and simulation (blue dashed line). Bottom panel: profile of the experimental FFT amplitude as a function of λ_s for the same mode.

resonant ISRS signal, as presented in section 4.1.2. The predicted jump of the phase at the maximum of the probe pulse is clearly visible from panel b in Fig. 4.5, which compares the simulated phase with the one retrieved from the time domain experimental oscillations.

On the contrary, the band at 384 cm^{-1} peaks around the central probe wavelength λ_s=555 nm, for which the only maximum in the reported spectral range occurs. To explain this behavior, we studied the role of phase matching conditions and probe phase shape in the ISRS experiment, including the chirp of the pulse and the specifics of the material response explicitly in eq. 4.8. Considering a sample of length L aligned with the probe pulse direction $\hat{z}$, eq. 4.8 becomes:

$$S(T,\omega_s) = \frac{2\mu_{ef}^2\mu_{e'f}^2}{\hbar^4}\Im\left\{\sum_j \int_{-\infty}^{\infty} d\omega_1 d\omega_2 \mathcal{E}_r^*(\omega_1,T)\mathcal{E}_r(\omega_2,T)\mathcal{E}_s(\omega_s+\omega_1-\omega_2)\mathcal{E}_s^*(\omega_s)\right.$$
$$\left.\operatorname{sinc}\left[\frac{\Delta\mathbf{k}(\omega_1,\omega_2)\cdot\hat{z}L}{2}\right]\exp\left(i\frac{\Delta\mathbf{k}(\omega_1,\omega_2)}{2}\cdot\hat{z}L\right)F_j(\omega_s,\omega_1,\omega_2)\right\} \tag{4.20}$$

where the correlation functions F_j that must be included in the summation are those of eq. 4.12. Explicitly, the phase mismatch $\mathbf{\Delta k}$ is

$$\mathbf{\Delta k}(\omega_1,\omega_2) = -\mathbf{k}_r(\omega_1)+\mathbf{k}_r(\omega_2)+\mathbf{k}_s(\omega_s+\omega_1-\omega_2)-\mathbf{k}_s(\omega_s) \tag{4.21}$$

Due to finite sample length, the phase-matching condition can significantly influence the signal. To evaluate the effect of $\Delta k \neq 0$ we performed a numerical integration of eq. 4.20 and Fourier transformed the result as shown in eq. 4.13. The pulses envelopes have been modeled as transform limited Gaussian functions, with central wavelengths and widths $\lambda_{s_0} = 540\,\text{nm}$, $\Delta\lambda_{s_0} = 100\,\text{nm}$ for the WLC probe and $\lambda_{r_0} = 545\,\text{nm}$, $\Delta\lambda_{r_0} = 60\,\text{nm}$ for the Raman pulse. Moreover, we considered a non-collinear geometry, in which the Raman and probe pulses are separated by an angle $\theta = 4°$. The result is reported in Fig. 4.6, where we show the dependence of $S(\Omega = 800\text{cm}^{-1}, \lambda_s)$ as a function of the sample length L. Specifically, in panel a, we report

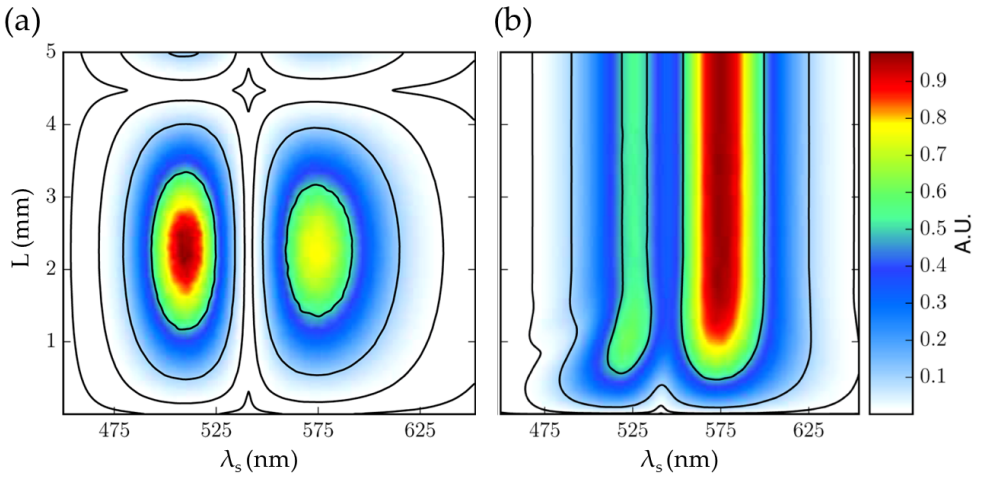

Figure 4.6: Simulated intensity of the 800 cm^{-1} ISRS feature as a function of the sample length L for nonresonant ISRS, in the case of a nondispersive medium (a) and considering the dispersion curve of cyclohexane (b).

the non physical case of a non-dispersive medium, in which the refractive index $n(\lambda)$ is constant over all the spectral range. The resulting phase factor is wavelength-independent and opposite for the two processes. Thus, the intensity of each ISRS peak is modulated by the sample length L but not distorted, and it shows two symmetric maxima as a function of the probe frequency. When we considered the actual dispersion curve of the Cyclohexane [114] to calculate the phase mismatch in Eq. (4.21), we recovered the actual asymmetric double peak profile, as shown in Fig. 4.6b, which corresponds to the behavior experimentally measured for the 801 cm^{-1}. In this case, the spectral shape of the signal is perturbed by the GVD, defined in eq. 4.19, which acts asymmetrically for the two pathways that generate the signal, being the two maximized at two different colors. The different phase mismatch of the two diagrams, once integrated, leads to a different amplitude of the two processes. This is shown by the asymmetric doubly peaked profile in Fig. 4.6b. Notably, the cancellation of the signal at λ_s =540 nm, which is expected from the interference at the maximum of the probe pulse, is not complete, because of the additional, unbalanced phase term due to the GVD.

Interestingly, we note that, since the GVD further induces a temporal broadening of the Raman and probe pulses during their propagation inside the sample, the coherent generation of the signal stops when the duration of the Raman pulse exceeds the vibrational mode period ($T_{vib} = \frac{2\pi}{\omega_{vib}}$). Hence, if the sample size is greater than a critical length (L_c, usually few millimeters), the signal reaches a stationary intensity. The critical length L_c depends on several parameters, namely the Raman pulse initial duration, the beams relative angle, the vibrational mode frequency and the sample group velocity dispersion. The suppression of the ISRS signal for $L > L_c$ also sets a lower bound to the decrease of temporal resolution in ISRS based pump-probe experiments due to the pulse broadening. This is a useful advantage over other kind of ultrafast measurements, where the temporal broadening of the pulses keeps diminishing the temporal resolution as the sample length increases.

Despite the combination between GVD and sample length can modulate the weights of the two diagrams, it is not enough to generate profiles with a single lobe centered around the maximum of the probe, such as those reported in Figure 4.5 for the low frequency modes. Indeed, the destructive interference is still dominant. We found that the monolobed intensity can be obtained by considering the chirp of the probe pulse. The effect of a linear chirp on the probe can be taken into account in eq. 4.20 by introducing it directly in the probe electric field envelope as shown in eq. 4.14. Thus, we set:

$$\mathcal{E}_s(\omega, C) = \tilde{\mathcal{E}}_s(\omega) e^{iC(\omega-\omega_0)^2} \tag{4.22}$$

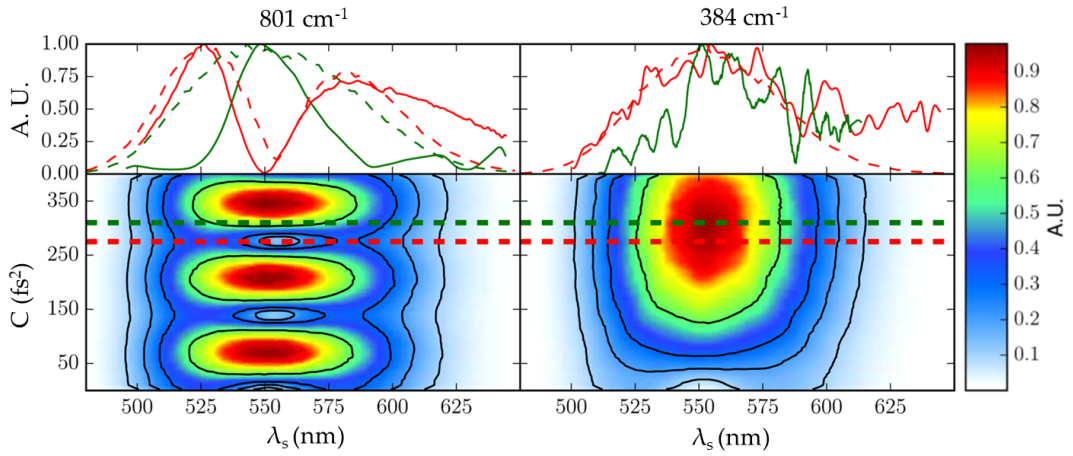

Figure 4.7: ISRS maps reporting the signal dependence on the probe chirp C and λ_s for a high frequency mode at 801 cm^{-1} (left) and a low frequency mode at 384 cm^{-1} (right) in liquid Cyclohexane. In the top panels, the experimental data (dashed lines) are overlapped with the theoretical simulations (solid lines) for two different values of the probe chirp, indicated by the dashed horizontal lines in the maps. The red features correspond to those presented in Fig. 4.5.

where C is the chirp and ω_0 is the central frequency of the Gaussian probe

$$\tilde{\mathcal{E}}_s(\omega) = \frac{1}{\sigma_s\sqrt{2\pi}} e^{-\frac{(\omega-\omega_0)^2}{2\sigma_s^2}}$$

A chirp in the probe pulse envelope reflects in an additional and mode-specific phase to the two ISRS diagrams, which strongly affects the spectral shape of the signal. Indeed, as we stressed in section 4.1.2, since the envelope of the probe pulse appears in the signal expression evaluated at $\omega \pm \omega_{vib}$ for the two diagrams, there is a mode dependent phase factor which is opposite in the two cases. The two dimensional maps in Fig. 4.7 report the simulated intensity of the 801 cm^{-1} and 384 cm^{-1} modes of Cyclohexane as function of C and λ_s. In the top panels, the experimental results (continuous lines) for two different chirped probe pulses are compared with the simulations (dashed lines), showing a good agreement. Modifying the chirp enables to reshape and enhance the signal profile, in particular switching from a bilobed to a monolobed dependence over the probe wavelength, as shown for the 801 cm^{-1} mode. Conversely, a small WLC chirp (50 fs^2) causes a phase shift between the diagrammatic contributions for 384 cm^{-1} Raman mode, making the two components no longer opposite in phase and turning the bilobed shape in a more intense monolobed one. Since this relative phase depends quadratically on the observed vibrational frequency, as can be seen in eq. 4.22, the 384 cm^{-1} mode depends more weakly on the probe chirp than the 800 cm^{-1}. Thus, the positive interference survives even for higher values of chirp ($> 400\,fs^2$), resulting in a monolobed profile in the whole explored region of chirp values. Only a higher value of C ($\approx 500\,fs^2$) would generate the bilobed profile, as a consequence destructive interference between the diagrams.

Critically, besides rationalizing the measured spectral dependence on the probe wavelength, this dependence can be turned to an advantage in performing the experiment. On one side, it is relevant for signal analysis. The identification of the signal dependence on the probe wavelength for each mode, indeed, allows to perform the correct weighted average over the entire probe spectrum, improving signal to noise ratio. More importantly, the possibility to tune the 801 and 384 cm^{-1} mode intensities as we showed suggests that an optimally shaped probe pulse can be used to selectively enhance specific vibrational modes, coherently controlled by means of the chirp profile.

4.2.3 Excited state selectivity of vibrational features

Excited state vibrations play a critical role in determining the dynamics in many photochemical and photophysical processes, as, for example, those involving energy transfers relevant for photosynthesis and photovoltaics [115]. It is important to assign unambigously a given spectroscopic feature to a specific electronic state, ground or electronically excited. In general, this is a challenging task, which has caused limitations to the interpretation of vibronic spectra and to the understanding of the underlaying physics [116]. If the ground state absorption is well separated from the stimulated emission or the excited state absorption of the sample, this task can be simply achieved tuning the resonance condition of a broadband probe pulse. However, in case of overlapping resonance regions in the transient absorption spectrum, this not effective and the resonance condition cannot be directly exploited to discriminate the involved electronic transition. Thus, there is the need to advance standard vibrational techniques and exploit new parameters in order to extract this additional information. To this aim, in ISRS, chirped pulses have been used mainly to control the excitation process of the coherence, rather than its detection. In particular, it has been shown that negatively chirped Raman pulses exceed their transform limited analogues in inducing vibrational coherences specifically in the ground state, while the opposite happens for positively chirped pulses [117–119]. This effect may be used to discriminate the formation of an oscillatory ground-state component via ISRS. However, it is not always effective and, critically, depends on the fate of the wavepacket evolving on the excited state along the molecular reaction trajectory. For example, the phase dependence imprinted by the Raman pulse may be lost as a consequence of the coupling to a thermal bath.

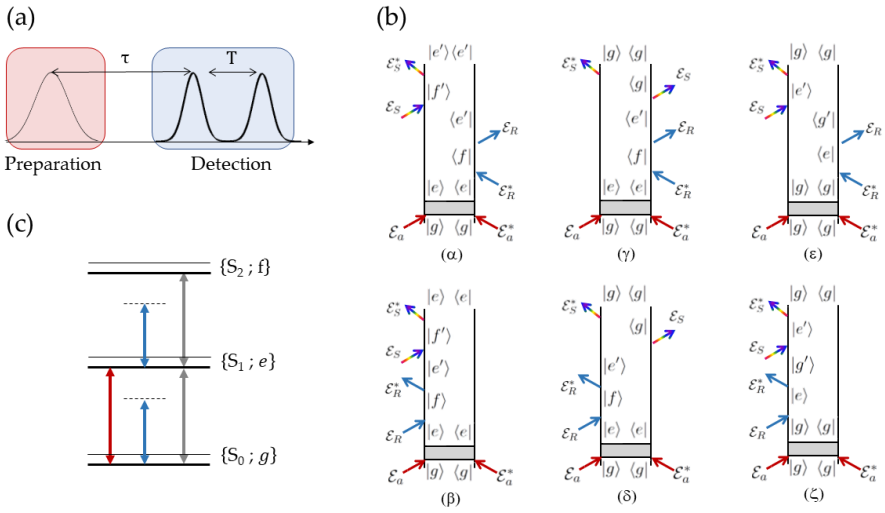

Figure 4.8: (a) Three beam ISRS geometry. (b) Feynman diagrams for the ISRS process. Upon resonant actinic excitation, the system may evolve ending up into an unknown population state, (either the ground g or the electronically excited e), depending on the specific relaxation pathway (gray boxes). (c) Energy level scheme of the model system. We consider three electronic states S_0, S_1 and S_2 with the associated vibrational manifold. The resonance conditions of the three pulses are shown too.

For these reasons, the effects of chirped probe pulses have recently been considered [120–122]. In this respect, we introduced a three beams experimental ISRS configuration which exploits chirped probe pulse to control the coherence detection [120]. The scheme uses a resonant actinic pulse to generate a population either in the ground or excited state, followed by an ISRS detection which combines an off-resonant Raman pulse and an ad-hoc chirped WLC probe. This configuration allows to unveil the undetermined population state, following the photoreaction process triggered by the actinic. Keeping the Raman pulse electronically off resonant guarantees that the vibrational coherence is solely generated in the electronic state manifolds which are

involved in the actinic excitation, preventing contributions arising from additional electronically excited state, which, conversely, may be reached by a resonant Raman pulse.

In particular, we calculated the ISRS signal arising from the following photophysical process. The system is modeled by three electronic states, g, e and f and the associated vibrational manifolds. The actinic pulse promotes the system into a non equilibrium excited state, which can only relax, before the Raman pulse arrival time, to the ground g or to the electronically excited state e, depending on its relaxation dynamics (indicated by the gray boxes in Fig. 4.8b). At this point, the system could be vibrationally excited, as it happens in presence of hot vibrational populations [18, 123] or time dependent frequencies along reaction coordinates [14, 124]. However, for the sake of simplicity, in this chapter we consider a vibrationally relaxed

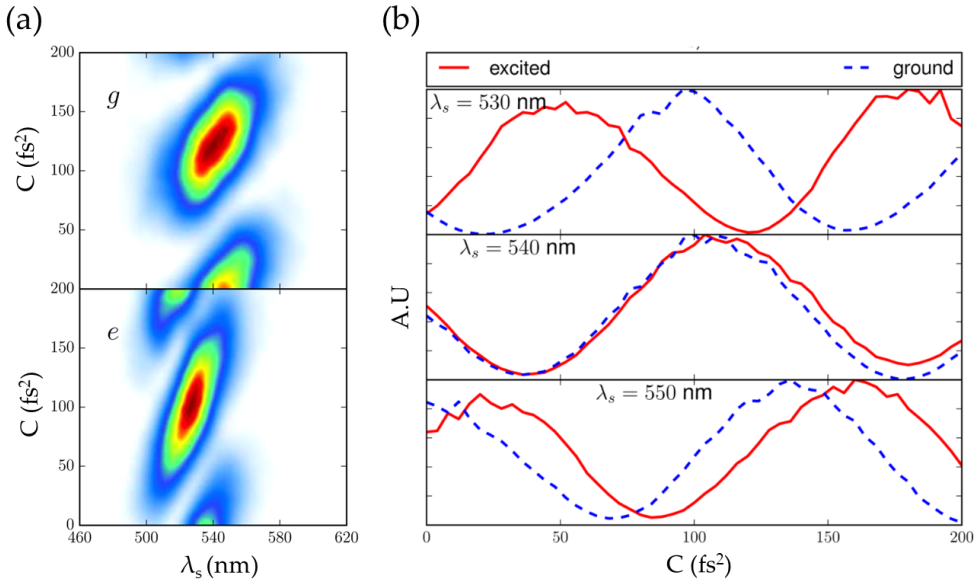

Figure 4.9: Excited state selectivity in chirp-controlled Impulsive Stimulated Raman Spectroscopy . (a) Simulated intensity of the 800 cm^{-1} ISRS feature as a function of the probed wavelength and the probe chirp, C, for ground and excited state coherences. (b) Slices for selected wavelengths show that the signal oscillates as a function of the chirp. The phase of this oscillations carries information about the electronic level in which the vibrational coherence is generated.

state. In other words, the role of the Actinic excitation is simply to create a population either in the ground g state or in the excited e. Accordingly, we will not include the actinic excitation pulse explicitly in the calculation. The extension to the case in which a coherence in created will be discussed in Chapter 6. The relevant Feynman diagrams that contribute to the signal under these conditions are represented in Fig. 4.8, together with the level scheme considered for the sample. We calculated again the signal using eq. 4.20 and considering in the summation the correlation functions F_j related to the Feynman diagrams α-ζ in Fig. 4.8. Moreover, we included a term $P_j(-T)$ in eq. 4.20 indicating the population in the relevant electronic state, ground or excited, at the arrival time of the Raman pulse, resulting from the photorelaxation upon the actinic excitation. The correlation functions $F_j(\omega_s, \omega_1, \omega_2)$ that have to be integrated in Eq. (4.20) are now given by

$$F_\alpha(\omega_s, \omega_1, \omega_2) = \frac{1}{(\omega_s - \tilde{\omega}_{fe'})(\omega_1 + \tilde{\omega}_{ef})(\omega_1 - \omega_2 + \tilde{\omega}_{ee'})} \tag{4.23}$$

$$F_\beta(\omega_s, \omega_1, \omega_2) = \frac{1}{(\omega_s - \tilde{\omega}_{fe})(\omega_2 - \tilde{\omega}_{fe})(\omega_2 - \omega_1 - \tilde{\omega}_{e'e})} \tag{4.24}$$

$$F_{\gamma}(\omega_s,\omega_1,\omega_2)=\frac{-1}{(\omega_s-\tilde{\omega}_{eg})(\omega_1+\tilde{\omega}_{ef})(\omega_1-\omega_2+\tilde{\omega}_{ee'})} \tag{4.25}$$

$$F_{\delta}(\omega_s,\omega_1,\omega_2)=\frac{-1}{(\omega_s-\tilde{\omega}_{e'g})(\omega_2-\tilde{\omega}_{fe})(\omega_2-\omega_1-\tilde{\omega}_{e'e})} \tag{4.26}$$

$$F_{\epsilon}(\omega_s,\omega_1,\omega_2)=\frac{1}{(\omega_s-\tilde{\omega}_{eg'})(\omega_1+\tilde{\omega}_{ge})(\omega_1-\omega_2+\tilde{\omega}_{gg'})} \tag{4.27}$$

$$F_{\zeta}(\omega_s,\omega_1,\omega_2)=\frac{1}{(\omega_s-\tilde{\omega}_{eg})(\omega_2-\tilde{\omega}_{eg})(\omega_2-\omega_1-\tilde{\omega}_{g'g})} \tag{4.28}$$

In Fig. 4.9, we present the result of the calculations, showing the simulated dependence of the 801 cm^{-1} Cyclohexane ISRS band on the probe chirp. In particular, $S(\Omega=801\mathrm{cm}^{-1},\lambda_s)$ as a function of C is separately reported for the diagrams α-δ, in which the vibrational coherence is generated on the excited state e and diagrams ϵ-ζ which are responsible for the ground state signal. We note that both the signals undergo an oscillatory behavior as a function of C. Critically, the phases of these oscillations are tilted along the probe wavelength axis by a different amount depending on the frequency of the electronic state. This results again from the chirp dependent phase factor carried by the envelope of the probe pulse, which is evaluated at the vibronic frequency of the state involved in the process, consequently ruling the interference between the different Feynman paths. Therefore, the information carried by the broadband probe can be used to discriminate among the two cases, studying the progressive phase shift of the oscillations in C along different slices in λ_s of the map $S(\Omega=801\mathrm{cm}^{-1};\lambda_s,C)$, reported in Fig. 4.9b.

4.3 Conclusions

In this chapter, we showed that shaping a broadband pulse, either by adding a phase jump or a linear chirp, can be used as a tool in the detection of vibrational signatures within different impulsive stimulated Raman schemes. In particular, we described the ISRS process by means of the diagrammatic approach, calculating the nonlinear polarization induced in the sample by the Raman and probe fields. We dissected the pathways that generate the nonlinear response and rationalized the spectral dependence on the probe wavelength in the off resonant measurements for liquid Cyclohexane.

Specifically, in off resonant ISRS with unchirped pulses, the signal for a given detected wavelength results from the sum of two concurring third-order processes, associated with photons which are red and blue shifted by the vibrational frequency with respect to the center wavelength of the probe. This gives rise to two contributions oscillating as a function of T with opposite phases, which interfere destructively, resulting in a strong signal suppression around the central wavelength of the probe pulse. When the sample dispersion is considered this interference pattern changes due to additional and mode dependent phase factors that contribute differently to the two diagrams. An even stronger effect can be achieved by chirping the probe spectrum, which allows to shape the dependence of the Raman peaks intensity in the Fourier transformed map $S(\Omega,\lambda_s)$, shifting from two to one maximum as a function of λ_s. Our results suggest that an optimal probe chirp profile can be used to selectively enhance specific vibrational modes and are relevant for signal analysis improvement.

Furthermore, it is possible to exploit a linearly chirped probe to assign a given vibrational dynamics to the relevant potential energy surface, due to the coupled phase dependence of the signal on both the electronic frequency and chirp. Consequently, the fine tuning of the relative phases between the processes contributing to the signal generation represents a control knob to discern excited from ground state vibrational coherences.

5 Probing electron-phonon coupling on femtosecond time scale in Lead Halide Perovskites

Correlations between electronic excitations and lattice vibrations are expected to play a role in determining the outstanding optoelectronic properties of metal halide perovskites, due to the soft fluctuating nature of their crystal structure. Thus, unveiling electron–phonon coupling upon ultrafast photoexcitation is a necessary step for the optimization and application of the groundbreaking capabilities of these semiconductors in photovoltaics and other light-based technologies. In this chapter, we present the study of the ultrafast vibrational response upon resonant excitation in hybrid lead-bromide perovskites by means of broadband ISRS. In the first part, we review the properties of hybrid perovskites and discuss the recently advanced hypothesis of polaronic effects upon charge generation. Even if polarons have been observed in other polar crystals sharing the perovskite structure, their role in the photophysics of hybrid organic-inorganic photovoltaics is still unknown. In the second part, we report the experimental results obtained in methylammonium lead-bromide perovskite thin films. The additional dependence of the signal on the dispersed probe wavelength has been exploited to dissect the origin of the different Raman bands under resonant and non-resonant conditions, leading to the experimental observation of polaronic signatures in selected excited state modes coupled to the photocarrier.

5.1 Photoinduced charge carriers in hybrid organic-inorganic perovskites

Hybrid organic-inorganic perovskites recently triggered a wide entusiasm in the scientific and technological community as a new promising class of materials for efficient photovoltaic and optoelectronic applications [125, 126]. Combining their flexibility when used as absorber layers for light harvesting with low production costs, they are emerging as preferential candidates within the so-called third generation solar cells, achieving a year-by-year monotonic increase of the power conversion efficiencies (PCE), from the few percents reported in 2009 when initially demonstrated in the dye-sensitized configuration [127], to 10% in 2010 [128] and exceeding 20% in 2015 [129]. In parallel with gathering the efforts of the photovoltaics community, these materials arouse interest for application to light-emitting diodes [130] and amplified spontaneous emission or lasing [131–133]. Here, we briefly summarize recent theoretical and experimental findings related to hybrid perovskites with particular emphasis on the photocarrier generation and recombination processes.

5.1.1 Structure and optoelectronic properties

The term perovskite broadly indicates the materials sharing the crystal structure of calcium titanium oxide mineral $CaTiO_3$, which are described by the stechiometry ABX_3. In particular, A and B are cations, while X is the anion. The remarkable optoelectronic properties that distinguish these materials have been demonstrated so far for X anions belonging to the class of

halogens, such as Iodine (I^-), Bromine (Br^-), and Chlorine (Cl^-). In all inorganic perovskites A and B are both metallic cations while, in the hybrid version, A is an organic molecule, tipically methylammonium($CH_3NH_3^+$, abbreviated as MA) or formamidinium ($HC(NH_2)_2$ or FA). The

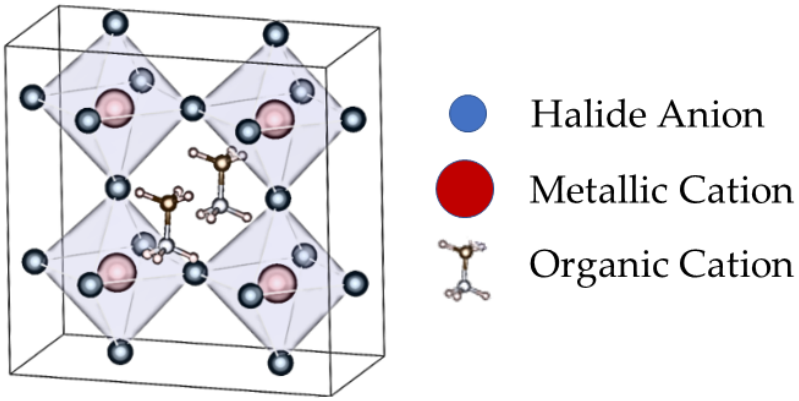

Figure 5.1: Structure of a hybrid organic-inorganic perovskite.

properties that make hybrid perovskites so appealing for light harvesting applications comprise low exciton binding energies, slow carrier recombination times and long diffusion lengths, as well as high absorption coefficients across the visible spectrum [134]. On the other hand, modest charge mobilities have been reported, lower than those of crystalline semiconductors albeit higher than those found in organic semiconductors. Because of these characteristics, solution-processed solar cells based on perovskite layers combine the capabilities of the well developed class of silicon-based devices and the low cost and versatility of organic photovoltaics.

However, despite the technological appeal, the fundamental processes underlying their photophysics are still matter of debates [134–139], with recent results discussing the role of electron-phonon coupling, defects and dynamical disorder of the organic cation in the soft polar structure of these perovskites. As an example, despite the soft nature of their ionic cage, these materials exhibit a surprisingly low level of electronic disorder resulting in sharp band edges and narrow distributions of the electronic energies. This attracted the efforts of heterogeneous communities, spanning from Raman and optical Kerr effect spectroscopy and 2D IR to picosecond electron diffraction, aimed to understand structural and dynamic disorder and its impacts on the optoelectronic properties of the hybrid perovskites [140–143]. These studies point to the role of structural fluctuations in reducing the carrier recombination rate, specifically linking the latter to the freely reorienting organic dipoles but also to the structural deformations of the inorganic lattice. However, how and how much this softness effectively determines the optoelectronic properties of the material is still debated and necessarily requires a deeper understanding of the carrier generation process.

The main open points currently under investigation can be summarized by the following two questions:

- Why are the recombination times so long, considering the structure of these materials?
- What are the relevant phenomena that determine the nature of photocarriers?

To date, the answers to these questions remain unclear, although, in the last few years, several mechanisms involving charge generation and screening have been proposed, in particular pointing to the role of the strong electron-phonon coupling in this class of systems, as we discuss in the next sections.

5.1.2 Charge relaxation and recombination processes

The efficacy of a semiconductor as a solar-cell material largely depends upon its ability to generate and maintain free carriers until their extraction. This is why the extended lifetime of charge carriers, and the associated electron and hole recombination processes, are among the most salient and studied features of the hybrid perovskites photophysics. The recombination process in solids usually starts with an initial carrier relaxation. Indeed, the photoexcitation drives an out-of-equilibrium charge-carrier distribution which subsequently relaxes through a range of different processes toward the band edge. These processes have been well documented over the years for inorganic semiconductors such as GaAs [144]. Since lead halide perovskites share many of the typical features of direct inorganic semiconductors, the same relaxation pathways are considered to be relevant also in hybrid materials [134], although further investigations are now being pursued. Typical relaxation pathways in both inorganic and hybrid semiconductors includes:

1. Charge carrier thermalization: immediately after photoexcitation, a coherent superposition of ground and electronically excited state arises and rapidly dephases, leaving the system in a population state. Here, the charge carrier distribution is not thermal, i.e. it is not possible to define an electron temperature. Then, within picoseconds, the charges thermalize by scattering within the conduction band to a Boltzmann distribution characterized by a carrier temperature T_c.

2. Charge carrier cooling: the initially hot distribution in which T_c is much higher than the lattice temperature relaxes in a two step process, interacting firstly with longitudinal optical phonons and then with acoustic phonons. For elevated excitation densities, a different mechanism, called phonon bottleneck [145], is also possible, in which a significant phonon reabsorption, due to acoustic phonon bath temperature raised toward the charge-carrier one, keeps charge carriers hot for an extended time period.

3. Many body effects: for high excitation densities, Pauli and Coulomb interactions between the multiple electrons start to play a role. For example,the need to minimize the exchange and the correlation energies leads to the bandgap renormalization (band edge redshift) and the finite density of available states causes state-filling effects (with a perceived band edge blueshift).

Studying thermalization and the associated timescales is particularly interesting in the context of photovoltaics since they determine the ultimate limit for carrier extraction. Indeed, the excess of energy carried by hot charges can in principle be harvested yielding higher PCEs. Recently, timescales as low as a few femtoseconds have been revealed by two dimensional electronic spectroscopy in $MAPbI_3$, with charge thermalization principally mediated by carrier-carrier scattering [146].

Throughout and after thermal relaxation, charge recombination takes place. The decay of the charge density $n(t)$ is usually modeled by the rate equation

$$\frac{\mathrm{d}n}{\mathrm{d}t} = -k_3 n^3 - k_2 n^2 - k_1 n \tag{5.1}$$

where k_1, k_2 and k_3 are called the monomolecular, bimolecular and three-body recombination rates. This gives rise to a density-dependent recombination dynamics which is reflected in photoluminescence (PL) and transient absorption measurements [147]. An example of monomolecular recombination is sketched in Fig. 5.2a where an electron in the conduction band is captured by a trap state. Notably, due to this mechanism, defects associated with intragap states limit photovoltaic performances. In a bimolecular process (Fig. 5.2b), conduction band electrons undergo radiative recombination with holes in the valence band. Finally, many-body process are possible, as happens in Auger recombination where the recombination of an electron with a hole is accompanied by the promotion of a second conduction band electron to a higher energy state (5.2c). These processes may occur in a direct or indirect way, depending on the change

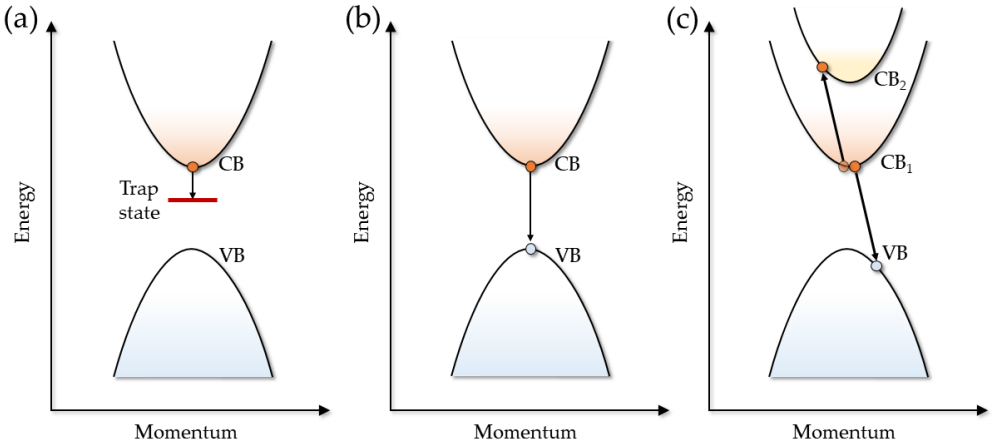

Figure 5.2: Direct recombination mechanisms of free carriers in organic-inorganic metal halide perovskites: (a) Trap-assisted recombination is a monomolecular process involving the capture of a charge carrier (electron in the sketched case) in a intragap trap state (for example due to defect). (b) Bimolecular recombination occurs between electrons in the conduction band CB and holes in the valence band VB. Since all processes have to satisfy energy and momentum conservation, indirect transitions may happen if mediated by a phonon (see Fig. 5.3). (c) Higher order processes are also possible. In e^- Auger recombination the energy of an electron in CB_1 is transferred to another electron in a different conduction band CB_2 to allow nonradiative recombination with a hole in VB. A similar process can involve two holes in the valence recombining with an electron in the conduction band.

of the charge momentum k. In a direct bandgap transition, a photon vertically projects the electron form the fully occupied valence band to conduction band. Since photons carry only a very weak momentum, the carrier momentum should remain unchanged during an electronic transition. Thus, an indirect transitions is momentum forbidden unless is mediated by another particle, for example a phonon, whose energy is either donated by or released to the solid. The nature of the transition reflects in the absorption constant: since the need of a phonon with a specific energy makes indirect transition less favorable, consequently the relative absorption rate will be lower.

Since the early day of hybrid perovskites, the low carrier recombination rates [148], comparable to single crystalline semiconductor, turned out to be as intriguing as somewhat unexpected. Indeed, strong absorption constant and a high photoluminescence quantum yield in the prototypical materials, as $MAPbI_3$ and $MAPbBr_3$, indicated a direct gap transition but the lifetimes exceed the Langevin limit for direct recombination by several order of magnitude [134, 149]. To solve this conundrum, mixed direct-indirect recombination has been proposed, in which a direct absorption motivates the optical response of the material while the long photocarriers lifetime is accounted for by an indirect recombination. Recent observations through temperature dependent time-resolved microwave conductance and photoluminescence experiments showed that the electron-hole recombination in MAPbI3 is a thermally activated process suggesting the possible role of slow phonons [150]. In particular, photogenerated electrons may relax into a distinct dark electronic state which extends the charge carrier lifetime.

However, no direct experimental evidences were available for a phonon-assisted recombination process. Therefore, both the nature of such state and the reaction pathway which would lead to its population remain unclear. Critically, we recently observed such evidences in $MAPbBr_3$ by means of ISRS and in section 5.2.3 we discuss their role in the recombination in the light of the literature presented in this section.

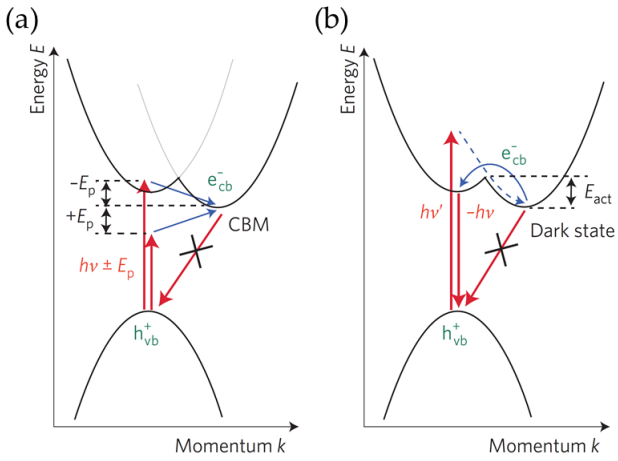

Figure 5.3: Forbidden momentum pathways for recombination of electrons and holes in perovskites. (a) An indirect transition to a minimum of the conduction band (CBM) that is shifted in the momentum (k) dimension requires a phonon coupled to the electronic movement. The change in momentum is then compensated by the phonon energy E_p. A non-vertical transition from the CBM back to the valence band maximum is forbidden, and no radiative recombination of photogenerated carriers is generally observed in this case. (b) Scheme of the recombination pathway proposed by Hutter and colleagues [150]. Following above bandgap photoexcitation, generated hot electrons relax down to a dark state (dashed curved arrow). An activation barrier of energy E_act must be overcome by the system to allow for radiative electron–hole recombination. Moreover, momentum conservation also requires the mediation of a phonon (solid curved blue arrow). Image adapted from [149].

5.1.3 Free carriers vs excitons

Upon photoexcitation, electron-hole pairs are created in the perovskite semiconductor. Since many acceptors are available to the light, the total carrier population will include both uncorrelated pairs, i.e. free carriers, and cases in which the positive and the negative charges of the same pair come from different atomic sites, correlated by the Coulomb interaction, and the resulting delocalized carrier bound state is called a *Wannier-Mott* exciton. As these delocalized excitations start interacting with the surrounding lattice, they can exchange both charge and energy[1]. Depending on their characteristics, excitonic carriers have a great impact on the application side. Since they posses their own binding energy E_b that needs to be overcome in order to separate electrons and holes and make them contribute to the photocurrent. Binding energies below thermal energies at room temperature are highly desirable because, in this case, thermal fluctuations may be sufficent to dissociate the exciton. Notably, E_b can be extracted from the absorption spectrum by means of the Elliott theory [151].

In general, in view of the application of a given material, there is the need to assess whether excitonic photoexcitations or free charge are dominant. Most organic-based devices fall into the cathegory of excitonic solar cells [152]. In contrast, recent measurements of the PL quantum yield dependency on the excitation density [153] pointed to identify free carriers as the dominant species in solution-processed lead iodide perovskites thin films. In particular, in presence of Wannier-Mott excitons, the fraction x of free charges over the total excitation density $n = n_{fc} + n_{exc}$ can be expressed by the Saha-Langmuir equation [153, 154]

$$\frac{x^2}{1-x} = \frac{1}{n}\left(\frac{2\pi\mu k_B T}{h^2}\right)^{\frac{3}{2}} e^{-\frac{E_b}{k_B T}} \tag{5.2}$$

[1] In other systems, mainly molecular, the average distance between atoms prevent charge transfer and excitons exchange only energy. These states are known as *Frenkel* excitons.

being h the Planck constant, μ the reduced mass of the exciton and k_BT the available thermal energy. The application of equation 5.2 shows that under equilibrium at room temperature free carriers are the primary source of photoexcitation for excitation densities representative of the operating condition in photovoltaics devices (n$< 10^{-15}$ cm^{-3}). Conversely, at low temperature the exciton population increases and may become dominant. However, the relative contribution between free carriers and excitons during the first few picoseconds of the dynamics is still debated.

5.1.4 Polarons

Given the polar nature of the perovskite lattice, it has been suggested [136] that carriers localize as large polarons in contrast to a pure band like picture where carriers act as delocalized Bloch waves. This picture would be suggestive of the presence of strong electron–phonon scattering mechanism, at ease with recently demonstrated carrier transport and temperature dependence of the homogenous linewidths of electronic transitions [155].

Polarons, firstly introduced by Lev Landau in 1933 [156], indicate quasi-particles created by the electron-phonon interaction in crystals. In general, charge carriers in inorganic and organic matter interact with ion vibrations. In covalently-bonded crystals, these interactions can be neglected and electrons described as freely moving in a frozen lattice, with the exception of the scattering with thermal phonons. In polar crystals, this picture does not hold anymore, even at low temperature, due to the Coulomb interaction between electrons in the conduction band and the lattice ions, resulting in a strong electron-phonon coupling. In this case, the electron attracts positive ions towards it and repeals the negative ones, binding itself to the surrounding cloud of virtual phonons induced by its presence (Fig. 5.4). The resulting self-trapped electron and the associated pattern of displaced atomic equilibrium positions can be treated as a unique entity, called polaron. Similarly, a polaron can be formed by a hole in the valence band.

At odds with a usual band-carrier, a polaron is characterized by its own binding energy, effective mass m*, different from the carrier band mass, and optical properties. When the radius of the polaron, i. e. the distance the electron can travel in the time of a phonon period, is much larger than the lattice constant of the crystal, the latter can be treated as a polarizable continuum. This situation is refered to as *large* or *Fröhlich* polaron [157, 158]. Large polarons have been observed in a broad class of materials, including inorganic perovskites. The properties

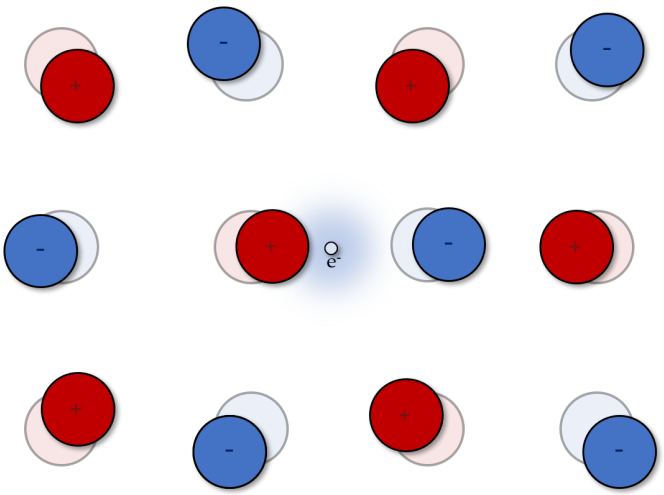

Figure 5.4: Schematic representation of a polaron: the electron shifts the equilibrium positions of the surrounding anions (blue) and cations (red). In turn, the ions in the lattice produce a potential felt by the carrier.

of large polarons are modeled by the coupling constant α, introduced by Fröhlich [159, 160].

In the Fröhlich model the electron-phonon interaction under the weak coupling assumption is described by the Hamiltonian:

$$H = \frac{\boldsymbol{p}^2}{2m_b} + \sum_{\boldsymbol{k}_j} \hbar\omega_{LO\,j} a^\dagger_{\boldsymbol{k}_j} a_{\boldsymbol{k}_j} + \sum_{\boldsymbol{k}_j} \left(V_{\boldsymbol{k}_j} e^{i\boldsymbol{k}_j \boldsymbol{r}} + h.c. \right) \tag{5.3}$$

where m_b is the band mass of the photogenerated electron, described by the position and momentum operators $\boldsymbol{p}$ and $\boldsymbol{r}$, $\omega_{LO\,j}$ is the frequency of the longitudinal optical (LO) phonon with wave vector $\boldsymbol{k}_j$ and creation (annihilation) operator $a^\dagger_{\boldsymbol{k}_j}$ ($a_{\boldsymbol{k}_j}$) to which the carrier couples and $V_{\boldsymbol{k}_j}$ is the corresponding Fourier component of the electron-phonon interaction matrix

$$V_{\boldsymbol{k}} = -i\frac{\hbar\omega_{LO}}{k} \left(\frac{4\pi\alpha}{V} \right)^{\frac{1}{2}} \left(\frac{\hbar}{2m_b\omega_{LO}} \right)^{\frac{1}{4}} \tag{5.4}$$

The dimensionless Fröhlich coupling constant α in eq. 5.4 is a measure of the strength of the electron-phonon interaction and is defined as

$$\alpha = \frac{e^2}{\hbar} \sqrt{\frac{m_b}{2\hbar\omega_{LO}}} \left(\frac{1}{\varepsilon_\infty} - \frac{1}{\varepsilon_0} \right) \tag{5.5}$$

being ε_∞ and ε_0 the high frequency and the static dielectric constant of the polar crystal, respectively. Building on the weak coupling theory of Fröhlich , a method for calculating perturbatively the polaron binding (or free) energy was initially developed by means of a formulation based on canonical transformations [161], obtaining

$$E_0 \approx -\alpha\hbar\omega_{LO} \tag{5.6}$$

An alternative all-coupling polaron approximation was developed by Feynman who introduced a variational principle for path integrals approach, providing an expansion in terms of α for the polaron ground state energy calculation [162]

$$E_0 \approx -\hbar\omega_{LO} \left[\alpha + 0.0123\alpha^2 + 0.00064\alpha^3 \right] \tag{5.7}$$

Over the years the perturbative coefficients of the expansion have been calculated with increasing precision, up to those by Selyugin and Smondyrev [163, 164]:

$$E_0 \approx -\hbar\omega_{LO} \left[\alpha + 1.59196220 \cdot 10^{-2}\,\alpha^2 + 0.806070048 \cdot 10^{-3}\,\alpha^3 \right] \tag{5.8}$$

This result holds under the hypothesis of weak coupling and low temperature regimes [165]. Analogously, perturbative expansions in the strong coupling limit can be obtained [164]. Taking into account finite temperature effects is a demanding task. In the case of weak and intermediate coupling regimes, evidences from Monte Carlo simulations and the Feynman variational approach point to an increase of the polaron free energy with temperature [166, 167]. Inasmuch as these results can be generalized to a broader class of cases, eq. 5.8 is an estimate of the lower bound for the polaron free energy at finite temperature.

In section 5.2, we present the application to the framework just discussed to study the polaron formation in $MAPbBr_3$ and estimate the relative parameters. We want to stress that a polaronic quasi-particle defines the phonon dressing of both correlated and uncorrelated carriers. Thus, whether the dominant photo-excitation source is from excitons or free carriers, this does not affect our conclusion. On the other side, polarons may offer the answer to the two questions we raised at the beginning of this chapter.

5.2 Impulsive stimulated Raman spectroscopy on lead bromide perovskites

Fueled by the motivations presented in the previous sections, we investigated the ultrafast vibrational response of methylammonium lead-bromide perovskite ($MAPbBr_3$) [168]. In particular, we aimed to study the nature of the charge carriers and the relation between electron-phonon

coupling and long recombination time in this material, by comparing the Raman spectra obtained under electronically resonant and non-resonant conditions. For this reason, we used ISRS with a Raman pulse tuned to two different wavelengths to explore the vibrational properties of the ground and excited electronic states in polycrystalline thin film of $MAPbBr_3$ and to identify the phonon energies coupled to the electronic excitations. As already emphasized in Chapter 4, ISRS offers the potentiality to resolve excited state Raman bands with high spectral resolution. Since the measurement is performed in the time domain, there are no spectral limitations neither artifacts arising from elastic pump-scattering and photoluminescence, which benefits the probing of the low frequency region, containing the most relevant modes of the inorganic moiety.

5.2.1 Preparation and characterization of $MAPbBr_3$

Pristine $MAPbBr_3$ polycrystalline thin films used in the experiments were synthesized by spin coated deposition on a clean glass substrate from commercially available Lead(II) bromide (PbBr2, $\geq$ 98 %), N,N-dimethylformamide (DMF, anhydrous, 99.8%) and methylammonium bromide (MABr). All the measurements have been conducted at room temperature, where the perovskite exhibits the cubic phase. In Fig. 5.5, we show a photo of the sample and a scanning electron microscope image of the coated surface.

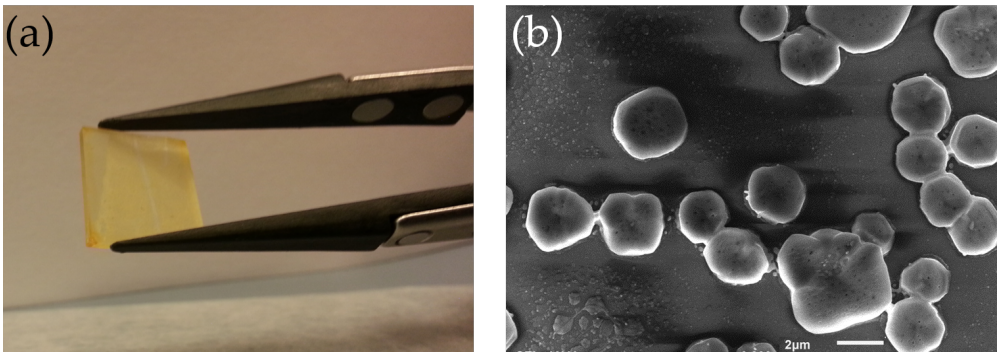

Figure 5.5: Photo (a) and SEM image (b) of one of the $MAPbBr_3$ samples used in the experiment.

The optical characterization of the sample is presented in Fig. 5.6. The linear absorption spectrum, reported in panel a, shows a sharp feature around 524 nm, corresponding to a direct band gap energy of 2.35 eV, with an excitonic resonance approximately at 2.37 eV, pointing to a binding energy larger than 40 meV, as estimated by the Elliot formula [148]. Photodamaging is known to be an issue in polycrystalline perovskite films exposed to intense electromagnetic fields [169]. This is shown in Fig. 5.6b where we report the photoluminescence (PL) spectra of $MAPbBr_3$ thin films obtained under two different excitation energy regimes, corresponding to excitation density comparable to the one used for the ISRS experiment ($\sim 10^{17}$ cm^{-3}, blue lines), and to lower values ($\sim 10^{15}$ cm^{-3}, red lines). The sample has been excited by fs pulses as in the ISRS experiment. Firstly, the measurements have been conducted in vacuum, measuring at low excitation density before or after the high energy as reported in top and central panel, respectively. The central panel shows the broadening of the red spectra related to sub-band gap emissive features, which indicates the formation of trap states. The differences between the two panels testifies that the low energy PL spectrum is modified by the exposition to the high density pump, due to damaging of the sample. In order to address this issue for ISRS measurements, the sample was encapsulated by a thick Poly(methyl methacrylate) (PMMA) layer and measured in air. The PMMA layer preserves the sample from water vapor and hampers the formation of intra-gap defect states. The PL spectrum relative to the encapsulated sample is shown in the bottom panel of Fig. 5.6b in which the protective effect of PMMA is visible, considering that the order of the measurement is the same as in the central panel, i.e. the sample was first exposed to the high density pump.

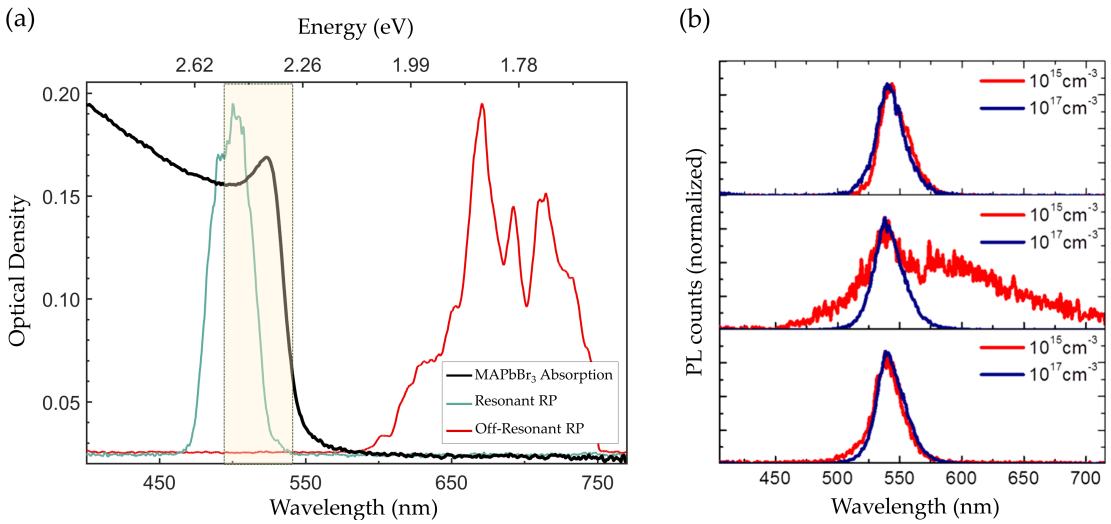

Figure 5.6: Characterization of the pristine $MAPbBr_3$ polycrystalline thin film. (a) Visible absorption spectrum of the sample (in black) and normalized spectral envelopes of the pulses used in the ISRS experiment. The red and green lines indicate respectively the 1.86 eV off-resonant and the resonant 2.46 eV Raman pulse energies while the shaded box represents the dispersed probe wavelengths considered in the analysis. (b) Photoluminescence spectra measured from the sample in vacuum (top and central panels) and the sample covered with a PMMA layer and measured in air (bottom panel). Red and blue lines refer to excitation densities equal to 10^{15} and 10^{17} cm^{-3}, respectively. In the top panel, low excitation density measurement preceded the one at high energy, while in central and bottom panel the order of the two measurements has been reversed. The PL measurements have been collected in the laboratories of the Center for Nano Science and Technology, Istituto Italiano di Tecnologia, Milan.

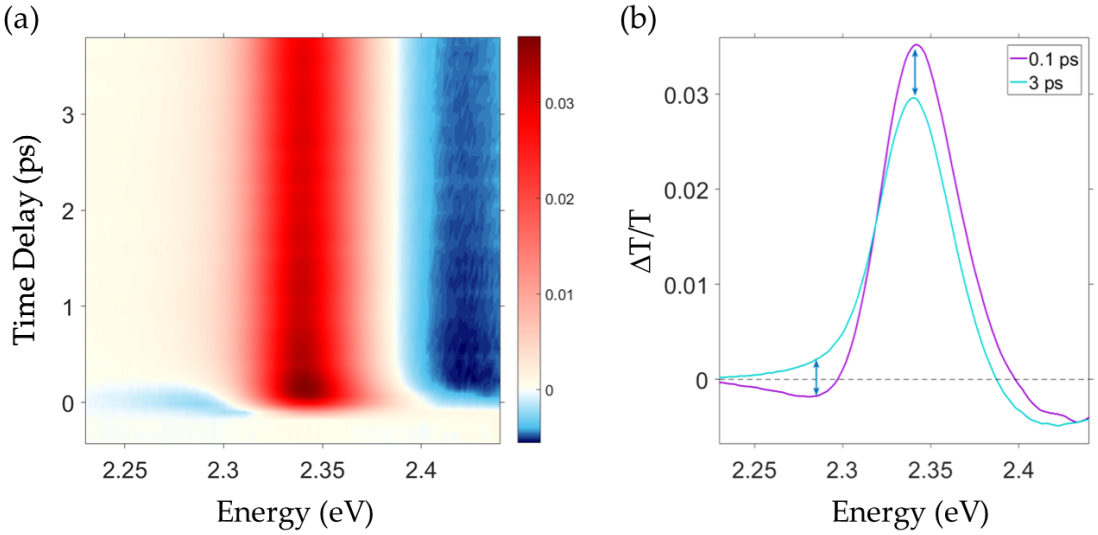

Figure 5.7: Ultrafast response of $MAPbBr_3$ upon resonant excitation at 2.46 eV. (a) Transient absorption of the sample the as a function of the probe photon energy within the first 3.5 ps of its photoinduced dynamics. (b) Selected TA traces at 100 fs (purple line) and 3 ps (blue line) time delays between the Raman and Probe pulse.

In Fig. 5.7, we report the ultrafast response of the sample upon photoexcitation at 2.46 eV

studied by transient absorption (TA). Interestingly, the TA spectrum presents a photo-bleaching (PB) band arising from the state-filling convolved with a derivative like line-shape, emphasized in Fig. 5.7b. This kind of features is generally associated to the presence of Coulomb effects in the electronic/excitonic transition [170]. While the PB follows the charge carrier dynamics, living for hundreds of picoseconds [135], the derivative feature decays within the first picosecond, on a timescale comparable to the lattice motion probed by the ISRS. We will further comment on that after presenting the ISRS measurements in the next section.

Since by the same experimental setup we acquired simultaneously the TA and ISRS data, TA has been used as a tool to further monitor photo-degradation during the ISRS experiment. In particular, the absorption maps collected during the ISRS measurements after different exposition times of the sample, from the beginning of the data collection to its end, did not show any changes. This is shown in Fig. 5.8, in which we present selected slices of the TA spectra taken at a time delay of 4 ps between the Raman and probe pulses for the first and the last acquisition of the experiment.

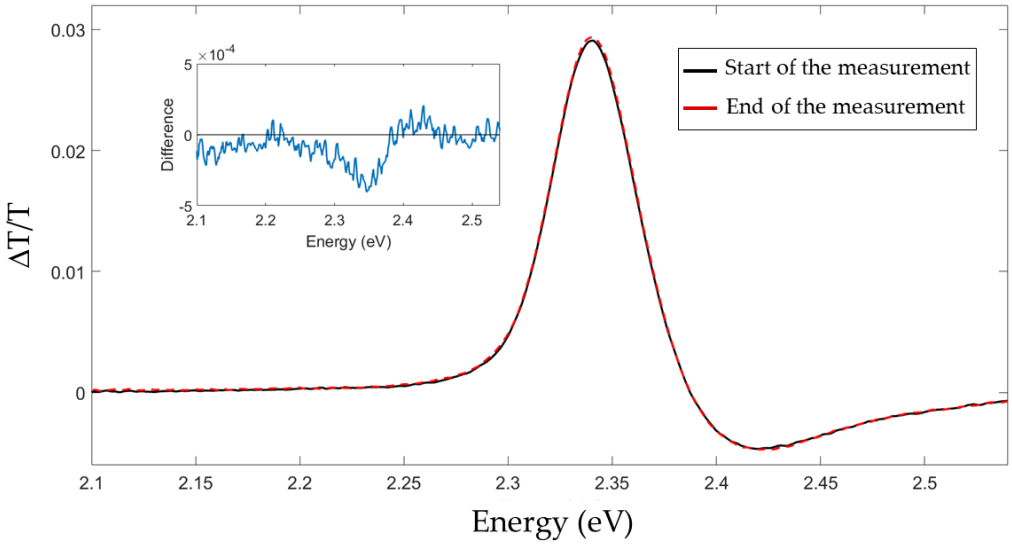

Figure 5.8: Slices of the TA maps corresponding to a time delay between Raman and Probe pulses of $T = 4$ ps, acquired at the beginning (black) and at the end (red) of the data collection for ISRS. The inset reports the difference between the two traces and testifies the absence of photo-degradation exposition in the sample.

5.2.2 ISRS experimental results

As already discussed in the previous chapter, in ISRS the ultrashort Raman pump pulse generates ground or excited state vibrational coherences by means of its large bandwidth. After a tunable temporal delay, the broadband ultrashort probe pulse records the evolution of the vibrational coherences in the form of transient absorption spectra, on the top of which coherent oscillations are visible, related to the photo-activated Raman modes [37]. In Fig. 5.9, we compare the ISRS measurements on $MAPbBr_3$ obtained upon resonant (top panel) and non-resonant (bottom panel) excitation by Raman pulses of two different colors. For the off-resonance measurements, $\Delta_{FWHM} = 30$ nm, 30 fs NOPA pulses centered at 665 nm were generated with the setup described in 3, while in the resonant ones, we used $\Delta_{FWHM} = 10$ nm, 50 fs pulses centered at 503 nm. Critically, the pulse durations were much shorter than the periods of the vibrational modes we aimed to probe, ranging in the 0-200 cm^{-1} spectral region. The spectra of the pulses are reported in Fig. 5.6, superimposed to the linear absorption of the sample. Since the detection of the probe was spectrally dispersed, we obtained probe-wavelength resolved

vibrational coherence maps. We focused the analysis on the dispersed probe wavelength region corresponding to the maximum of the TA signal, specifically optimizing the data collection from 510 to 540 nm (photon energies from 2.43 to 2.30 eV), where the ISRS cross section is enhanced.

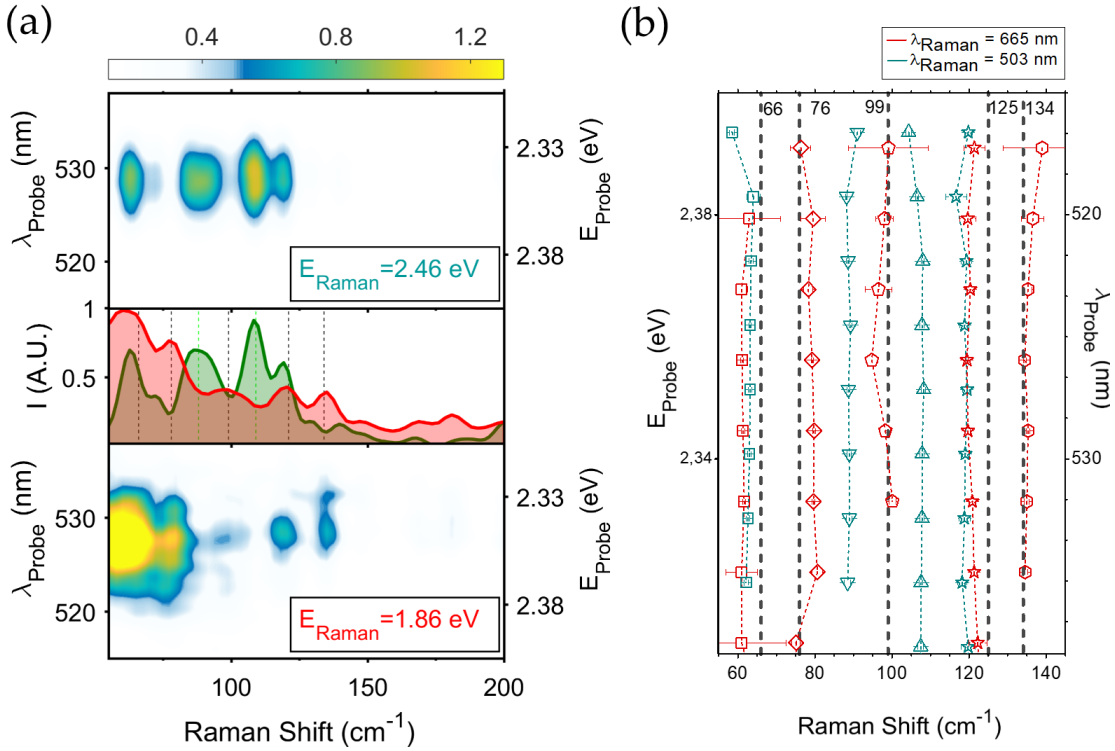

Figure 5.9: ISRS measurements of $MAPbBr_3$ under different resonance regimes. (a) Top and bottom panels report the probe wavelength resolved ISRS maps, upon resonant (E_{pump} = 2.46 eV) and non-resonant (E_{pump} = 1.86 eV) excitations, respectively. The maps have been obtained by Fourier transforming the oscillating component of the transient absorption data, to retrieve the vibrational spectra. The central panel shows the average of the ISRS map over all the measured probe wavelengths. Green and red shaded Raman spectra refer to resonant and non-resonant conditions, respectively. (b) Fitted peaks positions of the measured Raman modes as a function of the probed wavelength. Red and green symbols refer to Raman modes obtained by pumping at 1.86 eV and 2.46 eV, respectively. Vertical dashed lines indicate the position of the sample ground state vibrational modes reported in literature [171].

The experimental routine has been described in details in Chapter 3. In particular, here we recorded the coherent oscillations within a temporal window of 4.25 ps, covering time delays from 0.25 to 4.5 ps with steps of 83 fs. This corresponds to spectral resolution of $\Delta\nu = 7.8\ cm^{-1}$. Time traces have only been considered from 250 fs on-wards to avoid cross phase modulation artifacts, due to pump and probe temporal overlap. After removing the superimposed dynamics from the TA signal, we applied Fourier transformation at each probe wavelength. Zero padding algorithm together with to Kaiser-Bessel windowing with $\beta = 12$ was applied to increase the length of the probed delay vector of a factor three and enhance the spectral definition. In particular, in order to avoid artifacts due to pulse and instrumental instabilities, Raman pulse fluence was monitored during the experiment and the measurements were repeated using additional time steps of 33 fs and 54 fs, further improving the signal to noise ratio of the averaged ISRS map.

The average of the ISRS maps over all the detected probe wavelengths is reported in the middle panel of Fig. 5.9a, where the green and red shaded spectra correspond to resonant and off-resonant excitations, respectively. The obtained Raman spectra in both the resonance conditions have been fitted with Gaussian functions in order to extract the peak positions of

the various modes, reported in Fig. 5.9b. The results of the fit for the resonant data in selected probe spectral regions are shown by the blue line in Fig. 5.10 superimposed to the data.

In the off-resonant map, peaks at 64 cm^{-1} , 78 cm^{-1} , 98 cm^{-1} , 121 cm^{-1} and 134 cm^{-1} can be observed. These frequencies are in good agreement with theoretical calculations and continuous wave (CW) Raman spectra [140, 171, 172]. The peak positions of the modes from CW measurement reported in literature [171] are compared with those we obtained with ISRS in Fig. 5.9. These modes represent the vibrational degrees of freedom exhibited by the lead-halide octahedra and point to the inherent softness of the inorganic cage [173]. For what concerns their assignment, the bands at 98 cm^{-1} and 134 cm^{-1} have been linked to the symmetric stretch modes of the Br-Pb-Br bond and the one at 121 cm^{-1} to the asymmetric stretch. The 64 cm^{-1} and 78 cm^{-1} bands are related to the corresponding symmetric and asymmetric scissoring modes. The measured full widths at half maximum of the modes are in agreement with phonon dephasing times $\Gamma^{-1} \sim 1$ ps.

Using the resonant Raman pulse, we observed four bands. Two of them correspond to the 64 cm^{-1} and 121 cm^{-1} modes, also present in the non-resonant case. Remarkably, we observed additional phonon modes at 89 cm^{-1} and 106 cm^{-1} which are not present in the off resonant spectra nor in CW Raman. In the next section, we show that these two families originate from different physical processes.

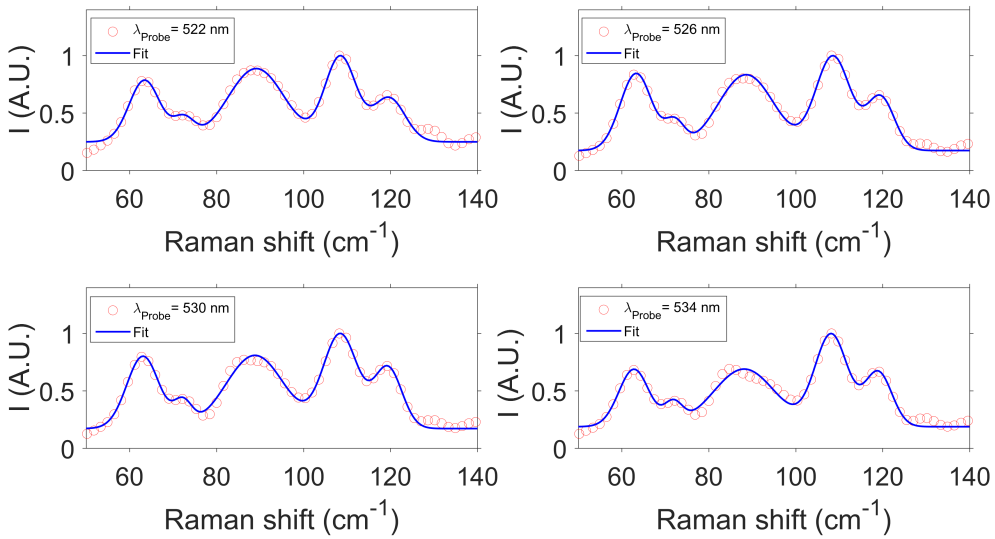

Figure 5.10: Slices of the resonant ISRS map shown in the top panel of Fig. 5.9, obtained averaging over 4 nm regions around selected probe wavelengths. The spectral profiles are fitted with the sum of 5 Gaussian profiles (continuous lines) in order to extract the peaks positions of the measured Raman modes.

5.2.3 Discussion

To understand the different nature of the spectral features in the ISRS maps, it is necessary to elucidate the mechanism of coherent phonons generation in crystalline materials. In non-resonant conditions, coherent phonons are generated exclusively in the electronic ground state and, consequently, the obtained spectrum is analogous to the CW Raman. Differently, under resonant excitation, two mechanisms are possible depending on the relative shift of the ground and excited state potentials along the vibrational coordinate, which we refer to as impulsive and diplacive excitation coherent phonons processes (IECP and DECP) [174, 175] [2]. These mecha-

[2] In the solid state community, IECP is denoted as Impulsive Stimulated Raman Scattering (ISRS), while we used the latter acronyms in relation to the spectroscopic technique. Thus, we introduce the acronymus IECP to distinguish between the two.

nisms are sketched in Fig. 5.11. In IECP, the ground state vibrational modes that are coupled to the electronic transition experience selective resonance enhancement, via electron-phonon interaction. This is the case of the 164 cm^{-1} and 121 cm^{-1} modes which we observe in both resonant and off-resonant spectra. This coupling is confirmed also by temperature dependent photoluminescence spectroscopy [155] and via mid infrared spectroscopy [176]. Differently, we

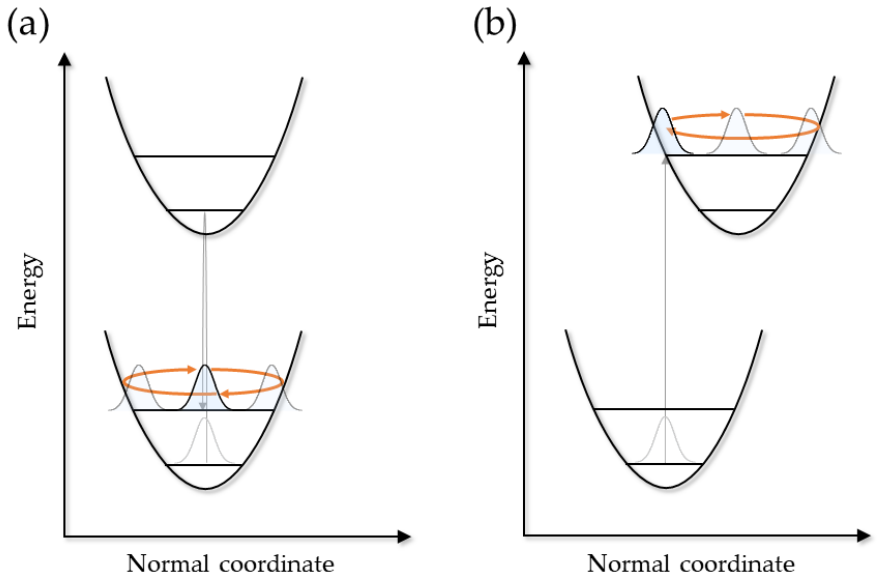

Figure 5.11: Representations of generation of ground and excited state coherences via ISRS. (a) In IECP, the resonant Raman pulse generates an oscillating coherence in the ground state. Immediately after photoexcitation, the vibrational wavepacket is peaked at the equilibrium position and then starts oscillating along the normal mode coordinate. (b) Excited state coherences can be created by DECP, provided that the ground and excited electronic potential are shifted along the corresponding normal mode. In DECP, the ground state wavepacket is projected by the Raman pulse onto the excited state, where it begins oscillating from a starting position far from the equilibrium.

assign the 89 cm^{-1} and 106 cm^{-1} modes to a DECP mechanism. In this case, the minimum of the potential energy surface of the excited state is shifted in the coordinate space with respect to that of the ground state. This leads to the generation of coherent phonons on the excited electronic state correlated to the photoexcitation. Specifically, the presence of photo-generated carriers leads to a re-adjustment of the crystalline lattice, which in turn modifies the phonon structure to include additional modes at frequencies distinct from those of the ground state vibrations.

Accordingly, the observed 89 cm^{-1} and 106 cm^{-1} are the modes driving the crystalline distortion through transient lattice oscillations. The new configuration is reached along the specific coordinate after a quarter of the period of the corresponding phonon, equal to 80 fs and 95 fs, respectively. Since electronic band states as well as Wannier excitons would not show an associated pattern of displaced atomic equilibrium positions, our results provide evidence for the polaronic nature of charges in this class of systems. Interestingly, the time interval taken by the new lattice geometry to equilibrate is comparable to the decay of the dispersive feature in the TA spectra of 5.7, suggesting that the presence of ionic displacements could potentially screen any Coulomb correlations. Recently, further evidences of DECP mechanism in $MAPbBr_3$ have been pubblished, reporting DECP frequencies of 92 cm^{-1} probed via time-resolved optical Kerr effect [141] and 92 and 340 cm^{-1} [177] using ISRS.

In order to corroborate the DECP assignment, we studied the dependence of the modes on the phases of the coherent oscillation and the Raman pulse fluence. Indeed, the phase analysis

gives information on the generation process underlying the features in ISRS maps. When the impulsive Raman excitation generates a coherence in the ground state, as it happens in both non-resonant condition and IECP process, the vibrational wavepacket starts oscillating from the energy minimum of the potential (Fig. 5.11a). On the contrary, the coherent oscillation induced by a DECP process on the excited state originates from a Franck-Condon projection of the initial ground state wavepacket onto an out-of-equilibrium position of the new lattice geometry (Fig. 5.11b). Consequently, the relative phases between the oscillations probed in non-resonant conditions result to be approximately null, while there is a non-zero phase difference between IECP and DECP modes observed in the resonant measurements.

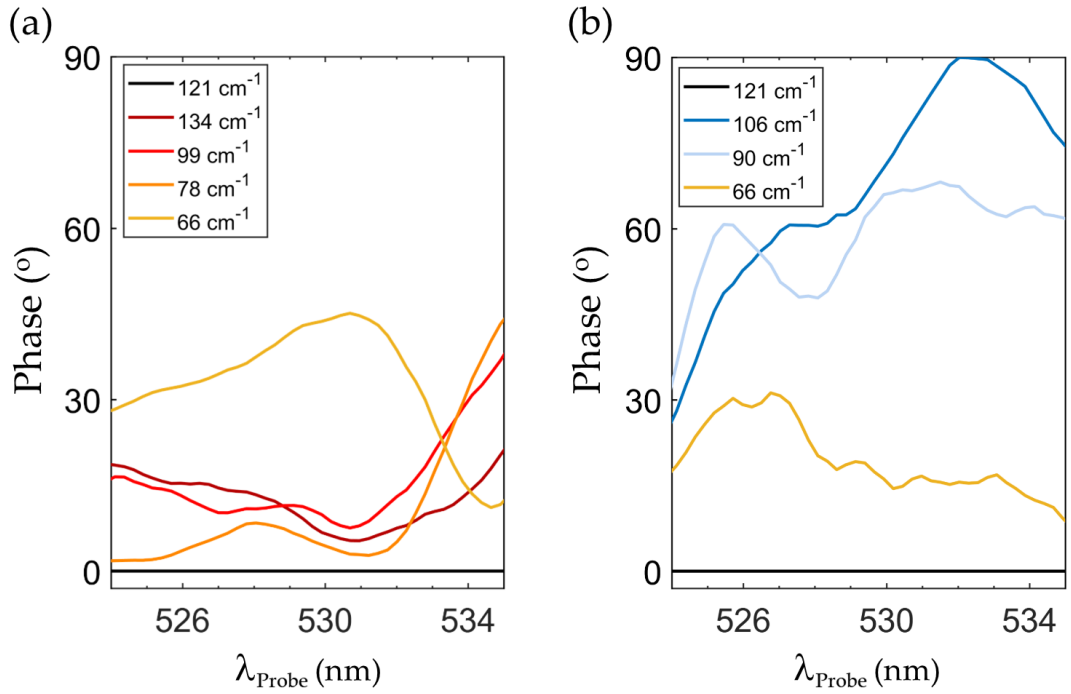

Figure 5.12: Phase analysis of the ISRS oscillations upon non-resonant (a) and resonant (b) photo-excitations. The phases have been retrieved from LPSVD reconstruction of time domain ISRS data before FFT. The phase differences with respect to the one of the mode at 121 cm^{-1} are reported for both ground state and DECP phonons.

Using as a starting point the observed frequencies of the modes reported in Fig. 5.9b, we reconstructed the phases of ISRS oscillations by decomposing the experimental wavelength dispersed time domain traces in the sum of damped oscillations, through a fitting algorithm with relative phases, amplitudes, peak positions and dephasing times as free parameters. The resulting relative phases with respect to the one of the 121 cm^{-1} mode are shown Fig. 5.12. In panel a, showing the off resonant data, the relative phases for all the modes are similar and contained in the same range of values despite a non trivial dependence on the probed wavelength, which is in line with the results presented in Chapter 4. With the same analysis for the resonant data, presented in panel b, we obtained phase factor between the 89 and 106 cm^{-1} and the 64 and 121 cm^{-1} modes, exceeding 60° for some values of the probed wavelength, indicating that the former are generated by DECP. Additionally, in Fig. 5.13, we compare two measurements performed with Raman energy of 0.3 nJ and 1.33 nJ, normalized to the intensity of the 121 cm^{-1} band. Notably, while the two IECP modes at 64 and 121 cm^{-1} scale similarly, the features 89 and 106 cm^{-1} modes do not follow the same scaling, further testifying their different nature.

On the line of the formalism presented at the beginning of this chapter, we calculated the Fröhlich coupling constant α using the weighted sum of the DECP frequencies to compute ω_{LO}

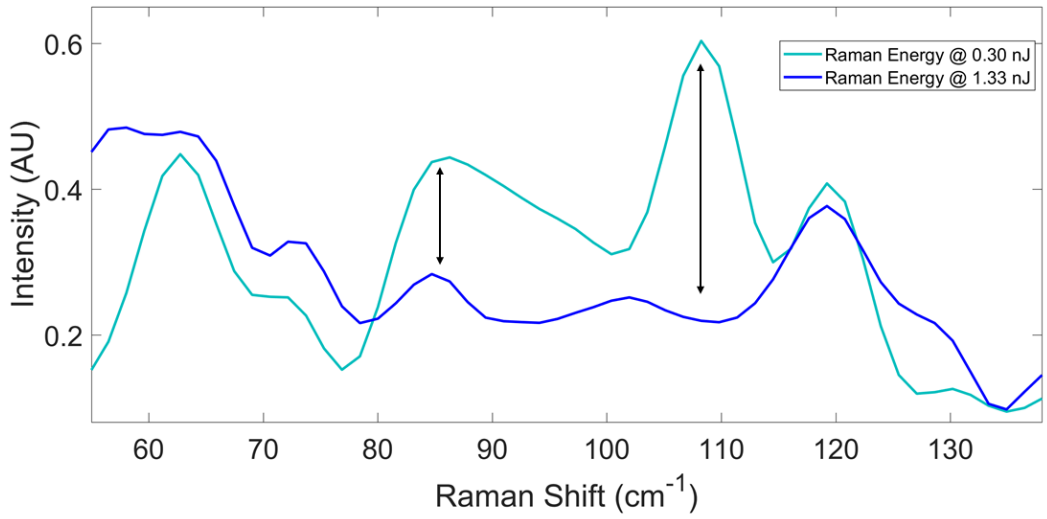

Figure 5.13: Dependence of ISRS spectra on the Raman pulse power, upon resonant excitation. The spectra have been obtained averaging over the detected probe wavelengths and normalized to the intensity of the ground state mode intensities at 64 and 121 cm^{-1} . The vertical arrows highlight the different scaling of the DECP phonons at 89 and 106 cm^{-1} as the excitation energy is changed, pointing to their different nature.

in eq. 5.5. The weighted sum ω_{eff} has been calculated through the relation

$$\omega_{eff} = \sqrt{\sum_i A_i^2 / \sum_i \frac{A_i^2}{\omega_i^2}} \tag{5.9}$$

being A_i the measured spectral amplitudes of the DECP modes. We note that, having considered time traces only from 250 fs onwards in the data analysis reduces the confidence interval in the DECP mode relative amplitudes but this reflects weakly on the estimation of α, introducing a total uncertainty of only the 3%. Using the values $\varepsilon_0 = 25$ and $\varepsilon_\infty = 6.7$ reported in literature for the static and high frequency dielectric constants in this material [178], we found $\alpha_e = 1.84$ and $\alpha_h = 1.28$, for electron and hole, respectively. We note that these values are in agreement with those obtained for other hybrid perovskites by previous studies [155], based on first-principles calculations and PL measurements.

Critically, these results allowed us to estimate also the polaron binding energy E_b, by means of eq. 5.8. We obtained $E_b = 46$ meV, corresponding to $\frac{E_b}{k_B} \sim 538K$, significantly above the thermal energy k_BT at room temperature. This suggests a possible rationale for the extended carrier lifetime. Indeed, for the carriers to relax back into the ground state, an energy barrier equal to E_b, should be crossed. This would allow the system to restore the original lattice geometry and relax back to the ground state. Notably, this value agrees well with the activation energy of the supposed dark state needed to explain temperature dependence of the carrier lifetime in $MAPBI_3$ in [150], as anticipated in section 5.1.2.

As already discussed, although the derivation of eq. 5.8 is strictly valid in the zero temperature limit, finite temperature effects lead to an increase of this estimate. Therefore, the value obtained for E_b has to be considered as a lower estimate for the polaron binding energy [157]. However, this would not change the argument on the blocking of recombination by polaron formation, as a higher binding energy would result in a even more strong bound to be overcome for the carrier to recombine. Interestingly, PL studies on a similar perovskite, $MAPbI_3$, show that the bimolecular recombination rate in the cubic phase decreases with decreasing temperature [179], which would be at ease with the absence of enough energy to allow band to band recombination. Our observations may indicate a suggestive hyphotesis for explaining the long

carrier lifetimes in hybrid perovskites, but further investigations are needed in order to link the presence of polaronic effects in $MAPbBr_3$ and other perovskites to momentum forbidden recombination.

Finally, we remark that our estimates of both α and E_b are based on electron-phonon interactions within a Frohlich-like mechanism, whilst the observation of lattice reorganization upon photo-excitation may be suggestive of the presence of additional strong coupling contributions. We calculated two-point nondiagonal Padé approximants $E_i(n, n-1)$ introduced by Selyugin *et al.*, using the first n terms of the weak ($i = w$) and strong ($i = s$) coupling limit [163]. In particular, $E_s(3,2)$ and $E_w(2,1)$ give lower and upper bounds for the actual polaron ground state energy[3]. In our case, we obtained $E_s(3,2) = 541$ K and $E_w(2,1) = 538$ K, validating the accuracy of the provided estimate.

5.3 Conclusions

In this chapter, we presented the application of ultrafast spectroscopy to address the electron-phonon coupling in hybrid organic-inorganic lead halide perovskites on the ultrafast time scale. After presenting a brief review of the exceptionally fast growing field of hybrid perovskites, we focused on the nature and recombination of photogenerated carriers, two of the main and more discussed characteristics that contributes to make these materials so promising for optoelectronic applications.

By contrasting the response obtained upon resonant and non-resonant Raman coherent excitation, we isolated the phonons that are coupled to the above-gap electronic transition. In addition to selected ground state modes which are resonantly enhanced, we revealed excited state phonons, absent in the ground state spectrum. These are the key modes generated via displacive excitation mechanism, which provide the pathway to the photo-induced lattice modification occurring upon carrier generation. Associating a pattern of displaced atomic equilibrium positions to the presence of the charge carrier, our results provide evidence for the polaronic nature of photo-excitation in this class of systems.

In particular, for $MAPbBr_3$ in the range 50-200 cm^{-1} we found two DECP phonons, at 90 and 106 cm^{-1}. Their frequencies allows to calculate the parameter of the polaron within the Fröhlich framework. In particular, the calculated polaron binding energy, significantly above the thermal fluctuations, offers a rationale for the long carrier lifetimes. In order for the carrier to recombine, the system would need to spend and additional amount of energy to dissociate the polaron and re-configure the lattice, which makes such a transition less favorable. The experimental ultrafast dynamics we presented here can offer experimental benchmarks in order to further develop polaron models in these materials.

[3]In the strong coupling limit, we considered $n = 3$ for the Padé approximant as the first and third order perturbative coefficients vanish.

6 Vibronic couplings during ultrafast chemical reactions probed by 2D Impulsive Stimulated Raman Spectroscopy

The properties of molecules undergoing physical or chemical reactions are determined by the shape of electronically excited potential energy surfaces over which the dynamics occurs. Aiming at studying ultrafast reactions requires the mapping of these electronic surfaces over multiple vibrational dimensions, typically hampered by the need of high resolution spectroscopic probes of two degrees of freedom, the electrons and the vibrations, that evolve with largely different energy and temporal scales. In this chapter, we introduce a three color 2D Impulsive Stimulated Raman Spectroscopy (2D ISRS) scheme which takes advantage of resonant pulses to selectively probe mode couplings between different active sites in molecular compounds, combining the capabilities of Fourier transformed multidimensional techniques with the structural sensitivity of Raman spectroscopy. In this technique, vibrational wavepackets are coherently generated and manipulated on electronically excited states, by means of three temporally delayed femtosecond pulses. After introducing the technique, we present a theoretical framework based on the density matrix perturbative approach to model resonant 2D ISRS on a multi-level molecular harmonic system in the presence of mode mixing in the excited states, namely the Duschinsky effect. We assign the origin of out-of-diagonal peaks in the 2D maps, connecting the evolution of the wavepackets between the pulses to the properties of the vibrationally structured potential energy surfaces of the system. Then, we benchmark the method addressing the experimental measurements on wild type Green Fluorescent Protein [180, 181], in order to probe vibronic couplings in this prototypical dye during the first steps of its photoinduced dynamics. We report the collected 2D ISRS data over the full vibrational fingerprint spectral region, and rationalize our experimental results by means of the harmonic treatment of the molecular Hamiltonian, showing that this simple model is able to isolate the specific origin of the different couplings. We show how, by wisely designing the experimental conditions, it is furthermore possible to observe dark/weak modes as coupling peaks, displacements among energy potential surfaces with their signs and signatures of harmonic mode mixing in the excited states beyond the linearly displaced approximation.

6.1 Multidimensional spectroscopies of vibronic interactions

Many of the mechanisms underlying biochemical and physical reactions reside on the interplay between different vibrational and electronic degrees of freedom [182–184]. Ultrafast spectroscopy aims at studying these properties by means of ad hoc sequences of laser pulses to photoexcite and subsequently probe the induced modifications over the relevant timescales, ranging in the ps and fs domain. Different pulse schemes and strategies have been developed over the years to access these temporal realms, using various combinations of wavelengths and durations. However, the vibronic properties are still challenging to track especially on the electronically excited states. Besides lacking sufficient temporal resolution, linear vibrational tech-

niques, such as IR and spontaneous Raman spectroscopy, cannot induce vibrational coherences on the excited states. On the other hand, visible and UV pulses are needed to exploit resonance enhancement and access the excited states in biological systems, but UV-visible absorption spectroscopy usually lacks the required structural sensitivity and, as a consequence, vibronic signatures are overwhelmed by multiple overlapping contributions. Nonlinear multidimensional techniques can cope with such demanding constraints and disentangle congested spectra, at the price of spreading spectral information over different dimensions [46, 185]. Infrared and UV/visible 2D spectroscopies have been demonstrated to be powerful and complimentary tools to gain quantitative information on ground state vibrational correlation and electronic couplings, respectively, tackling conformation and structural changes, system-bath fluctuations and energy transfer in biological systems [48, 186–189]. 2D electronic spectroscopy, for instance, is able to achieve femtosecond temporal resolution and show signature of electronic couplings but the structural information is hidden inside the lineshape. For these reasons, novel nonlinear and multidimensional schemes have been proposed in which IR and visible pulses are combined to excite electronic and vibrational resonances during different time intervals [49, 190–193] and recently, a new experimental paradigm has been realized to probe fourth-order correlations by means of the combination of resonant and non resonant pulses [54, 194].
Within such context, multidimensional coherent Raman spectroscopy has been advanced as an ideal candidate to directly address vibronic correlations in time and frequency domains [99, 195–197]. Raman scattering benefits from the ability of probing the full vibrational manifold of interest. Additionally, with respect to IR, it allows for resonance enhancements of specific chromophore signatures and opens the possibility to comprehensively investigate vibrational energy flow through a molecule during reactive transformations without the need to rely only on a few selected marker bands. This makes multidimensional Raman particularly attractive for the study of light-induced processes, such as vibrational energy redistribution following Franck-Condon (FC) photo-excitation as well as shining light on non-adiabatic crossing mechanisms with unprecedented structural clarity [198].
In particular, ISRS provides several advantages with respect to frequency domain Raman techniques for the detection of mode correlations [39, 120, 168, 199], especially for low frequency vibrations, being free from elastic scattering and background noise. Its two dimensional extension, 2D ISRS, has been initially theoretically proposed [42] and realized in both non resonant [200, 201] and resonant [202–204] versions to study ground state intramolecular vibrational anharmonicities, nonlinear corrections to the molecular polarizability, product-reactant correlations and solvation dynamics, up to the recent realization of single pulse 2D spectroscopy by means of appropriately shaped light [53].
Critically, electronic resonances can be applied to the study of the excited state of a molecule undergoing an ultrafast reaction. To this aim, we introduced a doubly resonant scheme for 2D ISRS and deciphered the nonlinear response by developing a method to read out the properties of vibronic coupling and enabling the mapping of multidimensional Potential Energy Surfaces (PES) from the intensities and positions of diagonal and out-of-diagonal peaks in the 2D spectra. Wisely tuning the optical wavelengths to match static and transient electronic resonances allows to isolate contributions from excited state PES. The resonant conditions have two main consequences, beside enhancing the Raman cross section. Firstly, vibrational coherences can be stimulated selectively in a specific excited electronic state, depending on the probed spectral region. Secondly, the harmonic fifth order response, vanishing in the off resonant regime, is accessible when pulses are tuned resonant with the electronic transitions.

6.2 Concepts of resonant 2D Impulsive Stimulated Raman Spectroscopy

The 2D ISRS pulses scheme is presented in Figure 6.1 (panel a) along with a sketch illustrating the working principle of the technique (panel b). A frequency tunable Actinic pump pulse $\mathcal{E}_a$ resonant with the ground state absorption S_0-S_1 promotes the system to an excited electronic

state S_1, in which vibrational coherences are generated owing to the large pulse bandwidth. After a time delay T_1, a Raman pulse $\mathcal{E}_p$, resonant with the excited state absorption S_1-S_n, induces additional vibrational coherences. Finally, after a delay T_2, a spectrally resolved WLC probe pulse records the temporal evolution of the vibrational coherences in the form of transient absorption spectra. Accordingly, the signal depends on both the tunable delays, T_1 and T_2, and on the dispersed probe wavelength. The induced nonlinear polarization oscillates during T_1 and T_2, with the frequencies of the photo-activated Raman modes, modulating the transmitted broadband probe pulse. As a result, Raman features, obtained by a 2D Fourier transform along T_1 and T_2, are associated with the correlations between different modes, which give rise to cross and combination peaks.

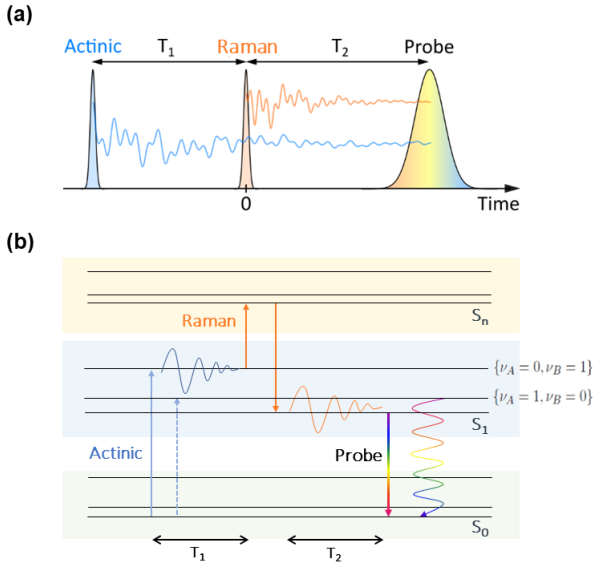

Figure 6.1: Concepts of 2D ISRS: (a) Pulse sequence used for the experiment and (b) Energy ladder scheme illustrating an example of signal generation. The Actinic pump pulse (blue) promotes the system to an excited electronic state S_1, in which vibrational coherences are impulsively generated and oscillate with the characteristic parameters of vibrations A and B. After a tunable delay T_1, the Raman pulse (orange), resonant with S_n, impulsively stimulates a different coherence, only associated with mode A. Lastly, after T_2, the interaction between the two vibrational coherences is recorded by the Probe pulse.

Tuning the resonance conditions of each pulse with different excited state transitions and averaging over different spectral regions of the probe increases the signal to noise ratio and critically selects the potential energy surface on which the vibrational coherences are created. In particular, averaging probe wavelengths over the stimulated emission isolates the vibronic response pertaining to the S_1 state.
For each probe wavelength, the 2D Raman maps were generated by extracting the oscillatory part along T_2 for every recorded time point along T_1, giving the signal $S(T_1, T_2)$, which is subsequently 2D-fast Fourier transformed to yield the 2D ISRS map $S(\Omega_1, \Omega_2)$. As a consequence of two dimensional Fourier transformation, 2D ISRS spectra depend on both positive and negative frequencies, as opposed to the one dimensional equivalent in which they carry the same information. Specifically, the 2D Fourier transform of a real time-domain signal is symmetric with respect to the inversion of the I-III and II-IV spectral quadrants, associated with signal components having the same and the opposite signs along the two frequency axes, respectively. Therefore, we folded the maps as shown in Fig. 6.2.
Notably, since the Raman pulse must necessarily interact with a molecule previously excited by the Actinic pulse in order to contribute to the 2D ISRS signal, this technique is free from lower

order background involving cascades between two different molecules that generally hinder fifth order spectroscopies [205–208]. Thus, in our realization, 2D ISRS probes genuine fifth order effects.

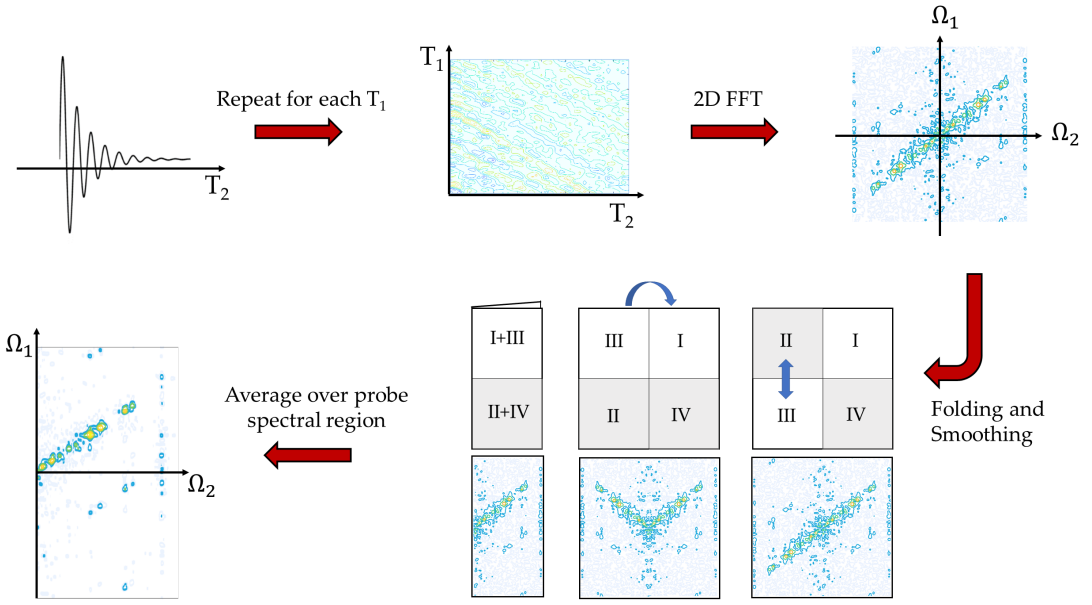

Figure 6.2: 2D maps generation routine: $S(T_1, T_2)$ is obtained removing the exponential dynamics along T_2 to isolate the oscillating component and repeating for each T_1. Then the time-time map is Fourier transformed by means of a 2D FFT algorithm and the obtained frequency-frequency maps $S(\Omega_1, \Omega_2)$ are folded and smoothed with a two dimensional filter to further suppress the residual baseline and increase signal-to-noise ratio. Finally, after repeating this routine for each recorded dispersed wavelength, the $S(\Omega_1, \Omega_2)$ signal is averaged over the selected probe spectral region,

6.2.1 Derivation of the signal

The interpretation of 2D ISRS spectra is hampered by the fact that similar spectral features may arise from different and concurring physical processes. Thus, the rich variety of structural information contained in these measurements can only be extracted by a careful modelling. To achieve this, we derived the 2D ISRS signal using the perturbative density matrix framework presented in Chapter 2. Since the 2D ISRS process requires that each of the three pulses induces a Raman transition in the sample, two interactions with each pulse are needed. Thus, 2D ISRS signals originate from the fifth-order terms of the nonlinear polarization $P^{(n)}$. We considered, as a reference model, the three electronic level system with a ground and two excited electronic states, S_0, S_1 and S_n, depicted in Fig. 6.1b, with the associated vibrational manifolds. In the semiclassical theory, 2D ISRS processes are described by the Hamiltonian

$$H = H_0 + H' \tag{6.1}$$

where H_0 is the free molecule and H' is the interaction term. In the dipole approximation, H' is the Power-Zienau radiation-matter interaction Hamiltonian

$$H'(t) = V \cdot \mathcal{E}^*(t) + c.c. \tag{6.2}$$

where V is the dipole operator and $\mathcal{E}$ the positive frequency component of the total field

$$E(\mathbf{r}, t) = \sum_j \mathcal{E}_j(t - T_j) e^{i\mathbf{k_j}\cdot\mathbf{r}} + c.c. \tag{6.3}$$

The summation runs over the spectral modes of the field which consists in the three delayed pulses described above: the Actinic pump $\mathcal{E}_a$ resonant with the ground state absorption S_0-S_1, the Raman pulse $\mathcal{E}_p$, resonant with the excited state absorption S_1-S_n and a the broadband continuum probe $\mathcal{E}_s$, resonant with the excited state emission from S_1. The probing protocols consists in the spectrally resolved detection of the broadband $\mathcal{E}_s$. We considered well separated pulses, with delays T_1, between the $\mathcal{E}_a$ and $\mathcal{E}_p$, and T_2, between $\mathcal{E}_p$ and $\mathcal{E}_s$, greater than the pulses temporal envelopes.
In the frequency dispersed heterodyne detection, the signal is given by the interferometric transmission of the field $\mathcal{E}_s$, which acts as a local oscillator:

$$S(\omega,T_1,T_2)=\Im\ \mathcal{E}_s^*(\omega)P(\omega,T_1,T_2)=\Im\,\mathcal{E}_s^*(\omega)\int_{-\infty}^{+\infty}dt\,e^{i\omega t}\mathrm{Tr}\left[Ve^{-\frac{i}{\hbar}\int_{-\infty}^{t}dt'H'_-(t',T_1,T_2)}\rho(-\infty)\right] \tag{6.4}$$

$P(t)=\langle V(t)\rangle=\mathrm{Tr}[V\rho(t)]$ represents the nonlinear polarization induced by the interactions and the Liouville superoperator $H'_-=[H',\cdot\,]$ acts on the equilibrium density matrix $\rho(-\infty)$ in the interaction picture, as detailed in Chapter 2. The 2D ISRS signal is obtained expanding the exponential in eq. 6.4 to the fifth order in field matter interaction and the expression depends on the delays T_1 and T_2 and on the dispersed frequency ω.
The total polarization in 6.4 is calculated by means of diagrammatic techniques. The pulse scheme and the detection geometry reduce the number of relevant Feynman diagrams needed to describe the signal to the eight shown in Fig. 6.3, since other processes are suppressed by the resonance conditions. For diagrams *i-iv* we obtain

$$\begin{aligned}S^{(5)}(\omega,T_1,T_2)=\Im\ \left(-\frac{i}{\hbar}\right)^5\int_{-\infty}^{\infty}dte^{i\omega t}\mathcal{E}_s^*(\omega)\int_{-\infty}^{t}\int_{-\infty}^{t_5}\int_{-\infty}^{t_4}\int_{-\infty}^{t_3}\int_{-\infty}^{t_2}dt_5\dots dt_1\\ \mathcal{E}_a(t_1)\mathcal{E}_a^*(t_2)\mathcal{E}_p(t_3-T_1)\mathcal{E}_p^*(t_4-T_1)\mathcal{E}_s(t_5-T_2-T_1)\,\mathcal{F}(t,t_1,t_2,t_3,t_4,t_5)\end{aligned} \tag{6.5}$$

The matter correlation function $\mathcal{F}$ is obtained from the Feynman paths:

$$\mathcal{F}=[F_i+F_{ii}+F_{iii}+F_{iv}] \tag{6.6}$$

where

$$F_i=\left\langle VG(t-t_5)V^\dagger G(t_5-t_4)VG(t_4-t_3)V^\dagger G(t_3-t_2)VG(t_2-t_1)V^\dagger\right\rangle \tag{6.7a}$$

$$F_{ii}=\left\langle VG(t-t_5)V^\dagger G(t_5-t_4)V^\dagger G(t_4-t_3)VG(t_3-t_2)VG(t_2-t_1)V^\dagger\right\rangle \tag{6.7b}$$

$$F_{iii}=\left\langle VG(t-t_5)V^\dagger G(t_5-t_4)VG(t_4-t_3)V^\dagger G(t_3-t_2)V^\dagger G(t_2-t_1)V\right\rangle \tag{6.7c}$$

$$F_{iv}=\left\langle VG(t-t_5)V^\dagger G(t_5-t_4)V^\dagger G(t_4-t_3)VG(t_3-t_2)V^\dagger G(t_2-t_1)V\right\rangle \tag{6.7d}$$

G is the retarded Green function in the time domain

$$G(t'-t'')=\theta(t'-t'')e^{-iH_0(t'-t'')} \tag{6.8}$$

Similarly, signal expressions for diagrams $v-viii$ can be obtained. In this case, since the last interaction is an absorption of $\mathcal{E}_s$, the heterodyne detected signal is

$$S^{(5)}(\omega,T_1,T_2)=-\Im\ \mathcal{E}_s(\omega)P^{(5)}(-\omega,T_1,T_2)=-\Im\ \int e^{-i\omega t}\mathcal{E}_s(\omega)P^{(5)}(t,T_1,T_2) \tag{6.9}$$

and the related correlation functions read:

$$F_v=\left\langle V^\dagger G(t-t_5)VG(t_5-t_4)VG(t_4-t_3)V^\dagger G(t_3-t_2)VG(t_2-t_1)V^\dagger\right\rangle \tag{6.10a}$$

$$F_{vi}=\left\langle V^\dagger G(t-t_5)VG(t_5-t_4)V^\dagger G(t_4-t_3)VG(t_3-t_2)VG(t_2-t_1)V^\dagger\right\rangle \tag{6.10b}$$

$$F_{vii}=\left\langle V^\dagger G(t-t_5)VG(t_5-t_4)VG(t_4-t_3)V^\dagger G(t_3-t_2)V^\dagger G(t_2-t_1)V\right\rangle \tag{6.10c}$$

$$F_{viii}=\left\langle V^\dagger G(t-t_5)VG(t_5-t_4)V^\dagger G(t_4-t_3)VG(t_3-t_2)V^\dagger G(t_2-t_1)V\right\rangle \tag{6.10d}$$

The brakets in the expressions 6.7 and 6.10 can be solved expanding the signal as a sum over states (SoS) corresponding to the eigenfunctions of H_0. Since the pulses are well separated, it is possible to extend the integration over t_2 and t_4 to $+\infty$, obtaining two delta functions that are used to break up the multiple integration. Then, the total signal can be expressed as

$$S^{(5)}(\omega, T_1, T_2) = S^{(5)}_{odd}(\omega, T_1, T_2) + S^{(5)}_{even}(\omega, T_1, T_2) \tag{6.11}$$

where in $S^{(5)}_{odd}$ and $S^{(5)}_{even}$ we gathered the contributions from even and odd numbered diagrams of Fig. 6.3

$$S^{(5)}_{odd}(\omega, T_1, T_2) = \Im \sum_{\substack{g,g',f \\ e,e',e''}} K(g) \left[\frac{\mu_{g'e''}\mu^*_{g'e'}\,\mathcal{E}^*_s(\omega)\,\mathcal{E}_s(\omega - \omega_{e''e'})}{2(\omega - \tilde{\omega}_{e''g'})} - \frac{\mu_{g'e''}\mu^*_{e'g'}\,\mathcal{E}_s(\omega)\,\mathcal{E}^*_s(\omega + \omega_{e''e'})}{2(\omega + \tilde{\omega}_{g'e'})} \right]$$
$$\mu_{e''f}\mu^*_{fe}\mathcal{W}_p(\omega_{e''e}, \tilde{\omega}_{e''e'} - \tilde{\omega}_{fe'})\mu_{e'g}\mu^*_{eg}\,\left[\mathcal{W}_a(\omega_{ee'}, \tilde{\omega}_{ee'} - \tilde{\omega}_{eg}) - \mathcal{W}_a(\omega_{ee'}, \tilde{\omega}_{ge'})\right] e^{-i\,\tilde{\omega}_{ee'}T_1 - i\,\tilde{\omega}_{e''e'}T_2} \tag{6.12}$$

$$S^{(5)}_{even}(\omega, T_1, T_2) = \Im \sum_{\substack{g,g',f \\ e,e',e''}} K(g) \left[\frac{\mu_{g'e}\mu^*_{g'e''}\,\mathcal{E}^*_s(\omega)\,\mathcal{E}_s(\omega - \omega_{ee''})}{2(\omega - \tilde{\omega}_{eg'})} - \frac{\mu^*_{e''g'}\mu_{g'e}\,\mathcal{E}_s(\omega)\,\mathcal{E}^*_s(\omega + \omega_{ee''})}{2(\omega + \tilde{\omega}_{g'e''})} \right]$$
$$\mu_{fe'}\mu^*_{e''f}\,\mathcal{W}_p(\omega_{e'e''}, \tilde{\omega}_{ef} - \tilde{\omega}_{ee'})\,\mu_{e'g}\mu^*_{eg}\,\left[\mathcal{W}_a(\omega_{ee'}, \tilde{\omega}_{ee'} - \tilde{\omega}_{eg}) - \mathcal{W}_a(\omega_{ee'}, \tilde{\omega}_{ge'})\right] e^{-i\,\tilde{\omega}_{ee'}T_1 - i\,\tilde{\omega}_{ee''}T_2} \tag{6.13}$$

where $\tilde{\omega}_{ij} = \omega_i - \omega_j - i\Gamma_{ij}$ and μ_{ij} is the matrix element of the dipole operator V. The weighted pulse spectral densities $\mathcal{W}_k$ for $k = a, p$ are defined as

$$\mathcal{W}_k(\omega_1, \tilde{\omega}_2) = \int d\omega' \frac{\mathcal{E}_k(\omega' + \omega_1)\,\mathcal{E}^*_k(\omega')}{2(\omega' + \tilde{\omega}_2)} \tag{6.14}$$

and rule the resonant bandwidth accessible by the finite widths of the Actinic and Raman pulse. The subscripts e, e', e'' run over the vibrational levels of S_1, while f and g, g' over those of S_n and S_0, respectively. At room temperature, modes above a few hundreds cm^{-1} are initially populated only in the vibrational ground state, i.e. g in eq. 6.12 and 6.13 is fixed. In general, the initial thermal population is ruled by the Boltzmann factor $K(g)$ that depends on temperature. We note that due to the symmetries of the diagrams only four of the eight terms need to be calculated. Indeed, diagrams in the pairs *i-viii*, *ii-vii*, *iii-vi* and *iv-v* can be obtained one from the other changing the side and reversing the arrows of the first four interactions, giving opposite and conjugates responses. Since the heterodyne detection is sensitive to the imaginary part, expressions in eq. 6.12 and 6.13 are equivalent. However, combining the diagrams in this way has the advantage that the integral in the weighted pulse spectral density of $\mathcal{E}_p$ needs to be evaluated only once: $\mathcal{W}_p(\omega_{e''e}, \tilde{\omega}_{e''e'} - \tilde{\omega}_{fe'})$ or $\mathcal{W}_p(\omega_{e'e''}, \tilde{\omega}_{ef} - \tilde{\omega}_{ee'})$ for odd and even numbered diagrams, respectively.
Finally, a Fourier transformation over the two delays and the integration on ω lead to the 2D frequency correlation map:

$$S^{(5)}(\Omega_1, \Omega_2) = \int_{-\infty}^{+\infty} d\omega \int_{-\infty}^{+\infty} dT_1 dT_2 e^{i\Omega_1 T_1 + i\Omega_2 T_2} S^{(5)}(\omega, T_1, T_2) \tag{6.15}$$

We note that, for a given combination of the dummy SoS indexes in eq. 6.12, each diagram contributes to the signal via a product of two weighted pulse spectral densities, ruled by the spectral widths of the Actinic and Raman pulse, a function of ω, related to the transition induced by the probe pulse and a complex exponential function of the delays T_1 and T_2 that selects the position of the associated peak in the 2D spectrum.
Using a WLC probe, the effective domain of integration over ω in eq. 6.15 is restricted by the bandwidth of the pulse $\mathcal{E}_s(\omega)$. In our experimental implementation, the measurement is spectrally resolved in ω, a selective average over specific spectral region can be exploited to isolate

the resonant contributions from the stimulated emission or the excited state absorption of the system.
In the SoS picture, the signal is determined by contributions of different pathways in the Liouville space, corresponding to the different permutation of the SoS indexes. In this way, the contribution of selected modes to the signal can be easily isolated, additionally giving the advantage to speed up the calculations by removing the contributions to unobserved region of the spectrum. In particular, in the simulations, we did not include the contributions to the signal laying on one of the two axes, originating from pathways in which populations instead of coherences evolve during T_1 or T_2, since they provide the same information of third order techniques and are suppressed by the experimental analysis routine.

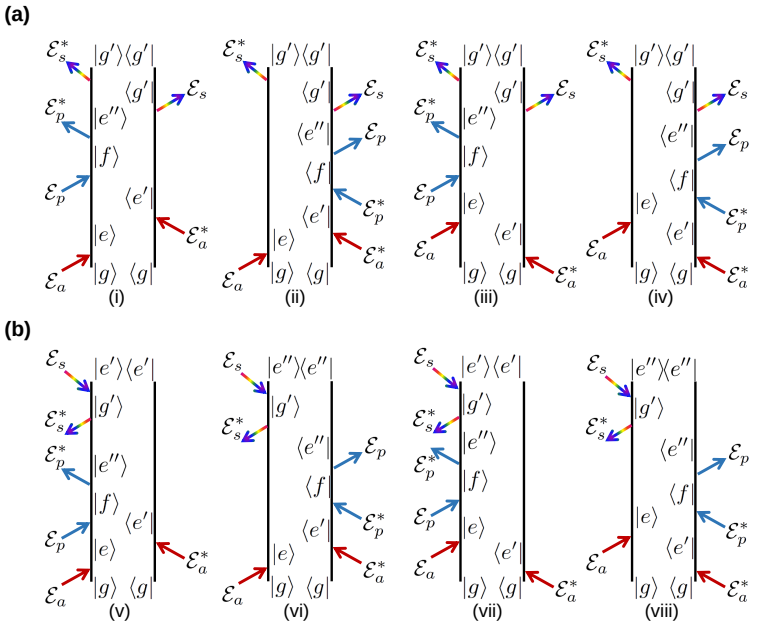

Figure 6.3: Double sided Feynman diagrams contributing to the 2D ISRS signal averaged in the SE region of the probe pulse.

6.2.2 The harmonic model of the molecular Hamiltonian

In the derivation presented in the previous section, the 2D ISRS signal depends parametrically on the frequencies ω_i and lifetimes γ_i of the modes and the dipole matrix elements μ_{ij}, in a way determined by the choice of the molecular Hamiltonian H_0. As H_0 is selected, these quantities can be computed fitting the experimental observations within the chosen model.
Here, we assume the harmonic oscillator (HO) approximation for H_0, in which the vibrational manifold associated to each electronic state can be depicted as a n-dimensional parabola, being n the number of normal modes of the sample. H_0 is then given by a collection of harmonic oscillators (HO):

$$H_0 = \sum_{j=0}^{2} = H_{S_j}^{HO} \quad \text{with} \quad H_{S_j}^{HO} = \sum_{\nu_j} \frac{\dot{Q}_{\nu_j}^2}{2} + \frac{\omega_{\nu_j}(Q_{\nu_j} - Q_{0\nu_j})^2}{2} \tag{6.16}$$

where ν_j runs over the vibrational manifold of S_j and Q_{ν_j} and $Q_{0\nu_j}$ are the corresponding mass-weighted normal coordinate and equilibrium position, i.e. $Q = \sqrt{M}\tilde{Q}$, being $\tilde{Q}$ the non-weighted coordinate. It is worth stressing that deviations from the harmonic regime manifest themselves mainly in off-resonance conditions, when the harmonic contribution vanishes, allowing to pinpoint the otherwise smaller contribution of single and multimode anharmonicities and

polarizability nonlinearities [200]. Conversely, under resonant conditions, the harmonic response is dominant. Nevertheless, single and multimode anharmonicities can be simply included in the molecular Hamiltonian H_0 perturbatively.
Within the Born-Oppenheimer approximation, the dipole matrix element relative to the vibronic transition $\{S, \nu\} \rightarrow \{S', \nu'\}$ reads

$$\boldsymbol{\mu}_{S\nu;S'\,\nu'} = \langle \nu'(\mathbf{Q}')|\, \boldsymbol{\mu}_{S';S}(\mathbf{Q})\, |\nu(\mathbf{Q})\rangle \tag{6.17}$$

where S,ν, Q are the initial electronic state, vibrational eigenfunction and normal mode coordinate involved in the transition, the primed symbols refer to the corresponding values in the final state, and $\mu_{S';S}$ is the electronic transition dipole. Since an analytical expression for $\mu_{S';S}(Q)$ is generally not available, the electronic dipole is usually expanded in Taylor series of Q_i around the initial state equilibrium geometry, described by the coordinates Q_{0i}

$$\boldsymbol{\mu}_{S';S}(\boldsymbol{Q}) = \boldsymbol{\mu}_{S';S}(\boldsymbol{Q}_0) + \sum_i \frac{\partial \boldsymbol{\mu}_{S';S}}{\partial Q_i}(Q_i - Q_{0i}) + \mathcal{O}(\boldsymbol{Q}^2) \tag{6.18}$$

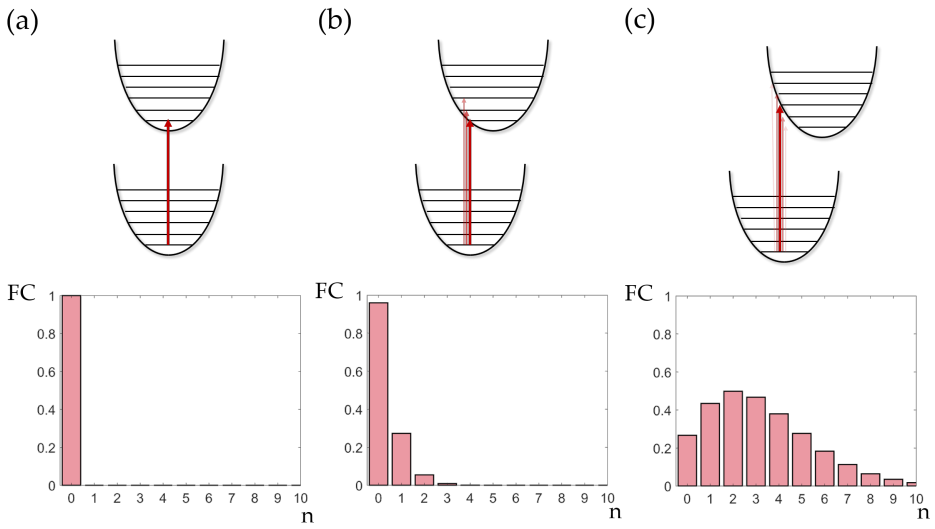

Figure 6.4: Franck-Condon progression in the harmonic model for different values of the PES displacement. (a) For non-displaced potentials, the only FC component different from zero is relative to the $0 \rightarrow 0$ transition. (b) For a small displacement, $0 \rightarrow 0$ remains the stronger component of the progression but weak transitions to the closest overtones are also possible. (c) Further increasing the displacement, transitions to higher overtones become dominant and the center of the FC distribution shifts.

In the Condon approximation, only the constant 0^{th} order term is retained, obtaining $\mu_{S';S}(Q) \approx \mu_{S';S}(Q_0)$ [62]. Since this term does not depend on the vibrational state, it is the same for all the pathways in (6.13)-(6.12) and can be simply included as a common multiplying factor. The linear term is the Herzberg-Teller correction [209], which accounts for different electronic levels mixing and intensity borrowing. Considering resonance transitions, the Condon term is usually dominating while it is vanishing off the resonance. Near the resonance conditions, both the term could contribute to the Raman cross section with a relative weight depending on the system. Since we are considering resonant transitions, we will work under the Condon approximation. Consequently, the relative intensities of different features in the 2D ISRS spectra are ruled by the overlap of ground and excited state vibrational wavefunctions: $\mu_{\nu',\nu} = \langle \nu'(Q')|\nu(Q)\rangle$. Generally, either the overlap integral or its squared value is denoted as the Franck-Condon (FC) factors and we will follow the first convention. The extension to higher

order transition integrals can be easily included in the model including in the calculation the general expression for $\boldsymbol{\mu}_{S';S}$. Analytic expression for both the FC and Herzberg-Teller terms in the HO are derived in the appendix on page 103.

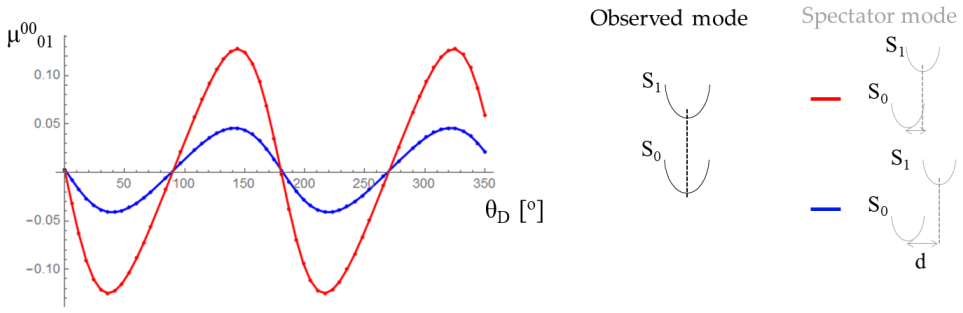

Figure 6.5: Coupling between a non-displaced mode at 730 cm^{-1} and a displaced spectator at 250 cm^{-1} : when $\theta_D \neq 0$, mode mixing switches on the FC inactive mode. The effect become higher as the displacement of the spectator increases, as shown by the red and blue lines corresponding to the two scenarios sketched on the right. The FC factor is indicated by the notation $\mu^{ab}_{\alpha\beta}$, in which a,b refer to the quantum numbers of the two modes in the initial state and α,β are the corresponding values in the final state.

The simple picture presented so far is complicated in real case scenarios by mode mixing. Because of the many modes that typically populate a vibration manifold, the resulting wavefunction lives in a multidimensional landscape and the normal modes of the ground and excited states are not in general identical. Consequently, calculating FC factors requires a multidimensional integration, which takes into account the rotation of the coordinate system in the excited state, namely the Duschinsky effect, and the changes in the vibrational frequencies [210–213]. The Duschinsky effect arises when two electronic states possess different equilibrium geometries for which the corresponding normal modes are nonparallel. This case can be treated by means of the transformation

$$\boldsymbol{Q'} = J\boldsymbol{Q} + \boldsymbol{D} \tag{6.19}$$

where the primed variables are those of the excited states, J is the orthogonal Duschinsky matrix and $\boldsymbol{D}$ is the vector of displacements. Thus, in general, the HO overlap integrals read

$$\langle \nu | \nu' \rangle = \int_{-\infty}^{\infty} d\boldsymbol{Q}\, d\boldsymbol{Q'}\ \psi_\nu(\boldsymbol{Q}) \psi_{\nu'}(\boldsymbol{Q'}) \tag{6.20}$$

being ψ_ν the HO eigenfunction relative to the mode ν

$$\psi_\nu(\boldsymbol{Q}) = \prod_i \left(\frac{\sqrt{\frac{\omega_i}{\hbar}} 2^{\nu_i}}{\nu_i! \sqrt{\pi}}\right)^{\frac{1}{2}} H_{\nu_i}\left(\sqrt{\frac{\omega_i}{\hbar}}\, Q_i\right) e^{-\frac{1}{2}\frac{\omega_i}{\hbar} Q_i^2} \tag{6.21}$$

Considering pair of modes, the changes in the normal coordinate system upon accessing the resonant state can be summarized as a displacement d, a distortion and a rotation by the Duschinsky angle θ_D between the associated two-dimensional PES of the initial and final electronic states, reflecting different equilibrium position, force constants and vibrational mixing in the molecule, respectively. If J is the identity operator, the total wavefunction is the product of uncorrelated single mode linearly displaced harmonic oscillators (LDHO), whose excited state PES are displaced along the normal mode coordinate with respect to the ground state potential. The FC factors in the linearly LDHO are simply calculated by the overlap of the single mode wavefunctions:

$$\langle \nu | \nu' \rangle = \prod_{i,j} \langle \nu_i | \nu'_j \rangle \tag{6.22}$$

The effect of each displacement d_i along the mode ω_i is to enhance or suppress a given component of the FC progression relative of that mode, gradually shifting the maximum from the $0 \rightarrow 0$ transition to higher overtones, as depicted by the sketch in Fig. 6.4.

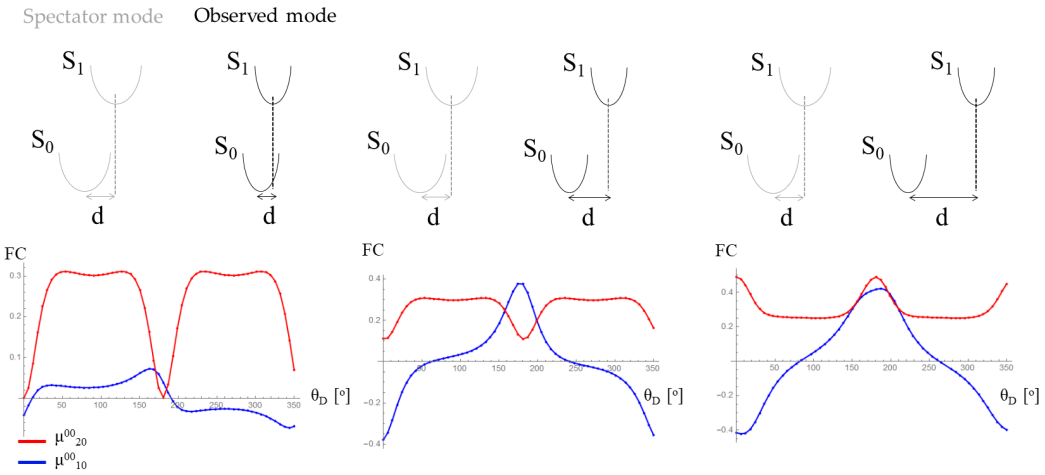

Figure 6.6: The effect the coupling of a low frequency spectator to a 1147 cm^{-1} mode: the dependence of the fundamental (blue line) and overtone (red line) transitions of the 1147 cm^{-1} mode on the Duschinsky angle θ_D between the two modes brings to the inversion of the sign and to zeroes in the corresponding FC factors. The three bottom panels represent three different values of the observed mode displacement, keeping the spectator displacement constant, as sketched by the parabola in the top panels.

If $J \neq \mathbb{I}$ the FC integrals are not separable since normal coordinates mix in the excited state. The effect of the Duschinsky rotation has been detected in linear spectroscopies, in particular resonance Raman and hyper-Raman [214, 215], but since the information collapses on the unique available dimension, the obtained parameters are highly correlated.
In 2D ISRS, mode mixing affects the relative intensity between off diagonal peaks, enabling FC transitions even if the relative displacement is zero. Thus, even if along some direction Q_j the excited state is not displaced, the transition $0 \rightarrow n$ with $n \neq 0$ can be strong, if the mode is coupled to a displaced one. This is illustrated in Fig. 6.5, in which we report the FC factor $0 \rightarrow 1$ for a non-displaced mode at 730 cm^{-1} coupled to a spectator FC active mode at 250 cm^{-1} not involved in the transition. In absence of mode mixing ($\theta_D = 0^{\circ}$) the FC factors vanish independently of the displacement of the spectator mode, as expected. On the contrary, as θ_D is changed, the FC activity of the 730 cm^{-1} mode is switched on by the Duschinsky effect and the value of the overlap integral starts oscillating. The amplitude of the oscillations depends on the displacement of the spectator mode.
In a similar way, the FC activity of a displaced mode can decrease due to the coupling to other modes. To show this, we consider a 1147 cm^{-1} coupled to a displaced low frequency spectator mode at 80 cm^{-1} , changing the displacement of the observed mode. The FC factors relative to the fundamental $0 \rightarrow 1$ and overtone $0 \rightarrow 2$ transitions of the observed 1147 cm^{-1} mode as a function of its displacement are reported by the blue and red lines in Fig. 6.6. In the left panel, at $\theta_D = 0^{\circ}$, due to the small displacement of the observed mode, only the fundamental transition is active. As θ_D increases, the fundamental FC factor decreases in magnitude, while the one relative to the overtone increases, resulting in a structured dependence of the FC factors on the angle θ_D. This includes the changes of the FC factors signs and, consequently, values of θ_D for which they vanish. In general, the position of the zeroes depends on the displacements of both the observed and spectator modes, as sketched by the central and right panels, and, loosely, on their frequencies. We stress that in absence of mixing, the magnitude of the FC factors of the fundamental and overtone transitions are comparable unless the displacement is enough small

to suppress the overtone. The opposite situation, in which the overtone is dominating and the fundamental is negligible, is only possible in presence of mode mixing.

6.3 Assigning the origin of the 2D ISRS peaks in the harmonic model

To understand how the structural information is carried by 2D ISRS maps, we first consider a Linearly Displaced Harmonic Oscillator (LDHO) model with two vibrational modes ω_l and ω_h organized in three electronic manifolds. Then we introduce mode mixing in the same model and analyze how the 2D ISRS maps are modified by the nonlinear vibronic interaction.

6.3.1 Linearly Displaced Harmonic model

Within a three electronic states system, two displacements per vibrational mode are needed to determine the 2D spectra. Considering two vibrations, with frequencies ω_l and ω_h, the signal depends on four parameters, i.e. the displacements between the electronic surfaces along each vibrational cut, $d_1^{h,l}$ and $d_2^{h,l}$. It follows from the expressions of the FC integrals what is the role of each parameter: $d_1^i \neq 0$ enables the FC activity of the mode i that can be consequently excited by the Actinic pulse and probed by the WLC as a diagonal peak in the map; in order to observe combination peaks both d_1 and d_2 of the involved modes have to be different from zero.

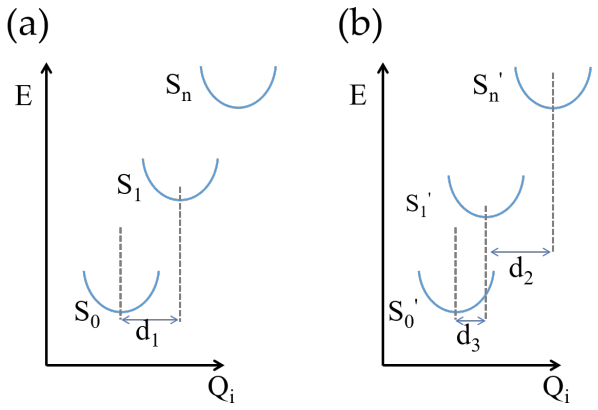

Figure 6.7: Different energy landscapes probed by the Actinic pulse (panel a) and the Raman and Probe pair (panel b). In the dynamic LDHO, even if three electronic energy potentials are involved, three different displacements among them have to be considered, since d_1 can be different from d_3, due to the relaxation of the molecule out of the FC region.

In real systems, excited state dynamics often modifies this simple scenario, even in the case of the LDHO model. For example, in case of dynamic shifts of the vibrational frequencies, due to the coupling to a thermal bath, peaks are asymmetrically broadened with respect to the diagonal [124, 202]. Here we consider a different situation in which the dynamics is exhausted within the finite duration of the femtosecond pulses. In this case, the displacement probed by the Actinic pulse is different to that probed by the Raman and probe pair as shown by Fig. 6.7 and three displacements per mode are required to appropriately describe the 2D ISRS spectra. Consequently, 2D ISRS is sensitive to a dynamics which is too fast to be resolved as a shift in the Raman peaks and does not modify the frequencies of the modes but only the dipoles. Specifically, a common situation is that upon photoexcitation by the Actinic pulse, the minimum of the harmonic potential of the excited state S_1 is shifted from the initial value corresponding to S_1^{FC} to a new value corresponding to a potential S_1', and we refer to this scenario as dynamic LDHO. This model corresponds also to the situation in which four electronic states are considered.

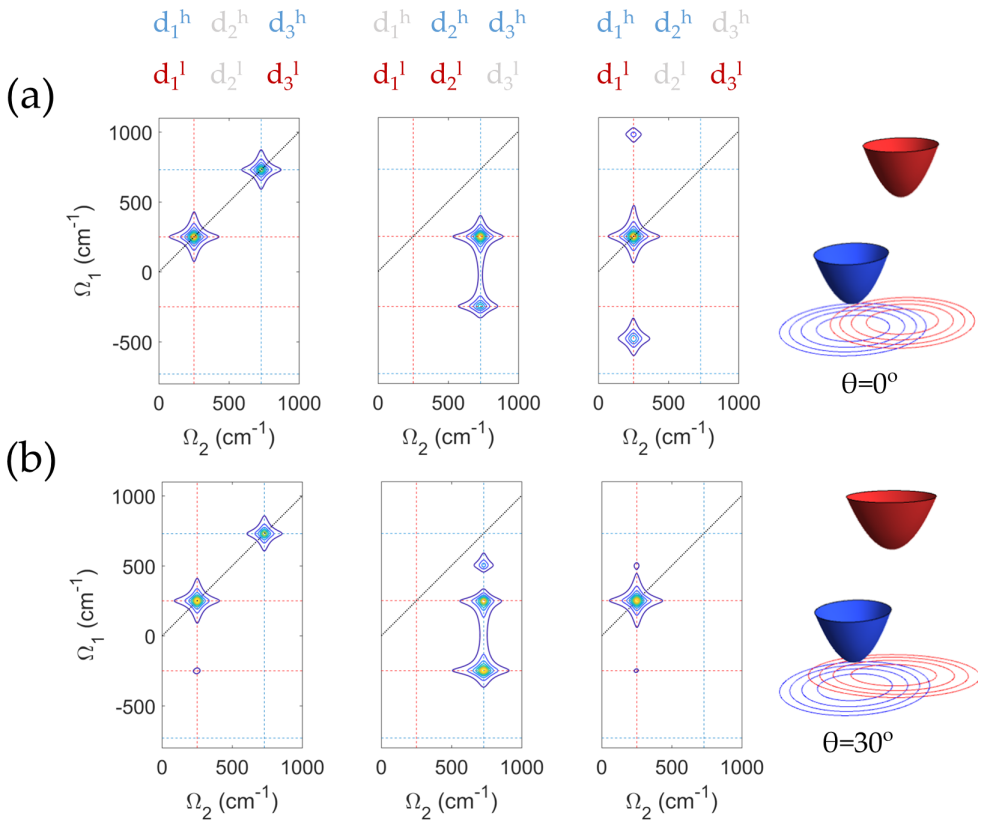

Figure 6.8: 2D ISRS response of the harmonic model for a two modes system $\omega_h = 730$ cm^{-1} and $\omega_l = 250$ cm^{-1} . (a) Simulation for the LDHO considering three different choices of the displacement set, in which two of the six parameters are set to zero: left panel shows diagonal peaks obtained for d_2^h, $d_2^l = 0$ and the other parameters different from zero; the central panel shows two cross peaks at $\Omega_1 = \pm\omega_l$, $\Omega_2 = \omega_h$ obtained by switching off d_1^h and d_3^l; in the right panel, the only vanishing displacements are d_2^l and d_3^h, which lead to a diagonal peak at ω_l and two combination bands at $\Omega_1 = \omega_h \pm \omega_l$ and $\Omega_2 = \omega_h$. Red (blue) horizontal and vertical lines highlight the ω_l (ω_h) frequency. The values of the non-zero displacements are all set to 0.05 amu$^{\frac{1}{2}}$ Å for d_2 and 0.01 amu$^{\frac{1}{2}}$ Å for d_1 and d_3. (b) Simulation in presence of mode mixing: the same model considered in (a) has been extended including a Duschinsky rotation of $\theta_D = 30°$ between S_1 and $S1'$. In the right panel, the ground (blue) and excited state (red) PES in the parallel and rotated cases simulated in (a) and (b) are sketched. The displacements are summarized on the top of the figure: red (blue) ds represent non-zero displacements along the low (high) frequency mode. Grey ds indicate non-displaced coordinates.

Notably, at odd with the simple picture holding for the static two mode LDHO described above, off diagonal peaks are possible even if d_1 or d_3 are vanishing for one of the modes. This is shown in Fig. 6.8a, in which we present the simulated 2D ISRS signal of the dynamic LDHO depending on three displacements for the three typical contributions that may appear in the 2D maps: diagonal peaks at (ω_i, ω_i), cross peaks at ($\pm\omega_i$, $\pm\omega_j$) and combination peaks at ($\omega_i \pm \omega_j$, ω_i). The choices of the displacements are specified in the caption and summarized by the color scheme on the top of the figure: displacements different from zero along the high and low frequency coordinate are highlighted by blue and red ds, respectively. The dominant

Liouville pathways contributing to these peculiar features are:

$$|00\rangle\langle 00| \rightarrow |01\rangle\langle 00| \rightarrow |01\rangle\langle 00| \rightarrow |00\rangle\langle 00| \tag{6.23a}$$
$$|00\rangle\langle 00| \rightarrow |11\rangle\langle 00| \rightarrow |01\rangle\langle 00| \rightarrow |00\rangle\langle 00| \tag{6.23b}$$
$$|00\rangle\langle 00| \rightarrow |01\rangle\langle 01| \rightarrow |01\rangle\langle 00| \rightarrow |00\rangle\langle 00| \tag{6.23c}$$
$$|00\rangle\langle 00| \rightarrow |01\rangle\langle 00| \rightarrow |10\rangle\langle 00| \rightarrow |00\rangle\langle 00| \tag{6.23d}$$

where $|h\,l\rangle\langle l\,h|$ represents the state of the density matrix with the corresponding occupational number for modes ω_l and ω_h and each arrow is the interaction with a field. These pathways offer an overview of the origin of the peaks in 2D ISRS maps: eq. 6.23a corresponds to a diagonal peak at ω_l, eq. 6.23b-c to combination peaks at the sum and difference frequencies along the y axis ($\Omega_1 = \omega_l \pm \omega_h$, $\Omega_2 = \omega_l$), and eq. 6.23d to a cross peak with $\Omega_1 = \omega_l$ and $\Omega_2 = \omega_h$.

6.3.2 Mode Mixing

Building on the 2D ISRS signal of eq. 6.12 and the simulations, we can summarize the effect of the three displacements in the dynamic LDHO as follows. The condition d_1^i, $d_3^i \neq 0$ is necessary for a diagonal peak at ω_i. A cross peak between ω_l and ω_h indicates that the displacement d_2 is non-vanishing and comparable for the two modes. A combination peak at $(\omega_i \pm \omega_j, \omega_i)$ implies not vanishing and comparable d_1 or d_3 for the two modes, if the combination frequency is along Ω_1 or Ω_2, respectively, and $d_2^j \neq 0$. Mode mixing complicates this scenario, correlating the FC activity along different vibrational modes because the corresponding excited and ground state normal modes are not orthogonal. In Fig. 6.8b we report the effect of mode mixing. We simulated the 2D ISRS maps for the same values of the displacements used in the panel a, additionally imposing a rotation of $\theta_D = 30^\circ$ between the normal modes of S_1^{FC} and $S_1^{'}$.

As can be seen from the simulations, diagonal peaks are loosely affected by the mode mixing. On the contrary, the Duschinsky effect causes the appearance of a new combination band in the central panel, without affecting the intensity of the cross peaks, while leads to the cancellation of the combination bands in the right panel. Additionally, the effect of the overtone of the ω_l mode is visible as a new weak feature at ($\Omega_1 = -500$, $\Omega_2 = 500$), in line with the mechanism described in Fig. 6.6.

In general, all these processes contribute to the total signal, with weights depending on the relative magnitude and signs of the displacements. Since the signal emission requires that the final state of the density matrix is diagonal, we stress that an off diagonal peak requires at least one two-photon process, in which two quantum numbers in the density matrix are changed by the same pulse. For the off diagonal peaks analyzed above, this process is mediated by the Raman, Actinic and the probe pulses, respectively. Even if in general more than two vibrational modes exist in real molecular system, correlation between multiple modes are negligible in the limit of small displacements because they imply multiple two-photon processes. Thus, the scheme we built for the two modes LDHO can be applied to multimode systems, considering all the possible pairs of modes.

Finally, we note that since resonant 2D ISRS explores three different electronic surfaces, it is sensitive to the sign of displacements, a key advantage over lower order one dimensional techniques. Indeed, if only two electronic states are probed (for instance S_0 and S_1), the Raman signal is totally symmetric with respect to an excited state S_1 displaced by the same amount to the right or to the left of S_0. This happens because, even if transitions with an odd difference of quantum numbers in the initial and final states scales linearly with the displacement, the FC factor is squared since two transitions between the same states are required to go back to a diagonal state of the density matrix. Probing an additional excited state breaks this symmetry. Even if the same line of reasoning applies when all the displacements are to the right or all to the left, a different sign of S_0-S_1 and S_1-S_n will change the spectrum. With linear and also third order techniques, resonances between two electronic states are usually probed, while resonant

2D ISRS is conceived specifically to probe three excited PES at the same time.

6.4 Excited-State Two-Dimensional Raman Spectroscopy on Green Fluorescent Protein

In this section, we report the resonant 2D ISRS spectra of wild type Green fluorescent protein (GFP) measured during the early stages of its photodynamics. GFP is a prototypical dye molecule widely used in the bioimaging community as a gene expression and protein target in living cells and organisms. GFP was first extracted [216] from the bioluminescent jellyfish *Aequorea Victoria* in 1962 and then expressed in other organisms [217] and genetically modified covering many color variants [180, 218]. This opened to the possibility to look inside a cell in vivo for the first time, motivating the 2008 Nobel prize to Osamu Shimomura, Martin Chalfie and Roger Tsien. Since then, green fluorescent proteins have been used in an extremely broad range of applications from superesolution microscopy [219] to the recently proposed usage as a source for polarization-entangled photon states [220]. The photochemical characteristics of GFP arise largely from the protein environment, which inhibits deactivation pathways dominating in the isolated chromophore, namely p-hydroxybenzylideneimidazolinone (HBDI). In particular, it provides the specific H-bonding channel that is functional for an Excited State Proton Transfer (ESPT) reaction, which leads to the bright luminescence from the deprotonated state of GFP instead of the radiationless decay of HDMI. [221]. Under physiological conditions, the GFP chromophore exists predominantly in a neutral, protonated A_0 form, shown by the grey structure in Fig. 6.9. Photoexcitation at $\approx$ 397 nm promotes the GFP chromophore to the first excited state, A* (blue structure in the figure), which subsequently undergoes the ESPT of the phenolic proton from chromophore's Tyr 66 to Glu 222, across an hydrogen bonding network. Within picoseconds, this reaction yields the highly fluorescent, deprotonated I* form, corresponding to the green structure, which decays radiatively in nanoseconds. Finally, re-protonation occurs on a time scale that vary from hundreds of picoseconds in water to nanoseconds in D_2O, due to the high kinetic isotope effect [222].

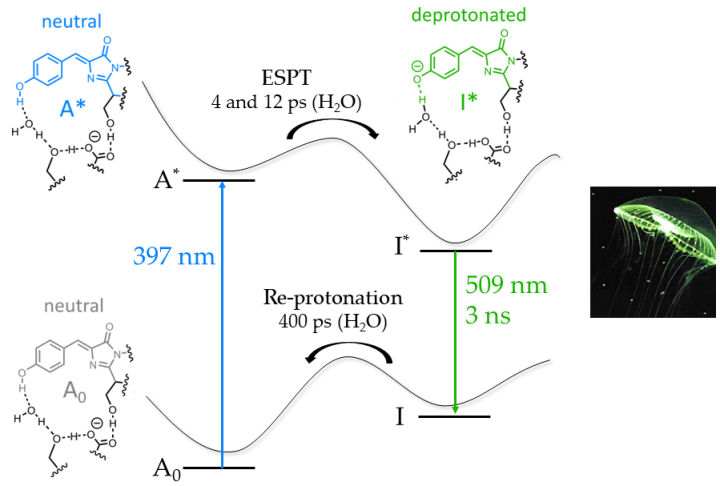

Figure 6.9: Photodynamics of wild type Green Fluorescent Protein. Photoexcitation of the neutral chromophore at 400 nm prepares A* which decays with biexponential rates of 4 and 12 ps to the fluorescently active deprotonated I* . On the left, a photo of *Aquorea Victoria* jellyfish from which the GFP has been isolated [223].

Lately, spectroscopic investigations reported hints of mode mixing and non-Condon effects in fluorescent protein and GFP in particular, suggested by the energy shift between the one and

two photon absorption profiles [224, 225]. Clearly, the effects of mode mixing and higher order couplings, as the Herzberg-Teller, are difficult to isolate in one dimensional spectroscopies in which all the contributions are overlapped on the same dimension. From another point of view, recent femtosecond stimulated Raman measurements on GFP in both frequency and time domain focused on the role of low frequency vibrational motion on the excited state during the ESPT reaction. Fang et al. measured the FSRS spectra of GFP in water and observed a low-frequency (125 cm^{-1}) modulation of the C-O (phenol) and C=N (imidazole) stretching vibrations during ESPT, assigned to an out-of-plane skeletal mode crucially promoting the reaction [226]. In a more recent study [99], the same low-frequency coupling (104 cm^{-1}) was tracked in time domain with the phenol C-H stretching vibration but, interestingly, marker bands at the early time production of I* form did not show similar modulation, suggesting that the low frequency mode does not impact the reaction. While the two studies disagree on the importance of this coupling for the ESPT, both attribute the observation of oscillatory modulation of the excited state Raman spectrum to anharmonic vibrational coupling. Conversely, related studies on other molecules suggest that anharmonic couplings are challenging to isolate in such experiments due to competitive lower order processes [207]. In addition, it is not always possible to extract unambiguous and quantitative parameters from data analysis because this depends from the anharmonic term included in the reference model.
These factors motivate the need for a clear interpretation of vibronic mode correlations in GFP. To this aim, we performed 2D ISRS on the wild-type GFP in water.

6.4.1 Experimental results

In Figure 6.10 we report the experimental characterization of wt-GFP. The ESPT proceeds with a large Stokes shift (5440 cm^{-1}) and the corresponding transient absorption spectrum after 1 ps from photoexcitation at 397 nm shows a stimulated emission band at 509 nm, corresponding to its well known fluorescent emission, as well as a broad photo-induced absorption band at higher wavelengths, centered at 720 nm, as shown by the traces in Fig. 6.10a and the transient absorption map in Fig. 6.11a.

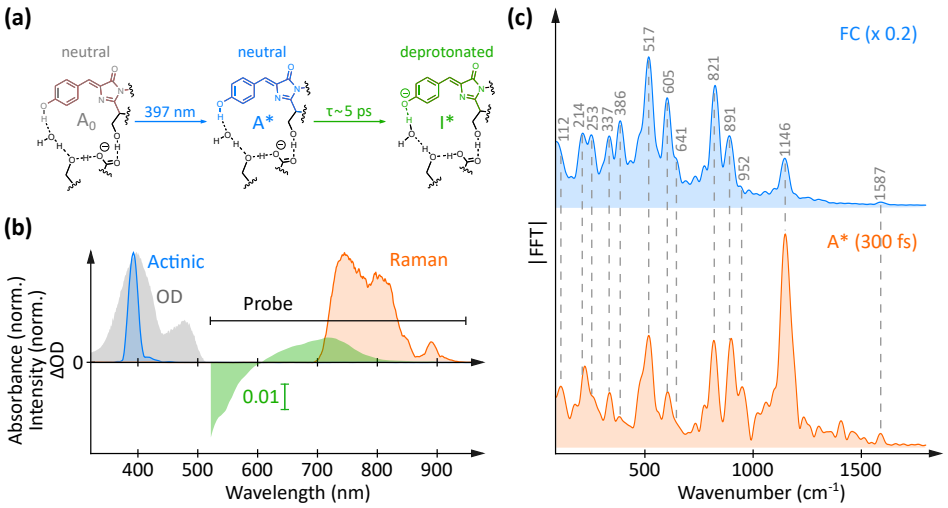

Figure 6.10: Experimental characterization of GFP. (a) Absorption spectrum (grey) and transient absorption spectrum at 1 ps (green) are shown with the employed Actinic and Raman pulse spectra (blue and orange). (b) FC (blue) and A* Fourier amplitude spectra (orange) binned in T_1 to 300 fs to average out any effect of oscillatory modulations. Spectra were averaged in the probed spectral region between 575 and 615 nm and coherent oscillations were Fourier transformed after 536 fs for 1 ps. Actinic pulse: 15 fs, 400 nm. Raman pulse: 9 fs, 800 nm.

We measured 1D and 2D ISRS of the wild-type GFP in water using a 15 fs Actinic and a 9

fs Raman pulse, whose spectral envelopes are shown in 6.10b and follow the resonant strategy previously described. Specifically, the three non-collinear ultrashort beams used for 2D ISRS have been synthesized from a common mode-locked laser source via two noncollinear optical parametric amplifiers (NOPAs): the first produces a 400 nm actinic pump, resonant with the ground-state absorption of the sample. The 800 nm output of the second NOPA was compressed and used as Raman pulse. A pulse energy of about 160 nJ was employed in order to keep two-photon absorption from the ground-state molecules below the 1%. The probe pulse has been synthesized via supercontinuum generation, focusing a portion of the fundamental into a sapphire plate. A triple-chopping scheme has been applied to remove lower order contributions to the signal. Measurements have been conducted by the Kukura's group in Oxford and additional details on the setup used for these measurements can be found in [40]. Critically, sampling delays of 1 ps on both dimensions, we focused on the faster relaxation that precedes ESPT, occurring on a longer timescale (≈6 ps). In Fig. 6.10b we report the preliminary one dimensional FC spectrum (blue area) obtained in absence of the Raman pulse together with the corresponding A* excited-state Raman spectrum (orange area) averaged over 300 fs along T_1. We observe that the position of Raman bands up to ≈ 1200 cm^{-1} are not altered by the FC relaxation on A*. This is in line with previous observations suggesting that the proton motion, leading to product formation, is not a dominant part in the GFP subpicosecond dynamics [226].

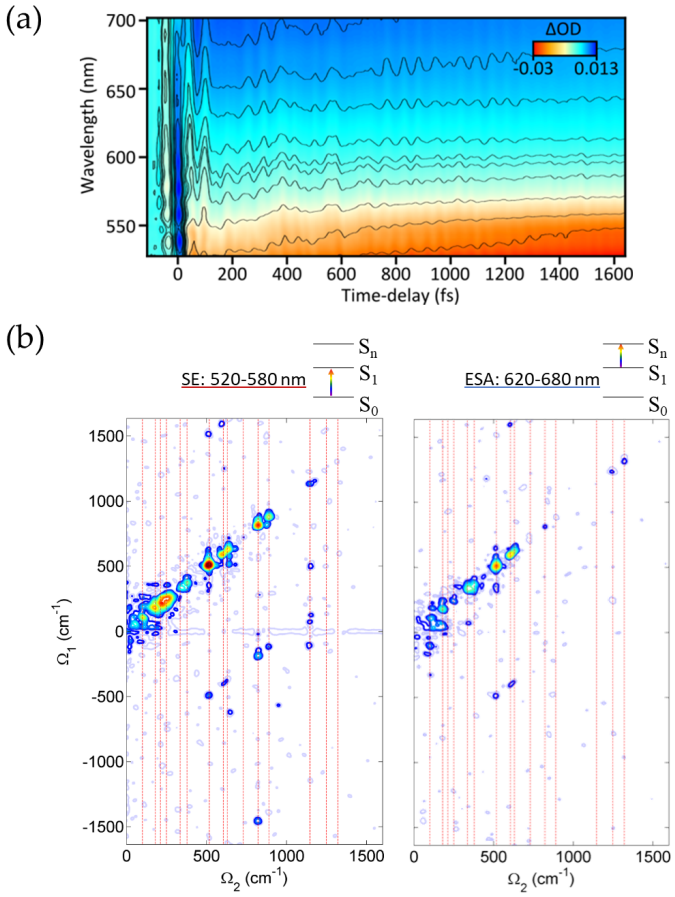

Figure 6.11: TA (a) and 2D ISRS (b) measurements on GFP in different resonance conditions of the probe pulse. The left and right panels in (b) have been obtained averaging the spectrally resolved maps over the SE (520-580 nm) and ESA (620-680 nm) region of the sample, respectively.

Resonant 2D ISRS maps averaged over the stimulated emission (SE) and excited state ab-

sorption (ESA) spectral region of the dispersed probe pulse are shown in Fig. 6.11b. As already emphasized, we focus on the SE averaged map, since it selectively reports on vibronic correlations laying on the A* (which we refer to as S_1 to be consistent with the previous section). In case of ESA resonances, additional diagrams have to be considered to account for vibrational coherences generated on the S_n excited state.

In particular, the highest signal to noise ration has been achieved for the probe region between 575 and 615 nm and the corresponding 2D ISRS spectrum, shown in Figure 6.12a, presents pronounced peaks along the diagonal (Fig. 6.12a, black line) that match frequencies obtained in the corresponding excited-state Raman spectrum. In addition, we find several prominent off-diagonal peaks that lie only along vertical lines (i.e. parallel to Ω_1, red dashed lines in Fig. 6.12), while horizontal connections appear to be missing. Off diagonal peaks are gathered mainly in three regions: a vertical stripe for Ω_2=1147 cm^{-1} , and two sub-diagonals for $\Omega_1 = \Omega_2 - 1010$ and $\Omega_1 = \Omega_2 - 2294$ cm^{-1} , highlighted in Fig. 6.12 by orange and blue arrows respectively. Weaker contribution are present also along $\Omega_1 \approx \Omega_2 - 2000$ cm^{-1} .

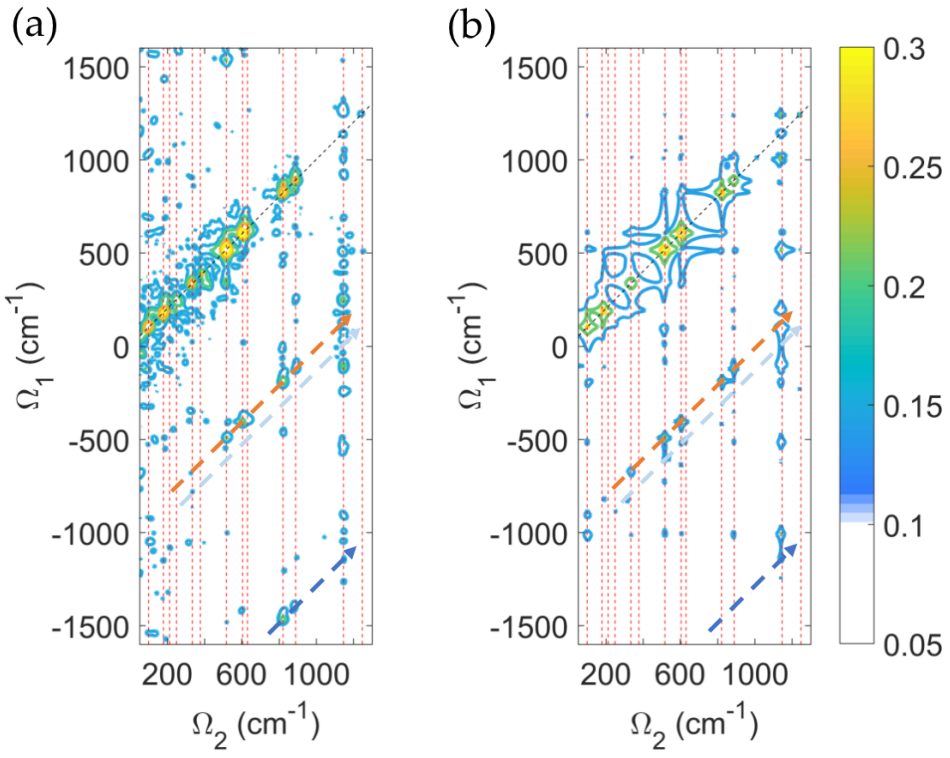

Figure 6.12: 2D ISRS characterization of the GFP excited state. (a) Experimental map and (b) fit result based on the linearly displaced harmonic model. Vertical lines correspond to the frequencies of the GFP excited state vibrations, extracted by fitting the principal diagonal. The blue and cyan arrows highlight combination bands involving the fundamental and overtone frequencies of the 1147 cm^{-1} mode, respectively. As it can be seen from the experimental map in (a), several couplings with the overtone are present, while there are no peaks on the cyan arrow. The orange arrow highlights combination bands involving the mode at 1010 cm^{-1}.

6.4.2 Discussion

We described the sub picosecond dynamics of the GFP through the dynamic shift of the S_1 potential induced by the Actinic pulse, at ease with the large Stokes shift in the absorption spectra, and fitted the experimental data with the dynamical LDHO model, which gave rise to the map in Fig. 6.12b.

In the light of the general results obtained for the HO model, we can now interpret the 2D ISRS measurements on GFP. The presence of vertical and diagonal correlations, rather than horizontal, points to the conclusion that combination rather than cross peaks are principally observed. The absence of cross peaks, in turn, indicates that most of the modes are displaced along d_1. On the other hand, this displacement is needed for the formation of combination bands. A mode at 1010 cm^{-1} shows high FC activity on the S_n state, testified by the two sub-diagonals at $\Omega_1 \approx \Omega_2 - 1010$ cm^{-1} and $\Omega_1 \approx \Omega_2 - 2020$ cm^{-1} , which correspond to a series of combination bands with other modes due to its large d_2. On the contrary, the absence of any features at 1010 cm^{-1} on the principal diagonal shows that $d_3 = 0$ for this mode, revealing directly the effect of the dynamics ($d_1 \neq d_3$). This testifies the capability of 2D ISRS to uncover dark or weak bands by boosting small FC displacements via another transition.

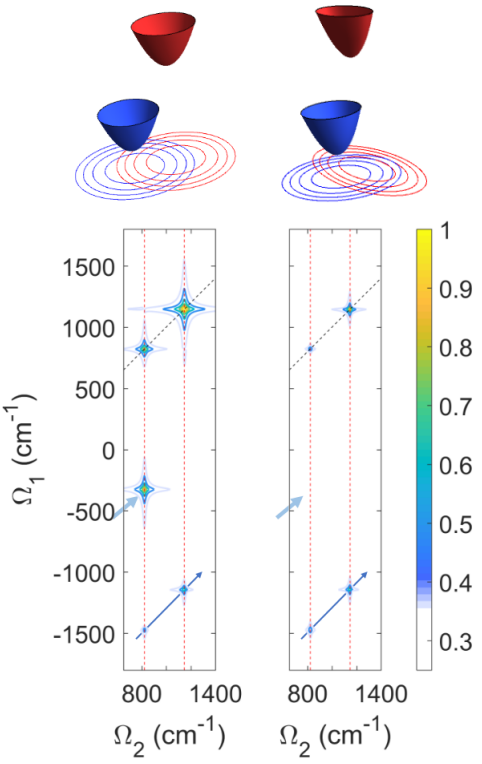

Figure 6.13: Effect of mode mixing in the 2D ISRS maps of an harmonic model. Simulation of the 2D ISRS signal of a two modes system with frequencies 822 and 1147 cm^{-1} coupled to a non-displaced low frequency mode at 80 cm^{-1} . If $\theta_D = 0^o$, the system behaves as a linearly displaced harmonic model and a displacement $d_2^{1147} \neq 0$ causes the progressive switching on of the combination bands involving this mode and its overtones (left panel). The cyan and blue arrows indicate the position of combination bands associated to 1147 cm^{-1} and $2 \cdot 1147$ cm^{-1}, respectively. In presence of a Duschinsky rotation θ_D=90^o between S_1 and S_n between the normal coordinates of the 1147 and 80 cm^{-1} modes, the combination band associated to the fundamental of the 1147 cm^{-1} is suppressed (right). The sketch in the top panel illustrates the projection onto the 822 and 1147 cm^{-1} modes of the corresponding potential energy surfaces in case of parallel normal modes (left) and rotated by the Duschinsky angle (right).

Additionally, we observed the coupling between the 1147 cm^{-1} O-H phenol mode and a low frequency mode at 120 cm^{-1} , which was the focus of debates we reported in the previous section related to the role of low frequency vibrational motion on the excited state during the ESPT reaction [99, 226] and was attributed to anharmonic vibrational coupling. Instead, here we show that a coupling between the 1147 cm^{-1} and 120 cm^{-1} mode can be also explained within

the harmonic model by the displacement of the excited state PES along these vibrational cuts, as testified by the agreement between the combination band in our 2D measurements and fit. Within this framework, any coupling peaks in GFP are not required to be functionally important for the ESPT reaction coordinate. Moreover, we remark that the intensity of this combination band is more intense above the diagonal than below, suggesting additional contributions due to a cross coupling between the 1147 cm^{-1} and the 1248 cm^{-1} mode.

We now discuss the interpretation of the other couplings of the O-H phenol mode at 1147 cm^{-1} showed by the 2D ISRS maps. According to the model discussed so far, the series of peaks along the vertical at Ω_2=1147 cm^{-1} indicates a large value of d_1 and d_3 for this mode, while the absence of a sub-diagonal at $\Omega_1 \approx \Omega_2 - 1147$ cm^{-1} points to a small value of d_2. Critically, the sub-diagonal $\Omega_1 = \Omega_2 - 2294$ cm^{-1} (highlighted by the blue arrow in Fig. 6.12) is not captured by the model. Indeed, within the LDHO, these feaures would indicate a strong d_2 displacement for the 1147 cm^{-1}, able to make both its fundamental and the overtone FC active on the S_n state. However, this is at odds with the absence of any peaks for $\Omega_1 = \Omega_2 - 1147$ cm^{-1} in the measured map, as highlighted by the cyan arrow in the left panel of Fig. 6.12.

This result can be interpreted as the signature of mode-mixing with low frequency modes in the excited state. In particular, as we discussed in section 6.2.2, the Duschinsky effect can modify the relative intensity between fundamental and overtone contributions to the combination bands. In Fig. 6.13, we evaluate the effect of Duschinsky rotation in 2D ISRS couplings for the two modes at 822 cm^{-1} and 1147 cm^{-1} , coupled to a non-displaced low frequency mode at 80 cm^{-1} . In absence of any mixing, i.e. for a vanishing Duschinsky angle $\theta_D = 0$, $d_2^{1147} \neq 0$ is needed to observe coupling with the overtone of the 1147 cm^{-1} mode, leading to the two sub-diagonals at $\Omega_1 = \Omega_2 - 1147$ cm^{-1} and $\Omega_1 = \Omega_2 - 2294$ cm^{-1} in panel 6.13a (cyan and blue arrows, respectively). On the contrary, a rotation of $\theta_D \neq 0^\circ$ between the 1147 and 80 cm^{-1} modes on the excited states S_1 and S_n leads to a suppression of the sub-diagonal peak at the fundamental frequency $\Omega_1 = \Omega_2 - 1147$ cm^{-1} and enhances the intensity of the overtone couplings, as shown in Fig. 6.13b. We found that the suppression is maximized at $\theta_D = 90^\circ$ for these values of the parameters, and is above 65% for all the values of θ_D in the range 65°-115°.

6.5 Conclusions

In conclusion, we introduced a resonant 2D ISRS approach for multidimensional Raman spectroscopy. We demonstrated a three color experimental scheme illustrating how to decipher the correlations between vibronic modes in electronically excited molecules with electronic state selectivity, using the density matrix perturbative approach to derive sum-over-state expressions for the signal. Critically, 2D ISRS efficiently suppresses lower order cascade signals, as opposed to other fifth-order Raman techniques. Moreover, using a WLC probe enables to select further the electronic states from which 2D ISRS features originate, averaging on different region of the transient absorption of the signal and opens to the possibility of studying vibrational manifolds on highly electronically excited states.

By the identification of the vibronic origin of each peak in 2D ISRS maps, we elucidated how different mechanisms, as linear displacement along specific normal coordinates and mode mixing, contribute to the signal within the harmonic approximation. Notably, while lower order techniques can only record one-dimensional projections of potential energy surfaces, 2D ISRS is able to map complex PES, determining multidimensional FC overlaps directly. In presence of ultrafast dynamics on the electronically excited state, the selectivity of 2D ISRS can be exploited to directly access the structural conformation on the state in which the dynamics starts, disclosing the initial stages of the reaction.

As a test-bed for the experimental scheme and the theoretical model, we applied the technique to study the subpicosecond FC relaxation in the green fluorescent protein. We revealed that high to low frequency mode correlations can be sustained even by fully harmonic interactions. In particular, we probed a large FC activity on the excited state for a mode dark in the stimulated emission transition, and an enhancement of mode overtones activity in determining out-of-

diagonal peaks, which we linked to the presence of Duschinsky mixing.

7 Conclusions and perspectives

Unveiling the mechanisms which underlay the vibronic interactions in molecules and solid state materials is the focus of a broad and interdisciplinary scientific effort, due to both a fundamental and applied interest. In particular, this challenging goal has been recently fueled by the outbreak of technological innovations whose working principle lays in different form of electron-phonon coupling, from optoelectronic devices to novel low dimensional materials.

In this work, we tackled the challenge by realizing novel multidimensional protocols for impulsive stimulated Raman spectroscopy. Thanks to its sensitivity to the vibrational structure of the material and the electronic resonant enhancement, stimulated Raman effect is the ideal tool to detect vibronic mechanisms. As a time domain technique, ISRS can induce and follow the vibrational coherent oscillations in a sample, encoding them in the signal dependence on the delay between the two incident pulses. Moreover, adopting a spectrally resolved detection of the probe pulse immediately provides an additional parameter in which spectroscopic information can be stored, leading to a bidimensional signal. Following this strategy, we presented different ways to exploit and extend this intrinsic multidimensionality, with the aim to perform resonant multidimensional Raman experiments.

The approach followed in this thesis grounded on a twofold toolbox. On one side, nonlinear response theory supplied a common, diagrammatic language to describe and compare different techniques. On the other hand, the ultrafast spectroscopy measurements allowed for experimental verification of the schemes designed by the theory. We applied the developed strategies to the solution of three different problems: the dissection between ground and excited state vibrations in molecules, the electron-phonon coupling in hybrid perovskites and the vibronic correlations in the excited state of the green fluorescent protein. The results are summarized below.

The first control knob that we discussed concerns the spectral properties of the probe pulse. Indeed, we have investigated the role of the phase matching condition and the probe chirp in determining the spectrally resolved bidimensional response $S(T, \lambda_s)$ of broadband ISRS experiments presented in Chapter 4. As a starting point, we focused on the dependence of the signal on the probe wavelength, rationalizing the experimental maps measured in off resonant conditions in liquid Cyclohexane. Using the Feynman diagrams approach, we isolated two different third-order processes that concur in the generation of the signal for a given detected wavelength. These processes arise from probe spectral components which are red and blue shifted by the vibrational frequencies with respect to the probed central wavelength, and are consequently peaked in opposite regions of the map. This gives rise to two oscillations as a function of the time delay between the Raman and probe pulses which interfere to determine the signals. In off resonant ISRS with transform-limited pulse, the interference is destructive, explaining the strong signal suppression that can be observed in the central part of the spectrum. A non-zero chirp, however, modifies the relative phase of the oscillations in a mode selective manner and, consequently, enhancement or annihilation of the signal can be controlled by varying the value of the chirp. Extending these findings to a three beam geometry, we demonstrated that, upon resonant Actinic excitation, a ISRS protocol performed with a chirped resonant probe pulse

and a off resonant Raman pulse induces an additional phase, dependent on both the electronic and vibrational frequencies. Consequently, excited and ground state vibrational coherences can be controlled and discerned by mapping the ISRS oscillation as a function of the chirp. This vibrational selectivity in the electronic resonant condition can be compared to the results presented in Chapter 1 for frequency domain SRS, where we showed that tuning the resonance condition of the narrowband Raman pulse affects the lineshapes of the Raman bands in a mode selective way. Notably, in ISRS, the control of relative mode intensities can be achieved also in off resonant conditions.

In Chapter 5, we applied spectrally resolved ISRS in a two beam configuration to study the ground and excited state Raman spectrum of hybrid lead halide perovskites. Specifically, we compared the ISRS maps obtained tuning the frequency of the Raman pulse above and below the band gap, in order to understand the role of ground and excited state phonon modes on the carriers photogeneration in a thin film of methylammonium lead bromide ($MAPbBr_3$). The broadband probe and the two dimensional map gave us two advantages to resolve the very weak oscillating component over the intense transient absorption decay in these materials. Firstly, we could select from a broad spectral range of dispersed wavelength λ_s and average in the region in which the contributions to ISRS interfere positively, enhancing the signal. Secondly, the quantities of interest extracted from the measurements, specifically the positions of the Raman peaks and the phases of the oscillations, have been monitored over multiple λ_s, reducing the impact of single wavelength noise on the analysis. Comparing the ground state features obtained in non-resonant conditions to the map in which resonant excitations produced photocarriers, we isolated the ground state modes coupled to the electronic excitation by the resonant enhancement. More importantly, we revealed additional phonon modes, absent in the ground state and assigned them to the excited state, generated via displacive excitation mechanism. This analysis, corroborated by the phase and power dependence, provided the proof of photo-induced modifications of the lattice as a result of carrier generation. Since neither delocalized or excitonic carriers would show such effect of displaced atomic equilibrium positions, our results are suggestive of polaronic signatures in the photocarrier generation process in this class of systems. Furthermore, we proposed a mechanism for recombination blocking due to the features of the polaron, which may provide a rationale for the extended carrier lifetime in lead halide perovskites. In general, the obtained results provide important contributions to the comprehension of electron-phonon interactions in hybrid perovskites films, with the aim of fostering their application in commercially available photovoltaics and optoelectronics.

To address the third case of study of this thesis, in Chapter 6, we introduced and experimentally implemented resonant 2D ISRS as a novel scheme for mapping excited state potential energy surfaces. We demonstrated its ability to study the correlation between vibronic modes in electronically excited molecules with selectivity on the excited electronic state. This is a combined consequence of the resonance scheme and the WLC probe, which additionally may offer the possibility to study vibrational manifolds on highly electronically excited states. Critically, the obtained 2D spectra are free from lower order cascade signals, generally affecting fifth-order Raman spectra. This is obtained through the three color scheme which resonantly suppress these artifacts. We benchmarked the technique investigating the subpicosecond Franck Condon relaxation in the green fluorescent protein. Using the diagrammatic theory, we deciphered the experimental maps isolating the effects of linear and nonlinear mode couplings.

These results suggest the impressive possibilities given by a multidimensional approach to stimulated Raman spectroscopies. Since multidimensional implementations are feasible and convenient in both the time and frequency domains, the methods developed in this thesis can be generalized to higher order spectroscopies which could take advantage of the properties of both the approaches. Critically, especially when considering complex dynamics, the interplay of different time and frequency scales may require the application of joint time and frequency representation of the spectroscopic signal. Indeed, dynamics in nature evolves in phase spaces of extremely high dimensionality, with mixed time-frequency coordinates and reducing the perspective to only one of these points of view could lead to a loss of available information. In

this respect, the research of novel spectroscopic tools, both theoretical and experimental, should be oriented beyond the pure time or frequency approach, pushing further the horizon of the existing multidimensional schemes to include novel approaches which combine the two, as the phase shaping techniques.

Appendix

Calculation of transition integrals in the linearly displaced harmonic model

The general transition integral of order r between two harmonic oscillators of mass M and frequency ω is defined as:

$$I_{kl}^{[r]} = \int_{-\infty}^{+\infty} \psi_k(x) x^r \psi_l(x+D) dx \tag{A.1}$$

where k and l are the quantum numbers associated to the initial and final state of the transition and D is the displacement between the equilibrium positions of the two oscillators. The integral in eq. A.1 can be calculated explicitly from the eigenfunctions of the harmonic oscillator

$$\psi_\nu(x) = (\frac{\sqrt{\frac{\omega}{\hbar}} 2^\nu}{\nu! \sqrt{\pi}})^{\frac{1}{2}} H_\nu(x) e^{-\frac{1}{2}\frac{\omega}{\hbar}x^2} \tag{A.2}$$

being $H_\nu(x)$ the Hermite polynomial of order ν. Nevertheless, it is convenient to derive a recursive relation to implement fast calculations. This can be done in the ladder operator representation [227]. We assume the usual expressions of the raising $a^\dagger$ and lowering operators a and define

$$\alpha = D \left(\frac{M\omega}{2\hbar} \right)^{\frac{1}{2}}$$

Eq. A.1 is equivalent to:

$$I_{kl}^{[r]} = (k!l!)^{-\frac{1}{2}} \left(\frac{D}{2\alpha} \right)^r \langle 0 | \, a^k (a + a^\dagger)^r e^{-\alpha(a^\dagger - a)} (a^\dagger)^l \, | 0 \rangle \tag{A.3}$$

The exponential can be split thanks to the Glauber formula [228]:

$$e^{-\alpha(a^\dagger - a)} = e^{-\alpha a^\dagger} e^{\alpha a} e^{-\frac{1}{2}\alpha^2 [a, a^\dagger]}$$

Using the identity operator we can write:

$$\begin{aligned} I_{kl}^{[r]} &= (k!l!)^{-\frac{1}{2}} \left(\frac{D}{2\alpha} \right)^r e^{-\frac{1}{2}\alpha^2} \underbrace{\langle 0 | \, e^{-\alpha a^\dagger}}_{1} \underbrace{e^{\alpha a^\dagger} \, (a)^k \, e^{-\alpha a^\dagger}}_{3} \underbrace{e^{\alpha a^\dagger} (a + a^\dagger)^r e^{-\alpha a^\dagger}}_{4} \underbrace{e^{\alpha a} (a^\dagger)^l e^{-\alpha a}}_{5} \underbrace{e^{\alpha a} \, | 0 \rangle}_{2} = \\ &= (k!l!)^{-\frac{1}{2}} \left(\frac{D}{2\alpha} \right)^r e^{-\frac{1}{2}\alpha^2} \langle 0 | \, (a - \alpha)^k \, (a + a^\dagger - \alpha)^r (a^\dagger + \alpha)^l \, | 0 \rangle \end{aligned} \tag{A.4}$$

The last equality is obtained expanding the exponential in 1 and 2, for which only the zero order term survives due to the definitions of the ladder operators, and using the canonical transformation and the displacement operator $\mathcal{D}_\alpha$ in 4, 5 and 6. Specifically for the term 3:

$$\begin{aligned} e^{\alpha a^\dagger} a^k e^{-\alpha a^\dagger} &= \left(e^{\alpha a^\dagger} a e^{-\alpha a^\dagger} \right)^k = \\ &= \left(e^{\alpha a^\dagger} e^{-\alpha a} a e^{\alpha a} e^{-\alpha a^\dagger} \right)^k = \left(\mathcal{D}_\alpha e^{-\frac{1}{2}\alpha^2} \, e^{\frac{1}{2}\alpha^2} \mathcal{D}_\alpha^\dagger \right)^k = (a - \alpha)^k \end{aligned}$$

We can now calculate the matrix elements using the binomial theorem and for $r = 0$ we obtain the expression of the Franck-Condon factor:

$$\begin{aligned}\mu_{kl}^{FC} = I_{kl}^{[0]} &= (k!l!)^{-\frac{1}{2}}\, e^{-\frac{1}{2}\alpha^2}\, \langle 0| \sum_{i=0}^{k} \binom{k}{i} a^i \alpha^{k-i} \sum_{j=0}^{l} \binom{l}{j} \left(a^\dagger\right) j\alpha^{l-j}\, |0\rangle \\ &= (k!l!)^{-\frac{1}{2}}\, e^{-\frac{1}{2}\alpha^2} \sum_{i=0}^{\min(l,k)} \binom{k}{i}\binom{l}{i} i!\, \alpha^{k+l-2i}\end{aligned} \tag{A.5}$$

Similarly, we can compute the expression for $r = 1$, which is related to Herzberg–Teller factor:

$$\begin{aligned}I_{kl}^{[1]} &= (k!l!)^{-\frac{1}{2}}\, \frac{D}{2\alpha} e^{-\frac{1}{2}\alpha^2}\, \langle 0| \sum_{i=0}^{k} \binom{k}{i} a^i \alpha^{k-i} \left(a + a^\dagger - \alpha\right) \sum_{j=0}^{l} \binom{l}{j} \left(a^\dagger\right) j\alpha^{l-j}\, |0\rangle = \\ &= (k!l!)^{-\frac{1}{2}}\, \frac{D}{2\alpha} e^{-\frac{1}{2}\alpha^2} \sum_{i=0}^{k}\sum_{j=0}^{l} \binom{k}{i}\binom{l}{j} \alpha^{k+l-i-j} \left[\langle 0|a^i a (a^\dagger)^j|0\rangle + \langle 0|a^i a^\dagger (a^\dagger)^j|0\rangle - \langle 0|a^i (a^\dagger)^j|0\rangle\right] = \\ &= (k!l!)^{-\frac{1}{2}}\, \frac{D}{2\alpha} e^{-\frac{1}{2}\alpha^2} \left[\sum_{j=1}^{\min(l,k+1)} \binom{k}{j-1}\binom{l}{j} j!\, \alpha^{k+l-2j+1} + \right. \\ &\left. + \sum_{j=0}^{\min(l,k-1)} \binom{k}{j+1}\binom{l}{j} (j+1)!\, \alpha^{k+l-2j-1} - \sum_{j=0}^{\min(l,k)} \binom{k}{j}\binom{l}{j} j!\, \alpha^{k+l-2j+1}\right]\end{aligned} \tag{A.6}$$

By proceeding in the same fashion, it is possible to derive closed expressions for every order of $I_{kl}^{[r]}$.

List of publications and conferences

Publications associated with this thesis

5. **G. Fumero***, C. Schnedermann*, G. Batignani, T. Wende, M. Liebel, G. Bassolino, C. Ferrante, S. Mukamel, P. Kukura, T. Scopigno, *Two-dimensional impulsively stimulated resonant Raman spectroscopy of molecular excited-states*, submitted (2019).

4. G. Batignani*, **G. Fumero***, A. R. S. Kandada*, G. Cerullo, M. Gandini, C. Ferrante, A. Petrozza and T. Scopigno, *Probing Femtosecond Lattice Displacement upon Photo-carrier generation in Lead Halide Perovskite*, Nat. Commun. 9, 1971 (2018).

3. C. Ferrante, G. Batignani, **G. Fumero**, E. Pontecorvo, A. Virga, L. C. Montemiglio, G. Cerullo, M. H. Vos and T. Scopigno, *Resonant Broadband Stimulated Raman scattering in Myoglobin*, J. Raman. Spectrosc. 1-8 (2018).

2. L. Monacelli, G. Batignani, **G. Fumero**, C. Ferrante, S. Mukamel and T. Scopigno, *Manipulating Impulsive Stimulated Raman Spectroscopy with a Chirped Probe Pulse*, J. Phys. Chem. Lett. 8, 966-974 (2017).

1. G. Batignani, E. Pontecorvo, G. Giovannetti, C. Ferrante, **G. Fumero** and T. Scopigno, *Broadband Stimulated Raman spectroscopy in electronically resonant biomolecules*, Sci. Rep. 6, 18445 (2016).

Other publications

4. G. Batignani, **G. Fumero**, E. Pontecorvo, C. Ferrante, S. Mukamel, T. Scopigno, *Genuine dynamics vs cross phase modulation artefacts in Femtosecond Stimulated Raman Spectroscopy*, accepted in ACS Photonics (2019).

3. **G. Fumero**, G. Batignani, K. E. Dorfman, S. Mukamel and T. Scopigno, *Probing ultrafast processes by fifth order Stimulated Raman Scattering*, Journal of Physics Conference Series 689, 012023 (2016).

2. **G. Fumero**, G. Batignani, K. E. Dorfman, S. Mukamel and T. Scopigno, *On the resolution limit of Femtosecond Stimulated Raman Spectroscopy: modelling fifth-order signals with overlapping pulses*, ChemPhysChem 16, 3438-3443 (2015).

*equally contributing authors

1. G. Batignani, **G. Fumero**, S. Mukamel and T. Scopigno, *Energy flow between spectral components in 2D Broadband Stimulated Raman Spectroscopy*, Phys. Chem. Chem. Phys. 17, 10454-10461 (2015).

Contributions to international conferences

6. 26^{th} International Conference on Raman Spectroscopy (ICORS 2018), August $26^{th} - 31^{th}$ 2018. Jeju Island, Korea.
   Oral contribution: *Unraveling vibronic couplings during ultrafast chemical reactions by 2D Impulsive Stimulated Raman Spectroscopy.*

5. 9^{th} International Conference on Advanced Vibrational Spectroscopy (ICAVS 9), June $11^{th} - 16^{th}$ 2017. Victoria, BC, Canada.
   Oral contribution: *Manipulating Impulsive Stimulated Raman Spectroscopy with a Chirped Probe Pulse.*

4. International Symposium on Two-Dimensional Correlation Spectroscopy (2DCOS), June $7^{th} - 10^{th}$ 2017. Victoria, BC, Canada.
   Oral contribution: *Unraveling vibronic couplings during ultrafast chemical reactions by two dimensional Impulsive Stimulated Raman Spectroscopy.*

3. 8^{th} International Conference on Coherent Multidimensional Spectroscopy (CMDS2016), June 29^{th} - July 1^{th} 2016. Groningen, The Netherlands.
   Poster contribution: *Energy flow between spectral components in 2D Broadband Stimulated Raman Spectroscopy.*

2. Dynamic Pathways in Multidimensional Landscapes 2016 - Young investigator workshop, $10^{th} - 15^{th}$ January 2016 Winklmoos-Alm, Reit im Winkl, Deutschland. Oral contribution: *Probing ultrafast processes by fifth order Stimulated Raman Scattering.*

1. 6^{th} *Young researcher meeting*, $12^{th} - 14^{th}$ October 2015. L'Aquila, Italy.
   Oral contribution: *Exploring the ultimate resolution limit of Femtosecond Stimulated Raman Scattering.*
   Poster contributions: *Probing ultrafast processes by fifth order Stimulated Raman Scattering.*

References

1. Zewail, A. H. Femtochemistry: Atomic-Scale Dynamics of the Chemical Bond. *J. Phys. Chem. A* **104,** 5660–5694 (2000).
2. Prince, R. C., Frontiera, R. R. & Potma, E. O. Stimulated Raman Scattering: From Bulk to Nano. *Chemical Reviews* **117,** 5070–5094 (2016).
3. Hargrove, L. E., Fork, R. L. & Pollack, M. A. Locking of He-Ne Laser modes induced by synchronous intracavity modulation. *Applied Physics Letters* **5,** 4–5 (1964).
4. Goulielmakis, E. *et al.* Single-Cycle Nonlinear Optics. *Science* **320,** 1614–1617 (2008).
5. Morgner, U. Single-cycle pulse generation. *Nature Photonics* **4,** 14–15 (2010).
6. Foglia, L. *et al.* First Evidence of Purely Extreme-Ultraviolet Four-Wave Mixing. *Physical Review Letters* **120** (2018).
7. Goulielmakis, E. *et al.* Real-time observation of valence electron motion. *Nature* **466,** 739–743 (2010).
8. Li, W. *et al.* Time-Resolved Dynamics in N2O4 Probed Using High Harmonic Generation. *Science* **322,** 1207–1211 (2008).
9. Rouxel, J. R., Kowalewski, M., Bennett, K. & Mukamel, S. X-Ray Sum Frequency Diffraction for Direct Imaging of Ultrafast Electron Dynamics. *Physical Review Letters* **120** (2018).
10. Inoue, I. *et al.* Observation of femtosecond X-ray interactions with matter using an X-ray–X-ray pump–probe scheme. *Proceedings of the National Academy of Sciences* **113,** 1492–1497 (2016).
11. Liu, M. *et al.* Terahertz-field-induced insulator-to-metal transition in vanadium dioxide metamaterial. *Nature* **487,** 345–348 (2012).
12. Polli, D. *et al.* Conical intersection dynamics of the primary photoisomerization event in vision. *Nature* **467,** 440–443 (2010).
13. Schoenlein, R. W., Peteanu, L. A., Mathies, R. A. & Shank, C. V. The first step in vision: femtosecond isomerization of rhodopsin. *Science* (1991).
14. Batignani, G. *et al.* Probing ultrafast photo-induced dynamics of the exchange energy in a Heisenberg antiferromagnet. *Nature Photon.* **9,** 506–510 (2015).
15. Monni, R., Haddad, A. A., van Mourik, F., Auböck, G. & Chergui, M. Tryptophan-to-heme electron transfer in ferrous myoglobins. *Proceedings of the National Academy of Sciences* **112,** 5602–5606 (2015).
16. Provencher, F. *et al.* Direct observation of ultrafast long-range charge separation at polymer–fullerene heterojunctions. *Nat Comms* **5,** 4288 (2014).
17. Takeuchi, S. *et al.* Spectroscopic Tracking of Structural Evolution in Ultrafast Stilbene Photoisomerization. *Science* **322,** 1073–1077 (2008).
18. Ferrante, C., Pontecorvo, E., Cerullo, G., Vos, M. H. & Scopigno, T. Direct observation of subpicosecond vibrational dynamics in photoexcited myoglobin. *Nature Chemistry* **8,** 1137–1143 (2016).

19. Tokmakoff, A. *Nonlinear Spectroscopy* Lecture notes. Departement of Chemistry, MIT. Boston. 2009.
20. Berera, R., van Grondelle, R. & Kennis, J. T. M. Ultrafast transient absorption spectroscopy: principles and application to photosynthetic systems. *Photosynth Res* **101,** 105–118 (2009).
21. Raman, C. V. & Krishnan, K. S. A New Type of Secondary Radiation. *Nature* **121,** 501–502 (1928).
22. Landsberg, G. S. & Mandelstam, L. I. New phenomenon in scattering of light (preliminary report). *Journal of the Russian Physico-Chemical Society, Physics Section* **60,** 335 (1928).
23. Potma, E. O. & Mukamel, S. in *Coherent Raman Scattering Microscopy* (eds Cheng, J.-X. & Xie, X. S.) (CRC Press, 2012).
24. Kumar, V. *Coherent Raman Spectroscopy from a single femtosecond oscillator* PhD Thesis. Department of Physics, Politecnico di Milano. 2012.
25. Cheng, J.-X. & Xie, X. S. *Coherent Raman Scattering Microscopy* (CRC Press, 2012).
26. Eckhardt, G. *et al.* Stimulated Raman Scattering From Organic Liquids. *Physical Review Letters* **9,** 455–457 (1962).
27. Bloembergen, N. The Stimulated Raman Effect. *American Journal of Physics* **35,** 989–1023 (1967).
28. Batignani, G., Fumero, G., Mukamel, S & Scopigno, T. Energy flow between spectral components in 2D Broadband Stimulated Raman Spectroscopy. *Phys. Chem. Chem. Phys.* **17,** 10454–10461 (2015).
29. Fumero, G., Batignani, G., Dorfman, K. E., Mukamel, S. & Scopigno, T. On the Resolution Limit of Femtosecond Stimulated Raman Spectroscopy: Modelling Fifth-Order Signals with Overlapping Pulses. *ChemPhysChem* **16,** 3438–3443 (2015).
30. McCamant, D. W., Kukura, P., Yoon, S. & Mathies, R. A. Femtosecond broadband stimulated Raman spectroscopy: Apparatus and methods. *Rev. Sci. Instrum.* **75,** 4971. `http://dx.doi.org/10.1063/1.1807566` (2004).
31. Yoshizawa, M., Hattori, Y. & Kobayashi, T. Femtosecond time-resolved resonance Raman gain spectroscopy in polydiacetylene. *Phys. Rev. B* **49,** 13259–13262. `http://link.aps.org/doi/10.1103/PhysRevB.49.13259` (18 1994).
32. Dietze, D. R. & Mathies, R. A. Femtosecond Stimulated Raman Spectroscopy. *ChemPhysChem* **17,** 1224–1251 (2016).
33. Kukura, P., McCamant, D. W., Yoon, S., Wandschneider, D. B. & Mathies, R. A. Structural Observation of the Primary Isomerization in Vision with Femtosecond-Stimulated Raman. *Science* **310,** 1006–1009 (2005).
34. Weigel, A. & Ernsting, N. Excited Stilbene: Intramolecular Vibrational Redistribution and Solvation Studied by Femtosecond Stimulated Raman Spectroscopy. *J. Phys. Chem. B* **114,** 7879–7893 (2010).
35. Ruhman, S., Joly, A. & Nelson, K. Coherent Molecular Vibrational Motion Observed in the Time Domain Through Impulsive Stimulated Raman Scattering. *IEEE J. Quant. Electron.* **24,** 460–469 (1988).
36. Dhar, L., Rogers, J. A. & Nelson, K. A. Time-resolved vibrational spectroscopy in the impulsive limit. *Chemical Reviews* **94,** 157–193 (1994).
37. Liebel, M. & Kukura, P. Broad-Band Impulsive Vibrational Spectroscopy of Excited Electronic States in the Time Domain. *J. Phys. Chem. Lett.* **4,** 1358–1364. `http://dx.doi.org/10.1021/jz4004203` (2013).
38. Yan, Y.-X., Gamble, E. B. & Nelson, K. A. Impulsive Stimulated Scattering: General Importance in Femtosecond Laser Pulse Interactions with Matter, and Spectroscopic Applications. *J. Chem. Phys.* **83,** 5391–5399 (1985).

39. Kuramochi, H., Takeuchi, S. & Tahara, T. Femtosecond time-resolved impulsive stimulated Raman spectroscopy using sub-7-fs pulses: Apparatus and applications. *Review of Scientific Instruments* **87,** 043107 (2016).
40. Liebel, M., Schnedermann, C., Wende, T. & Kukura, P. Principles and Applications of Broadband Impulsive Vibrational Spectroscopy. *The Journal of Physical Chemistry A* **119,** 9506–9517 (2015).
41. Cheng, J.-X. & Xie, X. S. Coherent Anti-Stokes Raman Scattering Microscopy: Instrumentation, Theory, and Applications. *J. Phys. Chem. B* **108,** 827–840 (2004).
42. Tanimura, Y. & Mukamel, S. Two-dimensional femtosecond vibrational spectroscopy of liquids. *The Journal of Chemical Physics* **99,** 9496–9511 (1993).
43. Zhuang, W., Hayashi, T. & Mukamel, S. Coherent Multidimensional Vibrational Spectroscopy of Biomolecules: Concepts, Simulations, and Challenges. *Angewandte Chemie International Edition* **48,** 3750–3781 (2009).
44. Buckup, T. & Léonard, J. Multidimensional Vibrational Coherence Spectroscopy. *Topics in Current Chemistry* **376** (2018).
45. Aue, W. P., Bartholdi, E. & Ernst, R. R. Two-dimensional spectroscopy. Application to nuclear magnetic resonance. *The Journal of Chemical Physics* **64,** 2229–2246 (1976).
46. Jonas, D. M. Two dimensional femtosecond spectroscopy. *Annual Review of Physical Chemistry* **54,** 425–463 (2003).
47. Fuller, F. D. & Ogilvie, J. P. Experimental Implementations of Two-Dimensional Fourier Transform Electronic Spectroscopy. *Annual Review of Physical Chemistry* **66,** 667–690 (2015).
48. Hamm, P. & Zanni, M. *Concepts and Methods of 2D Infrared Spectroscopy* (Cambridge University Press, 2012).
49. Turner, D. B., Stone, K. W., Gundogdu, K. & Nelson, K. A. Three-dimensional electronic spectroscopy of excitons in GaAs quantum wells. *The Journal of Chemical Physics* **131,** 144510 (2009).
50. Harel, E., Fidler, A. F. & Engel, G. S. Single-Shot Gradient-Assisted Photon Echo Electronic Spectroscopy. *The Journal of Physical Chemistry A* **115,** 3787–3796 (2011).
51. Réhault, J., Maiuri, M., Oriana, A. & Cerullo, G. Two-dimensional electronic spectroscopy with birefringent wedges. *Review of Scientific Instruments* **85,** 123107 (2014).
52. Tian, P., Keusters, D., Suzaki, Y. & Warren, W. Femtosecond Phase-Coherent Two-Dimensional Spectroscopy. *Science* **300,** 1553–1555 (2003).
53. Frostig, H., Bayer, T., Dudovich, N., Eldar, Y. C. & Silberberg, Y. Single-beam spectrally controlled two-dimensional Raman spectroscopy. *Nature Photonics* **9,** 339–343 (2015).
54. Spencer, A. P., Hutson, W. O. & Harel, E. Quantum coherence selective 2D Raman–2D electronic spectroscopy. *Nature Communications* **8,** 14732 (2017).
55. Goodknight, J. & Aspuru-Guzik, A. Taking six-dimensional spectra in finite time. *Science* **356,** 1333–1333 (2017).
56. Ferrante, C. *et al.* Resonant broadband stimulated Raman scattering in myoglobin. *Journal of Raman Spectroscopy* **49,** 913–920 (2018).
57. Batignani, G. *et al.* Electronic resonances in broadband stimulated Raman spectroscopy. *Scientific Reports* **6,** 18445 (2016).
58. Harbola, U., Umapathy, S. & Mukamel, S. Loss and gain signals in broadband stimulated-Raman spectra: Theoretical analysis. *Phys. Rev. A* **88,** 011801(R) (2013).
59. Mukamel, S. *Principles of Nonlinear Optical Spectroscopy* (Oxford University Press, 1999).
60. Lee, S.-Y., Zhang, D., McCamant, D. W., Kukura, P. & Mathies, R. A. Theory of femtosecond stimulated Raman spectroscopy. *J. Chem. Phys.* **121,** 3632 (2004).

61. Dorfman, K. E., Fingerhut, B. P. & Mukamel, S. Time-resolved broadband Raman spectroscopies: A unified six-wave-mixing representation. *J. Chem. Phys.* **139,** 124113 (2013).
62. Condon, E. U. The Franck-Condon Principle and Related Topics. *American Journal of Physics* **15,** 365–374 (1947).
63. Lee, D., Stallard, B. R., Champion, P. M. & Albrecht, A. C. The inverse transform in resonance Raman scattering. *The Journal of Physical Chemistry* **88,** 6693–6696 (1984).
64. Sakurai, J. J. *Modern Quantum Mechanics* (Addison Wesley, 1993).
65. Fano, U. Pressure Broadening as a Prototype of Relaxation. *Phys. Rev.* **131,** 259–268 (1 1963).
66. Loudon, R. *The Quantum Theory of Light* (Oxford University Press, 2000).
67. Weisskopf, V. & Wigner, E. P. in *Part I: Particles and Fields. Part II: Foundations of Quantum Mechanics* 30–49 (Springer Berlin Heidelberg, 1997).
68. Kubo, R. in *Advances in Chemical Physics* 101–127 (John Wiley & Sons, Inc., 2007).
69. Dyson, F. J. Divergence of Perturbation Theory in Quantum Electrodynamics. *Phys. Rev.* (1952).
70. Boyd, R. W. *Nonlinear Optics, Third Edition* (Academic Press, 2008).
71. Rahav, S. & Mukamel, S. in *Advances in Atomic, Molecular, and Optical Physics* (2010).
72. Milonni, P. Semiclassical and quantum-electrodynamical approaches in nonrelativistic radiation theory. *Physics Reports* **25,** 1–81 (1976).
73. Dorfman, K. E. & Mukamel, S. Multidimensional spectroscopy with entangled light: loop vs ladder delay scanning protocols. *New J. Phys.* **16,** 033013 (2014).
74. Dorfman, K. E., Schlawin, F. & Mukamel, S. Stimulated Raman Spectroscopy with Entangled Light: Enhanced Resolution and Pathway Selection. *J. Phys. Chem. Lett.* **5,** 2843–2849 (2014).
75. Power, E. A. & Zienau, S. Coulomb Gauge in Non-Relativistic Quantum Electro-Dynamics and the Shape of Spectral Lines. *Philosophical Transactions of the Royal Society A: Mathematical, Physical and Engineering Sciences* **251,** 427–454 (1959).
76. Rahav, S. & Mukamel, S. Stimulated coherent anti-Stokes Raman spectroscopy (CARS) resonances originate from double-slit interference of two-photon Stokes pathways. *Proceedings of the National Academy of Sciences* **107,** 4825–4829 (2010).
77. Hahn, E. L. Nuclear Induction Due to Free Larmor Precession. *Physical Review* **77,** 297–298 (1950).
78. Strickland, D. & Mourou, G. Compression of amplified chirped optical pulses. *Optics Communications* **56,** 219–221 (1985).
79. Svelto, O. *Principles of Lasers* (Springer US, 2010).
80. Service, R. F. Laser Labs Race for the Petawatt. *Science* **301,** 154–156 (2003).
81. Alfano, R. R. & Shapiro, S. L. Observation of Self-Phase Modulation and Small-Scale Filaments in Crystals and Glasses. *Phys. Rev. Lett.* **24,** 592–594 (11 1970).
82. Gaeta, A. L. Catastrophic Collapse of Ultrashort Pulses. *Phys. Rev. Lett.* **84,** 3582–3585 (16 2000).
83. Cerullo, G. & Silvestri, S. D. Ultrafast optical parametric amplifiers. *Review of Scientific Instruments* **74,** 1–18 (2003).
84. Manzoni, C & Cerullo, G. Design criteria for ultrafast optical parametric amplifiers. *Journal of Optics* **18,** 103501 (2016).
85. Tzankov, P. *et al.* 300 µJ noncollinear optical parametric amplifier in the visible at 1 kHz repetition rate. *Optics Letters* **31,** 3629 (2006).

86. Shirakawa, A., Sakane, I., Takasaka, M. & Kobayashi, T. Sub-5-fs visible pulse generation by pulse-front-matched noncollinear optical parametric amplification. *Applied Physics Letters* **74,** 2268–2270 (1999).

87. Wilson, K. *Guide to NOPAs from the McCamant Group* Published online, last accessed October 2018.

88. Pontecorvo, E. *et al.* Femtosecond stimulated Raman spectrometer in the 320-520nm range. *Opt. Express* **19,** 1107–1112 (2011).

89. Marangoni, M. *et al.* Synthesis of picosecond pulses by spectral compression and shaping of femtosecond pulses in engineered quadratic nonlinear media. *Opt. Lett.* **34,** 241–243 (2009).

90. Moutzouris, K., Adler, F., Sotier, F., Träutlein, D. & Leitenstorfer, A. Multimilliwatt ultrashort pulses continuously tunable in the visible from a compact fiber source. *Opt. Lett.* **31,** 1148–1150 (2006).

91. Pontecorvo, E., Ferrante, C., Elles, C. G. & Scopigno, T. Spectrally tailored narrowband pulses for femtosecond stimulated Raman spectroscopy in the range 330-750 nm. *Opt. Express* **21,** 6866–6872 (2013).

92. Rulliere, C. *Femtosecond Laser Pulses* (Springer New York, 2007).

93. Harris, F. On the use of windows for harmonic analysis with the discrete Fourier transform. *Proceedings of the IEEE* **66,** 51–83 (1978).

94. Ruhman, S., Joly, A. G. & Nelson, K. A. Time-resolved observations of coherent molecular vibrational motion and the general occurrence of impulsive stimulated scattering. *The Journal of Chemical Physics* **86,** 6563–6565 (1987).

95. Kahan, A., Nahmias, O., Friedman, N., Sheves, M. & Ruhman, S. Following Photoinduced Dynamics in Bacteriorhodopsin with 7-fs Impulsive Vibrational Spectroscopy. *J. Am. Chem. Soc.* **129,** 537–546 (2007).

96. Schnedermann, C. *et al.* Vibronic Dynamics of the Ultrafast All- Trans to 13- Cis Photoisomerization of Retinal in Channelrhodopsin-1. *J. Am. Chem. Soc.* **138,** 4757–4762 (2016).

97. Cerullo, G. *et al.* Time Domain Investigation of Excited-State Vibrational Motion in Organic Molecules by Stimulated Emission Pumping†. *The Journal of Physical Chemistry A* **107,** 8339–8344 (2003).

98. Ruhman, S., Kohler, B., Joly, A. G. & Nelson, K. A. Intermolecular Vibrational Motion in CS_2 Liquid at $165 \leqslant T \geqslant 300$ K Observed by Femtosecond Time-Resolved Impulsive Stimulated Scattering. *Chem. Phys. Lett.* **141,** 16–24 (1987).

99. Fujisawa, T., Kuramochi, H., Hosoi, H., Takeuchi, S. & Tahara, T. Role of Coherent Low-Frequency Motion in Excited-State Proton Transfer of Green Fluorescent Protein Studied by Time-Resolved Impulsive Stimulated Raman Spectroscopy. *Journal of the American Chemical Society* **138,** 3942–3945 (2016).

100. Polli, D., Brida, D., Mukamel, S., Lanzani, G. & Cerullo, G. Effective Temporal Resolution in Pump-Probe Spectroscopy with Strongly Chirped Pulses. *Phys. Rev. A* **82,** 053809 (2010).

101. Lozovoy, V. V. & Dantus, M. Systematic Control of Nonlinear Optical Processes Using Optimally Shaped Femtosecond Pulses. *ChemPhysChem* **6,** 1970–2000 (2005).

102. Silberberg, Y. Quantum Coherent Control for Nonlinear Spectroscopy and Microscopy. *Annual Review of Physical Chemistry* **60,** 277–292 (2009).

103. Herek, J. L., Wohlleben, W., Cogdell, R. J., Zeidler, D. & Motzkus, M. Quantum control of energy flow in light harvesting. *Nature* **417,** 533–535 (2002).

104. Weiner, A. M., Leaird, D. E., Wiederrecht, G. P. & Nelson, K. A. Femtosecond Pulse Sequences Used for Optical Manipulation of Molecular Motion. *Science* **247,** 1317–1319 (1990).

105. Tannor, D. J., Kosloff, R. & Rice, S. A. Coherent pulse sequence induced control of selectivity of reactions: Exact quantum mechanical calculations. *The Journal of Chemical Physics* **85,** 5805–5820 (1986).

106. Prokhorenko, V. I. *et al.* Coherent Control of Retinal Isomerization in Bacteriorhodopsin. *Science* **313,** 1257–1261 (2006).

107. Hauer, J., Buckup, T. & Motzkus, M. Quantum control spectroscopy of vibrational modes: Comparison of control scenarios for ground and excited states in β-carotene. *Chemical Physics* **350,** 220–229 (2008).

108. Broers, B., van Linden van den Heuvell, H. B. & Noordam, L. D. Efficient population transfer in a three-level ladder system by frequency-swept ultrashort laser pulses. *Physical Review Letters* **69,** 2062–2065 (1992).

109. Marrocco, M. Simple model of coherent anti-Stokes Raman scattering signals generated by means of linearly chirped ultrashort Gaussian laser pulses. *Journal of Raman Spectroscopy* **49,** 1109–1115 (2018).

110. Cerullo, G., Bardeen, C., Wang, Q. & Shank, C. High-power femtosecond chirped pulse excitation of molecules in solution. *Chemical Physics Letters* **262,** 362–368 (1996).

111. Oron, D., Dudovich, N., Yelin, D. & Silberberg, Y. Narrow-Band Coherent Anti-Stokes Raman Signals from Broad-Band Pulses. *Physical Review Letters* **88** (2002).

112. Frostig, H., Katz, O., Natan, A. & Silberberg, Y. Single-pulse stimulated Raman scattering spectroscopy. *Optics Letters* **36,** 1248 (2011).

113. Wand, A. *et al.* Chirp Effects on Impulsive Vibrational Spectroscopy: a Multimode Perspective. *Phys. Chem. Chem. Phys.* **12,** 2149–2163 (2010).

114. Kozma, I. Z., Krok, P. & Riedle, E. Direct Measurement of the Group-Velocity Mismatch and Derivation of the Refractive-Index Dispersion for a Variety of Solvents in the Ultraviolet. *J. Opt. Soc. Am. B* **22,** 1479–1485 (2005).

115. Brédas, J.-L., Sargent, E. H. & Scholes, G. D. Photovoltaic concepts inspired by coherence effects in photosynthetic systems. *Nature Materials* **16,** 35–44 (2017).

116. Hutson, W. O., Spencer, A. P. & Harel, E. Isolated Ground-State Vibrational Coherence Measured by Fifth-Order Single-Shot Two-Dimensional Electronic Spectroscopy. *The Journal of Physical Chemistry Letters* **7,** 3636–3640 (2016).

117. Hartke, B., Kosloff, R. & Ruhman, S. Large amplitude ground state vibrational coherence induced by impulsive absorption in CsI. A computer simulation. *Chemical Physics Letters* **158,** 238–244 (1989).

118. Bardeen, C. J., Wang, Q. & Shank, C. V. Selective Excitation of Vibrational Wave Packet Motion Using Chirped Pulses. *Physical Review Letters* **75,** 3410–3413 (1995).

119. Bardeen, C. J., Wang, Q. & Shank, C. V. Femtosecond Chirped Pulse Excitation of Vibrational Wave Packets in LD690 and Bacteriorhodopsin. *The Journal of Physical Chemistry A* **102,** 2759–2766 (1998).

120. Monacelli, L. *et al.* Manipulating Impulsive Stimulated Raman Spectroscopy with a Chirped Probe Pulse. *The Journal of Physical Chemistry Letters* **8,** 966–974 (2017).

121. Dobryakov, A. L. & Ernsting, N. P. Lineshapes for resonant impulsive stimulated Raman scattering with chirped pump and supercontinuum probe pulses. *The Journal of Chemical Physics* **129,** 184504 (2008).

122. Gdor, I., Ghosh, T., Lioubashevski, O. & Ruhman, S. Nonresonant Raman Effects on Femtosecond Pump–Probe with Chirped White Light: Challenges and Opportunities. *The Journal of Physical Chemistry Letters* **8,** 1920–1924 (2017).

123. Leitner, D. M. Energy Flow in Proteins. *Annu. Rev. Phys. Chem.* **59,** 233–259. https://doi.org/10.1146%2Fannurev.physchem.59.032607.093606 (2008).

124. Mukamel, S. & Biggs, J. D. Communication: Comment on the effective temporal and spectral resolution of impulsive stimulated Raman signals. *J. Chem. Phys.* **134,** 161101 (2011).

125. Snaith, H. J. Perovskites: The Emergence of a New Era for Low-Cost, High-Efficiency Solar Cells. *J. Phys. Chem. Lett.* **4,** 3623–3630. http://dx.doi.org/10.1021/jz4020162 (2013).

126. Stranks, S. D. & Snaith, H. J. Metal-halide perovskites for photovoltaic and light-emitting devices. *Nature Nanotechnology* **10,** 391–402. http://dx.doi.org/10.1038/nnano.2015.90 (2015).

127. Kojima, A., Teshima, K., Shirai, Y. & Miyasaka, T. Organometal Halide Perovskites as Visible-Light Sensitizers for Photovoltaic Cells. *Journal of the American Chemical Society* **131,** 6050–6051 (2009).

128. Lee, M. M., Teuscher, J., Miyasaka, T., Murakami, T. N. & Snaith, H. J. Efficient Hybrid Solar Cells Based on Meso-Superstructured Organometal Halide Perovskites. *Science* **338,** 643–647 (2012).

129. Yang, W. S. *et al.* High-performance photovoltaic perovskite layers fabricated through intramolecular exchange. *Science* **348,** 1234–1237 (2015).

130. Tan, Z.-K. *et al.* Bright light-emitting diodes based on organometal halide perovskite. *Nature Nanotechnology* **9,** 687–692 (2014).

131. Xing, G. *et al.* Low-temperature solution-processed wavelength-tunable perovskites for lasing. *Nature Materials* **13,** 476–480 (2014).

132. Stranks, S. D. *et al.* Enhanced Amplified Spontaneous Emission in Perovskites Using a Flexible Cholesteric Liquid Crystal Reflector. *Nano Letters* **15,** 4935–4941 (2015).

133. Saliba, M. *et al.* Structured Organic-Inorganic Perovskite toward a Distributed Feedback Laser. *Advanced Materials* **28,** 923–929 (2015).

134. Herz, L. M. Charge-Carrier Dynamics in Organic-Inorganic Metal Halide Perovskites. *Annual Review of Physical Chemistry* **67,** 65–89. http://dx.doi.org/10.1146/annurev-physchem-040215-112222 (2016).

135. Grancini, G. *et al.* Role of microstructure in the electron–hole interaction of hybrid lead halide perovskites. *Nature Photonics* **9,** 695–701 (2015).

136. Zhu, X.-Y. & Podzorov, V. Charge Carriers in Hybrid Organic-Inorganic Lead Halide Perovskites Might Be Protected as Large Polarons. *J. Phys. Chem. Lett.* **6,** 4758–4761. http://dx.doi.org/10.1021/acs.jpclett.5b02462 (2015).

137. Zhu, H. *et al.* Screening in crystalline liquids protects energetic carriers in hybrid perovskites. *Science* **353,** 1409–1413 (2016).

138. Ziffer, M. E. & Ginger, D. S. How hybrid perovskites get their groove. *Science* **353,** 1365–1365 (2016).

139. Nah, S. *et al.* Spatially segregated free-carrier and exciton populations in individual lead halide perovskite grains. *Nature Photonics* **11,** 285–288 (2017).

140. Yaffe, O. *et al.* Local Polar Fluctuations in Lead Halide Perovskite Crystals. *Physical Review Letters* **118** (2017).

141. Miyata, K. *et al.* Large polarons in lead halide perovskites. *Science Advances* **3,** e1701217 (2017).

142. Selig, O. *et al.* Organic Cation Rotation and Immobilization in Pure and Mixed Methylammonium Lead-Halide Perovskites. *Journal of the American Chemical Society* **139,** 4068–4074 (2017).

143. Wu, X. *et al.* Light-induced picosecond rotational disordering of the inorganic sublattice in hybrid perovskites. *Science Advances* **3,** e1602388 (2017).

144. Yu, P. Y. & Cardona, M. *Fundamentals of Semiconductors* (Springer Berlin Heidelberg, 2010).

145. Yang, Y. *et al.* Observation of a hot-phonon bottleneck in lead-iodide perovskites. *Nature Photonics* **10,** 53–59 (2015).

146. Richter, J. M. *et al.* Ultrafast carrier thermalization in lead iodide perovskite probed with two-dimensional electronic spectroscopy. *Nature Communications* **8** (2017).

147. Yang, Y. *et al.* Comparison of Recombination Dynamics in CH3NH3PbBr3 and CH3NH3PbI3 Perovskite Films: Influence of Exciton Binding Energy. *The Journal of Physical Chemistry Letters* **6,** 4688–4692 (2015).

148. Kandada, A. R. S. & Petrozza, A. Research Update: Luminescence in lead halide perovskites. *APL Materials* **4,** 091506 (2016).

149. Moser, J.-E. Slow recombination unveiled. *Nature Materials* **16,** 4–6 (2017).

150. Hutter, E. M. *et al.* Direct–indirect character of the bandgap in methylammonium lead iodide perovskite. *Nature Materials* **16,** 115–120 (2016).

151. Elliott, R. J. Intensity of Optical Absorption by Excitons. *Physical Review* **108,** 1384–1389 (1957).

152. Gregg, B. A. Excitonic Solar Cells. *The Journal of Physical Chemistry B* **107,** 4688–4698 (2003).

153. D'Innocenzo, V. *et al.* Excitons versus free charges in organo-lead tri-halide perovskites. *Nature Communications* **5** (2014).

154. Saha, M. N. On a Physical Theory of Stellar Spectra. *Proceedings of the Royal Society A: Mathematical, Physical and Engineering Sciences* **99,** 135–153 (1921).

155. Wright, A. D. *et al.* Electron–phonon coupling in hybrid lead halide perovskites. *Nature Communications* **7** (2016).

156. Landau, L. D. in *Collected Papers of L.D. Landau* (ed Haar, D. T.) English translation of the original work from Landau L., Phys. Z. Sowjet., 3, 664, 1933, 67–68 (Elsevier, 1965).

157. Alexandrov, A. S. & Devreese, J. T. *Advances in Polaron Physics* (Springer Berlin Heidelberg, 2010).

158. Emin, D. *Polarons* (Cambridge University Press, 2012).

159. Fröhlich, H. Electrons in lattice fields. *Advances in Physics* **3,** 325–361 (1954).

160. Devreese, J. T. *Fröhlich Polarons. Lecture course including detailed theoretical derivations* 2016. eprint: `arXiv:1611.06122`.

161. Lee, T. D., Low, F. E. & Pines, D. The Motion of Slow Electrons in a Polar Crystal. *Physical Review* **90,** 297–302 (1953).

162. Feynman, R. P. Slow Electrons in a Polar Crystal. *Physical Review* **97,** 660–665 (1955).

163. Selyugin, O. V. & Smondyrev, M. A. Phase Transition and Padé Approximants for Fröhlich Polarons. *physica status solidi (b)* **155,** 155–167 (1989).

164. Smondyrev, M. A. Diagrams in the polaron model. *Theoretical and Mathematical Physics* **68,** 653–664 (1986).

165. Cataudella, V., Filippis, G. D. & Perroni, C. A. in *Polarons in Advanced Materials* 149–189 (Springer Netherlands, 2007).

166. Becker, W., Gerlach, B. & Schliffke, H. Monte Carlo calculation of the ground-state energy of an optical polaron. *Physical Review B* **28,** 5735–5738 (1983).

167. Peeters, F. M. & Devreese, J. T. Comment on "Monte Carlo calculation of the ground-state energy of an optical polaron". *Physical Review B* **31,** 6826–6828 (1985).

168. Batignani, G. *et al.* Probing femtosecond lattice displacement upon photo-carrier generation in lead halide perovskite. *Nature Communications* **9** (2018).

169. Motti, S. G. *et al.* Photoinduced Emissive Trap States in Lead Halide Perovskite Semiconductors. *ACS Energy Letters* **1,** 726–730 (2016).

170. Schmitt-Rink, S., Chemla, D. S. & Miller, D. A. B. Theory of transient excitonic optical nonlinearities in semiconductor quantum-well structures. *Physical Review B* **32,** 6601–6609 (1985).

171. Niemann, R. G. *et al.* Halogen Effects on Ordering and Bonding of CH3NH3+ in CH3NH3PbX3 (X = Cl, Br, I) Hybrid Perovskites: A Vibrational Spectroscopic Study. *The Journal of Physical Chemistry C* **120,** 2509–2519 (2016).

172. Leguy, A. M. A. *et al.* Dynamic disorder, phonon lifetimes, and the assignment of modes to the vibrational spectra of methylammonium lead halide perovskites. *Physical Chemistry Chemical Physics* **18,** 27051–27066 (2016).

173. Quarti, C. *et al.* The Raman Spectrum of the CH3NH3PbI3 Hybrid Perovskite: Interplay of Theory and Experiment. *The Journal of Physical Chemistry Letters* **5,** 279–284 (2013).

174. Stevens, T. E., Kuhl, J. & Merlin, R. Coherent phonon generation and the two stimulated Raman tensors. *Physical Review B* **65** (2002).

175. Trommer, R. & Cardona, M. Resonant Raman scattering in GaAs. *Physical Review B* **17,** 1865–1876 (1978).

176. Sendner, M. *et al.* Optical phonons in methylammonium lead halide perovskites and implications for charge transport. *Materials Horizons* **3,** 613–620 (2016).

177. Ghosh, T., Aharon, S., Etgar, L. & Ruhman, S. Free Carrier Emergence and Onset of Electron–Phonon Coupling in Methylammonium Lead Halide Perovskite Films. *Journal of the American Chemical Society* **139,** 18262–18270 (2017).

178. Zhao, D. *et al.* Low-frequency optical phonon modes and carrier mobility in the halide perovskite CH3NH3PbBr3 using terahertz time-domain spectroscopy. *Applied Physics Letters* **111,** 201903 (2017).

179. Milot, R. L., Eperon, G. E., Snaith, H. J., Johnston, M. B. & Herz, L. M. Temperature-Dependent Charge-Carrier Dynamics in CH3NH3PbI3Perovskite Thin Films. *Advanced Functional Materials* **25,** 6218–6227 (2015).

180. Tsien, R. Y. The Green Fluorescent Protein. *Annual Review of Biochemistry* **67,** 509–544 (1998).

181. Acharya, A. *et al.* Photoinduced Chemistry in Fluorescent Proteins: Curse or Blessing? *Chemical Reviews* **117,** 758–795 (2016).

182. Scholes, G. D. *et al.* Using coherence to enhance function in chemical and biophysical systems. *Nature* **543,** 647–656 (2017).

183. Fuller, F. D. *et al.* Vibronic coherence in oxygenic photosynthesis. *Nature Chemistry* **6,** 706–711 (2014).

184. Gong, X. *et al.* Electron-phonon interaction in efficient perovskite blue emitters. *Nature Materials* **17,** 550–556 (2018).

185. Cho, M. Coherent Two-Dimensional Optical Spectroscopy. *Chemical Reviews* **108,** 1331–1418 (2008).

186. Fayer, M. Dynamics of Liquids, Molecules, and Proteins Measured with Ultrafast 2D IR Vibrational Echo Chemical Exchange Spectroscopy. *Annual Review of Physical Chemistry* **60,** 21–38 (2009).

187. Shim, S.-H. & Zanni, M. T. How to turn your pump–probe instrument into a multidimensional spectrometer: 2D IR and Vis spectroscopiesvia pulse shaping. *Phys. Chem. Chem. Phys.* **11,** 748–761 (2009).

188. Halpin, A. *et al.* Two-dimensional spectroscopy of a molecular dimer unveils the effects of vibronic coupling on exciton coherences. *Nature Chemistry* **6,** 196–201 (2014).

189. Borrego-Varillas, R. *et al.* Two-dimensional electronic spectroscopy in the ultraviolet by a birefringent delay line. *Optics Express* **24,** 28491 (2016).

190. Lewis, N. H. C. & Fleming, G. R. Two-Dimensional Electronic-Vibrational Spectroscopy of Chlorophyll a and b. *The Journal of Physical Chemistry Letters* **7,** 831–837 (2016).

191. Courtney, T. L., Fox, Z. W., Slenkamp, K. M. & Khalil, M. Two-dimensional vibrational-electronic spectroscopy. *The Journal of Chemical Physics* **143,** 154201 (2015).

192. Finneran, I. A., Welsch, R., Allodi, M. A., Miller, T. F. & Blake, G. A. Coherent two-dimensional terahertz-terahertz-Raman spectroscopy. *Proceedings of the National Academy of Sciences* **113,** 6857–6861 (2016).

193. Grechko, M. *et al.* Coupling between intra- and intermolecular motions in liquid water revealed by two-dimensional terahertz-infrared-visible spectroscopy. *Nature Communications* **9** (2018).

194. Harel, E. Four-dimensional coherent electronic Raman spectroscopy. *The Journal of Chemical Physics* **146,** 154201 (2017).

195. Hoffman, D. P., Ellis, S. R. & Mathies, R. A. Characterization of a Conical Intersection in a Charge-Transfer Dimer with Two-Dimensional Time-Resolved Stimulated Raman Spectroscopy. *The Journal of Physical Chemistry A* **118,** 4955–4965 (2014).

196. Valley, D. T., Hoffman, D. P. & Mathies, R. A. Reactive and unreactive pathways in a photochemical ring opening reaction from 2D femtosecond stimulated Raman. *Physical Chemistry Chemical Physics* **17,** 9231–9240 (2015).

197. Zhang, Z., Huerta-Viga, A. & Tan, H.-S. Two-dimensional electronic-Raman spectroscopy. *Optics Letters* **43,** 939 (2018).

198. Kowalewski, M., Bennett, K., Dorfman, K. E. & Mukamel, S. Catching Conical Intersections in the Act: Monitoring Transient Electronic Coherences by Attosecond Stimulated X-Ray Raman Signals. *Physical Review Letters* **115** (2015).

199. Musser, A. J. *et al.* Evidence for conical intersection dynamics mediating ultrafast singlet exciton fission. *Nature Physics* **11,** 352–357 (2015).

200. Tokmakoff, A. *et al.* Two-Dimensional Raman Spectroscopy of Vibrational Interactions in Liquids. *Phys. Rev. Lett.* **79,** 2702–2705 (14 1997).

201. Blank, D. A., Kaufman, L. J. & Fleming, G. R. Direct fifth-order electronically nonresonant Raman scattering from CS2 at room temperature. *The Journal of Chemical Physics* **113,** 771–778 (2000).

202. Molesky, B. P., Guo, Z., Cheshire, T. P. & Moran, A. M. Perspective: Two-dimensional resonance Raman spectroscopy. *The Journal of Chemical Physics* **145,** 180901 (2016).

203. Guo, Z., Molesky, B. P., Cheshire, T. P. & Moran, A. M. Elucidation of reactive wavepackets by two-dimensional resonance Raman spectroscopy. *The Journal of Chemical Physics* **143,** 124202 (2015).

204. Kuramochi, H. *et al.* Probing the early stages of photoreception in photoactive yellow protein with ultrafast time-domain Raman spectroscopy. *Nature Chemistry* **9,** 660–666 (2017).

205. Cho, M. *et al.* Intrinsic cascading contributions to the fifth- and seventh-order electronically off-resonant Raman spectroscopies. *The Journal of Chemical Physics* **112,** 2082–2094 (2000).

206. Blank, D. A., Kaufman, L. J. & Fleming, G. R. Fifth-order two-dimensional Raman spectra of CS2 are dominated by third-order cascades. *The Journal of Chemical Physics* **111,** 3105–3114 (1999).

207. Wilson, K. C., Lyons, B., Mehlenbacher, R., Sabatini, R. & McCamant, D. W. Two-dimensional femtosecond stimulated Raman spectroscopy: Observation of cascading Raman signals in acetonitrile. *The Journal of Chemical Physics* **131,** 214502 (2009).

208. Dunlap, B., Wilson, K. C. & McCamant, D. W. Phase-Matching and Dilution Effects in Two-Dimensional Femtosecond Stimulated Raman Spectroscopy. *J. Phys. Chem. A* **117,** 6205–6216 (2013).

209. Herzberg, G. & Teller, E. Schwingungsstruktur der Elektronenübergänge bei mehratomigen Molekülen. *Zeitschrift für Physikalische Chemie* **21B** (1933).

210. Duschinsky, F. The importance of the electron spectrum in multi atomic molecules. Concerning the Franck-Condon principle. *Acta Physicochim. URSS* **7,** 551–566 (1937).

211. Kupka, H. & Cribb, P. H. Multidimensional Franck–Condon integrals and Duschinsky mixing effects. *The Journal of Chemical Physics* **85,** 1303–1315 (1986).

212. Dierksen, M. & Grimme, S. Density functional calculations of the vibronic structure of electronic absorption spectra. *The Journal of Chemical Physics* **120,** 3544–3554 (2004).

213. Gnanasekaran, R. Normal modes and the Duschinsky mixing of the ground- and excited-state vibrations of the green fluorescent protein chromophore. *Chemical Physics Letters* **587,** 61–67 (2013).

214. Siebrand, W. & Zgierski, M. Z. The dushinsky effect in resonance Raman spectroscopy. *Chemical Physics Letters* **62,** 3–8 (1979).

215. Hassing, S. & Mortensen, O. S. The roles of vibronic coupling and the Duschinsky effect in resonance Raman scattering. *Journal of Molecular Spectroscopy* **87,** 1–17 (1981).

216. Shimomura, O., Johnson, F. H. & Saiga, Y. Extraction, Purification and Properties of Aequorin, a Bioluminescent Protein from the Luminous Hydromedusan,Aequorea. *Journal of Cellular and Comparative Physiology* **59,** 223–239 (1962).

217. Chalfie, M. Green fluorescent protein as a marker for gene expression. *Trends in Genetics* **10,** 151 (1994).

218. Heim, R. & Tsien, R. Y. Engineering green fluorescent protein for improved brightness, longer wavelengths and fluorescence resonance energy transfer. *Current Biology* **6,** 178–182 (1996).

219. Duwé, S. *et al.* Expression-Enhanced Fluorescent Proteins Based on Enhanced Green Fluorescent Protein for Super-resolution Microscopy. *ACS Nano* **9,** 9528–9541 (2015).

220. Shi, S., Kumar, P. & Lee, K. F. Generation of photonic entanglement in green fluorescent proteins. *Nature Communications* **8** (2017).

221. Van Thor, J. J. Photoreactions and dynamics of the green fluorescent protein. *Chemical Society Reviews* **38,** 2935 (2009).

222. Salna, B., Benabbas, A., Sage, J. T., van Thor, J. & Champion, P. M. Wide-dynamic-range kinetic investigations of deep proton tunnelling in proteins. *Nature Chemistry* **8,** 874–880 (2016).

223. Eccleston, A. GFP in Motion 2. *Trends in Cell Biology* **11,** 311 (2001).

224. Drobizhev, M., Makarov, N. S., Tillo, S. E., Hughes, T. E. & Rebane, A. Describing Two-Photon Absorptivity of Fluorescent Proteins with a New Vibronic Coupling Mechanism. *The Journal of Physical Chemistry B* **116,** 1736–1744 (2012).

225. Kamarchik, E. & Krylov, A. I. Non-Condon Effects in the One- and Two-Photon Absorption Spectra of the Green Fluorescent Protein. *The Journal of Physical Chemistry Letters* **2,** 488–492 (2011).

226. C. Fang, R. R. Frontiera, R. Tran, R. A. Mathies. Mapping GFP structure evolution during proton transfer with femtosecond Raman spectroscopy. *Nature* **462,** 200–204 (2009).

227. Witschel, W. Harmonic oscillator integrals. *Journal of Physics B: Atomic and Molecular Physics* **6,** 527–534 (1973).

228. Messiah, A. *Quantum Mechanics* (John Wiley & Sons Inc, 1964).